12-22-2016

Improvements to Micro-Contact Performance and Reliability

Tod V. Laurvick

IMPROVEMENTS TO MICRO-CONTACT PERFORMANCE AND RELIABILITY

DISSERTATION

Tod V. Laurvick, Major, USAF

AFIT-ENG-DS-16-D-003

DEPARTMENT OF THE AIR FORCE
AIR UNIVERSITY

AIR FORCE INSTITUTE OF TECHNOLOGY

Wright-Patterson Air Force Base, Ohio

AFIT-ENG-DS-16-D-003

IMPROVEMENTS TO MICRO-CONTACT PERFORMANCE AND RELIABILITY

DISSERTATION

Presented to the Faculty

Graduate School of Engineering and Management

Air Force Institute of Technology

Air University

Air Education and Training Command

in Partial Fulfillment of the Requirements for the

Degree of Doctor of Philosophy

Tod V. Laurvick, B.S.E.E., M.S.E.E.

Major, USAF

22 December 2016

AFIT-ENG-DS-16-D-003

IMPROVEMENTS TO MICRO-CONTACT PERFORMANCE AND RELIABILITY

DISSERTATION

Tod V. Laurvick, B.S.E.E., M.S.E.E.
Major, USAF

Committee Membership:

Dr. Ronald A. Coutu, Jr.
Committee Co-Chair

Capt. Robert A. Lake, Ph.D.
Committee Co-Chair

LtCol Michael R. Hogsed, Ph.D.
Committee Member

Dr. LaVern A. Starman
Committee Member

Dr. Adedeji B. Badiru
Dean, Graduate School of Engineering and Management

Abstract

Microelectromechanical Systems (MEMS) based devices, and specifically micro switches, continue to offer many advantages over competing technologies. To realize the benefits of micro-switches, improvements must be made to address performance and reliability shortfalls which have long been an issue with this application. To improve the performance of these devices, the micro-contacts used in this technology must be understood to allow for design improvements, and offer a means for testing to validate this technology and determine when such improvements are ready for operational environments. To build devices which are more robust and capable of continued operation after billions of cycles requires that improved fabrication techniques be identified and perfected to allow for more sophisticated designs to be tested. This work explores and advances two potential fabrication techniques to suit this task: nanosphere lithography and grayscale lithography. By utilizing 3-D printed deposition vessels, a method of nanosphere assembly is demonstrated which repeatably produces over 50% surface coverage. A hybrid photoresist / nanosphere patterning technique is then demonstrated, to allow for precise alignment of nanospheres required for integration into device fabrication. An alternate method of fabrication which utilizes improved grayscale lithography is also demonstrated. This technique allows for rapid fabrication of complex three dimensional structures as part of a full wafer fabrication process, resulting in twice the resolution from previous efforts using the same hardware. This provides a customizable patterning technique for the thousands of devices with near-perfect repeatability of duplicate devices, or complete customization of each device if desired. Another crucial fabrication characteristic of micro-contacts involves the thin-films used as a contact surface. This work demonstrates that integration

of thin-film spreading resistance theory into the most advanced contact resistance models to date results in a reduction in the variance between predicted vs. observed results by approximately 70%. External factors to micro-contact performance are also explored, providing information critical to designers to create devices better suited for extremely long performance. Low frequency AC testing was conducted to bridge the gap between RF applications and DC conditions typically used to characterized these devices. The results show that low frequency, low amplitude AC signals have potential to greatly accelerate device failure. For example, in devices proven to work well under DC conditions (e.g. still operating after 10 million cycles), with AC signals applied, 10 out of 11 devices failed before reaching 10 million cycles. However, the addition of protective external circuit configurations conclusively shows this damage can be mitigated, with only 2 out of 15 devices failing in subsequent tests. Finally, data gathered from devices during failure reveal an indicator which may provide a novel method of predictive failure detection. This method could one day be applied in-situ, to diagnose and identify devices in which failure is imminent and allow for corrective action to minimize impacts to overall functionality.

Acknowledgements

I would first like to sincerely thank my advisor, Dr. Ronald Coutu for his guidance, persistence, friendship, and never-ending efforts over the past three years in setting me up for success not only in completing this degree, but in my career for many years to come. I would also like to thank for Dr. Robert Lake for taking up the challenge of co-advising me on this research and supporting this work during and after Dr. Coutu's transition to Marquette University. I also appreciate the support of the rest of the MEMS group, many students and friends who have made this such a successful team along the way, as well as the AFIT cleanroom technicians and AFRL sensors group for tirelessly providing support every step of the way. I would finally like to thank my family and friends for the constant support and never doubting in my ability and will to see this challenge through.

Tod V. Laurvick

Table of Contents

Page

Page

List of Figures

Figure Page

List of Tables

List of Abbreviations

IMPROVEMENTS TO MICRO-CONTACT PERFORMANCE AND RELIABILITY

I. Introduction

Microelectromechanical Systems (MEMS) based devices, and specifically micro-switches, continue to offer many advantages over competing technologies. The scale of these devices allows for a large numbers to be fabricated in a single run and because there is little material used, this translates to very small material costs per device. The size offers an advantage in that less weight is required to carry them, less room to house them and less power to operate them. This size also comes with a disadvantage in that the power which can be carried through these smaller structures is limited when compared to a larger device made of the same material. Thus high-power applications may prove challenging for these types of devices. However, the miniaturization trend of other electronics such as cell phones, laptops, tablets, etc. demand lower power consumption, reduced size and all at a reduced cost. So for most applications, power limitations may not necessarily be an issue. As many of today's potential military applications rely either on commercially available technology or on components used in commercially manufactured devices, we too have an interest in seeing this technology advance. Considering the circuit design limitations on applications such as satellites, aircraft, and weapons systems. Smaller, cheaper, lower power consuming devices are a prime concern, just as they are in commercial applications. But this is only acceptable if performance and reliability can be ensured. Making these assurances requires that we not only possess the ability to test devices to sufficient lifetimes, but also that we understand the underlying theory behind their

operation and failure so issues can be identified and corrected, and those corrections validated in future designs.

The improvement of these devices will provide benefits in many areas of technology as was already mentioned, but these benefits will come in many forms. These may include greater bandwidths, lower power consumption, and enhanced reliability. To make these improvements, MEMS engineers need the capability to study the performance evolution of micro-contacts by examining the physical and chemical phenomena at the interface under controlled conditions. Previously at AFIT, a novel test fixture concept was realized and tested, and advancing this capability is key to conducting the necessary reliability testing. This research focused on full utilization of that test fixture which would allow future MEMS engineers to study the performance evolution of micro-contacts.

To test devices to their expected lifetime can be a time consuming effort without the proper approach. First, we will consider what is an appropriate 'expected lifetime.' The answer to this question depends entirely upon the application. If we're talking about a weapon system, then one cycle may be sufficient provided we have 100% reliability. Other applications will carry other requirements and possibly under a different set of conditions. For example, satellites may be in operation for up to decades, but in an environment of extreme temperatures, pressures, radiation exposure, etc. However, something like a mobile communication application is likely to present a much more temperate environment, but with potential air contaminants, moisture and whatever rough treatment the user inflicts on the device. Many factors such as temperature, vibration, shock, atmospheric exposure, etc. can be mitigated through design, but three basic factors are inherent to the micro switch and no amount of mitigation will correct for any shortcomings:

- What contact resistance is reached by the micro-contact within the micro switch?

- How much variance is present in the contact resistance?
- How many cycles does the device operate before failure or unacceptable degradation of performance?

The most current models for micro-contact resistance account for many critical considerations. As we continue to improve resolution and drive for further miniaturization, other considerations which may have once been negligible may now be of much greater significance. For example, improvements in material deposition techniques allow for thinner, more uniform thin films. The ability to now produce these high quality yet extremely thin-films require us to make special considerations in our models to account for their impact on overall performance.

The variance in contact resistance is the second factor which must be considered. How critical a factor this variance is depends entirely upon the application. Also, it is important to note that variation in a measured value depends entirely on how large that number is. For example, two contacts may vary in contact resistance by +/- 0.1 Ω, but if that variance is an issue depends on the mean values observed. For a contact which we expect to have a resistance of approximately 100 Ω then this variation is likely to be considered excellent, but if the contact nominally operates at 0.01 Ω then this variance is a bit more difficult to work with. Because of this, the necessity of minimal contact resistance must be evaluated, as well as how much that resistance may vary. The methods for fixing these variabilities may be entirely different, but are not necessarily independent of each other. To address the ability to be able to fine-tune contact resistance and hold it to a specific amount of variability requires that improvements in fabrication techniques be incorporated. To accomplish this, both utilization of key materials and surface engineering techniques are critical.

Finally, there is the question of reliability. Mature MEMS designs for RF applications are between 100 million to 40 billion cycles, however many systems require up to

200 billion cycles of operation[1]. Holding this high number of cycles ensures a design which will work for any application, even a single shot weapon system. Several applications are very likely to demand billions of cycles, such as radio frequency (RF) or other communications and/or high speed data processing applications. Others might be able to sacrifice 1 or 2 orders of magnitude if it means better performance and/or smaller variation such as low speed digital logic, control signals, etc. To test to these large numbers of cycles requires specifically designed hardware. Such a test stand must be able to impose realistic loads upon the switches being tested while mechanically cycling them, all while metering performance. Most importantly, it must be able to reach billions of cycles in a reasonable time. The first generation of this test stand has already been built and validated, and with the hardware used is capable of operating up to 2.5 kHz. While this is sufficient for millions of cycles, to reach even 10 billion cycles at this speed would require 47 days of cycling, plus the time required to take measurements. Fortunately, even though this technology is only a few years old, in that time improvements have been made to the underlying hardware which can increase our testing frequency significantly. Focusing on the speed limiting components, the piezo actuator is currently the limiting factor in our testing speed. Replacing this actuator with a more current state of the art version allows for an increase to the operating frequency to a range of 20-40kHz, which allows for 10 billion cycles to be reached in 3-6 days.

Thus, the focus of this work is to identify and incorporate changes which address these factors by addressing three areas: innovative device design, accurate contact resistance modeling and a better understanding of operational considerations. Design elements will focus on determining if a device can be fabricated in a way that takes advantage of the physics of ballistic electron transport. This can be done in theory by restricting the contacting surface to several small areas and designing these features

to withstand billions of cycles of operation. This will require a review of the best techniques which are readily available to identify those that can provide adequately sized feature, with repeatability between devices, which can be fabricated in a reasonable amount of time, and can be integrated into the overall device fabrication process. To improve modeling of contact resistance, thin-film spreading resistance needs to be integrated. By starting with theoretical models of thin-film spreading resistance, these can be applied to the existing contact resistance models and through utilizing test data, the effectiveness of these new models can be evaluated. Finally, operational considerations will be explored. In an effort to better understand how these devices operate and fail under RF conditions, low frequency AC will be considered. In addition to examining electrical loading, neighboring circuits and the effects of these type of elements will also be explored to identify which practices should be avoided and which may be used to our advantage.

II. Literature Review

2.1 Background

The ability to quickly and reliably control current flow is one of the most basic requirements of any circuit. The first macro-scale switches eventually led to solid state alternatives which then found their way into many applications. These solid state devices went through a continual reduction in scale which is still going on today in the form of computers, cell phones, etc. However, for other applications such as relays, light switches, appliances and many commercial products, mechanical-contact based switches are still widely utilized. Micro-scale versions of these mechanical contact based switches have been developed. For the past decade or more, possible applications which could benefit from micro switch technology have been widespread, including RF devices [2–4], integration with solid state electronics [5] and microwave applications [6].

The scale of a MEMS switch provides many benefits but imposes some unique challenges. These challenges required modifications to the models we used to describe macroscopic switches to ensure they applied to devices of this scale. As with any switch, selecting a material with a suitable resistance is important, but a material's other properties may be just as critical. The smaller scale of these devices translate to extremely small contact areas. This means higher current density which may lead to higher heat production over this smaller area. At the same time, the smaller amounts of material contains very little volume, which means relatively small total heat capacity. Thus, these devices often require very little energy in the form of heat for the entire device to become malleable or even become liquid [7]. Similarly, considerations of surface roughness, hardness, elasticity, etc. or what we might call

mechanical properties are just as great a concern. In order to identify areas in which contributions can be made in this field, a review of each needs to be conducted.

How to change fabrication of these devices to address what we learn from modeling and experimental data is the next logical step. MEMS devices commonly use thin films in their construction which imparts some additional unique physics to their design. Work continues in theorizing thin film behavior. Validating this theory and integrating it with modern contact resistance models still needs to be accomplished.

Also, at these smaller scales the impact of non-uniform surfaces adds a great deal of complexity to estimating true contact area. Fortunately, incorporating more advance fabrication techniques to build these smaller features will aid in controlling this source of variability. Engineering the contacting surfaces such that they have smaller, more controllable features minimizes the effects of surface features of the thin-films used to cover these features. The ability to build these features becomes possible with techniques such as nanosphere lithography (NSL) or grayscale lithography. Therefore, as we engineer these smaller features to address our immediate design goals, effects such as surface asperities become less influential, but concepts such as spreading resistance become more influential.

2.2 Micro Switch Contact Resistance Modeling

While there are many physical characteristics which influence the performance of a typical micro-contact, we will focus on the two issues mentioned previously: which material to use and how to design our contacting surfaces. While that limits the scope of the problem to a degree, this is still an extremely complex issue with many areas to consider simultaneously, as illustrated in Figure 1 below. In general, most of the issues encountered in micro-contact performance will fall into one of the three categories shown. Thermal effects relate primarily to heat buildup or dissipation,

Mechanical effects are those which change our contact area, and Chemical effects are those which change the material itself at the surface and/or bulk of the material. Also shown are examples of how these effects can influence each other. All may factor into the overall design and how we choose materials to use, processes to follow, and structures to build.

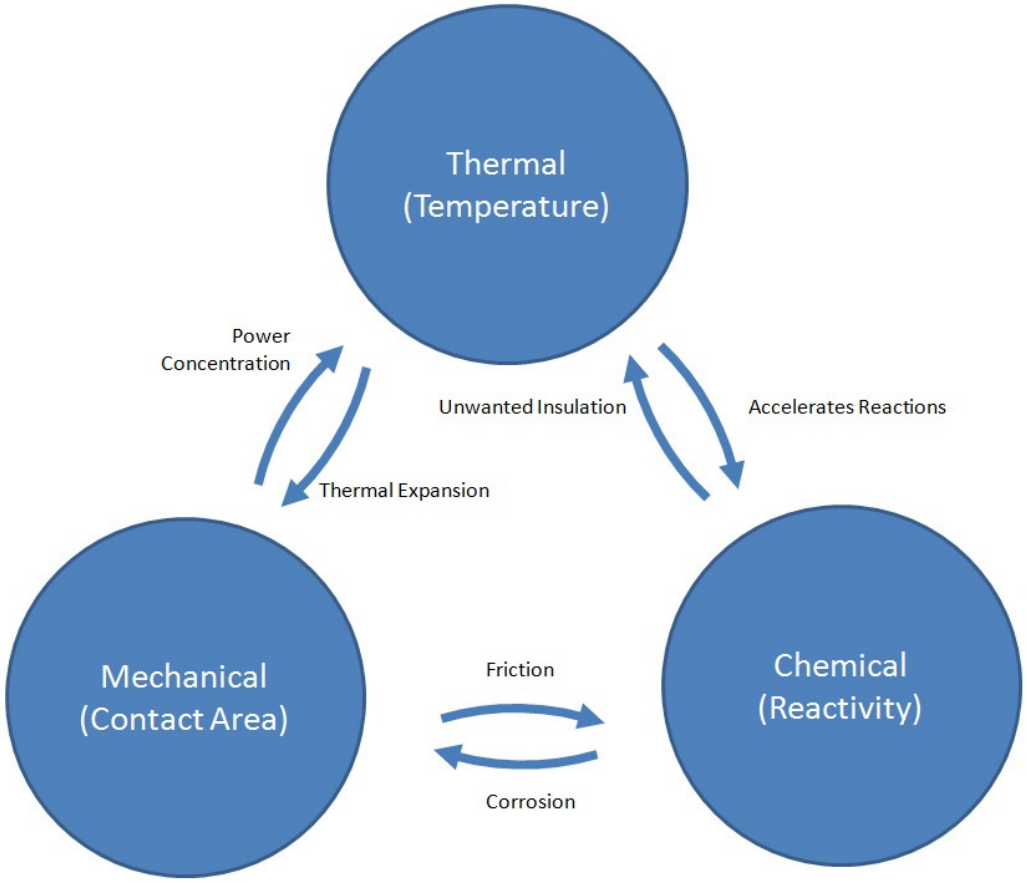

Figure 1. Interaction between Thermal, Mechanical, and Chemical effects in relation to micro switch behavior.

If we examine each of these categories more closely, each category can be characterized by a number of material parameters summarized in Figure 2 below. For each of the three categories, this provides a reference of the kinds of properties which ultimately may affect each category. For example, under thermal effects, in general

a low thermal expansion is advantagous as this minimizes geometric changes to our device, but under Mechanical effects, a high yield is in general preferred to minimize the chance of our contacts forming fractures when cycled. There may be specific cases in which a particular effect is not desired. For example, we may choose materials that have high and low thermal conduction in the same design in order to direct heat flow. In general however, for the contact itself this chart gives us an idea of what properties are desired or at least which should be considered.

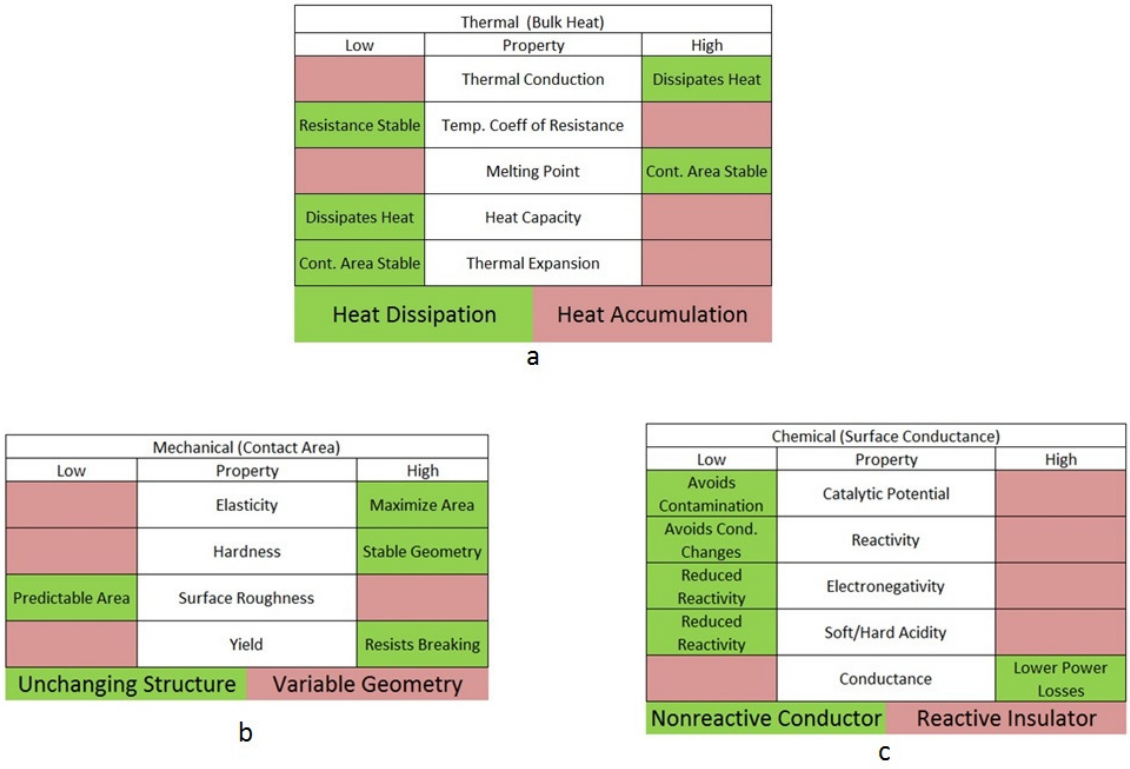

Figure 2. Classification of a) Thermal, b) Mechanical, and c) Chemical parameters of interest in micro-switch material selection and design indicating desirable conditions for each.

It should be noted that this is not an all-inclusive list. For example, quantum effects could be included as a fourth category, but to avoid over-complicating the discussion we present this arrangement as a starting point.

To begin the search for what work has been done in relating these effects to micro contacts, it's also worth mentioning that we may choose a material for a specific material property it possesses, but how we process that material or how it is operated may alter its properties. In the selecting materials, we must consider how those materials are deposited as that deposition may change properties we are interested in. Also, we must consider what the exact composition is and how that may change due to different deposition methods or post processing [8]. For example, different methods exist for depositing many metals but they also may vary the uniformity and density of the material, which may in turn change the overall hardness, as well as the roughness of the surface. As surface roughness changes, depending on the number and size of what surface features are present, we may change the surface area of a micro-contact made from this material. This change in overall surface area may then affect the ability to dissipate heat by minimizing paths of thermal conduction or cause heating by concentrating current density across the smaller area. If our material was chosen for its ability to dissipate heat, we must ensure that we do not inhibit its ability to do so. Thus, something as simple as choosing between sputtering versus electroplating may result in significant differences in the final design even though we started with the same material.

In addition to material considerations, we also need to consider the design itself and how that design is to be used. While that design may be limited by various constraints, design choices impact how the device operates which impacts performance. For example, the force at which our contact closes, the shape of our contacting surfaces, the overall contact area, how our surfaces meet geometrically; all are just a few of the considerations we have some level of control over in designing the contact, but at the same time we must consider how these impact the overall design.

It also helps at this point to define exactly what we consider an ideal contact. We mentioned in Chapter 1 that this might be one in which contact resistance is minimized, but resistivity is only one of the three defining traits; variability and lifetime must also be considered. If we assume ideal to imply a contact that has the lowest resistance overall, the lowest observed resistance may not occur until after a device has been broken in, or exposure to a particular gas may cause a reaction and change the material properties at the surface. How consistent that resistance is and the overall longevity may be just as important, and possibly in some cases more important than contact resistance. We won't attempt to balance these items, but instead focus on the minimization of resistivity as our primary goal. In the end, all of these factors should be addressed during contact design.

2.2.1 Thermal effects.

Thermoelectric effects have been studied from as far back as the 1800s with Seebeck, Magnus and Peltier to name a few. The history of thermoelectric effects (summarized in Figure 76 in Appendix C) have found its way into a variety of MEMS applications, but those applicable to micro-contacts are limited in the current literature. The effects of temperature upon not only resistivity, but all of the other material properties that affect operation are still substantial. We can partially mitigate thermal difficulties by assuming standard temperatures and controlling to that temperature, or at least bound our operating temperatures to a small range (i.e. cryogenically induced superconductivity). In those smaller ranges of temperature, the resistivity of the bulk material is well understood and can accurately be modeled as linear [9]. Note however that as we discuss other effects like surface oxidation, friction polymerization, etc., considering the effect of temperature on resistivity alone isn't enough. As will be mentioned later, temperature and pressure are the two pri-

mary driving forces in almost any chemical reaction, as temperature provides the energy often needed to hasten these reactions while pressure ensures reactants are in close enough proximity to react. We can go through the exercise of defining our optimal operating temperature, but we must keep in mind that even in a relatively stable environment, the temperatures our contact experiences may be vastly different [10].

In the operation of a contact, especially over several cycles we can expect repeated mechanical impact to generate heat caused by the initial impact and repeated bouncing of the contacting surfaces. This idea of contact bounce has been well studied on larger scale devices [11–19]. As we will discuss with mechanical effects, thermal effects can be minimized to a degree in our design if we consider how this impact velocity will affect the materials which initially come in contact during contact closure. Ideally, we can design a contact to close with less force, but in the event that we require rapid cycling we may not have this luxury. In that case, we must then look to materials properties, possibly choosing one with a higher melting point or better thermal conductivity and thus capable of withstanding the impact of this repeated closure without softening or melting, but at the same time still delivering consistent results.

Related to this issue is the consideration of hot versus cold switching [20]. In general, it is much easier to design a contact which delivers repeatable, low resistance for many cycles in a cold switch environment. One source reported that in testing spluttered gold contacts, it was observed that average device lifetime was over 2 billion cycles when cold switched, but only 500 million cycles if hot switched [21]. Other materials show similar trends [22–25]. However, how a contact is utilized in an overall circuit design may operationally make it impractical to operate under cold switching conditions. For that reason, both modes of operation may need to be considered.

There have been a number of studies in this area which attempt to quantify acceptable limits which can prevent detrimental conditions which can contribute to premature degradation or failure during rapid cycling [26–30]. Also, the reliability and lifetime of contacts could be impacted by electrical loading conditions [10], more specifically the types of circuit elements connected to the contact during operation.

Finally, we must also consider unwanted heat and how it may damage our contacts [31]. Fortunately, most materials which are typically used in contacts also tend to be good thermal conductors. However, any surface chemistry may induce a film which acts as an insulator, inhibiting thermal conductivity. Similarly, should we consider design features that are out of the ordinary, we must consider the impact these decisions may have on thermal conduction. For example, devices packaged in an inert gas to minimize exposure to reactants may also limit cooling in the process. Should temperature differentials be allowed to develop between the contact and the bulk temperature, contact resistance can be impacted [32–34]. Also, it has been observed that unwanted heat accumulation in a contact metal can affect the chemical makeup of the material by promoting diffusion oxidation which will be discussed more in the chemical effects section [35, 36] or possibly inducing a phase change or other thermally induced condition.

2.2.2 Mechanical effects.

To date, the mechanical considerations which go into designing a contact have been considered quite extensively as shown in Figure 78 found in Appendix C. This is due in large part to the impact of these properties on actual contact area, and as will be discussed later the importance of contact area in micro-contact performance. From the most basic forms which assume ideally smooth contact areas and diffuse electron transport [37], numerous modifications have been included to address non-

idealities which are known to drastically affect how a contact performs. Among these variations to ideal theory are how low contact force, which in turn produces small contact areas can lead to more ballistic electron transport characteristics [38, 39], the effects of elastic versus plastic behavior of contact materials on resistance [37, 40, 41] and a great deal of work in addressing the impact of surface roughness on contact resistance [42–46].

2.2.2.1 Surface roughness.

Research in surface roughness addresses that in micro-contacts, small irregularities on the surface of a contact (a.k.a. asperities) play a much more drastic role than they do in macroscopic contacts. Since this idea of surface roughness inhibiting contact area affects both macroscopic and microscopic contacts, there is an extremely large body of work dating back several decades to describe surface roughness using a variety of methods. Since these asperities are often on a scale much smaller than even micro-contacts surface area, this work is in general applicable to both kinds of contacts. Under relatively large forces, models have existed for quite some time which describe how these multiple asperities can be treated as a single effective contact area [47, 48]. Under smaller forces, how these asperities behave in conjunction with elastic behavior has also been modeled and tested [9, 40]. These various models have been combined forming unified theory providing better results [41, 49], however the currently accepted model also adopts the use of a gamma function to combine the effects of ballistic vs. diffuse transport [41]. This is in recognition that a model which attempts to use an effective equivalent area for use in predicting contact resistance is going to arrive at two very different answers depending on which approach is taken. Conceptually this makes sense. If we were to consider a field of asperities versus a single region of equal contact area, the equation for purely ballistic electron transport is proportional to

$1/r_{eff}^2$ [50], as illustrated by Equation 3. This relationship is found by starting with the expression for the Sharvin resistance given by:

$$R_B = \frac{4\rho K}{3\pi r_{eff}}. \tag{1}$$

Noting that ρ is simply the resistivity and K is the Knudsen number, which is the ratio of the mean free path of an electron to the unit of length representative of the area through which the electron is able to pass [38, 51, 52], given by:

$$K = \frac{l}{r_{eff}}. \tag{2}$$

Thus if we substitute this back into Equation 1 we obtain:

$$R_B = \frac{4\rho l}{3\pi r_{eff}^2}. \tag{3}$$

Now compare this to Holm's standard diffuse theory in which this proportionality is just $1/r_{eff}$[37]:

$$R_D = \frac{\rho}{2r_{eff}}. \tag{4}$$

Thus, the two approaches form the upper and lower boundaries to unify the two theories into a single model. A model describing the spectrum from purely diffuse to purely ballistic electron transport, and is given by [53]:

$$R_W = R_B + \Gamma(K)R_D \tag{5}$$

As is evident, this number drives the function $\Gamma(K)$ which varies from 0 for a purely Ballistic transfer where the relatively large diffusive term vanishes to 1 for purely Diffusive, where the smaller Ballistic term is negligible. This was originally

derived by Mikrajuddin *et al.*, and is given by Equation 6 and plotted in Figure 3 [53].

$$\Gamma(K) \approx \frac{2}{\pi} \int_0^\infty e^{-Kx} Sinc(x) dx \tag{6}$$

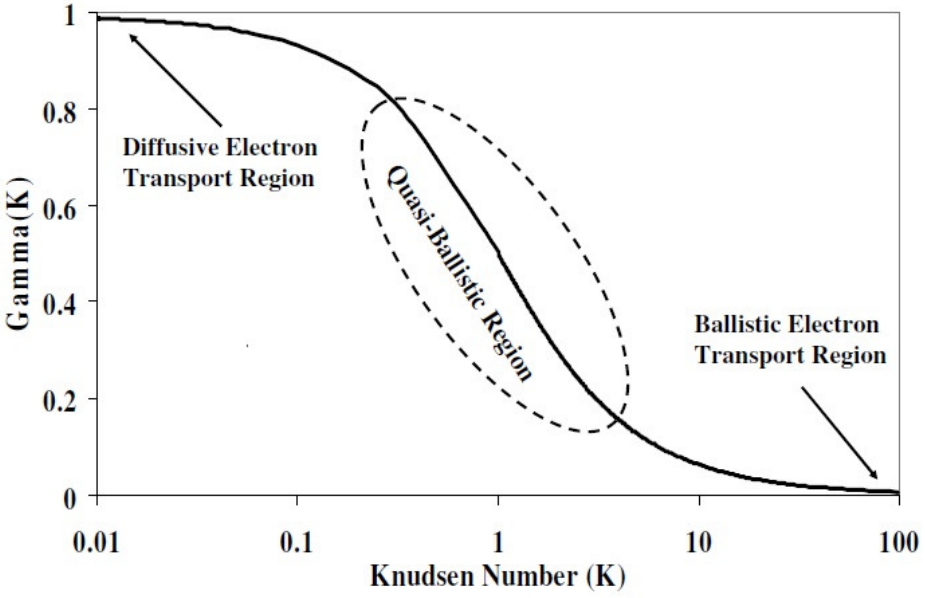

Figure 3. A plot of Mikrajuddin *et al.*'s derived Gamma function [53].

One inherent issue in studying and characterizing roughness of surfaces is how to account for these non-uniformities, specifically when a surface contains a variety of asperity sizes simultaneously [54]. This is another area that has been studied for several decades, utilizing approaches ranging from mathematically averaging radii of curvature [55], statistical analyses [56, 57], fractal geometric and finite element modeling [58–60]. As with most models, these were improved over time to encompass physical aspects not considered in the original model. For example, basic fractal models were modified to include elasticity [61, 62], and remove resolution dependence [63, 64]. From this, more recent models have been developed to better represent this

complex characteristic through more practically useful means, and applicable to more common applications [54, 65].

As already mentioned, these asperities and the resulting ballistic and quasi-ballistic transport can affect contact performance under light loading, but even under steady-state conditions the surface roughness may have a direct impact on the overall contact area, particularly if two dissimilar materials are used and neither can conform to the shape of the other. To evaluate the impact of various material properties, studies have been performed with contacts of various material compositions [66–68].

Depending on the material, the quality of the surface may be impacted by either selecting different deposition methods or treating the deposited material through some form of post-processing including annealing, chemical processes, or some other surface treatment. While exact details can be material dependent, fortunately this question of surface roughness has been identified for a long time and there is a great deal of research available in this area [40, 44, 46, 55–57, 60, 61, 69–71].

2.2.2.2 Hardness and Elasticity.

In considering the idea of surface quality being impacted by the deposition process, other physical characteristics which are just as important to contact performance can also be greatly impacted during the fabrication process. For example, the hardness of material such as gold can vary with the technique used for deposition [8], how it is post-processed, and how the final device is operated. Thus, while models have been developed to indicate predictive hardness of various materials, in reality there is a wide variety of methods of deposition, post-processing, and environment of operation. It is also possible that such models only provide an ideal estimate and as hardness and elasticity may change over time, these models may begin to deviate from actual measured resistances. Consider how soft materials would behave in a contact after

several million cycles as opposed to a harder material, better capable of withstanding such repeated impacts without becoming deformed. How such characteristics are modeled are difficult to capture considering all of these subtle nuances. Such models may serve as a good starting point, but it must be recognized that in some cases they may only serve as an estimate. As material properties may change, even measuring something such as hardness in deposited layers only provides an initial indication of performance. Unless its deformation remains entirely elastic for every cycle throughout the life of the device, some compression will eventually occur effectively changing the hardness, even if just in a few small regions.

We also must consider in our design how the contact will operate and if that operation will affect the physical structure we've built [32]. For example, let's assume a micro-switch is actuated electrostatically, one of the more common forms of actuation [72]. The amount of force applied is inherently limited, as the area between the actuating arm and the applied actuation voltage defines this force. Let's assume our primary concern is overall lifetime of the switch (i.e. wear of the contacting surfaces) and so we may wish to choose an extremely hard material for one of the surfaces. This may imply that a more elastic material may be ideal for the mating surface, to provide better surface contact area by allowing the contacts to better form to each other's surface geometries. If we consider the speed at which the switch operates this may not be the case. If the actuation voltage is changing rapidly this results in swift actuation and possibly a corresponding large impact force. With a softer mating contact surface, we are repeatedly impacting hard material onto a soft material. This hammering of the softer material may in fact induce plastic deformation, gradually deforming the contact by inducing creep [73], or even cause it to fracture. In any case it becomes much less elastic than what we anticipated in our design. Thus for such a situation we may be forced to choose a softer material that is somewhat less

elastic but with a higher yield strength and/or a more elastic harder material. Ideally if we are striving for contacts that lasts indefinitely, then we want to stay as much as possible in the area of elastic deformation only, ideally well below the yield strength of the material [74]. The key point however is that regardless of what the intended mode of operation may be, any one material property may contribute both positively and negatively to a contact when everything is considered together.

2.2.3 Chemical effects.

Next we will discuss three types of chemical effects which are of interest when considering micro-switches. These are corrosion and oxidation, frictional polymers and electromigration.

2.2.3.1 Corrosion and Oxidation.

The effects in this category are simply addressing the issue of a material's susceptibility to other components it will be exposed to during operation. Since most contacts operate under standard atmospheric conditions, vulnerability to oxygen, water, and carbon dioxide are the primary concerns, as these are the most reactive elements commonly found in this environment in high enough concentrations.

While oxidation is probably the most common form of contact contamination, regardless of its composition a nonconductive contamination layer can have a severe impact on contact resistance [75–77]. Therefore, for pure metals this is typically quantified by determining how easily the material oxidizes and if that oxide is or is not conductive. How easily this oxidation occurs is well-documented for most pure materials. For example, some metals such as magnesium take very little energy to completely oxidize upon exposure to the environment. Other metals, such as gold, are extremely resistant to oxidation and are therefore often employed as contact materials

[78, 79]. Most other metals will fall somewhere between these extremes, but even in this spectrum, behaviors will vary. For example, iron is easily and quickly oxidized under normal atmospheric conditions, but once started the oxide formed accelerates the process destructively to the point of the metal being completely consumed.

Compare this to aluminum, which also reacts with oxygen quite readily but does so in a way in which it forms a self passivation layer preventing further oxidation from consuming the material. This may be desired to hinder corrosion while undesired as it impacts contact resistance. The most common way to avoid unwanted oxidation is through the formation of alloys. For example, by adding a little over 10 % chromium to pure iron we can form stainless steel, which shows the strength of iron without susceptibility to rusting. This approach is effective because the chromium present oxidizes much more readily than the iron, migrating to the surface as it reacts with oxygen and in effect creates a passivation layer of chromium oxide which can resist further oxidation much the same as aluminum does and protect the iron underneath. Some work has been performed which starts to develop this concept in using Au and Ru contact materials [53, 66, 80], and similar approaches may be possible with electrical contacts if either the oxide formed is highly conductive, or some other material other than oxide is intentionally deposited on the surface as an engineered passivation layer, such as current research which has been developed in graphitic layers [81, 82] and carbon nanotubes (CNTs) [83–91].

While other atmospheric compounds could be researched and addressed, it is far more efficient to instead review the contact material of interest and what components it is susceptible to react with. For example, consider that the most conductive pure metal is Silver. Silver is extremely resistant to oxidation and in fact does not oxidize in air. It does however react with any amount of hydrogen sulfide, as well as other gasous forms of sulfer, pulling even the smallest concentrations from the air and forming what

is commonly known as tarnish. The sulfer in this layer retains its attraction to silver, and thus it is extremely difficult to remove. It is also non-conductive, causing silver to be an unpopular choice for MEMS contacts despite its excellent conductive properties.

2.2.3.2 Frictional polymers.

Another phenomena often discussed in literature is various forms of organic films forming on contacts, which have the effect of slowly degrading contact resistance [33]. This phenomena is often referred to as frictional polymerization [92]. In some cases these films can form spontaneously, in other cases they seem to be accelerated through the mechanical application of energy, a process which some have referred to as tribochemistry [93]. Tribochemistry was a term first cited by T.E. Fischer in 1988 as the branch of chemistry dealing specifically with chemical reactions influenced specifically by mechanical energy. The most basic premise of chemical kinetics is that three conditions must be met for a reaction to occur: the reactants must be in close proximity, there must be enough energy to cause the reaction to occur, and the product of the reaction must exist at a lower overall energy level. In all electrical contacts, the contact closure provides the proximity and the impact can easily provide the energy. Thus, Fischer published around 20 papers in this area, primarily in the interest of beneficial polymers used to protect and lubricate moving metals, ceramics, etc. Regardless of the mechanism, this is simply the susceptibility of the contact material to a reactant present during its operation.

Recent studies have shown metals such as ruthenium, platinum, and rhodium as being susceptible to the formation of these nonconductive films [94]. It is not a coincidence that these are the same metals commonly used as catalysts in a variety of carbon-based reactions. In the case of ruthenium and platinum, these metals serve as fuel-cell catalysts [95] and for platinum and rhodium, in catalytic converters

[96]. In catalytic converter however, without mechanical friction or electrical current present, carbon which attaches to the surface of platinum is held in place long enough for it to fully oxidize and be released as carbon dioxide. In contacts, the impact of contact closure may disrupt this process. Just as the automotive industry has spent decades searching for a more ideal solution to using platinum, palladium and rhodium [96] so too a designer may need to go through a similar process of finding an ideal alloy resistance to the most common materials present in the atmosphere, hard enough to withstand the impact of contact closure, elastic enough to form a sufficiently large contact area, and all of this while providing excellence conductivity. Research conducted several decades ago suggests some potential in this approach to the introduction of silver to palladium in order to resist this film formation [97]. Just as chromium is able to prevent iron from oxidizing in stainless steel, by keeping the silver ratio low, similar prevention of tarnishing can be accomplished while the silver helps mitigate polymer formation on the palladium [97].

As with the case discussed above regarding oxidation, a similar approach to prevent friction polymerization may lie in utilizing another form of a passivation layer. Organic thin films have been researched for their use in other microelectronic devices [98]. Thus, the use of carbon-based conducting materials such as graphene may protect metals which otherwise would be susceptible to friction polymerization. The challenge then becomes operation of these contacts without damaging this protective surface through physical actuation.

2.2.3.3 Electromigration.

Another consideration probably best addressed under the group of chemical considerations is the concept of electromigration. Strictly speaking, this particular consideration is really a combination of thermal, mechanical and chemical phenomena.

This phenomena occurs when the contact material moves (or migrates) across the contact during any given cycle, a dynamic which has also been studied for some time [99–101]. If during the contact closure, the bond between the two contact surfaces become strong enough, then the force induced by electrons moving through the material and across the contact may be enough to overcome the forces attempting to hold the contacts in one piece, and tear material loose as a result. If at the same time one of the materials is heated sufficiently such that the metallic bonding holding it together was weakened, then when the contact opens that material may be left behind due to the new thermally assisted, chemical bond between the surfaces. This could be addressed by reducing the likelihood that the two contact materials will bond. One possible approach to this is by ensuring temperature differentials between the two materials are present, a condition which is known to cause poor solder joints. Possibly a better approach is to ensure that the contacts are resilient enough to hold together in the first place. This theory has been supported by research which has indicated that electromigration tends to happen in the direction which electrons are flowing [102], and can be mitigated using the previously addressed idea of creating a metal alloy to help resist breakdown using ruthenium with gold [67, 103–106], tungsten-titanium alloys to resist the effects of hot switching [107] and with tungsten [108, 109]. However, in the experiments involving tungsten the increased current in the metal provided enough energy to hasten the surface oxidation of the metal, ultimately leading to gradual degradation through another mechanism.

2.2.4 Quantum effects.

During the closure of two contacting surfaces, contact begins as a very small contact area. If this closure happens with a charge between these surfaces, this can result in extremely large field effects right before physical contact is made. These field

effects have been an active area of study for several decades [110], but as newer and smaller devices are realized, further research has become warranted [111]. In addition to the ballistic electron transport which has already been mentioned, quantum effects have also been observed under these conditions. These quantum step changes in voltage [50, 112] have been predicted by theory derived for this condition and under carefully designed tests been created and measured [50, 113]. While this effect is often only observed immediately before contact closure, cycling may subject surfaces to this condition repeatedly. Material such as CNTs naturally form pointed contacts in which an electromagnetic field can extend considerable distances from the tip, and have been used to accelerate electrons in the process. This phenomena has been applied to atomic force microscopy, where the sensor tip is passed over the surface being detected without physical contact. The distortion of the field off the end of the carbon nanotube can then provide information regarding the surface being measured. As already mentioned, if a potential exists such that electron flow occurs through these CNTs, this field effect is often exploited as these sharp points help to facilitate the emission of ballistic electrons. If this phenomena occurs due to a sharp point in bare metal, similar to the electromigration discussed previously these field emissions can also cause material transfer [20, 114]. It is conceivable that this effect could be used to our advantage if a bundle of CNTs could be tightly packed and aligned as one of the contact surfaces. Research up to this point has shown that CNTs possess superior current carrying capacity, but suffer from unavoidably large contact resistances [115]. The highlights of research in this field is summarized in Figure 74 found in Appendix C.

On a similar note, under normal circumstances, ballistic transport of electrons during initial contact closure is typically considered undesirable. While high current is synonymous with low resistance, and lower resistance is desirable this seems coun-

terintuitive. The disconnect is not because electrons are transported ballistically, but because that method of transport is not sustainable throughout the entire device. Inevitably, one of the two contacting surfaces must absorb the energy of impact caused when the electrons collide with atoms within the contact and transfer their energy to phonons, becoming heat. These concentrated currents typically result in an increase of temperature, which can then cause the material to become susceptible to undesirable deformation of the contact surfaces if it can't be dissipated quickly enough. Recent work however has indicated that a ballistic-type electron behavior is theoretically induced through the use of alternating layers of material in which electrons passing through have alternating positive and negative effective mass [116]. This sort of composite metamaterial in effect provides a mechanism by which electrons can be pulled through the material at a speed faster than if they were traveling uninhibited, as shown in Figure 4 below where those energy levels at which the predicted results fall below a ratio of 1 predict this effect, and are shown by the horizontal dotted line.

While this is called ballistic transport in the research, it is subtly different in that the electrons may not necessarily have the undesired momentum imparted by a field which is powered externally. Electrons transported in this manner are moved through the material by quantum effects within the stacked layer rather than just the traditional electrostatic potential propelling these electrons across the contact. Unfortunately, the list of materials which can be used to induce this phenomena is currently very limited, and such materials can be fabricated individually, but producing the stacked layers of the required dimensions has not yet been demonstrated. Currently the only known materials which would behave in this manner are only functional in extremely low temperatures less than 5K as well as extremely high electric and/or magnetic fields [117, 118]. While such conditions are less than conducive for a typical switch to operate, at least the potential exists to build and test this

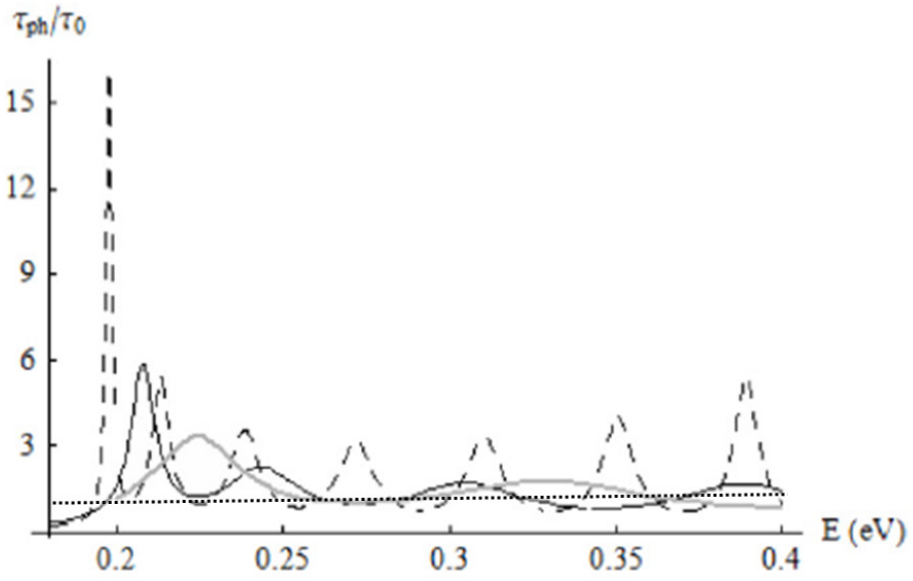

Figure 4. Energy dependence of the normalized phase time (τ_{ph}/τ_0) in the metamaterial range for three representative cases of varied electron effective mass, layer thicknesses and number of layers in the composite metamaterial modeled [116], illustrating that at certain potentials, there exists the possibility of electrons transport substantially faster than the unhindered electron speed which would be observed.

theory in an actual device. The materials which have been noted as potentially useful in this aspect include GaN [117], GaAs-AlGaAS quantum wells and InAs [119]. There are also studies showing this phenomena in other materials such as quantum wires [120] and manifesting in specific directions within the reciprocal space of some semiconductors [120, 121], and are even in use currently within ballistic diodes that utilize quantum wells [119]. While currently these materials aren't suited for this sort of electromagnetic-Bragg reflector configuration, research is very likely to continue in this area and as it does, if such materials become available which display the ability of providing an electron with an effective negative mass under reasonable operating conditions, it will likely be incorporated in typical semiconductor fabrication processes. A small example of some of the more relevant research currently being conducted is summarized in Figure 75 found in Appendix C.

2.3 Micro Switch Fabrication Considerations using MEMS

Finally, we will discuss the work done in areas used to fabricate micro switches. Due to the scale of micro-contacts, typical MEMS processes are used to fabricate these kinds of devices. A substrate such as Silicon is the starting material of choice, and after making the surface non conductive through oxidation or depositing some other non-conductive material, devices can then be built. Photoresist is patterned and used with either deposition or etching techniques to selectively place material down to approximately 1 μm feature size. Repeating this process through different patterns and materials builds the three dimensional structures desired. These sorts of processes have already been used to build micro-contacts suitable for this manner of testing [49], however some parts of this fabrication require special consideration to advance the field. Thin-films for example are commonly used for a contact surface in these kinds of devices.

2.3.1 Engineered contacts.

One approach we can use to fabricate contacts of low, yet known contact area is to employ a technique in which we directly shape the contact regions. Preliminary work in engineered lower surfaces has shown promising results in this area in terms of controllability, but even with our high resolution lithography processes, contact areas are still on the order of microns. A focused ion beam or E-beam lithography technique could be used to push this limit, but one fundamental limitation is that these techniques require us to individually fabricate each device as opposed to mass producing a pattern like we would with a masked photoresist technique. In reviewing available techniques which are likely to succeed based on currently published results, three methods will be considered in this effort: Focused Ion Beams (FIB), Nanosphere Lithography (NSL), and Grayscale Lithography.

2.3.1.1 Focused Ion Beam Lithography.

The use of ion beams has been suggested for decades, but much of the pioneering work from the late 1970 and early 1980s contributed to the development of this tool for lithography [122]. The steady progression of technology has only advanced the technique and its capability as can be seen from the example shown in Figure 5.

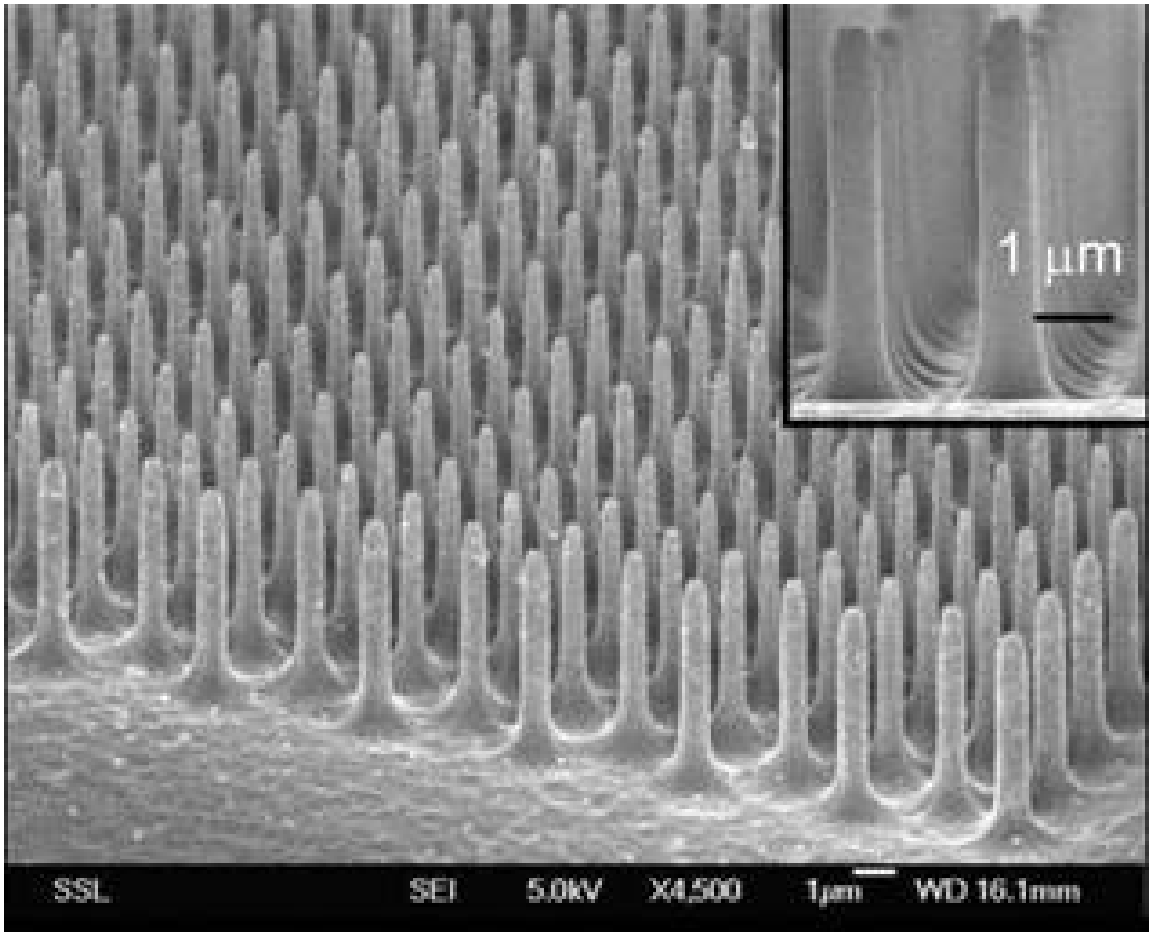

Figure 5. Etched silicon over a region of 200 square microns, in which the substrate was irradiated with ions prior to etching.

This image shows one method in which ions can be used in lithography. In this instance, a silicon substrate was selectively irradiated with ions forming a matrix of spots where the material was made less porous after ion implantation. This resulted in a greater etch rate of the more porous, non-irradated regions which lead to a

selective etching. Many other methods are possible using ions to form the sort of controlled contact areas in question. But one commonality of all focused ion beams is that it is inherently a scanned process. This means each region must be scanned individually. This is an inherent disadvantage compared to the other two methods yet to be reviewed. Additionally, very specialized hardware is required for this technique and the health and availability of that hardware becomes a critical factor to consider.

2.3.1.2 Fabrication Using Nanosphere Lithography.

Another technique which is of interest is the ability to pattern nano-scale particles through a method called nanosphere lithography (NSL). In this process, a solution containing regularly sized spheres which are of uniform size and nanometers in scale will naturally form regular, ordered single particle arrays if processed properly [123–126]. These layers of tightly packed spheres can then be used in a variety of methods. In the case of growing CNTs, spheres of nickel can be deposited and then etched down to a desired size, which determines the radius of the CNT growth site [123, 127]. While these fields of CNTs may not necessarily be an ideal contact material, this idea of being able to form regular arrays of nano particles could be used in other ways. A similar approach was attempted through the use of nano wire arrays, but instead of taking advantage of the current carrying capacity which CNTs bring, this experiment sought to better control contact area by using a field of tangled nickel nano wires to in effect simulate an extremely elastic contact [128]. Another possibility is to look to NSL to push the boundary on the smallest feature size we can fabricate by using these deposited structures as part of the contact itself. If we are to use this approach, we will need to review the various methods of deposition and other factors which can affect nanosphere patterning in general.

To accomplish successful NSL pattering, various methods can be used. These methods can be categorized as one of three types: spin on coating, dip coating or convective coating [129], as illustrated in Figure 6. The goal in this process is to deposit nanospheres of a known, uniform size on a substrate in a way that a uniform, close packed structure is formed. This structure will then have periodic openings which are spaced equidistant, depending on the size of the sphere used and these openings can be used as a deposition mask. Depending on the thickness of the deposition and geometry of the nanospheres after being etched, this tends to produce a triangular-shaped deposition due to the triangular shape of the opening formed when spheres meet in this arrangement. One method to change this triangular shape back to a more circular one is to utilize a thin photoresist layer beneath the nanospheres prior to deposition [130]. The theory behind this method is that the nanosphere etching is a gaseous process, and the reactants which pass through this triangular opening will not maintain this shape. Instead, they dispurse in an approximately Gaussian shape beneath these interfaces, producing more circular deposition patterns centered on each opening in the layer [130].

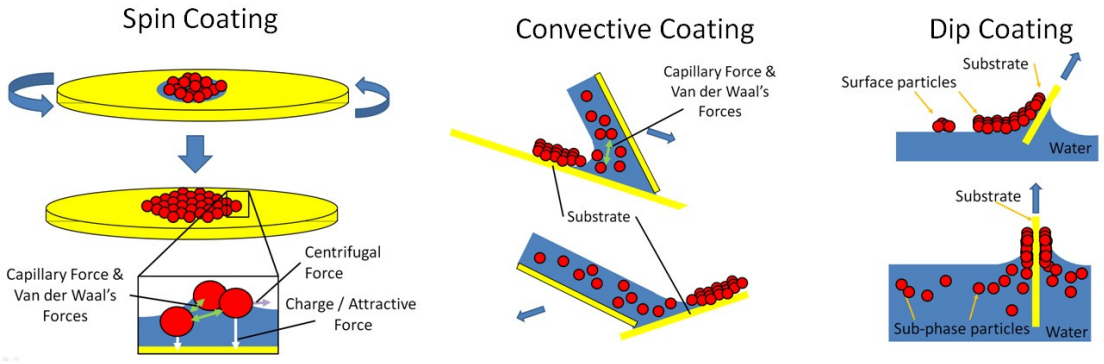

Figure 6. Nanosphere deposition techniques used to form close packed arrangements on a substrate for use in lithography [131].

The size of these openings can be enlarged slightly as well if the layer is etched, typically through RIE or plasma ashing. This increases the exposed area but maintains the nano-scale spacing. Additionally, interesting geometries can theoretically be achieved if a directional etch and/or deposition is used with this layer of nanospheres as shown in simulation results from work done in this area, in Figure 7 below [132].

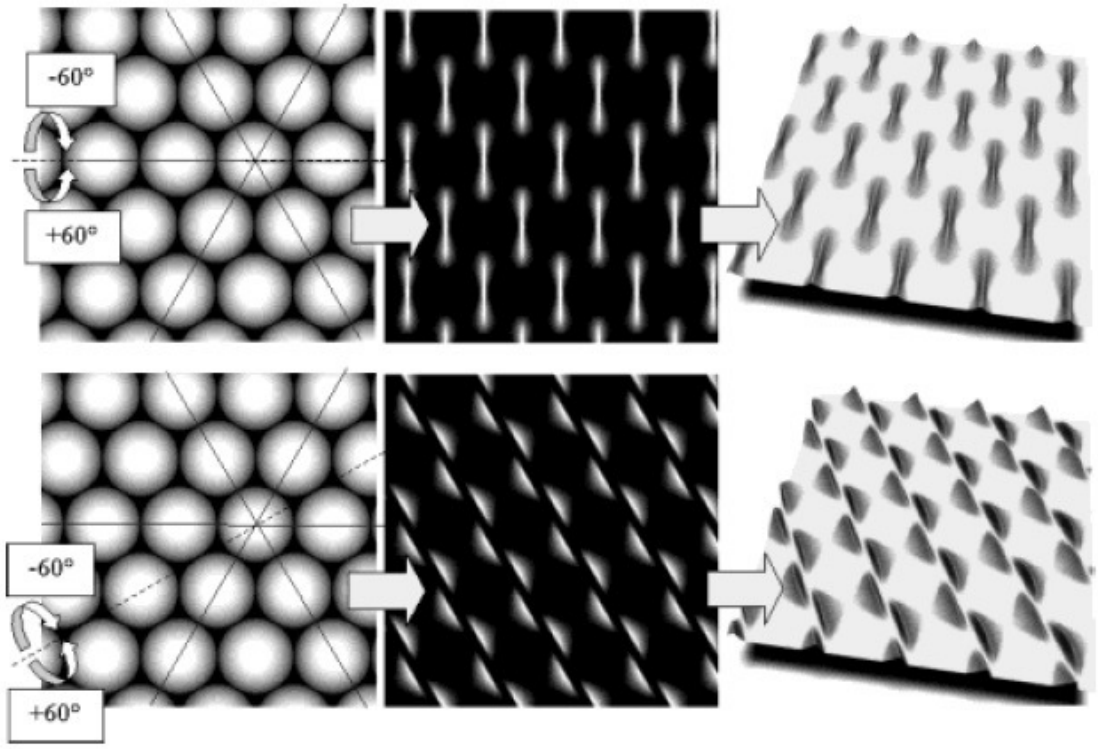

Figure 7. Simulation results for the evaporation through an hcp mask of ordered spheres with the tilting angle oscillating between -60^o and 60^o during the process. The tilting axis is parallel to the [100] direction (top), and [110]) bottom) [132].

Spin coating is often attempted as it doesn't require a custom hardware setup other than a spin coating system, which are common in labs which perform photoresist-based lithography [129]. However, these spinners were designed to be used with photoresists which have high adhesive properties and the viscosity of photoresists can be engineered to produce a desired final thickness. With NSL, the thickness

is controlled, not the viscosity or adhesion. Thus, for successful spin-coating, great lengths must be met to modify these secondary properties to produce good results [123, 129, 133, 134].

Among the earliest techniques attempted in patterning nanospheres is the use of convective forces encountered during simple evaporation. This is normally considered a type of convective coating, as it uses the edge of an evaporating drop of liquid to create the moving boundary region rather than a secondary carrier [129]. While evaporation can be extremely simple, it typically produces poor structure for one basic reason: convective coating depends on keeping the interface between the liquid and substrate linear and uniform throughout the process in order to allow for rows to form neatly in a close-packed formation [135]. In a simple evaporation process, a drop of liquid is circular. When the drop is large the boundary is close to linear on the nano scale, but as the drop evaporates and the circle becomes smaller, the radius of curvature decreases. This causes problems as the deposited layers join together and are forced to reconcile this discontinuity. With a mechanically driven deposition process, this can be overcome through angling the substrate relative to the surface and passing it across the air-liquid boundary. This requires the alignment of the substrate and carrier to remain linear and aligned throughout, but while one is in motion and the accuracy required is still critical [129]. For convective coatings in general, since this is on the scale of nanometers, the control required makes this a challenging problem even with today's motion control hardware.

Dip coating has been a bit more prominent in recent research, or more precisely a variation of dip coating which involves removing the liquid containing the nanospheres rather than physically lifting the substrate through that surface. If the substrate is angled to the surface, then this ensures the interface remains linear, and as long as the level of the fluid is not disturbed the alignment will also remain true. In

2009 this technique was published with evaporation to remove the liquid and transfer floating, assembled layers to the substrate [133]. More recent publications from HP Laboratories have focused on this technique, reportedly accomplish the same effect in a quicker period of time [130].

Regardless of the method used, the interaction between nanospheres may inhibit self patterning. To address this behavior, a few surface treatment options appear repeatedly in the literature and may be worth incorporating. The first is a chemical called Triton-X which is a form of Polyethylene Glycol ($C_{14}H_{22}O(C_2H_4O)_n$) or t-octylphenoxypolyethoxyethanol, which is a very viscous detergent-like material, possessing both hydrophilic and lipophilic regions. This chemical is capable of acting as a non-ionic surfactant, meaning it lowers the surface tension between organic polymer nanospheres without inducing a charge in the process. Thus, if we need the spheres to flow amongst each other without separating, adding this material may help facilitate free movement between spheres. This chemical has been used on and off since at least 1994 if not sooner [136] but still shows up in more recent publications as it is effective, safe, and inexpensive to use.

A second chemical which shows up more recently is Polyethylene Oxide (PEO) which is also used with polymer nanospheres, but as a binding agent. It is a polymer formed from a ring of ethylene oxide molecules. If small particles of this polymer are added in trace amounts, this can greatly promote adhesion with similar organic molecules [130]. This can be beneficial in applications where we try to form regular mono-layers first and then transfer then to our substrate. This material keeps individual spheres from breaking off as they are prone to do without this additional binding agent.

A visual summary of some of the applicable research in NSL conducted over the past few decades is available in Figure 77, found in Appendix C.

2.3.1.3 Grayscale Lithography.

When looking at the multiple studies addressing surface asperities in micro-contacts, it is apparent that this unpredictability is a vital factor in predictability. In general, minimizing these multiple small asperities and thus maximize contact area prior to applying an electrical current is key in avoiding asperities from carrying the full current. One method which has been explored briefly but may warrant further work is the concept of engineering surface texture of one of the contact areas [49, 137]. Ideally, we would like a contact to close in such a way that we reach large contact area faster than any residual charge could induce field effects of any sort across the contact, yet without enough impact force to affect either of the contacting surfaces. In reality however, we have to find a balance between these two and in doing so have to recognize that surface asperities of our contacts will start conducting first. We know that these surface asperities form extremely small contact areas which often causes performance variations, concentrating current flow which then leads to extreme heat differentials caused by this isolating current rush.

With engineered contacts, the intent is to design a surface that is known to be non-ideal in that it is not perfectly flat, but more predictable and stable than a surface covered by random asperities. We do this by introducing features into the design which if done successfully will be able to find a compromise between the ideal flatness and the non-ideal, asperity covered surface, similar to recent research in controlling asperity junctions [138]. This raises interesting possibilities of being able to use such a contact surface to our advantage. Such a surface could theoretically be designed such that with each closure, the process of making contact also aids in moving particles which have broken loose. To accomplish this sort of surface engineering, a method called grayscale lithography can be employed [139]. In a standard lithography process, patterns are either present or absent depending on how the photoresist is exposed.

Grayscale lithography provides a means to create three-dimensional features within the photoresist by varying the exposure across its surface. Thus by creating an image with various levels of gray and using this in the exposure process, the final form the photoresist results in is whatever three-dimensional pattern was imaged [140, 141]. If this three-dimensional photoresist structure in on top of a wafer, and both are then put through a process such as reactive ion etching (RIE), the result is the three-dimensional pattern being transferred to the wafer [142]. This can then be put through the same sort of layer deposition which would occur with the flat wafer creating a current carrying, engineered lower contact [143–146].

One particular method of writing lithography masks involve the use of the laser lithography system such as the Heidelberg μPG-101. The system uses a small diameter UV laser with a precise positioning system. The device as built is provided from the manufacturer with a guaranteed beam diameter not to exceed 1 μm, and with a positioning step size of 400 nm in both the X and Y dimensions. Because other models are available from the same manufacturer with more precise positioning capabilities, it is likely that higher accuracy can be achieved on this model, but cannot be guaranteed with this particular machine design as most manufacturers save significant cost in carrying commonality between product lines. Also, the exact diameter of the beam may in fact be slightly smaller than 1 μm. Both of these characteristics are critical in defining the smallest feature which can be realized. The system as supplied includes software which allows for two modes of operation: grayscale image exposure or direct writing using computer aided design (CAD) files.

Grayscale Image Exposure

The first mode involves utilizing images instead of CAD files. In this mode, each pixel within the image is scaled down to the size of the beam (1 μm) as illustrated in Figure 8. The system then positions the beam at each pixel location and scales the

amount of power delivered based on the shade of gray of that particular pixel. When the photoresist is developed, these regions of partial exposure only result in partial removal and the final result is photoresist with a three dimensional element due to this exposure method.

Line Scan Exposure

The second mode of operation utilizes files designed in CAD software which establish basic geometric shapes. To print the shapes, the software determines the number of lines which need to be written to be able to fully expose these regions such as that shown in Figure 9. Before printing, both the power and the duty cycle of the laser is set and everything within these regions is exposed to the laser at those settings. Typically this is set high enough to fully expose these regions, and after further processing this results in a standard lithographic mask. The beam positioning is calculated using the full resolution capability of the system, and because continual lines of exposure are used this allows for the highest resolution of the machines capability to be realized.

At this point, consider the sort of structure that would be ideal for micro-contacts in which we want small, repeatable surface area. To construct the sort of columns that were discussed previously, it would be ideal if we could use this idea of grayscale lithography. Using bitmaps however, this extremely limits the resolution that can be achieved because of the nature of the software. We could however combined these two methods to form higher resolution grayscale results.

2.3.2 Thin films.

Current is often carried through thin films of materials in MEMS devices, thus these thin films are an area of interest from a research standpoint. We know that thin films impose a limiting factor in overall current carrying capacity [147] but at the

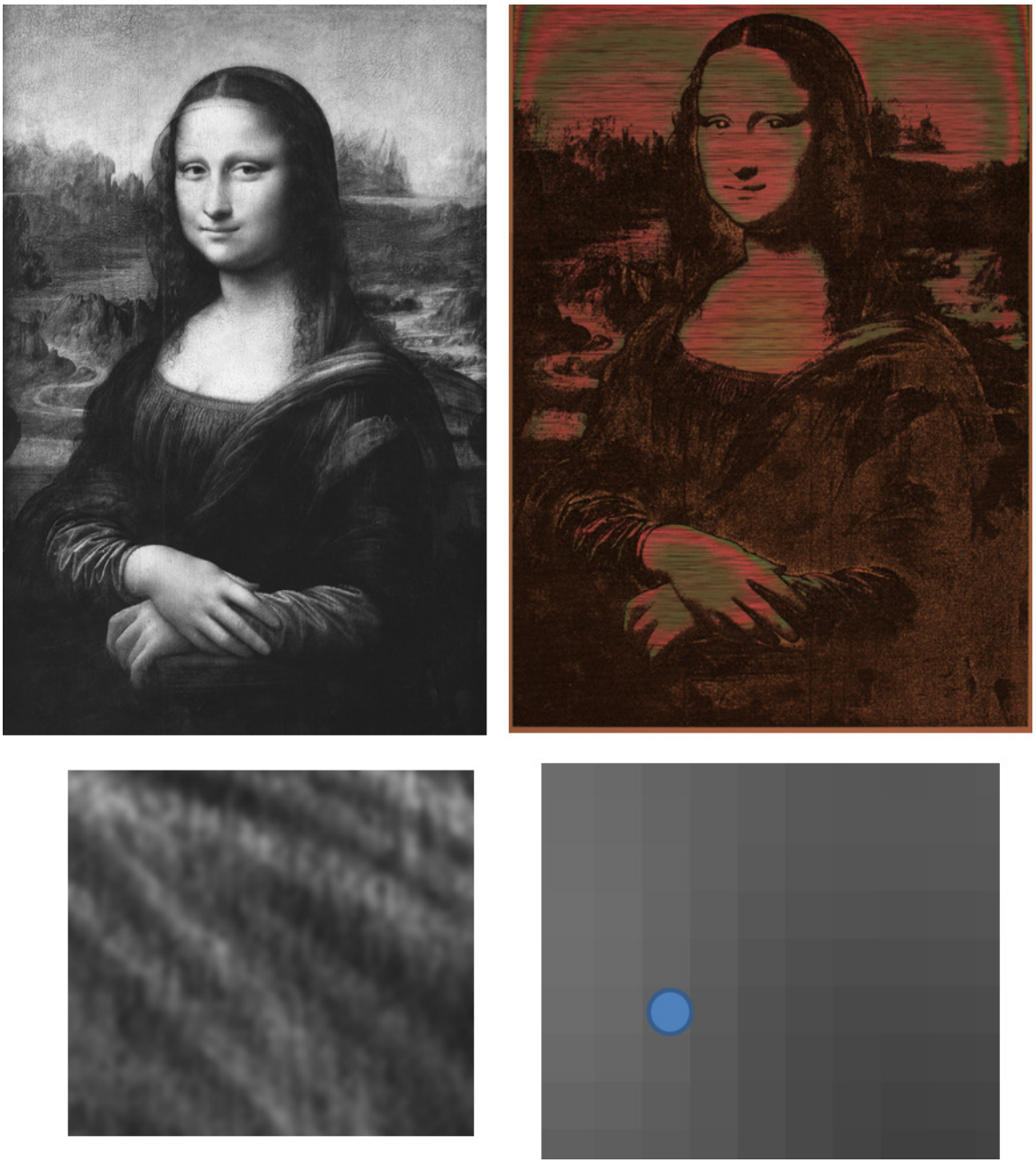

Figure 8. Illustration of bitmap image based grayscale lithography. Starting with a grayscale image (upper left), the system translates each pixel as an exposure depth in photoresist (upper right). To accomplish this, individual pixels are scaled to the size of the beam and exposure is determined by overall grayscale of each pixel (bottom).

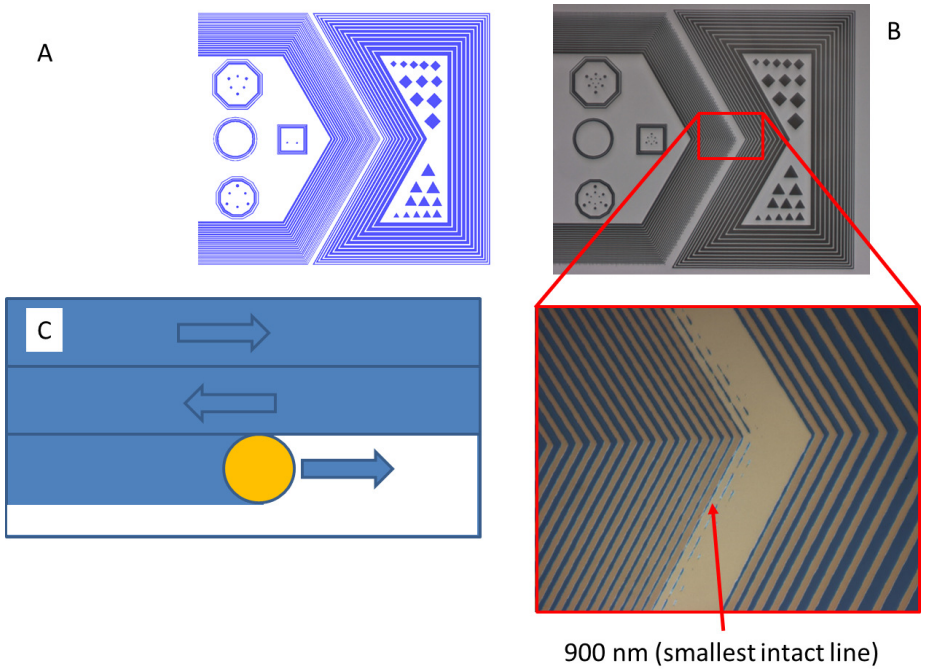

Figure 9. Conceptual illustration of lithographic printing from a CAD-based file (A), resulting in fully exposed or unexposed areas (B). To accomplish this, the beam used to print is swept horizontally along precalculated lines, and beam is activated and deactivated to expose only the geometric shapes provided.

same time, exhibit other interesting properties. Models have been developed which describe the way electrons experience what is known as spreading resistance when traveling into a thin film, characterized by the electrons attempting to reach a uniform density after passing into the material [148–153]. However, the theory behind these models predicts some very non-intuitive behavior in these thin films [151]. Some of these phenomena have yet to be observed experimentally due to limitations in fabrication at extremely small scales, thus validating this theory experimentally may be warranted. By validating spreading resistance models, the next step is in determining how best to incorporate them into contact resistance models. Should this theory be fully validated it then indicates that depending on geometry, spreading resistance can be incorporated in the design simply through consideration of the geometry of these thin film conductors [153, 154].

When depositing these thin films, this is often done in conditions where the material experiences considerable heat. In larger volumes, this may not be a concern as the core of the material is able to form a stable crystal lattice structure, but in thin films these stresses can easily become overwhelming due to the extreme scale. Thus the stress in the deposited layer upon cooling may be much greater than any force holding film in place, and may cause great difficulty or even change the way in which deposition occurs if not addressed during fabrication. For example, RuO_2 changes its preferred orientation to a glass substrate at different temperatures [155], and at an even higher temperatures will produce interference fringes during high-resolution x-ray diffraction measurements, thus indicating a very uniform, smooth depositions [156]. While various methods exists which can prevent the stress from manifesting (e.g. allowing the deposited material to cool slowly, application of adhesion layers, etc.), this may not be possible depending on the fabrication process for the materials used. In these cases, the effects of the induced stress in the thin film must be evaluated to determine its impact on overall contact performance. Also, repeated cycling can change stresses already present or induce other forms of stress in a contact (e.g. creep deformation [73, 157]).

2.4 Environmental Considerations

In addition to considering design geometries, materials, and other internal factors, consideration will also be given to external factors and how those can affect micro-contact performance over time. Those external factors that a contact may be exposed to fall into two groups: electrical loading and external circuitry.

2.4.1 Electrical Loading.

As with all MEMS devices, the theory which describes the behavior of micro-contacts originated from macroscopic theory. There has been a great deal of interest in applying these devices to RF applications for years, and even today this remains an active research topic [158–160]. Yet as we review a majority of the research efforts to develop theories and the models which were derived from them, most of the fundamentals were developed under DC conditions. We also know that under DC conditions, material transfer due to electromigration can be induced critically affecting device performance [161]. Research into the performance of these devices under low frequency conditions is lacking, and this region of operation may provide crucial insight into failure mechanisms, as well as validate the applicability of applying DC based theory to higher frequency AC applications such as RF.

2.4.2 External Circuitry.

The second external factor which should be considered is the circuit elements connected to the micro-contact during operation. It has been theorized that external circuit elements in specific configurations can greatly impact the performance and reliability of these devices when operated under cold-switched conditions [10]. The theory implies that a device such as a capacitor when in parallel, may build up a potential. If this capacitor is in parallel to the contact, and that contact is closed this charge will now have the ability to discharge through the lightly loaded micro-contact and could induce effects similar to those experienced when a device is closed in a hot-switched manner.

Experimental validation of this theory would aid in providing practical guidance in how micro-switches should and should not be operated utilized to optimize performance. More importantly however, it would also provide a solid understanding of

design considerations which could have similar impact. In other words, if connecting a capacitor in parallel during operation is detrimental, then any capacitance inherent in the design of the device should also be avoided for the same reasons. Additionally, this theory suggested that other configurations may provide some level of protection to micro-contacts. Validation of this theory could likewise prove useful for similar reasons.

2.5 Testing

Micro-contact testing has been documented for several decades, but really starts with the theory describing macro-devices characterized by Ragnar Holm in the late 1960 in his book on the subject [37]. This work defines classical diffuse electron transport across a contact and has since been refined to include considerations which are more pertinent to micro-contacts, and are discussed at length in the previous discussion on modeling. Most data published on the performance of any contact is in the form of contact resistance. This idea of performance is important, but there is another area to consider which is reliability (i.e. how the contact resistance changes over its lifetime and how likely it is to eventually fail).

Recall the previous discussion on hot vs. cold switching and the affects it can have over time on contact performance [20]. This is just one way in which a contact may initially perform well, but later degrade. Additional effects which can impact performance can include age, wear, contamination, or environmental factors just to name a few. These all must be considered in addressing how to conduct testing. To gather reliability data for a large number of cycles requires a great deal of time for even a few million cycles of operation. To address all these issues, a specialized test stand was developed. Commercially available technology in high frequency piezo actuators, force sensors capable measurements accurate to μN of force, and readily

available hardware capable of extremely low-voltage and low-current measurements has allowed for this test stand to be built which automates this testing process [162]. This stand has already been used to characterize contact evolution of dissimilar materials [49], implantation of CNTs in micro-contacts [163], and thin-film spreading resistance validation [164] up to 10s of millions of cycles of actuation. To increase the test rate and obtain larger numbers of cycles in smaller testing times requires a higher frequency piezo actuator, as this is currently the limiting factor in the overall speed of operation. Since the time of the test stand's initial development, hardware in this area has improved by approximately an order of magnitude or more, and the piezo actuator is now capable of rates exceeding 20 kHz but possibly reaching up to 40 kHz according to publicly available literature on the hardware. Current hardware would require approximately 3 to 4 months of continuous testing to reach 30 billion cycles, but this hardware improvement would allow this testing to be accomplished in less than 2 weeks to reach the same number of cycles.

2.6 Chapter Summary

A great deal of progress has been made in understanding and modeling the physics behind micro-contacts. The multidisciplinary nature of their operation, and therefore means to improving them require an understanding of several fields. How those fields interact with each other is equally critical to fully understand all the nuances of micro-contact operation. Thermal effects were discussed, and while the fundamental understanding exists of some of the basic effects temperature can have on contacts, extreme temperatures or wide temperature ranges produce results we are only beginning to understand. Mechanically, several advancements have been made which address a variety of concerns, but as more sophisticated models are developed, more subtle nuances that affect micro-contact operation are identified which require

attention. Chemical susceptibility, while being widely identified as an issue seems to be the most lacking in terms of progress. However, this is not surprising considering the sensitivity of a materials reactivity to its composition as well as environment, therefore every material in every environment would have to be studied in order to consider this area truly complete. While some aspects of various quantum effects have been identified, research in this area has only begun to scratch the surface. Finally, in order to build the needed devices to push our understanding in some of these areas, more advanced fabrication techniques are likely to be required, such us grey scale or nanosphere lithography. Overall, one theme seems to carry through all of these areas; the materials we use and the processes to deposit those materials seem to be critical in a micro-contacts performance. As with so many other technologies, as new materials and new processes are identified, applying them to some of these issues will undoubtedly improve performance in years to come.

III. Methodology

3.1 Chapter overview

As outlined in previous chapter, the performance and reliability of micro-contacts is a complex topic with many potential areas for advancement. A test stand built specifically for this task is the foundation for this research, and was used to gather the necessary data. This hardware has already proven extremely useful in initial efforts to gather contact resistance data [49, 162, 163, 165, 166], and with a few minor modifications continued to be ideal in furthering this work. Both hardware and software of this station, as well as the devices tested were reviewed and modified as necessary.

One common theme that has reoccurred repeatedly in the study of micro-contact performance is the ability to accurately predict contact area. This seems intuitive as contact area is a critical variable in contact resistance models, but here the interest in contact area serves another purpose. When we consider ballistic electron transport and the potential benefit of being able to better understand and capitalize on this phenomenon, we require not only the ability to predict contact area with extreme accuracy, but also the ability to control it during device fabrication with as much precision as possible. To that end, two potential fabrication methods which could allow us the ability to fabricate extremely small scale features were explored: nanosphere lithography and improved grayscale lithography. If either of these provide the scale and controllability we need, these are the first steps in achieving ballistic-based devices.

The next step will then be maintaining these features through fabrication of full devices. The most direct method would be to fabricate these structures in the underlying substrate upon which the devices are to be built, but we still must deposit a thin

conductive layer on these features. Thin-film depositions are typically used for this purpose, and to preserve such small features even thinner films may be required than what is typically the norm. This brings up a second topic to be addressed: thin-film spreading resistance. Thinner conductive films will aid in maintaining features, but may also impact contact resistance due to the physics of thin-films themselves.

Finally, the last topic explored addressed external influences on micro-contact performance and reliability. In the last chapter, we discussed theory that predicts the influence of external circuitry on device lifetime, and how certain configurations may prolong or shorten life. Another topic worth pursuing is the effects of the electrical load imposed on these micro-contacts. It was suggested that there is a gap in the literature regarding low-frequency characterization, and experimentation in this area could also provide clues regarding the susceptibility of these devices to polarity changes. Both of these topics are covered experimentally.

3.2 Test Stand and Testing Procedure

Research in micro-contacts of this nature require a specific combinations of measurements to be made simultaneously. To do this, a novel test fixture was designed to characterize the performance over the lifetime of a micro-contact [49, 162]. While this test fixture was designed specifically to allow for rapid actuation of a micro-contact with a known force and frequency, it can be easily adapted to do much more. A picture of this fixture is shown in Figure 10 [163], which includes a detailed view of the force sensor and a reticule with 16 devices (upper right inset) as well as a schematic overview of the physical interconnections (lower left inset).

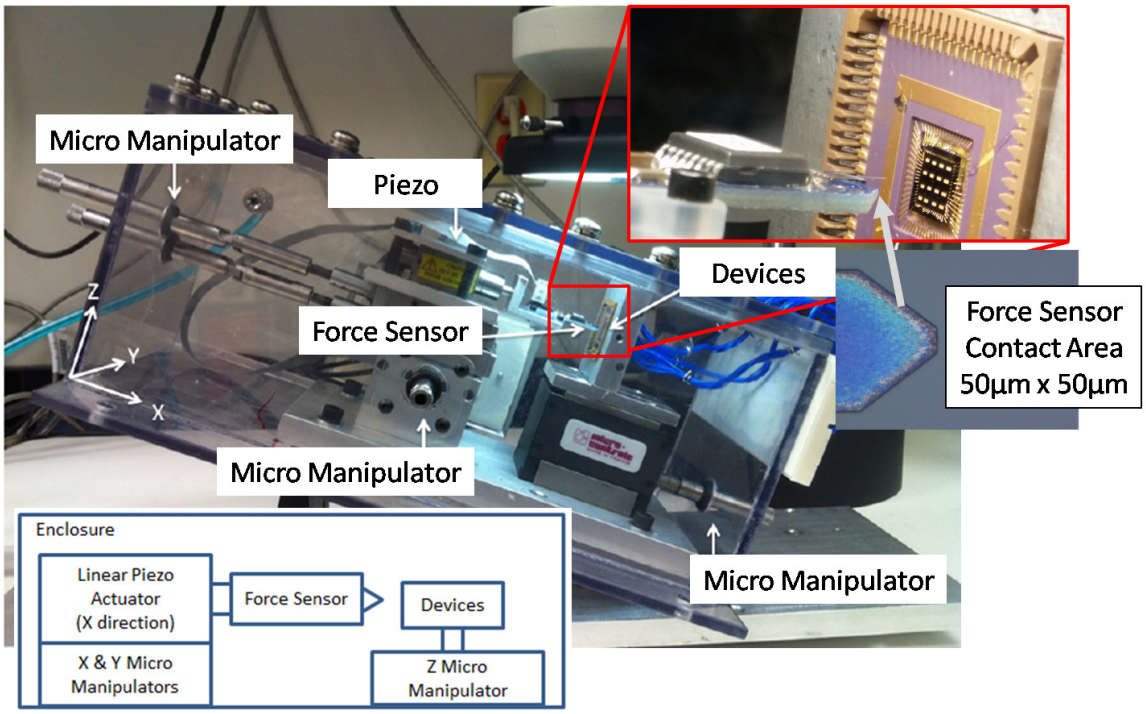

Figure 10. Test fixture for measuring micro-contact resistance through the piezo-actuation of a μN scaled force sensor, encased in an enclosure capable of controlling atmospheric conditions.

3.2.1 Hardware Overview.

This test stand is comprised of several parts, starting with the enclosure. While this is currently configured to minimize moisture exposure by purging dry nitrogen through the enclosure, this could easily be modified to provide whatever gaseous environment is required for testing. For the topics we are interested in for these efforts, a nitrogen environment was used.

The heart of the system is a Labview controlled National Instruments rack which simultaneously controls two devices which are physically mounted together. This system utilizes an NI 4070FLEXEMM ^{TM} module for measuring currents and voltages. This hardware provides measurements accurate enough to calculate contact resistance within +/- 110 nΩ. These measurements are taken while contact force is applied and monitored. This is accomplished using a THORLab ^{TM} PAZ005 actuator upon which

is mounted a force sensor manufactured by Femto tools ^{TM}, model FT 5270. This allows us to simultaneously measure contact force with an accuracy of approximately 50 nN. The piezo-actuator has approximately 20 μm of travel, with 5 nm resolution, and can also oscillate at approximately 2kHz of frequency. The relative positioning of these devices are manually adjusted such that the force sensor is positioned in proximity to a sample holder with 68 electrical connections, accessible through a breadboard on the back of the hardware. In this sample holder, we can put whatever design is suitable, in this case a contact which we will discuss next.

The contact design currently in use in the test fixture is a legacy design from other studies conducted on this fixture [163]. An illustration is included in Figure 11, which shows a model of the contact [164]. This design is based on a classic experiment from Ragnar Holm used to study the contact resistance between two crossed metallic rods. The basic premise of the experiment is that by applying a known voltage, and precisely measuring the current to one set of measurement pads, the resistance of the micro-contact is calculated by using a high impedance voltage meter across the other set of pads, and as the current flow to this meter is negligible, the measured voltage is across just the contact itself. Using the known current, this gives you the contact resistance regardless of the resistances of the other components of the circuit [37].

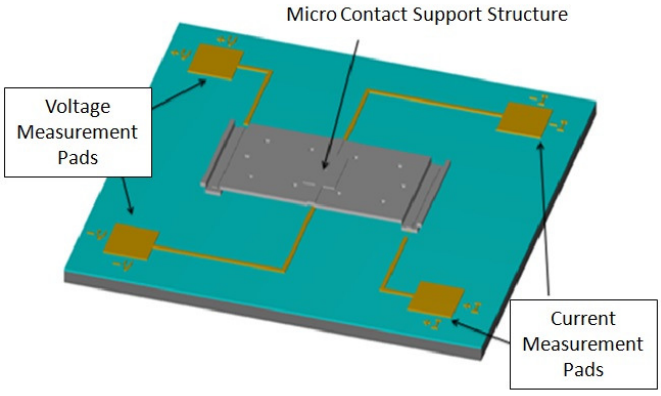

Figure 11. 3D model of fixed-fixed beam micro-contact support structure [163].

To accomplish this measurement at high speeds, this needs to be controlled through a common rack and user interface (UI), which is discussed next.

3.2.2 Software Overview.

The rack which controls all the hardware mentioned is operated using Labview. This allows for high speed, repetitive contact testing needed for lifetime data to be achievable. The test stand was originally designed to accomplish a single initial contact cycle in which the probe tip slowly approaches the device until either a safety limit is reached or a force is measured. If a force is measured, the probe tip continues to advance, continually recording position and force until the current and voltage change, indicating electrical contact of the beam to the bottom contact has been made. This point is marked and the probe advances until a preset contact force is reached, still recording force and position, but now also current through and voltage across the contact.

The next iteration of the controls is what resided on the system at the beginning of this work. This software performed this measurement process semi-automatically, with contact cycling added. The process involves the cycling of the piezo-actuator synchronized with the application and removal of a 1 voltage DC load to the contact during the closed portion of the cycle while measuring and recording the current, voltage, force and position simultaneously. This process was repeated at a specific frequency for a specific period of time, which produced a known number of cycles, followed by a repetition of the measurement process, followed by more cycling, etc. This continues until contact failure is detected, a predetermined number of cycles have been reached, or a hardware error (e.g. a broken force sensor) require the test to be aborted. Contact failure is defined as either a contact which is fused shut or a contact which no longer conducts upon closure.

To further improve the system, before any additional tests were conducted this software was modified further. Some of the changes were to reduce the likelihood of error during operation by simply removing unused code and simplifying the interface. A complete description of all the changes made is provided in Appendix D, but a sample illustration of the new interface is shown in Figure 12 below.

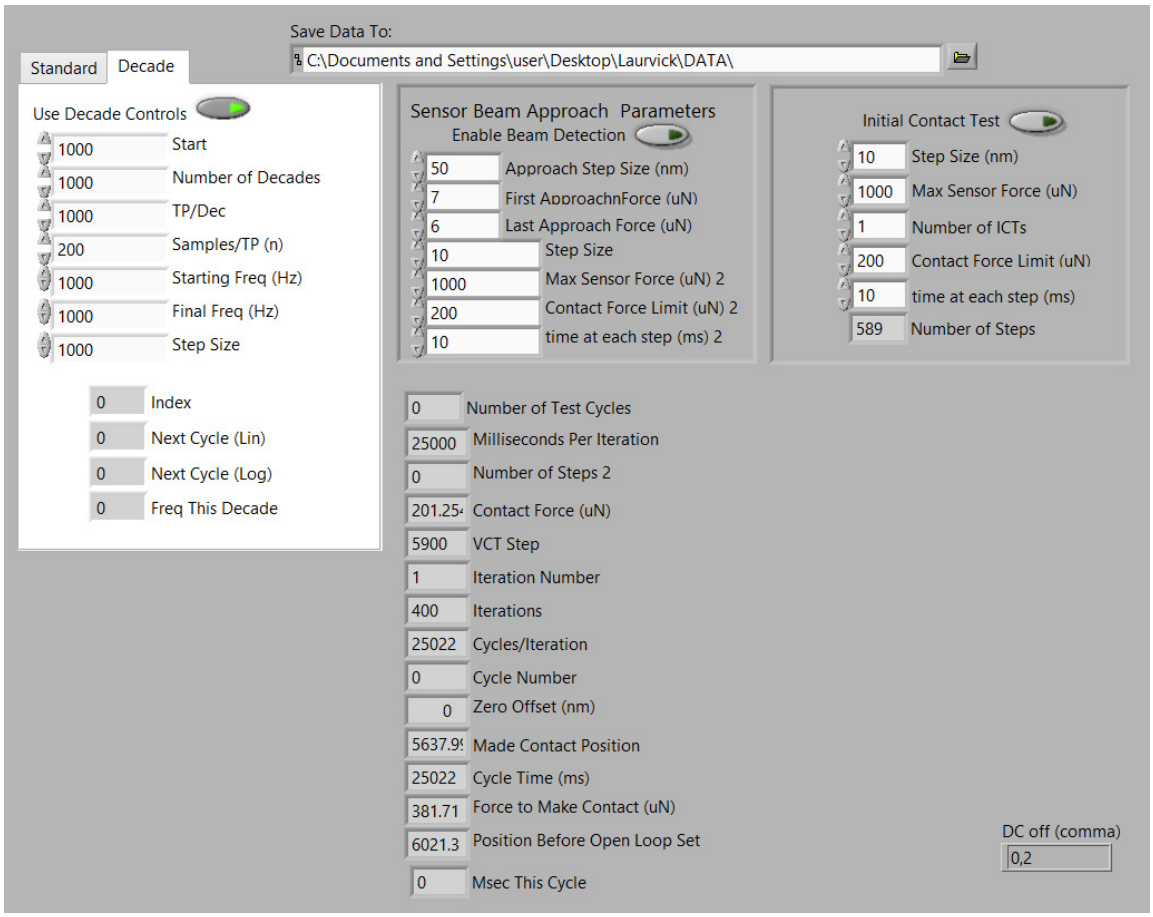

Figure 12. Screenshot of the new user interface, simplifying the interface through removal of redundant/unused control elements as well as improved cycling control for higher cycle count efficiency.

In addition to the general housekeeping, improvements were made to the overall automation for long periods of testing. The original controls were written such that each device was tested, cycled for a specific number of cycles, another contact resistance measurement was made, etc. The issue with this scheme is that when a

device has only been operated for a small number of cycles, the number of cycles per test point needs to be small. As cycles begin to build however, this number needs to increase. For example, consider a device being tested from 1,000 cycles to 10,000 cycles with measurements every 200 cycles. Once the device has reached 10 million cycles, it is impractical to still be testing every 200 cycles, especially considering that each measurement cycle can last between 2-5 minutes depending on how precisely the device was aligned during setup. With the old software, the only way to avoid this issue is for the user to only schedule tests between various start and stop points and wait for completion. Once completed, the user can then return and manually increment the cycle count along with the start and stop points, repeat for the next decade, etc. This requires the user to frequently update these settings to test each decade, ultimately wasting a lot of time while the machine sits idle waiting for the operator to adjust these settings.

To correct this, optional controls were added. The user still has the ability to operate the original testing schedule, or alternatively decade testing control could be used. Under the new controls, the user can now specify all the parameters shown on the left side of Figure 12, including the starting and ending number of cycles to test between (as before), the number of test points per decade, the number of measurements per test point, and settings to allow for lower frequencies early in testing and higher frequencies for sufficiently large numbers of cycles. For example, the user could specify measurements start at 1,000 cycles and continue until 10^{10} cycles, with 5 measurements per decade, and for each measurement, repeat the measurement process 3 times, starting at 1 kHz and increasing by 500 Hz / decade. This software will then automatically adjust these values between each decade and proceed immediately through the entire test series, greatly increasing efficiency overall. One item to note is the calculation of intermediate test points. The code was written to calculate di-

visions such that when the data is plotted on a logarithmic scale, the data points are equidistant. Numerically equidistant points are also calculated but currently not used in the software. See Appendix D for more details and example calculations illustrating this.

3.2.3 Data Management.

The current UI conducts the test cycle mentioned autonomously over either a predetermined number of cycles or until device failure. For a single test cycle, a file is produced which contains current, voltage, calculated contact resistance, displacement, and both absolute and relative contact force. The data is sampled at a set rate, but for a single test one of these files typically has between 500 to 2,000 entries which represent the full test cycle from initial probe contact to full measured contact closure. After each cycle, a new file is created for each test point taken with an incremented index in the filename, resulting in all the files in any one folder correspond to all the test measurements made for one device over its lifetime.

While the intention was to produce a test stand to evaluate lifetime performance of these devices, the result was much more. In gathering the data mentioned and synchronizing these responses, there is a great deal more information stored for any one device because not only are the instantaneous values stored, but the time responses of these variables through the full contact closure. For example:

- Force and distance are recorded for each cycle throughout the device lifetime, and observing how that relationship changes from cycle to cycle can be used to determine changes to the beam in the form of plastic deformation.

- The slope of the force vs. compression curve and how that slope changes from device to device indicates differences in elasticity of the beam material (i.e. changes in the spring constant of the beam).

- Temporary variation in the final measured resistance used to indicate debris within the contact, or a gradual increase over time may indicate a contaminant film being formed.

These are just a few examples of how this data could be used beyond the scope of the original design. While this large volume of data carries a lot of potential, it also illustrates a pitfall as well. Previous work with this hardware during a few months of testing produced data on 101 devices, and if we look at the total number of times the measurement cycle described was performed, 14,813 data files were produced for these devices. Each of these data files contained on average approximately 800 measurements so addressing data management is critical in keeping all collected data in a usable format. While careful documentation has been enough thus far to ensure no data is lost, as data is passed between researchers and projects and modifications made which change the format of the data files, this will need to be addressed along the way. For existing data this means adding missing parameters of interest to the data files themselves (i.e. contact materials, geometry, beam size, contact bump configurations, etc.) and for future tests ensuring this information is stored when the device is tested to avoid possible errors later.

3.3 Micro-contact Fabrication

The next consideration involves the devices to be tested. Recall from previous discussions that electron transport across a contact is more ballistic in nature with higher Knudsen numbers. Since this Knudsen number is the ratio of the mean free path of the electron to the cross sectional area through which it is allowed to pass, there are two ways we can induce a high Knudsen number: increasing the electron's mean free path length or decreasing the surface area through which it passes.

Searching for materials which inherently possess a greater mean free path or finding means to increase this characteristic is one approach. This method however requires more of a discovery approach, and as it is not the only method of inducing quasi-ballistic electron transport, it is not the method of choice. Another method in which we can increase the Knudsen number is to decrease the cross sectional area through which the electron is allowed to pass. If we consider geometry alone, this makes MEMS contacts prime for inducing ballistic electron transport, intentionally or otherwise.

To test micro-contacts with more precisely controlled contact areas, the most feasible approach was to augment the existing micro-contacts design with small, controllable areas through modifying our fabrication process. Using more advanced fabrication techniques during the creation of the lower contact region, we can construct contact surfaces with the ability to maintain relatively small contact areas, but still be viable with contact forces typical of MEMS switches. This is accomplished only if we can build repeated, regularly spaced structures with extremely small, but known surface area. The structures must be rigid enough to withstand repeated cycling. If the engineered surface is relatively inelastic compared to the mating surface, then we have a much more accurate estimate of true contact area and can ensure that area changes minimally over the lifetime of the device. This then gives us the ability to not only validate the theory behind ballistic electron transport, but possibly capitalize on it.

One approach we can use to fabricate contacts of low, yet known contact area is to employ some technique in which we directly shape the contact regions. Preliminary work in engineered lower surfaces has shown promising results in this area in terms of controllability, but even with our high resolution lithography processes, contact areas are still on the order of microns. A focused ion beam or E-beam lithography

technique could be used to push this limit, but one fundamental limitation is that these techniques require us to individually fabricate each device as opposed to mass producing a pattern like we would with a masked photoresist technique. In reviewing all the available techniques which are likely to succeed based on currently published results, prior successes, and availability of the required systems, two methods are considered in this effort: Nanosphere Lithography (NSL), and Grayscale Lithography.

3.3.1 Nanosphere Lithography.

One method of creating patterns over large surfaces with features smaller than 1 μm is nanosphere lithography (NSL). To use this option, several factors were considered together as they are interdependent. Among these considerations are:

1. ease of obtaining large, regular patterning of nanospheres
2. material used and how that factors into test proposed
3. size of the nanospheres
4. method of deposition
5. overall processing steps needed to build desired contact surfaces.

As was already mentioned in the last chapter, several papers exist which explore the current state of this fabrication technique [129]; here is a summary of the results that apply specifically to this effort. In order to organize this process, let's consider each item listed above in turn.

Patterning efficiency is a prime concern in fabricating full devices. Consider that the bottom contact area of one of these devices presides directly below the contact bump, and each bump is only 12-16 μm in diameter, but these are spread out at very specific locations across a 3" diameter wafer. If we achieve large but incomplete

coverage, we may or may not pattern over the desired areas. The only way to know for certain is to individually inspect the 1,536 target locations on each wafer and document which are patterned and which are not. These spots represent less than 0.0075% of the total surface area of the wafer, but patterning in any location other than the contact regions provides no benefit. If we assume 100% coverage without this inspection, there is no way to determine which micro-contacts contained nanospheres and which were flat other than this inspection process. Also consider that this inspection is over a full 3" wafer which would not fit in any SEMs we have available with enough travel to inspect the entire surface. So this inspection must happen with an optical microscope. The literature suggests that areas up to 100 μm are achievable, but where those regions are located is not necessarily controllable. A few isolated instances of better coverage have been reported but only with very specific techniques, such as Si immersed in photoresist [129], so determining a suitable material which is appropriate for fabricating lower contacts for these types of devices with the other required fabrication steps is next.

Nanospheres are made from conductors (i.e. metals), semiconductors such as silicon (Si) or insulating materials, polystyrene (PS) and polymethyl methacrylate (PMMA) to name a few. All of these options are readily commercially available from a variety of suppliers, but different suppliers and different materials carry with them variance in sphere size as well as how often larger spheres are encountered to disrupt periodic placements. For our purposes, either patterning with a mask type material (i.e. PS) or directly placing metal spheres is the most direct way to fabricate the small contact areas desired while preserving our current device fabrication processes as much as possible.

The size of the spheres is another variable which must be considered. We can process the deposited layer to adjust the feature size, but the periodicity is deter-

mined strictly by the size of the spheres used. Previous work with nanospheres have suggested that 400 to 800 nm diameter spheres tend to be the best behaved in terms of large areas coverage [123]. Trying a range of diameters is one approach, however it has been theorized that successful deposition is a function of the size of the spheres, the viscosity of the carrier liquid, the radius of the meniscus between the fluid and substrate, and angle of the substrate to the liquid - at least with dip and/or convective type depositions [129]. With this many variables and the fact that the pitch of the features is not critically important to this work, we'll settle on 500nm diameter as a standard to eliminate this variable from the overall problem, which gives us a small enough pitch to provide several contact peaks under one of our upper contact bumps, and provides large enough spheres to be viewed optically to conduct the required inspection on a full wafer.

Next let's discuss the method of deposition. To date, the only recorded instance found of large scale coverage using spin coating has been with Si nanospheres immersed in photoresist. Processing for this however poses problems with our design. Thus, spin-coating is a last resort method in favor of other options. The most recent works suggest that dip coating seems to be the method of choice as it allows for simultaneous control over many of the key variables, specifically a variation of dip coating in which water is removed rather than moving the substrate up through the surface of the liquid. For this method, the literature available suggests there are six key parameters to be considered which are indicated in Figure 13 below.

When placing PS nanospheres at the surface, these spheres will either float on the surface, or sink and float close to the surface, or a combination of both. This depends on a number of factors including the density of the material used, its surface properties, how the spheres were pretreated, how they were deposited onto the carrier fluid, what the carrier fluid is, and how the test apparatus was handled after depo-

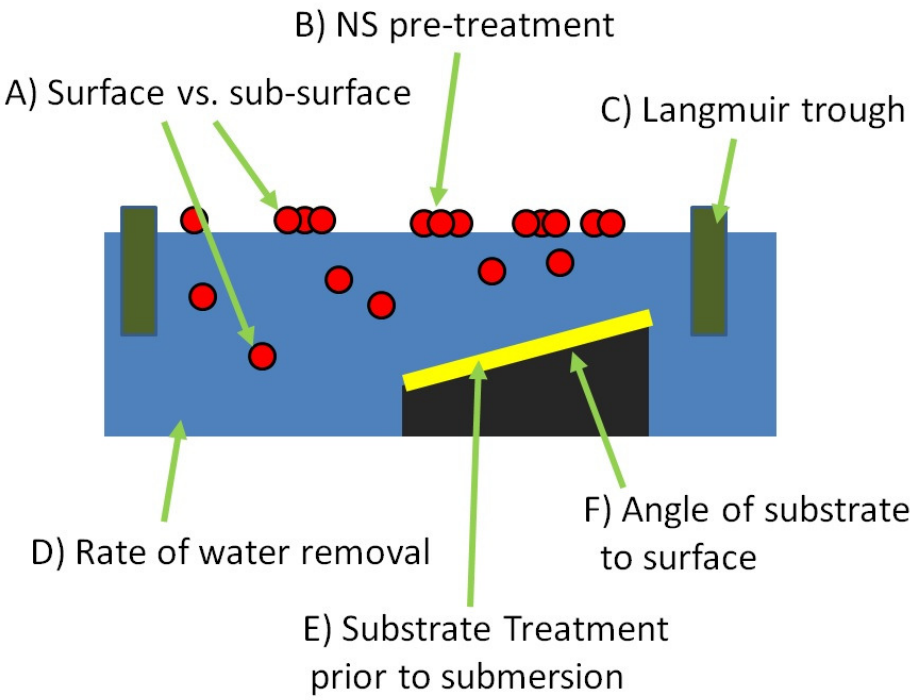

Figure 13. Six primary variables to consider during nanosphere deposition through drainage including A) Surface vs. Subsurface sphere placement, B) Pretreatment of spheres prior to placement, C) Use of a Langmuir trough to compress spheres prior to deposition, D) Rate of Water Removal, E) Condition of Substrate prior to deposition, and F) Angle of Substrate to Surface of Water [131].

sition [129], just to name a few. Where the spheres are placed seems to be largely a matter of finesse, but their placement is essential in achieving successful patterning. If the spheres are primarily floating, then the goal is to induce patterning on the liquid's surface and quickly transfer that layer to the substrate before it breaks apart or starts to fall beneath the surface. Under these conditions, we need the spheres to be able to flow among each other freely and be fairly attracted to each other, and the rate of water removal will need to be relatively high. However, if the spheres fall beneath the surface then patterning is achieved by slowly draining the liquid and using capillary forces to induce patterning through a more convective means along the air-water interface. In this case flow between the particles is less important, but

instead we need strong interactions between the particles and there needs to be some attraction between the particles and the substrate. Also, this instant requires a much slower drain rate as the particles need time to repopulate near the interface as they are patterned.

The next question addresses the use of a Langmuir trough, which is illustrated in Figure 14 below [167]. This depends largely on the above issue of surface vs. subsurface sphere placement as it is only beneficial in pushing together surface monolayers to induce a tighter packing. In subsurface spheres, this is simply a method of increasing sphere concentration which may or may not be beneficial depending on the other factors in capillary pattern formation.

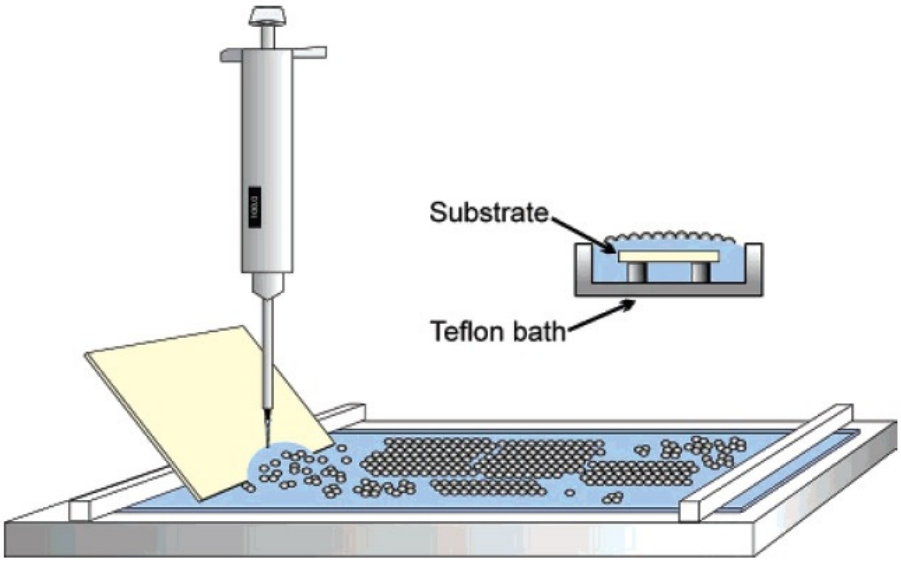

Figure 14. Self-Assembly at a water/air interface. The water surface is used as a medium to facilitate the self-assembly. The inset shows a cross section of the bath, demonstrating the transfer of a monolayer onto a solid substrate [167].

Finally there is the question of the optimal angle of the substrate to the liquids surface. In the extreme case (i.e. parallel placement), then as the liquid is drained we will trap some of this liquid in the form of droplets and as that liquid evaporates be faced with non-linear interfacing lines as these drops evaporate, so some angle is

necessary. It's been suggested that this angle is a function of primarily the size of the nano-spheres and the viscosity of the liquid being used, as this viscosity changes the geometry at the air-water interface [129]. Verification of this could be an entirely separate research project, so instead we will find an optimal angle based on trial and error, and since we've fixed the size of the nanospheres and will likely be using de-ionized (DI) water as our liquid, this fixes most of these variables so we could then just base our transfers on this optimal angle found through experimentation.

All of these issues are being explored by building containers to perform the NSL depositions. These containers have been fabricated using 3D printing. This technique uses a plastic filament made of either acrylonitrile butadiene styrene (ABS) or poly-actic acid (PLA) which is fed through a heated extruder. This extruder is passed over a heated glass plate and ejected in layers approximately 0.2mm thick. The extruder is controlled in both the x and y directions by servo motors while the plate height is controlled with a third motor. This allows for structures to be built from this material in a relatively short time, directly from 3D models built in AutoCAD or any similar software package. The plastic used is not susceptible to water, ethanol, methanol or isopropyl alcohol, but acetone will soften and partially dissolve it. The plastics used are rigid but flexible, so multiple part assemblies can be printed separately and locked together. Acetone can also be used to fuse pieces together if required. While these containers are not always water-tight, the surface can be treated with acetone or coated with liquid rubber to seal them from leaks.

Once we accomplished this deposition, focus was shifted to determining how to integrate this layer into our fabrication process. To incorporate this technique into device fabrication, a hybridized approach was pursued with the nanospheres to confine their deposition to specifically placed and oriented regions. These sites were controlled through traditional patterning of photoresist thick enough to accommodate only a

single layer of nanospheres, and in small enough regions to retain these spheres during deposition. The masks used to accomplish this were aligned to the rest of the masks such that this is simply another fabrication step. Once the deposition was complete, the nanospheres were removed and the device fabrication process continued with the formation of the beam for the upper contact.

To produce the hybrid masks discussed, photoresist was the next area of focus. To capture a monolayer of spheres which are 500 nm in diameter, then ideally we want our photoresist to be approximately the same thickness. To capture a bilayer, we must increase this thickness to approximately 800 nm to accommodate for stacking of layers. Since photoresists are designed for precise thicknesses, we need only match the desired thickness on the spin speed curve provided by the manufacturer. Figure 15 below shows such a pairing for 500 nm spheres within 1800 series photoresist [168].

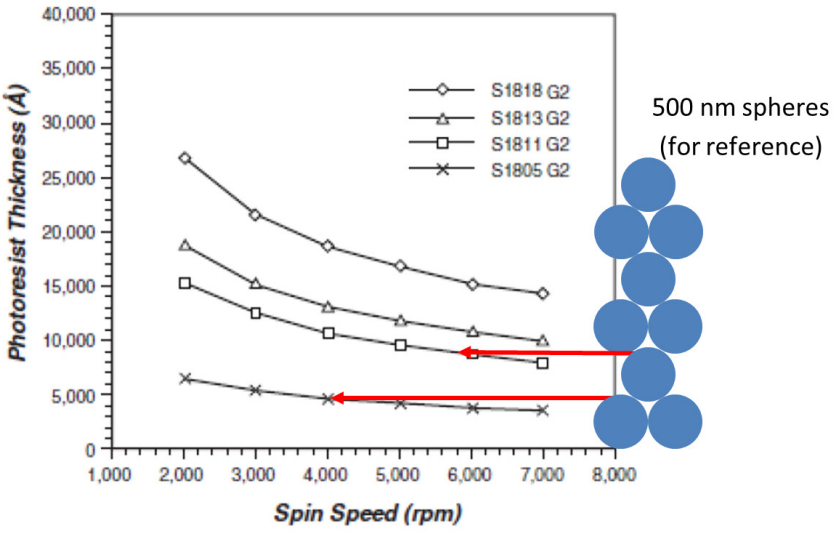

Figure 15. Comparison of 500nm nanospheres to the spin-speed curves for an 1800 series photoresist, indicating the proper material selection and spin rates to match thicknesses for single or stacked layer [131].

Optionally, another set of techniques explored in multiple publications involves the incorporation of nanosphere manipulation after nanosphere layer formation, but prior to using the nanosphere layer as a mask for deposition or etching. For this

experiment, polystyrene nanospheres are used exclusively which offers a variety of scaling methods. Plasma ashing has been used to accomplish this, but reactive ion etching (RIE) allows for a more precise control of the rate of etching. Figure 16 illustrates the difference between using a non-etched monolayer of nanospheres as a deposition mask (a) vs. the same nanospheres after being reduced in size through etching (b). In this paper, only additive processes were used, but nanospheres could be used as a mask for etching the substrate. To do so, a suitable chemistry would be needed to selectively etch the substrate instead of the nanosphere material. This would maintain the spheres during the process, and instead etch the substrate, the result of which is shown in part (c) of Figure 16.

What is not shown in this figure, but must also be considered is the addition of photoresist to this process, and specifically consideration of the selectivity between the three materials used (substrate, nanospheres, and photoresist). This depends on finding a suitable chemistry to accomplish selective etching and material selections may need to be altered. If these concerns are addressed properly, photoresist can provide a valuable additional tool to shaping nanospheres prior to deposition.

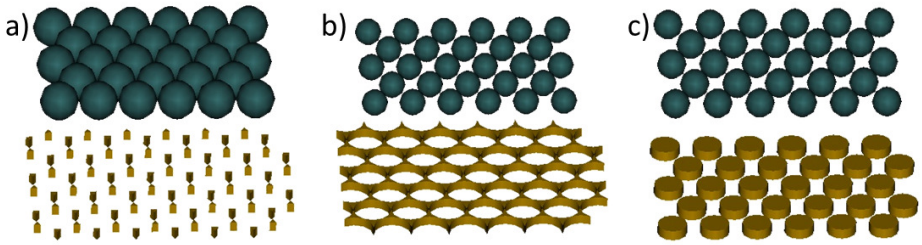

Figure 16. Methods of nanosphere manipulation and use in NSL. If used as a mask without alteration (a), with RIE prior to deposition (b), and if the nanospheres are deposited on top of the layer and used as an etch mask after RIE (c) [131].

Additional post processing may also be considered at this point. For example, if we have regions of self-assembled layers captured within pockets formed by patterned photoresist, we may expect the edges of these layers to possess gaps which may be

undesirable. If however a photoresist is selected which reflows at a relatively low temperature, these side gaps could be at least partially closed, leaving only the inter-sphere spaces within the center of the patterned region left for deposition to occur, which may be critical if the number of patterned spots needs to be precisely controlled.

3.3.2 Improved Grayscale Lithography.

One particular method of writing lithography masks involves the use of a laser lithography system such as the Heidelberg μPG-101. The system uses a small diameter UV laser along with a precise positioning system. This was the device used for this work, and was supplied from the manufacturer with a guaranteed beam diameter not to exceed 1 μm, and with a positioning step size of 400 nm in both the X and Y dimensions. Because other models are available from the same manufacturer with more precise positioning capabilities, it is possible that higher accuracy is achievable but cannot be guaranteed with this particular machine design. Also, the exact diameter of the beam may be slightly smaller than 1 μm. Both of these characteristics are critical in defining the smallest feature which can be realized.

The system as supplied includes software which allows for two modes of operation. The first mode involves using files designed in CAD software which establish basic geometric shapes. To print the shapes, the software determines the number of lines which need to be written to be able to fully expose these regions. Before printing, both the power and the duty cycle of the laser is set and everything within these regions is exposed to the laser at those settings. Typically this is set high enough to fully expose these regions, and after further processing this results in a standard lithographic mask. The beam positioning is calculated using the full resolution capability of the system, and because continual lines of exposure are used this allows for the highest resolution of the machines capability to be realized.

The second mode of operation utilizes images instead of CAD files. In this mode, each pixel within the image is scaled down with a minimum step size of 1 μm (the diameter of the beam). The system then positions the beam at each pixel location and scales the amount of power delivered based on the shade of gray of that particular pixel. When the photoresist is developed, these regions of partial exposure only result in partial removal and the final image has features in the third dimension because of this.

At this point, consider the sort of structure that would be ideal for micro-contacts in which we want small, repeatable surface area. To construct the sort of columns that were discussed previously, grayscale lithography offered a feasible approach. Using bitmaps however, this extremely limited the resolution because of the nature of the software. Combining these two methods will allow us to create higher resolution grayscale results, similar to a concept proposed a decade ago before this technology was readily available [142]. Consider Figure 17 below, which illustrates this concept.

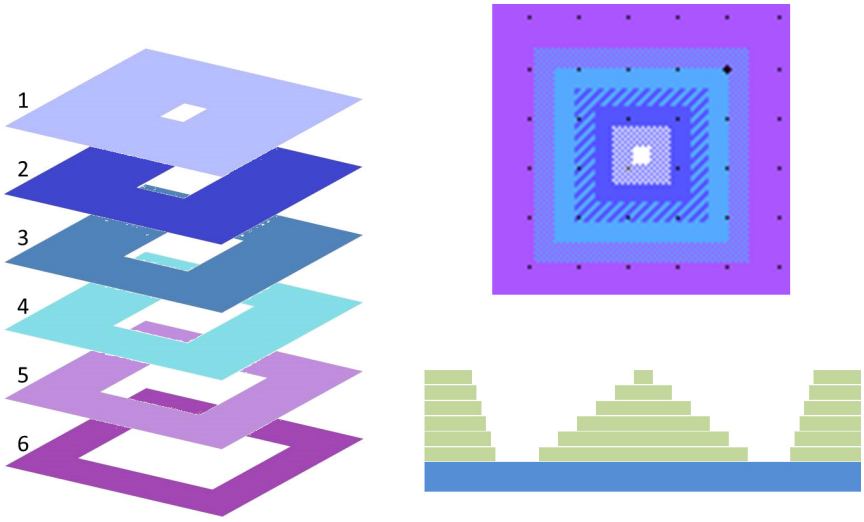

Figure 17. Hybrid method of grayscale lithography utilizing multiple CAD designs exposed in line scan mode, obtaining greater beam position accuracy than an image based mode can provide.

The first step was to characterize what power levels and duty cycles achieved the desired results. Using a combination of simple rectangular shapes which partially overlapped, various combinations of power and duty cycle were characterized for optimal exposure, which is shown in Figure 18 .

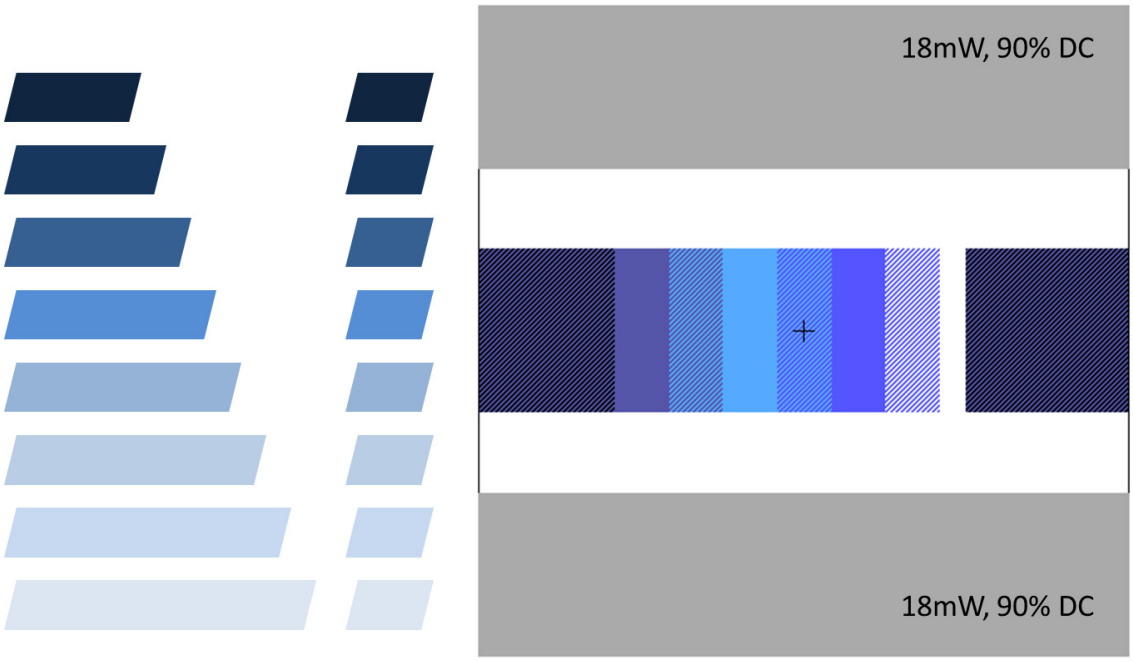

Figure 18. Illustration of multi step exposure test files which when run in succession produce a stairstep profile which is easily measured to characterize step changes. Top and bottom regions are full exposures to determine overall depth reached relative to photoresist depth.

Once the CAD files were created for the various layers used in this test. A variety of power and duty cycle settings will be used with this pattern to obtain the optimal recipes. In order to run these tests, the automated procedure is required which specifies the location of each repeated pattern, along with the power and duty cycles required for each step, eventually producing a script file to be run by a mouse and keyboard emulator. A sample of this code and screenshot of the script writing software is shown in Figure 19.

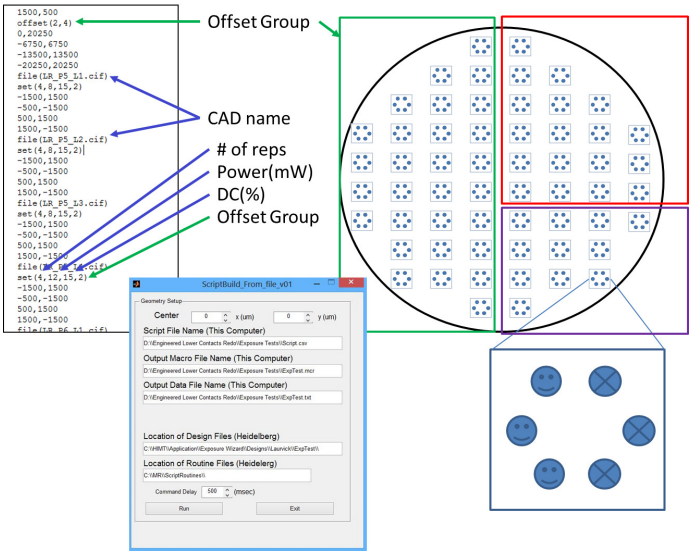

Figure 19. Sample code segment showing format of automation software. A text file is created which describes relationships between offset groups and files parameter. The text file is used to create the script file which when run automates the multi-CAD writing method.

When the script file that is generated is moved to the Heidelberg system and executed, it performs all the necessary file loading, offset positioning, parameter setting, and exposure triggering for each layer of the process. The software then waits for confirmation at each step, which comes in the form of observing the expected change in the images on the screen. If each step is executed correctly, then the system behaves as expected and the emulator is able to continue. If however anything unexpected occurs, the emulator waits for a conformation screen which never appears, and it will simply not be able to proceed. Thus this process was run safely and autonomously without a requirement for constant oversight. A detailed description of this process is provided in the appendices.

3.3.2.1 Exposure Study.

Instead of the standard method of grayscale exposure, this approach uses several different CAD designs along with repeated, low-dose exposures to achieve the same

effect as the bitmap approach, but with the resolution of the CAD approach. This does however require characterization of how much power must be used in each step to achieve repeatable depths of exposure. Using a combination of simple rectangular shapes which partially overlap, various combinations of powers and duty cycles were characterized for optimal exposure, which is shown in Figure 20 below. Characterization was performed using a seven step process, intended to yield recipes more suited for two, four, and six step designs.

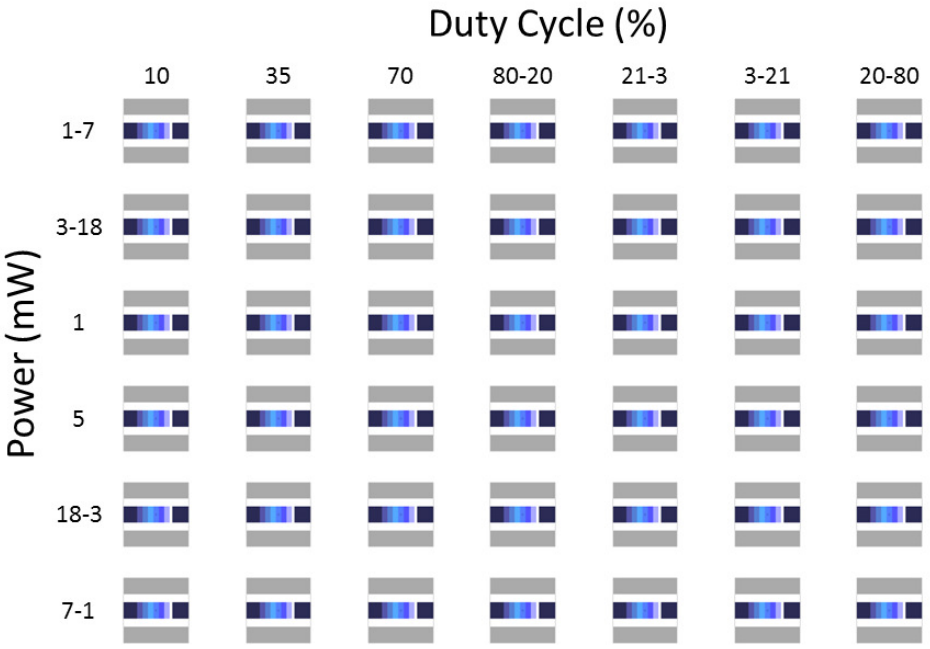

Figure 20. Matrix of power and duty cycle settings to determine optimal series of exposure settings required for multiple exposure grayscale lithography through repetitive CAD files.

Once the power requirement to expose the photoresist was determined for either two, four, or six steps, this was applied to making actual device surfaces. The next challenge however was repetition. Consider a single 3 inch wafer which contains approximately 250 reticules. Each reticule contains up to 16 micro-contacts, and each contact may require up to six steps. This would require 24,000 repetitive runs on this laser lithography system. While each run may only take a few seconds, the process of

loading and positioning this number of files becomes overwhelming. To address this, an additional level of automation were applied using keyboard and mouse emulation.

After creating the CAD files for the various layers of the contacts, these were stored on the system. Next, the exact position of each of the reticules was stored in text file, along with the position of each device within a reticule, as well as the desired power and duty cycle for each step of the process. A text file was created containing this information, and was then run through a program which translates this information along with the names of the design files into a script file which was loaded by the emulator. When the script file was executed it performed all the necessary file loading, offset positioning, parameter setting, and execution for each layer of the process. The software then waited for confirmation at each step, and if this was not received it simply did not proceed. Thus this process can be run safely and autonomously. A detailed description of this process is provided in Appendix A.

3.3.2.2 True Resolution Limits.

Before discussing how this can be applied in making micro-contact surfaces, we should first test the true limits of the system to determine how small a feature can be realized. While the manufacturer guarantees a beam diameter not to exceed 1 μm, a simple test was run to determine exactly how small a channel can still be exposed, which indicates actual beam size.

In addition to determining the true beam diameter, the actual minimum step size should also be investigated. This particular system was manufactured with 400 nm repeatability, but other models are available with an additional order of magnitude of resolution. These high-resolution systems, are much larger and heavier, which was presumed to be a requirement to hold these tolerances. This does not mean however that they do not use the same control hardware, and therefore the actual resolution

of this system may be better than the guaranteed 400 nm. If this was true, then we should expect to see at higher resolutions more variability in the shapes of identical repeated features. To test this characteristic of the system, two sets of design files were built. The first, low-resolution files were built under the assumption that 400 nm was the smallest step size available. A second set which was called medium resolution was built with 80 nm step sizes, which was considerably better but not the highest theoretical resolution.

This step size was important not only because it defined the size of the smallest feature, but along with the beam width established the minimum possible pitch between features. As shown in Figure 21 below, the beam must pass between the outermost patterns, which ultimately determined the pitch. Patterns which utilize only two steps however can be placed much closer than those with six steps, which is also explained in this figure.

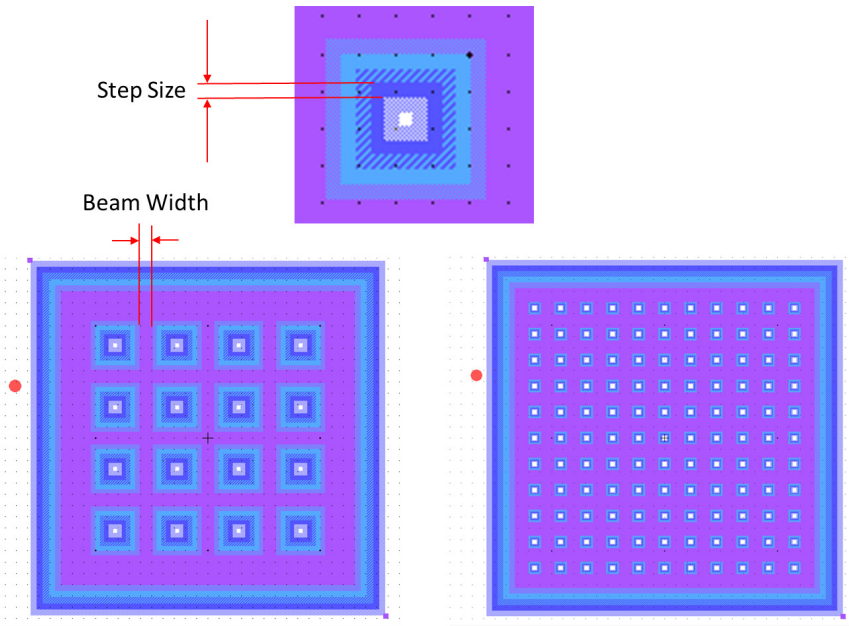

Figure 21. Potential layouts for 6 step hybrid grayscale patterns which accomodate a 1 μm beam diameter with two different step sizes. The lower left image represents the spacing requirements for a low resolution patterning where a 400nm step size is required while the lower right shows the spacing for an 80nm step size.

The next area to consider was how to utilize these patterns in building micro-contacts. Previous work in this area which used the bitmap grayscale approach, patterned contact features in 1800 series photoresist on a silicon substrate. An etch study was conducted to determine what settings provided a selectivity between silicon and photoresist of 1.0, and this was executed to transfer the patterned photoresist into the substrate. Following this step, a passivation layer was added followed by the lower contact metal and the contacts built as normal upon the structures. To provide passivation however requires we use methods that do not maintain perfect conformal deposition. To avoid this unnecessary feature blurring, passivation will occur before the grayscale lithography step. This requires however a new etch study between the photoresist and silicon nitride. Following this step, the bottom contact surface can be applied. This could be a thin-film of gold, and application of some other conductor using atomic layer deposition, or combination of both. In depositing that thin-film conductive layer, the next concern was how to improve our ability to predict contact resistance in a device which utilizes these kinds of films.

3.3.2.3 Etch Study.

The goal of this etch study was not only to identify a set of reactive ion etching (RIE) parameters which are able to etch both 1800 photoresist and silicon nitride at a selectivity of 1.0, but at other selectivities near this value so that we might explore the possibility of elongating or shortening features during the etching process. This idea is illustrated in Figure 22.

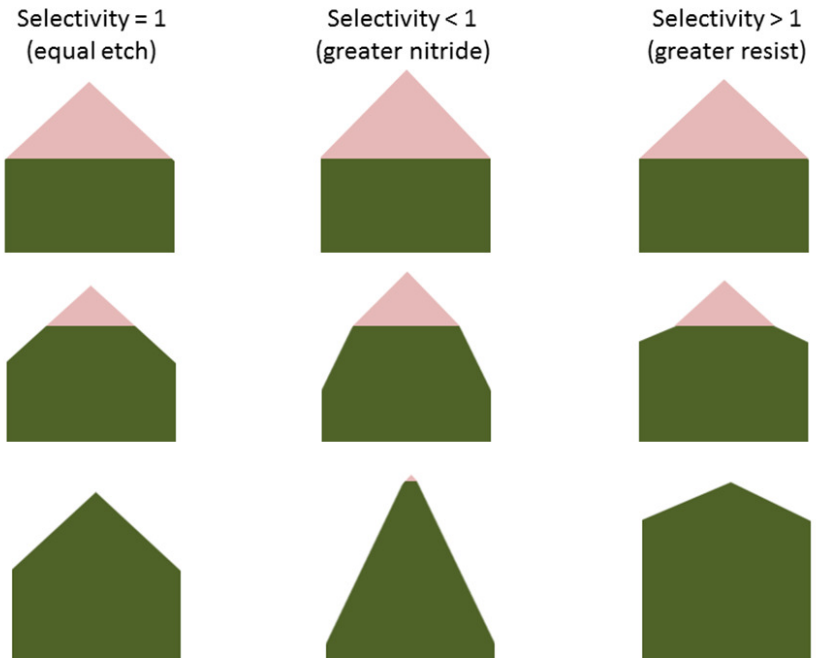

Figure 22. Results of varying selectivity of RIE etch of 1800 series photoresist pattern over silicon nitride substrate. On the left, a selectivity of one indicating equal etch rates of both materials transfers unaltered features to the substrate, where selectivity less than one indicates nitride is etched faster than photoresist resulting in elongation of features, where on the right selectivity greater than one indicates photoresist etched faster than substrate and resulting flattening the features.

3.4 Thin-film Contact Resistance Modeling

In Chapter 2, a number of factors which can influence contact resistance were discussed along with citations of relevant work done in that area. Several of these areas still need to be addressed an a scale appropriate for use with micro-contacts.

As was already mentioned, the classical contact resistance model based on Maxwell's spreading resistance theory is [37]:

$$R_{con} = \frac{\rho}{2r_{eff}} \tag{7}$$

Here R_{con} is the constriction resistance and ρ is resistivity and r_{eff} is the effective radius due to surface asperities [37]. We previously mentioned that contamination can affect this resistance, but if this is neglected then the constriction resistance is

equal to the contact resistance. This form of contact resistance is more commonly referred to as the diffusive contact resistance model. This can however be modified to include the effects of elastic and plastic deformation, which gives us Equations 8 and 9 which now incorporates contact force F_c in determining the contact resistance R_c [41]. Contact resistance for diffusive electron transport is represented by R_{cDE} for elastic material deformation and R_{cDP} for plastic material deformation.

$$R_{cDE} = \frac{\rho}{2}\sqrt[3]{\frac{4E'}{3F_cR}} \tag{8}$$

$$R_{cDP} = \frac{\rho}{2}\sqrt{\frac{H\pi}{F_c}} \tag{9}$$

Here E' is the Hertzian modulus, R is the asperity peak radius of curvature, H is the Meyer hardness of the softer material, and F_c is the contact force [53]. To accurately describe micro-contact closures however, we must recognize that some of these asperities deform plastically while the bulk of the contact may still be deforming elastically. This was accomplished through the derivation of a modified effective contact radius given by Equation 10.

$$r = \sqrt{\frac{F_c}{H\pi\left[1.062 + 0.354\left(\frac{2}{3}K_Y + 3\left(\frac{\alpha_c}{\alpha}\right)\right)\right]}} \tag{10}$$

Here, K_Y is a function of the Poisson ratio, given by $K_Y = 1.1282{+}1.158\nu$. Finally, the ratio of $\frac{\alpha_c}{\alpha}$ is a measure of how far past the point where we've reached elastic-plastic behavior. While this works well for large scale devices, for micro-contacts the effective contact area is typically much smaller not only because of the scale of the devices, but also because of the reduced contact forces when compared to macro devices. Because of this, ballistic transport which was mentioned in Chapter 2 must be considered as well. Recall the model for combined elastic-plastic, ballistic-diffuse

model from Equation 5, the two resistance terms for ballistic elastic-plastic contact resistance (R_{cBEP}) and diffusive elastic-plastic contact resistance (R_{cDEP}) are given by:

$$R_{cBEP} = \frac{4\rho K}{3\pi r} \tag{11}$$

$$R_{cDEP} = \frac{\rho}{2r} \tag{12}$$

While these equations have correlated well with experimental results [49], some variance between observed and predicted results remains. One possible explanation is the previously mentioned behavior of extremely thin-films and how that can effect contact resistances of devices which use these films.

3.4.1 Integration of Theory into Contact Resistance Models.

To address this, focus was placed on recent work which summarizes a simplified method of incorporating spreading resistance which applies spreading resistance theory in a purely geometric method. From the work of Zhang *et al.* [169], this simplification was made for both radial and Cartesian geometries. For our case, our typical device utilized hemispherical bumps for upper contact, so the radial geometry solution was more appropriate. For this, the appropriate equation to describe this overall resistance in this device is given by Equation 13 [164, 169].

$$R_{Ss} = \frac{\rho}{4a}\bar{R}_{Sx} \tag{13}$$

where ρ is the resistivity of the material and a is the radius of the circular contact. The definition for $\bar{R}_{Sx}$ is dependent upon the ratio of the radius of contact to the thickness of the film (a/t) and for $(a/t) > 1$ is given by [169]:

$$\bar{R}_{Sx} = 0.28 + 0.0502\left(\frac{t}{a}\right) + 0.0523\left(\frac{t}{a}\right)^2 \tag{14}$$

and for $(a/t) \leq 1$ [169]:

$$\bar{R}_{Sx} = 1 - 2.2968\left(\frac{a}{t}\right) + 4.9412\left(\frac{a}{t}\right)^2 - 6.1773\left(\frac{a}{t}\right)^3 + 3.811\left(\frac{a}{t}\right)^4 - 0.8836\left(\frac{a}{t}\right)^5 \tag{15}$$

To use this model with our typical contact geometry, consider Figure 23 which shows the expected current pattern in our thin film from the circular contact. Zhang *et al.* derived the above equations starting with a circularly uniform current flow, but if we go through this derivation more closely, we can still apply it to our situation with a few assumptions. Where the original derivation defines a circular region near the contact area in which current is 'spreading' through the thickness of the film and in this region, spreading resistance takes effect. The outer ring of this region is defined as the point where spreading no longer occurs, or in other words we have reached uniform current distribution throughout the thickness of the thin-film. In our case, we can make the assumption that we can define some arbitrary boundary at which this uniform distribution is still reached, then the theory will still apply, we simply won't know the exact region over which spreading resistance is physically occurring due to our more complicated geometry [164].

Recall that in order to take our contact resistance measurement, some small amount of current, shown as 'B" in Figure 23, must be present to obtain a voltage measurement across the contact. While we did not know the exact path these electrons followed, we relied on the fact that this measurement was with a high impedance device and the current was small enough to be negligible [164].

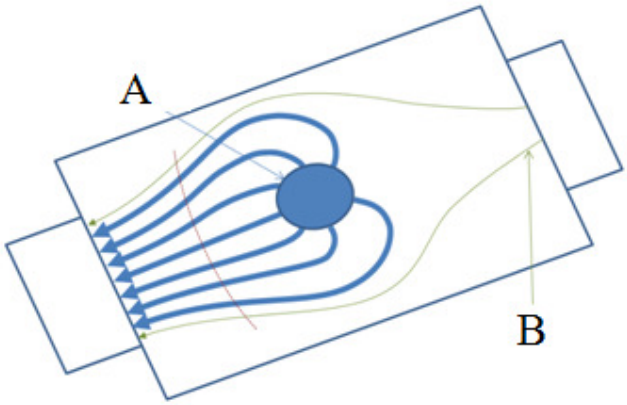

Figure 23. Horizontal current distribution in thin film portion of micro-contact. Relatively high current flow from micro-contact closure (A) along with near-zero current returning from the voltage measurement (B) [164].

If we consider the current flow through the thickness of the thin film, as shown in Figure 24 it was also assumed that while our geometry was not radially circular, the net effect is still some volume of material in which spreading resistance occurred until uniformity was reached through the thickness of the thin-film contact.

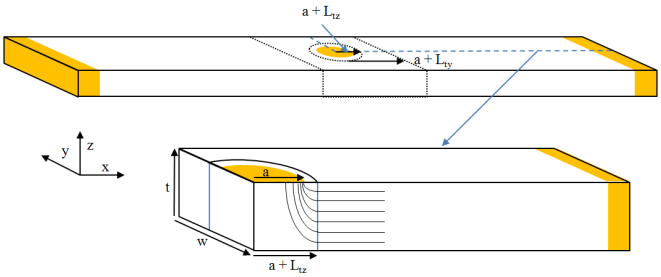

Figure 24. Vertical current distribution in thin film portion of micro-contact.

Another consideration in fabricating and testing these devices was to recognize the impact of contact force on this apparent effective radius term a [53], as shown in Figure 25, which is synonymous to the radius r used in Equation 10. We have already mentioned that we are adjusting the effective contact area for contact force to account for plastically deforming small surface asperities while elastically deforming

the bulk of the material, but that is a slightly different consideration. This is simply stating that even if we had perfectly smooth, asperity free surfaces we would still have a relationship between contact force and contact area as the contacts pressed together and shared more surface area as the contacts elastically or plastically pressed together[164].

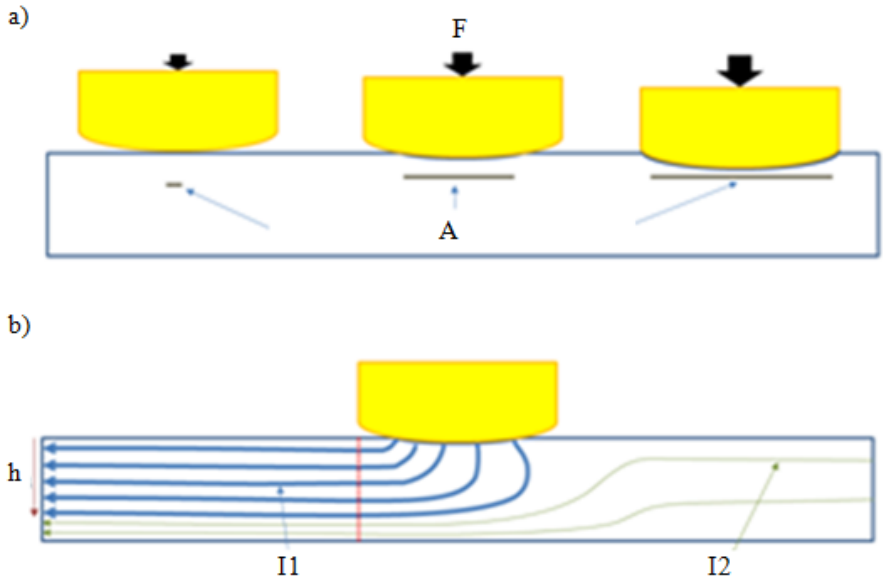

Figure 25. Cross section of current flow distribution a) representing the effect of contact pressure on effective area, A and b) view of interaction of the currents flowing through a cross section of lower contact pad during data collection.

The model derived by Zhang *et al.* [169] suggests that this corrective factor could be applied to any expected resistance calculation in which thin-film spreading resistance is expected to apply. For our case, this can easily be tested by using thin-film devices and operating them in a regime in which we expect a certain model to be relevant, and compare the results with and without this correction factor.

Our starting point was to use data gathered from prior testing in which this phenomenon was considered to be negligible. That data was obtained from devices that were designed for the suitability with the test stand in which they were tested,

and their applicability to existing contact resistance models. Recall the geometry of these devices from previous discussions. These were designed to emulate Holm's crossbar experiment in which a known current is passed through the contact, and using the other pair of measurement pads the voltage is measured. This method eliminates any complications of estimating bulk resistance, or resistances of any other part of the circuit because the combination of voltage and current measured apply only to the contacting surface itself. The upper contact was fabricated in such a way that the underside of the beam has a hemispherical contact bump which allows greater accuracy in estimating contact area. The amount of force applied to this upper beam was controlled and monitored, eliminating any error in estimating contact force through electrostatic actuation or some other means of closing the contact. While the expected current pattern resulting from this geometry was radial, it was not uniform in all directions. The suitability of the polar model was evaluated with this initial geometry, however better results are possible with a modified approach.

Zhang *et al.* also offers a second geometry for the theory provided. This geometry was used as a basis for a revised contact design such as shown in Figure 26 below.

With this geometry, a more predictable current pattern was expected with much less deviation from the spreading resistance model geometry. For this rectangular version of the model, Eqn 13 is replaced with Eqn 16:

$$R_{Ss} = \frac{\rho}{4\pi W}\bar{R}_{Sx} \tag{16}$$

where ρ is the resistivity of the material and W is the width of the rectangular contact region. The definition for $\bar{R}_{Sx}$ in this geometry is much simpler, and in all cases is given by Eqn 17 [169]:

$$\bar{R}_{Sx} = 2\pi\frac{a}{h} - 4ln\left[sinh\left(\frac{\pi}{2}\frac{a}{h}\right)\right] \tag{17}$$

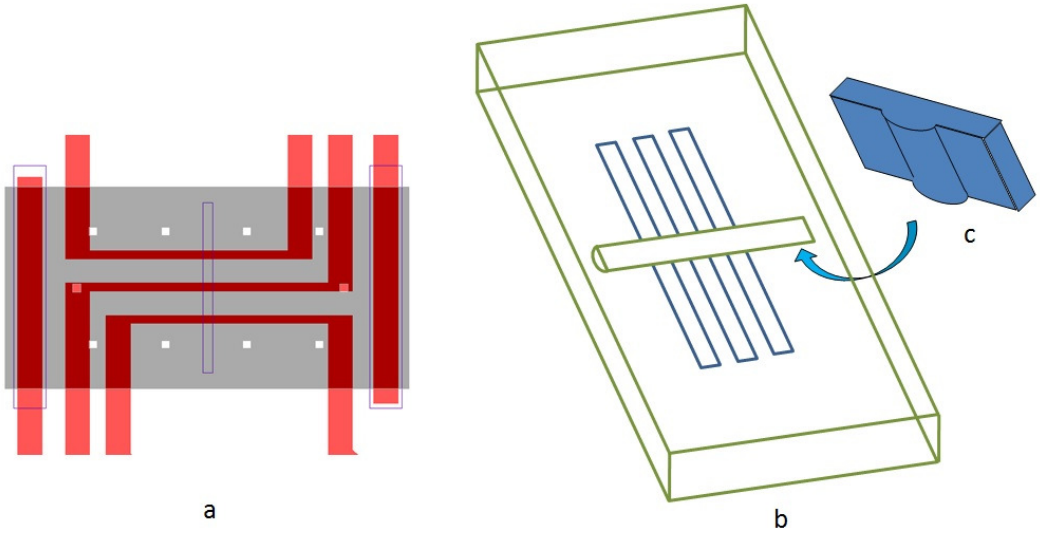

Figure 26. Proposed beam design for testing thin-film spreading resistance illustrating a) top view of design file showing traces in relation to beam and cross-member, b) isometric view of structure, and c) under view of cross member after fabrication.

To predict how much of an impact this design should have on overall contact resistance values, we used the theory provided by Zhang *et al.*, and assume an otherwise 'perfect' contact, free from any surface irregularities. Using this model, we can predict the range of values we would see for various scale sizes as outlined in Table 1.

Table 1. Predicted Spreading resistance for various geometric configurations of new device design.

metrics (μm)					
a	h	W	a/h	$\bar{R}_{sc}$	R total (Ω)
1	0.28	1	3.57143	13.89855	0.0243
1	0.28	0.5	3.57143	13.89855	0.0487
1	0.2	1	5	18.97628	0.0332
2	0.28	1	7.14286	26.59292	0.0466
2	0.2	0.5	10	36.74845	0.1287

While this does address any errors in matching current flow in the devices with our models, it does raise an additional challenge. In our radial case, we utilized the

concept of an equivalent contact radius which conveniently has been used widely in prior works addressing how to treat surface roughness, and therefore we could directly replace this value with one calculated from our improved models. This new geometry however uses a contact width instead. As surface asperities are inherently more of a circular rather than rectangular feature, we will need to take this into account. The simplest method would be to calculate the theoretical area of our rectangular contact, and determine what the equivalent ideal radius would need to be to yield the same overall area. We could then simply use this ideal radius as before and apply all the existing models using this revised number instead. This provides a means of approximating a rectangular contact area comprised of several smaller asperities, just as the circular contact models accomplished.

3.5 External Influences on Contact Reliability

A second area of interest to be explored involves a better understanding of the breakdown mechanisms in micro-contacts, understanding root causes of failure and exploring ways in which lifetime and reliability can be extended. To accomplish this, a phenomenological-based modeling approach was pursued using data obtained from the effects of circuit configuration, contact polarity, dissimilar materials, and applied power experiments.

3.5.1 Effects of Circuit Configuration.

We have the opportunity to explore a number of aspects of how micro-switches are used from a circuit configuration standpoint and what configurations might be harmful or beneficial to a particular design and/or material. Within this subtopic there are two areas to be focused on. First, it has been proposed that the reliability of contacts can be greatly impacted by what kinds of circuit elements are in

series and parallel to the micro-contact, either reactive or passive [10]. This theory was explored using the test stand and contact design directly, and in observing any premature failures those devices provide the foundation for further investigation to better understand the breakdown mechanism observed. Understanding that breakdown mechanism will give us clues as to what materials or contact design will better withstand these destructive mechanisms. Second, we were able to test how we could use various circuit configurations in a protective manner, much the same as was done with macro devices that must deal with macroscopic breakdown mechanisms such as arc suppression in a high voltage switch.

To test this theory, we'll use identical devices and simply insert them into a variety of circuit configurations and maintain these configurations during repetitive loading. Under DC conditions, the results of these circuits as a previously theorized [170]. Some circuit configurations may be detrimental to device performance, such as parallel capacitance. Under such conditions, charge maybe presents on this capacitor prior to a contact closing and induce effects similar to those resulting from hot switching during contact closure. Other configurations are theorized to be beneficial to the overall lifetime of device. If a parallel circuit path was present for example, this may have allowed for an alternate path for charge to dissipate prior to closure providing some level of protection for the device. The theory goes on to state that these components need not be reactive, passive devices may also offer some level of protection. A range of circuits which will test a variety these conditions is shown in Figure 27 below.

Finally, the results of these DC-based tests were used to give us some validation for the theory. We then repeated these tests with low-frequency, low-amplitude AC loads under otherwise identical conditions. Consideration was given regarding the sizing of reactive components relative to the frequency of the loads which were ap-

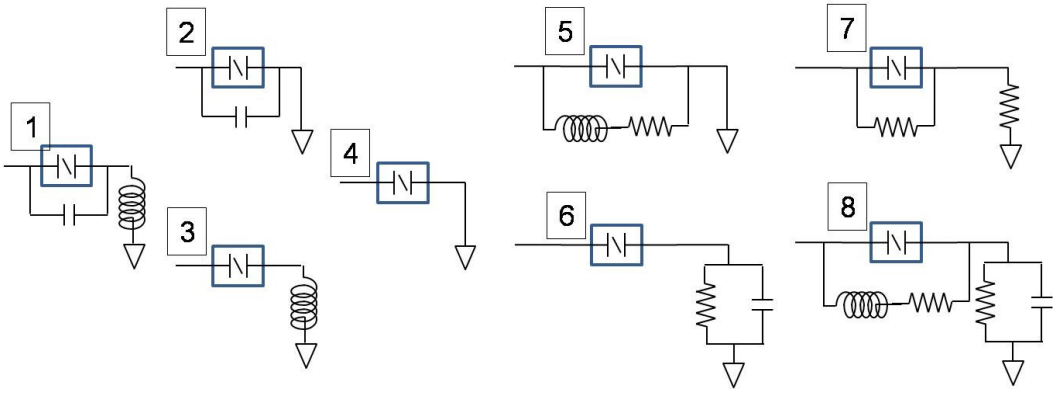

Figure 27. External circuit configurations to be explored. Circuits 1, 2, and 3 represent potentially detrimental active element circuits. Circuits 5, 6, and 8 show potentially beneficial active circuit configurations and circuit 7 shows a passive circuit configuration.

plied. In general, capacitors and inductors were small enough so any time constants associated with these circuits occurred much faster than any the frequencies applied, and therefore should have no effect. However, some testing was conducted in which the size of some of these components was altered to see if there is any obvious affect. The overall purpose of observing the effects of these kinds of AC loads are twofold. First, as there is a keen interest in eventual applications of micro-switches with RF applications, much of our understanding of breakdown mechanisms is based purely on results obtained under DC conditions. Thus, low-frequency AC allows us a better means to bridge the gap and help understand how applicable our current theory is to RF applications. The second purpose of this kind of loading involves recent observations regarding the sensitivity of these devices to the polarity of the load applied.

3.5.2 Effects of Polarity.

Another area of interest is to test the sensitivity of micro-contacts to various polarity configurations, or even exposure to an alternating current (AC) load. Even

devices in which both contact surfaces are the same material will vary in certain material properties depending on the method of deposition. Gathering data to better characterize how susceptible micro contacts are to these variations with respect to contact polarity would prove valuable in deciding how to fabricate and utilize these devices more effectively. As mentioned in the last chapter, MEMS switches have been explored for RF applications and will likely continue to be as we improve performance and reliability. For this work, we're asking a more fundamental question with lower frequency AC loading which isn't often considered in the literature. If so, then a better understanding of this underlying property of micro-contacts will allow for improved designs for all uses and applications.

Previous works have suggested that a common cause of failure in micro-contacts is due to electromigration. As current flows between contacting surfaces, the passing electrons are capable of providing enough force to break free sections of material on the surface. As current flows through this closed contact, some degree of Joule heating occurs in this material. Depending on the material which was dislodged as well as the surface it was in contact with, this small piece of material might break free when the contact is opened, and upon the next closure change the contact resistance or in extreme cases short the contact or prevent closure entirely. Data was gathered on devices which fail in this manner to better explain how this occurs and again, what can be done to prevent this failure mechanism in the future.

3.5.3 Timing Considerations.

In previous discussions, the impacts of hot versus cold switch testing have been differentiated. While for these tests both conditions are of interest, it was important to consider how the testing must be conducted in order to maintain hot or cold switch conditions so that any data collected can be evaluated properly. As a devices

cycled rapidly in order to induce wear, the speed of the device actuation must be carefully considered relative to the frequency of an AC load being applied; specifically at extremely low frequencies. To understand this fully consider Figure 28 below.

As shown in part a of this figure, if we consider the blue sine wave which drives the opening and closing of the contact, there was only a portion of the cycle in which the contact was fully closed. This is shown as the green area between (b) and (c) in part A of the figure. If we wish to induce one full cycle at a specific frequency this period of time during which the contact was fully closed had to be long enough to accommodate the load applied. As the load frequency gets smaller, the time required increases and therefore the frequency of actuation must decrease. As shown by this figure, we must allow for approximately 20% of the actuation cycle to be able to accommodate the test signal. Therefore the maximum actuation frequency can be no faster than approximately 20% the frequency of the test signal. This means for a test frequency of 100 Hz, the contact must remain closed for approximately 10 ms. If we then calculate the actuation frequency required to maintain this, it will take approximately 50 ms of closure time, which corresponds to a 20 Hz overall actuation cycle rate. If we wish to test to large numbers of cycles, this would take a significant amount of time which must be accounted for. We must also consider the phase of the load relative to the overall actuation cycle, particularly if we are only able to induce one cycle during each closure as shown in part B of the figure. If this is true, then half of the load was under unfavorable polarity while the other half was reversed, and the sequence of these may be relevant when considering overall device performance. Finally the effects of hot switching under these conditions was considered. To do so, we only needed to extend the load cycle slightly (or induce a slightly slower load frequency with the same actuation frequency) as shown in part three of the figure.

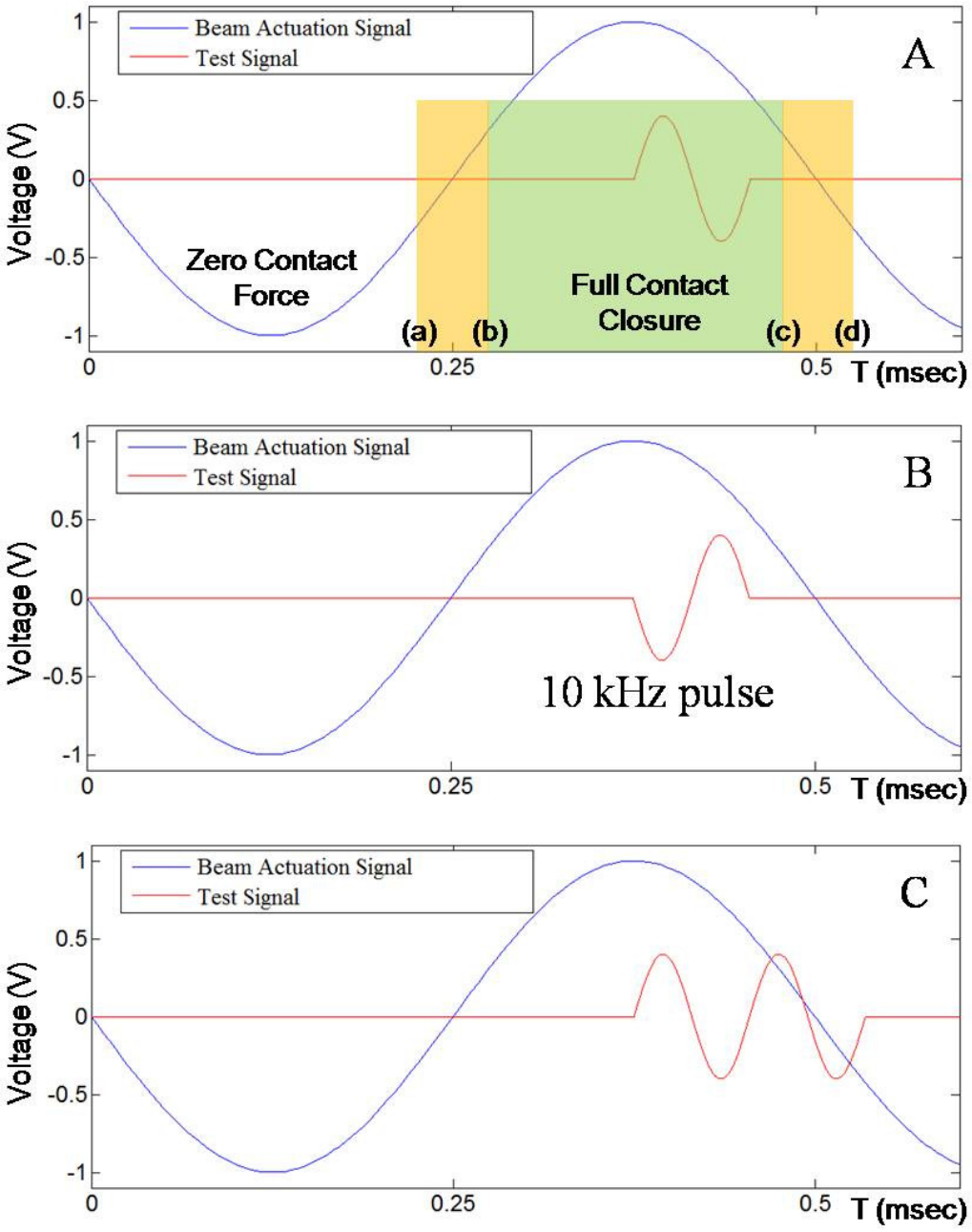

Figure 28. Relationship between timing of an AC load and actuation Frequency. Part A illustrates the relationship needed to obtain a cold-switched load relative to the overall contact closure cycle. Part B illustrates the concept of an inverted load, and part C shows one method of hot-switching obtained simply through extending the pulse time during loading.

3.6 Chapter Summary

The test stand's current configuration was discussed and while it was configured primarily for lifetime testing, the hardware was all present and configured in such a way that it was easily modified for everything being considered. Some software modifications were desired for some of the data which was required, but these modifications were minor and easily implemented. The devices which are currently used worked well for some of the proposed testing, but ultimately we will need to devise a method of fabrication which can provide extremely small, controllable contact areas. To this end, three methods were discussed but only two were pursued: nanosphere lithography and improved grayscale lithography. The use of NSL was contingent on our ability to adequately control placement of the nanospheres as well as obtain a high enough level of coverage so that we can safely assume our devices contain the necessary spheres to be fabricated correctly. Alternatively, improvements to previous attempts to conduct grayscale lithography can give features which are nearly as detailed as those from using nanospheres, but with much higher confidence during fabrication.

To these surfaces we will need to apply a thin-film conductive layer. To accurately predict how such a film will perform in our devices, we will revise prior modeling such that it incorporates recent theory in spreading resistance to improve accuracy. New devices will also be designed which incorporate a cartesian geometry to determine if accounting for this phenomena is enough to account for any remaining variance, and establish a much improved method for calculating theoretical contact resistances in devices that utilize these thin-films.

Finally, we will discuss investigation of external effects on micro-contact performance. External to a micro-contact, other elements may drastically impact performance of these devices. As such, several circuit configurations were evaluated to

validate this theory and help identify some key choices in both the design and application of these devices. Low-frequency AC loading will also be investigated as a means to validate RF applications as well as aid in investigating polarity effects. Finally, these two ideas will be explored together, and the application of protective circuit configurations to devices subjected to AC loads will be evaluated.

IV. Data and Results

4.1 Chapter overview

In this chapter, data and results which were obtained will be presented for analysis and discussion in the next chapter. There are no reportable result regarding the test stand hardware or software, and device issues are reported in each of the sections as applicable. The broad areas of interest include surface feature engineering using both nanosphere lithography and grayscale lithography, thin-film spreading resistance of the materials used to cover those structures, and external effects influencing micro-contact performance including both electrical loading (i.e. low frequency AC loads) and external circuit effects.

4.2 Nanosphere Lithography

The first topic of interest is nanosphere lithography. This discussion will include the deposition vessels constructed, the kinds of layering achievable with these vessels (i.e. monolayer vs. bilayer depositions), nanosphere scaling and deposition results, and finally pattering techniques for positioning nanospheres.

4.2.1 Deposition Vessels.

Previously it was noted that in order to ensure the greatest chance of success in our ability to deposit self-assembled layers of nanospheres, the method of choice was a modified dip-coating process in which the carrier fluid would be drained away from a submerged substrate. One common theme among publications which discussed this technique was that most of the critical factors which affect nanosphere assembly had been generalized in the sense that a single vessel was made with little flexibility to

explore the effects of changing these subtle parameters and how these changes affects deposition.

To go through the iterative process of building deposition vessels which test these various parameters, 3D printing was employed. Vessel designs originated in Auto-CAD, which was used to create stereolithographic files (.stl). These contained virtual, scaled copies of the vessels to be printed. These were used with a DaVinci 1.0-Pro 3D printer which utilized ABS plastic filaments which passed through a heated extruder onto a heated bed. The system was designed to handle jobs which did not exceed 8" x 8" x 8" in volume. A step size of 2 mm per pass was used, and to eliminate any leaks in the vessels, the entire surface was washed with acetone to seal any gaps in the printing process, and in some cases further sealed with a silicone based sealant or in some instances coated with teflon to aid in repelling nanospheres from the walls of the vessel.

A number of design iterations were explored, and each will be covered in detail.

1. The first vessel was designed to address the ideal angle between the substrate and liquid surface. This depends largely on the size of the nanospheres, and based on published ease of deposition, a sphere size of 500 nm was chosen as inter-sphere spacing at this scale was sufficient for this application. When using nanospheres of 500nm in diameter and deionized water as a transfer fluid, a vessel was built to test the effects of this angle. Figure 29, part (a) shows an illustration of this container. It was built with 9 separate sample holding pillars, each in increments of 5^o ranging from a 5^o incline to a 45^o incline. This vessel was tested repeatedly. Most devices which contained recognizable patterned layers were found to be between 15^o and 25^o, so further designs simply used 20^o as the optimal application angle and the sphere diameter and carrier fluid were fixed as well.

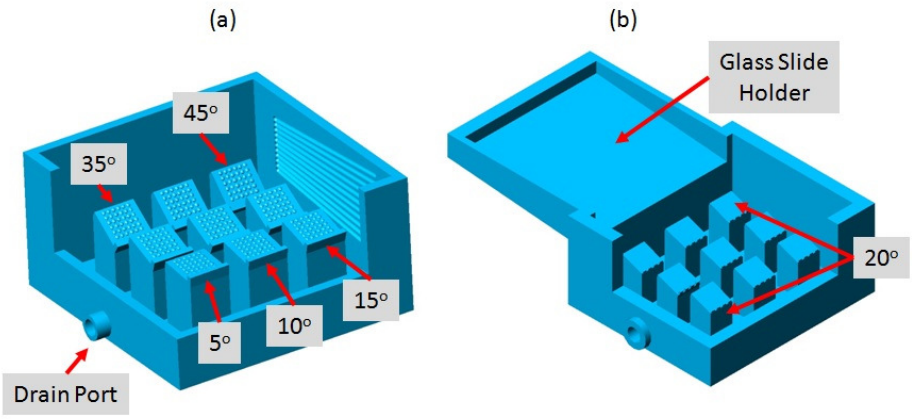

Figure 29. Computer-aided design images of the first two nanosphere deposition container. Figure (a) shows a container which tests multiple angles between the substrate and liquid surface ranging from 5^o to 45^o. The second shows the addition of a holder for a glass slide to facilitate loading nanospheres on the liquid's surface, with all sample holders set at 20^o to the liquid surface [131].

2. Next, a variation of this was designed, printed, and tested which had the ability to hold a glass slide near the surface of the liquid for more consistent application of the nanospheres to the surface as shown in Figure 29, part (b). While this approach didn't appear to necessarily ensure nanospheres remained on the surface, it did provide more consistent results. As such, it became the default vessel for many applications which followed, including samples which were fabricated for other research efforts as it was capable of producing areas of fairly uniform coverage which were on the order of mm^2 in size.

3. The next two iterations went through several modifications which attempted to incorporate a Langmuir trough as discussed in Chapter 2. As this approach of draining liquid from below the sample has the advantage of no moving parts, the introduction of a moving trough would be problematic. Thus, the goal was to accomplish a trough which didn't require mechanical operation. The first few attempts involved building floating dams which could be filled with fluid to submerge them further as shown in Figure 30.

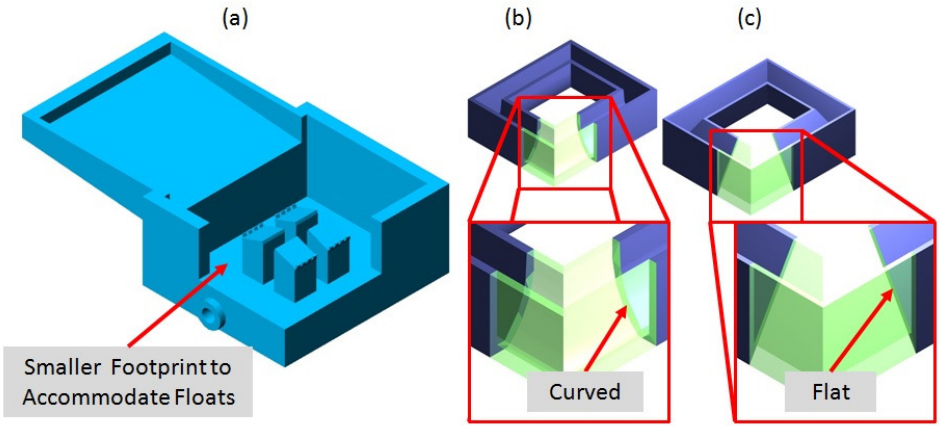

Figure 30. Computer-aided design images of modified nanosphere deposition container with two floats designed to mimic a Langmuir trough while suspended on the surface of the liquid (a). As the floats are filled with water, the float will sink relative to the surface of the liquid in the container but remain at that level as the container is drained. The first (b) has a curved inner profile and the second (c) a straight edged inner profile [131].

The design concept was based on the goal that the trough would remain at the same level of submergence relative to the water's surface, even as the water was drained. This would in theory allow for a surface area reduction initially, and then maintain that reduced surface area through the process of draining the carrier fluid. The problem was that introducing the dam to the surface of the liquid or even attempting to submerge the float tended to knock the spheres below the surface, and as was already mentioned a trough is only beneficial with spheres floating on the surface. Surface treatment of the spheres may have been a suitable method to avoid this issue, but instead a different design was attempted which was less disruptive to floating nanospheres.

4. This new iteration eliminates the need for a removable trough. Rather than decreasing the surface area by inserting a float, the apparatus was redesigned so that as the liquid drains, it automatically experiences this reduction in surface area, as shown in Figure 31, part (a) below. The results thus far have indicated

very sporadic results which is believed to be caused by the drainage valve intermittently becoming plugged. Avoiding these large changes in the drain rate appears to be critical, thus controlling this parameter would be the next task to address in perfecting this technique.

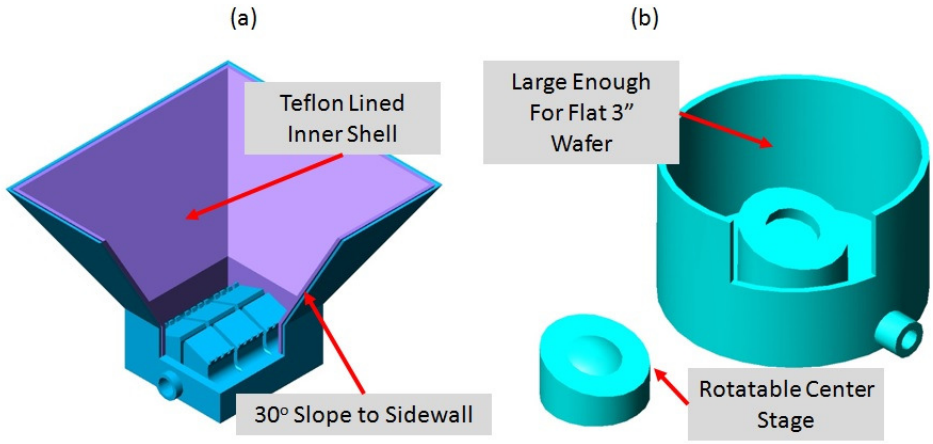

Figure 31. Computer-aided design images of modified nanosphere deposition container. Figure (a) shows a modified sidewall to provide a reduction in surface area without the need to disrupt the surface. Figure (b) is a modification of the overall design to allow for transfer to a full 3 inch diameter wafer, with an adjustable inner stage which when assembled and rotated changes relative angle between the surface of the substrate and liquid between 0^o and 45^o [131].

5. Eventually, we will want to apply this technique to a full wafer. To accomplish this condition the container shown in Figure 31, part (b) was conceived. The overall container is large enough to fit a 3 inch wafer with a center stage that can be varied between 0^o and 45^o. Note that we just discussed setting this angle at 20^o, but this container was designed before this angle was determined. This angle was addressed by placing the smaller, center stage on top of the pillar inside the container. The rotation between the two 22.5^o surfaces would allow for adjustment between 0^o and 45^o overall angle, should this adjustment be needed. Since the time of the design, the center pillar is too unstable, so instead it was made removable so that a pillar with any angle could be swapped

for any given run. Also, ports were added to the design to allow for carrier fluid to circulate back into the chamber. We will also have to consider that in covering such a large area, we may find that using the two additives mentioned (Triton-X and PEO) as needed during testing to see which combination produces the best results. The prototype of this vessel has been printed but not yet tested, and is shown in Figure 62.

4.2.2 Monolayer vs. Bilayer Application.

It was mentioned that increased nanosphere concentration may lead to multilayer rather than monolayer formation. While the funnel shaped vessel shown in Figure 31, part (a) tended to concentrate nanospheres near the surface, the number of layers formed repeatedly depended on the concentration near the substrate at any given time. Figure 32 below indicates a typical deposition pattern resulting from nonuniform nanosphere concentrations during deposition. Repeatedly sections of multilayers, followed by monolayers, followed by bare substrate resulted from some areas of the carrier fluid carrying clusters and nanospheres while others carried relatively low concentrations. This indicates uniform coverage is best achieved by maintaining concentration throughout the deposition.

For certain applications, bilayer or even multilayer may still prove useful. To illustrate this, refer to Figure 33. On the left side of this figure, the sphere placement (top) and an SEM image (bottom) of the patterning which is produced from a monolayer of nanospheres is shown. This monolayer was then subjected to plasma enhanced laser deposition (PLD) of zinc oxide. This highly conformal process resulted in deposition particles tightly packed beneath the nanospheres, producing the distinctive honeycomb patterning. Typically this patterning would require a pre-deposition etching to produce this effect, but because this particular PLD process was optimized for ex-

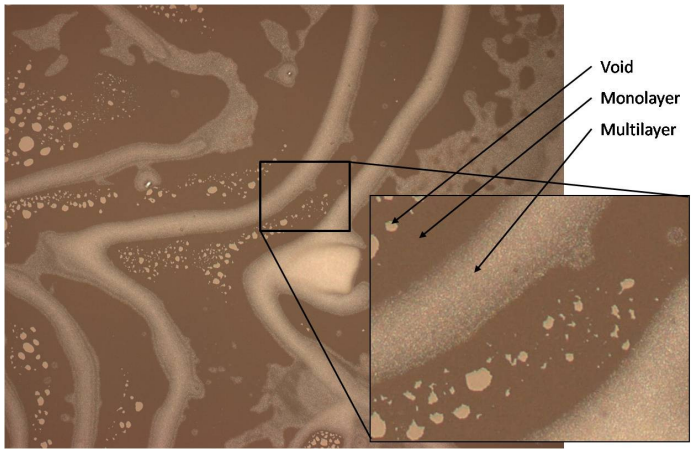

Figure 32. Deposition pattern obtained from drain coating method showing predominantly patterned monolayer formation, but with regions in which both voids and multilayer depositioning (both patterned and unpatterned) occurred.

tremely slow depositions, the result is much more conformal. On the right of Figure 33, we see the results of patterning a bilayer of nanospheres. The distinction is evident from the triangular rather than hexagonal spacing of the particles which resulted after deposition. In this case, gold was plasma sputtered resulting in non-conformal islands of sputtered material.

One additional observation which affects the formation of monolayers versus multilayer depositions, is initial placement of the nanospheres. Trials indicated that spheres which are floated on the surface of the carrier fluid and were able to pre-form patterned layers required a faster drain rate to be successfully transferred to the substrate. Subsurface spheres however require more time to migrate to the interface and therefore require a much lower drain rate. If both types of spheres are present, then multilayers may still form. There was no indication that this was a result of attraction between the subsurface spheres and the substrate, which implies the spheres can still be driven out a solution and onto the substrate even with a layer of spheres floating on the surface.

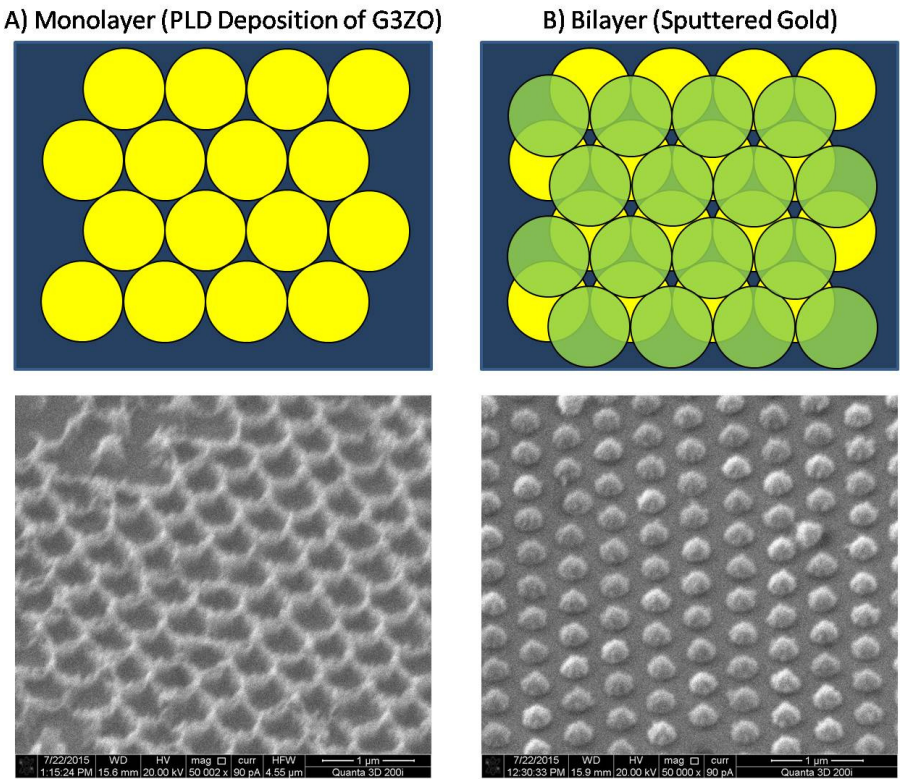

Figure 33. Illustration of nanosphere placement for both a Monolayer (A) and Bilayer (B), and resulting patterns after RIE with sputtered gold. In the case of a monolayer, hexagonal patterning results compared to a bilayer, which results in a triangular pattern [131].

4.2.3 Nanosphere scaling and deposition.

As previously mentioned, the spacing of features deposited using NSL are set by the selection of a particular sphere diameter. The size of this opening however can be modified prior to deposition through plasma ashing or RIE for more precise control, anisotropic etching, or utilizing a recipe which possesses some selectivity control when etching both nanospheres and substrate [171].

Figure 34 illustrates the effects of adjusting the sputtering time and preprocessing of the nanospheres using RIE. In part a, no etching was performed and a short sputtering was conducted resulting in extremely shallow features with a low aspect ratio. Part b shows the result of a longer deposition but still over unetched spheres.

Part c is the result of both a longer sputtering deposition as well as 45 seconds of etching prior to deposition. Note in all three cases triangular rather than hexagonal pattern is shown, indicating a bilayer of spheres were present for all three runs.

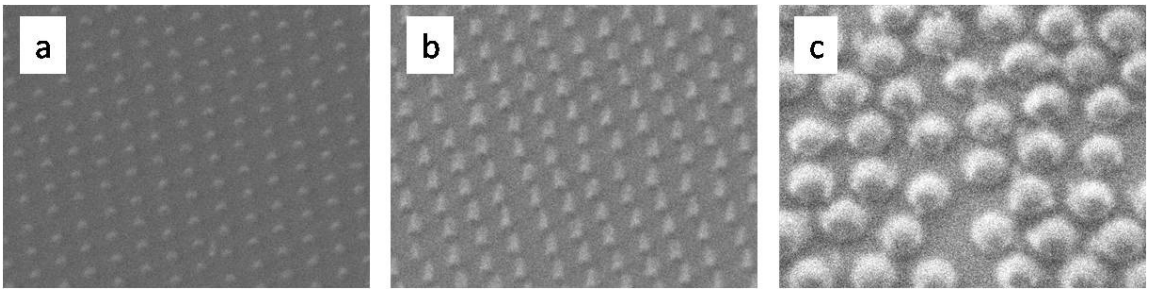

Figure 34. Resulting patterning from variations of RIE and deposition depth of evaporated gold. Part a) shows the results of no RIE and thin deposition, part b) is a thicker deposition also without RIE, and part c) shows the thicker deposition but with RIE prior to deposition [131].

From these results we can see that NSL holds the potential of producing a variety of surfaces capable of more precise contact area control. For example, consider the patterns shown in Figure 34 if such patterns were sputtered over a thin-film of gold. For shallow deposition such as part a, we could use this simply to alter the ratio of exposed surface area of gold relative to a material such as ruthenium oxide to control resistivity or even a dielectric to simply limit conducting area. Consider if the patterns shown in part b or part c were ruthenium oxide over a thin-film of gold, yielding two distinctive feature shapes with two distinctly different contact areas.

Another method which was investigated was the effects of including a layer of 1805 beneath the nanospheres prior to deposition for use as an intermediary mask. This additional step requires reactive ion etching to occur, but as can be see in Figure 35 this additional step provides noticable height to the deposited material.

This process uses the nanospheres as a mask during the etching phase. The result is an etch through the photoresist but only at the spaces between the spheres. This

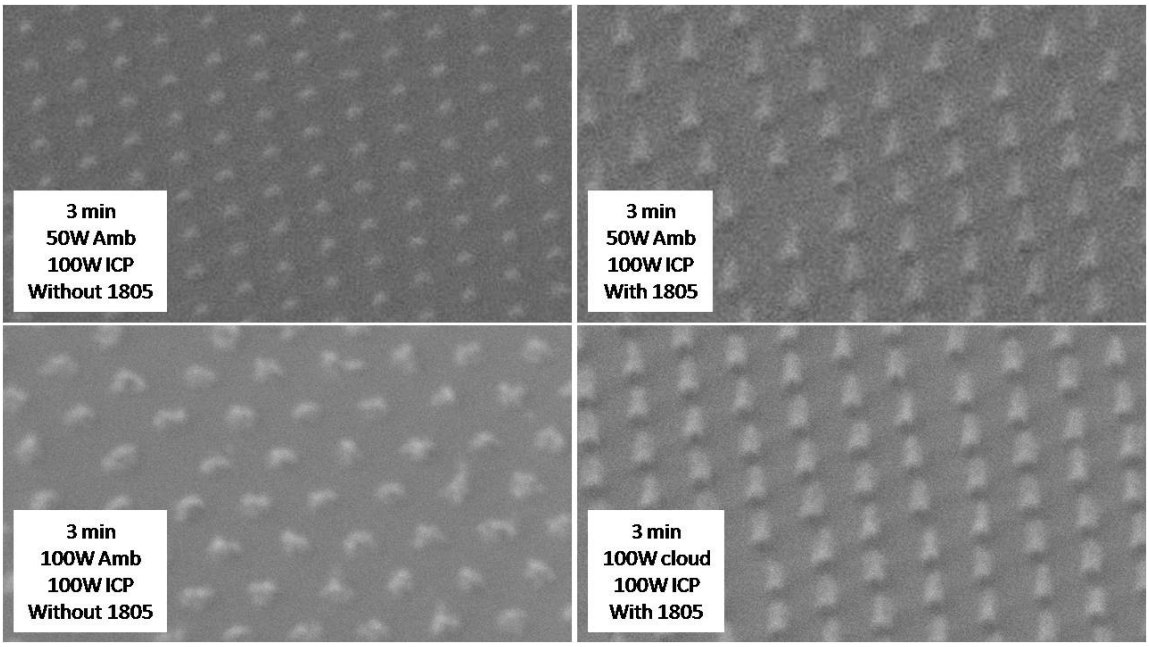

Figure 35. Effects of including an underlying 1805 layer of photoresist beneath nanospheres. The upper two images are at 50W RIE power while the bottom two are at twice the power. The left two images show the effects of using nanospheres directly against the substrate and on the right the effects of including a layer of 1805 prior to nanosphere deposition.

was followed by a metal deposition over both materials, and with these depositions being performed simultaneously, the resulting structures with the photoresist under layer are noticeably heightened as a result of this photoresist underlayer.

4.2.4 Patterning Nanosphere Layers.

If we wish to use these kinds of patterns in actual devices, we need the ability to control their placement as part of the overall fabrication process. In the last chapter, it was suggested that pre-patterning photoresist at an appropriate thickness to create wells in which to capture nanospheres would be used to attempt to this. Two methods were investigated in which patterning can occur: surface nanosphere pre-patterning or subsurface patterning through capillary forces.

The result of the first of these trials is shown in Figure 36 which shows a pre-patterned monolayer formed on the carrier fluid surface. This was transferred to a substrate which was pre-patterned with an 1800 series photoresist, which was approximately 600 nm thick.

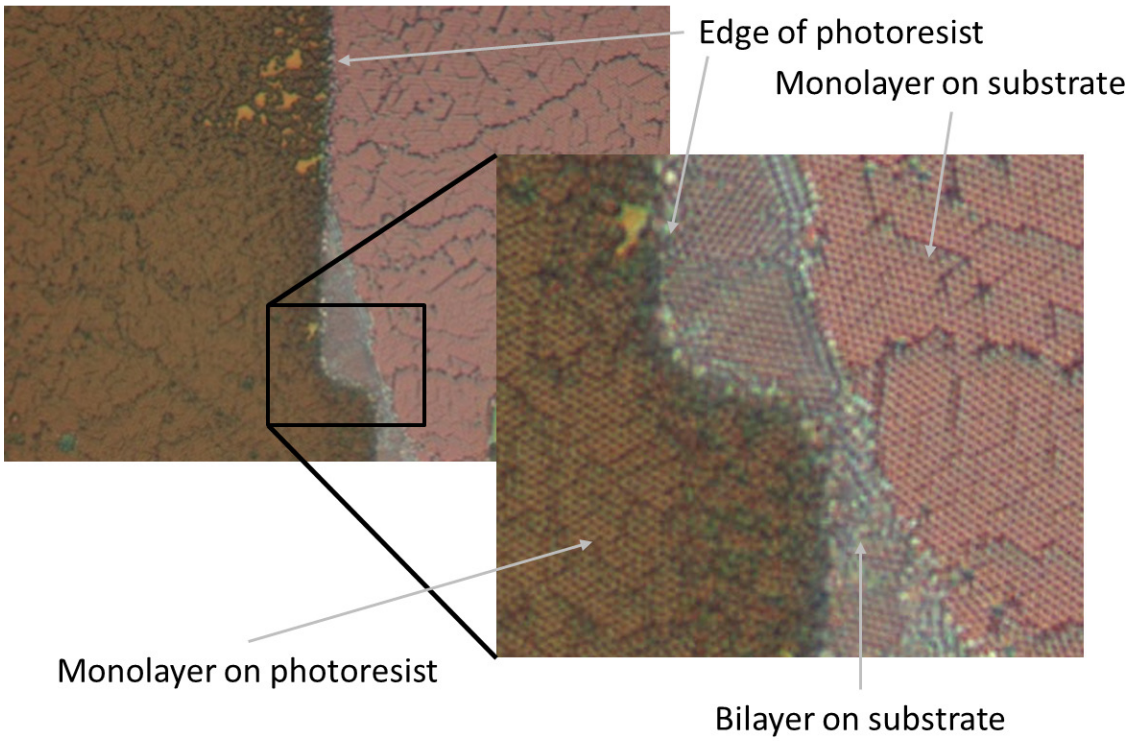

Figure 36. Sphere patterning results of depositing pre-assembled surface monolayers onto patterned substrate with photoresist of comparable thickness [131].

The left side of both images show the region where photoresist was present, and the right side bare substrate. While overall the transferred nanospheres were still in a monolayer formation, a large number of dislocations are apparent and are visible as dark lines throughout the pattern. Additionally, where the step change in height occurred the upper portion of the monolayer appeared to remain continuous, but approximately halfway down the monolayer teared and partially folded over indicated by a triangular gray region in which a bilayer is present. This dislocation also caused

a number of holes to open in the upper left portion of the monolayer sheet. For applications in which nanometer scale features are desired, but the arrangement need not be exact, this approach may be suitable. For our application however, the reduced surface area we desire must still be somewhat predictable. We could estimate this number and likely obtain reasonable results, but a more uniform pattern would be ideal if it can be attained.

The second trial was conducted by growing a monolayer within a pre-patterned area. Initially it was attempted to grow these layers with the same patterning, which had large open regions of exposed substrate. While some monolayer formation was observed, it was primarily over photoresist or only near the edges of the open substrate area. Rather than attempting to accomplish this over a large open area, a test pattern was developed and is shown in Figure 37.

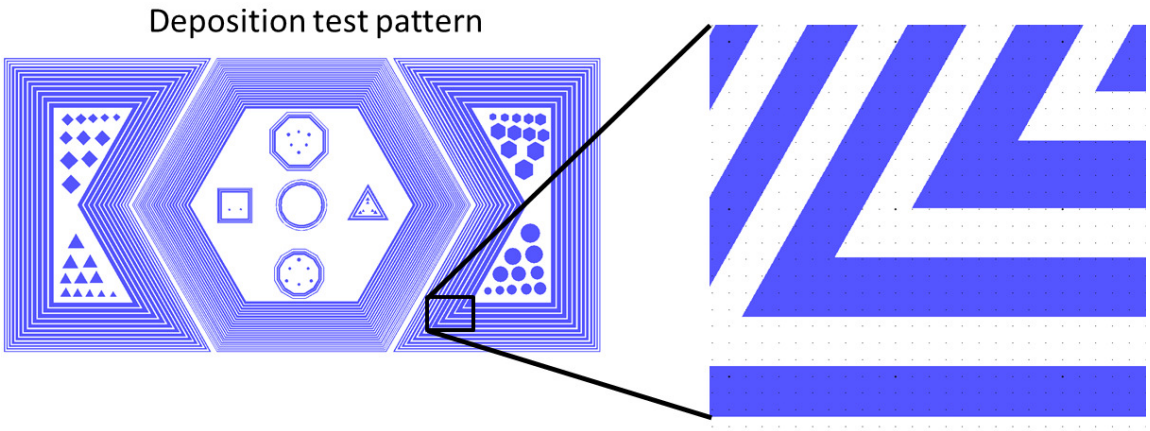

Figure 37. Test pattern used in deposition of sub-surface 500 nm nanospheres on test pattern. Full test pattern on the left and enlarged section on the right showing channels of gradually increasing widths [131].

This pattern was designed specifically for 500 nm nanospheres, with multiple channels in features in a range of sizes designed to work with that size sphere. It was theorized that these channels would accommodate from 2 to 12 rows of nanospheres

based on their size and assuming a close packing formation. This test pattern was printed onto a standard lithography mask using a Heidelberg laser lithography system with a 1 μm laser. As will be discussed in the next chapter, the precision of the placement of this laser is better than 1 μm, and the actual beam width is approximately 900 nm. This allowed many of the fine scale features of this test pattern to be realized with better precision than should have been geometrically possible. This mask was then used to pattern photoresist of approximately the same thickness (600 nm) and samples of the diced wafer were then put through the deposition process and evaluated.

While the quality and controllability of the nanosphere placement in some areas was greatly improved, this only occurred in a very small percentage of surface area (less than 1%). Figure 38 shows one such region in which patterning did occur.

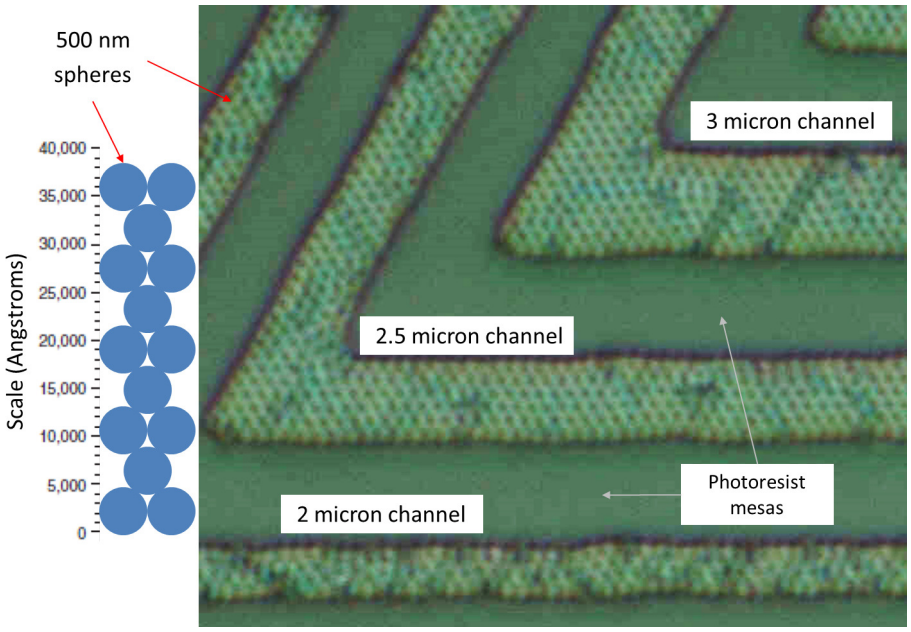

Figure 38. Magnified image of captured nanospheres in channels of photoresist of 700nm thickness, showing pattern irregularity varying with channel width. For the 500 nm diameter spheres used, the bottom channel is oversized for 4 rows of spheres, but not enough space for 5 resulting in irregularities. For the 2.5 micron channel however, this is just enough space to accommodate 6 rows of spheres and in the 3 micron channel, 7 rows will fit [131].

Recall the relationship between the 500 nm nanosphere being used and the distance required to accommodate these in a packed formation. This scale explains the results shown in Figure 38. As can be seen, the 2.5 and 3 μm channels are spaced slightly larger than the space required to accommodate six and seven rows respectively. The 2 μm channel however is not quite large enough to accommodate a fifth row, so the four rows which are present are extremely scattered and nonuniform.

4.3 Improved Grayscale Lithography

Recall from Chapter 3 discussion regarding a mutli-layer line-scan approach involving multiple design files and the addition of third party automation. With this capability in hand, a suitable or even possibly superior lower contact surface was fabricated into a silicon nitride coated wafer. To step through how this was accomplished, we must first consider some characterization of the system which must first take place. Recall the rectangular patterns which were to be used to characterize the power and duty cycle requirements for multiple exposures which are shown in Figures 18 and 20. With the CAD files created with this basic pattern, a series of test exposures at various combinations of powers and duty cycles were conducted. The powers and duty cycles attempted are shown in Figure 39.

In this figure, power is either held constant for all seven layers, incrementally decreased, or incrementally increased. For the powers ranging from 1-7 mW, the step size is 1 mW per layer, and for the 3-18 the step size is 3 mW. Similarly, the duty cycle was either held constant, incrementally increased or decreased. For the 20-80% ranges, the step size is 10% per layer, and for the 3-21% ranges the step size is 3%. The positioning of each run was arranged in a similar matrix on the test wafer. Each successful pattern resulted in a staircase which were then measured by a profilometer to determine the incremental change for that particular recipe.

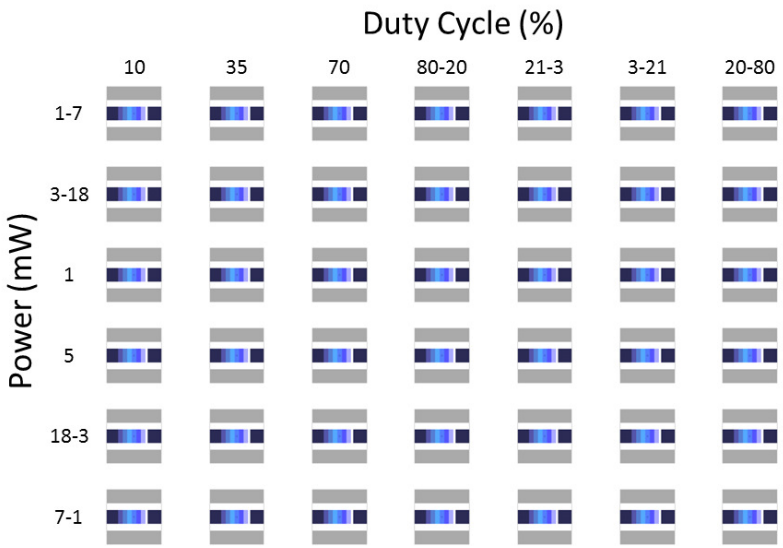

Figure 39. Matrix of power and duty cycle settings used to evaluate optimal grayscale processing using a seven step masks. For powers ranging from 1 to 7, each masks power setting was increased in steps of 1 mW, and from 3 to 18 mW the step size was 3 mW. For duty cycles between 20 to 80%, step sizes were in 10% and for duty cycles ranging between 3 and 21%, 3% step sizes were used.

For one such set of results, this is illustrated in Figure 40. The top shows a microscope image of the pattern being measured and the bottom shows the resulting profilometer depths for each step. Note that the bottom of the scale is from the upper and lower wells which were patterned separately at 18 mW and 90% duty cycle, in order to identify the true thickness of the photoresist at the deepest point, for those recipes which did not completely pattern though the entire thickness.

This approach was applied to all 42 test cases and the resulting cross sections were plotted alongside the images for each case. From this we can identify several which should be suitable for our purposes as shown in Figure 41. If we want to test two, four, and six layer patterning capabilities, then the cases circled are all potential solutions after some minor adjustments.

The data from this etch study are supplied in the appendices, but after analyzing the results from this study, the parameter best suited to control this selectivity is the ratio of the reactant gases: O_2 and CF_4 as shown in Figure 42. If this ratio is held to

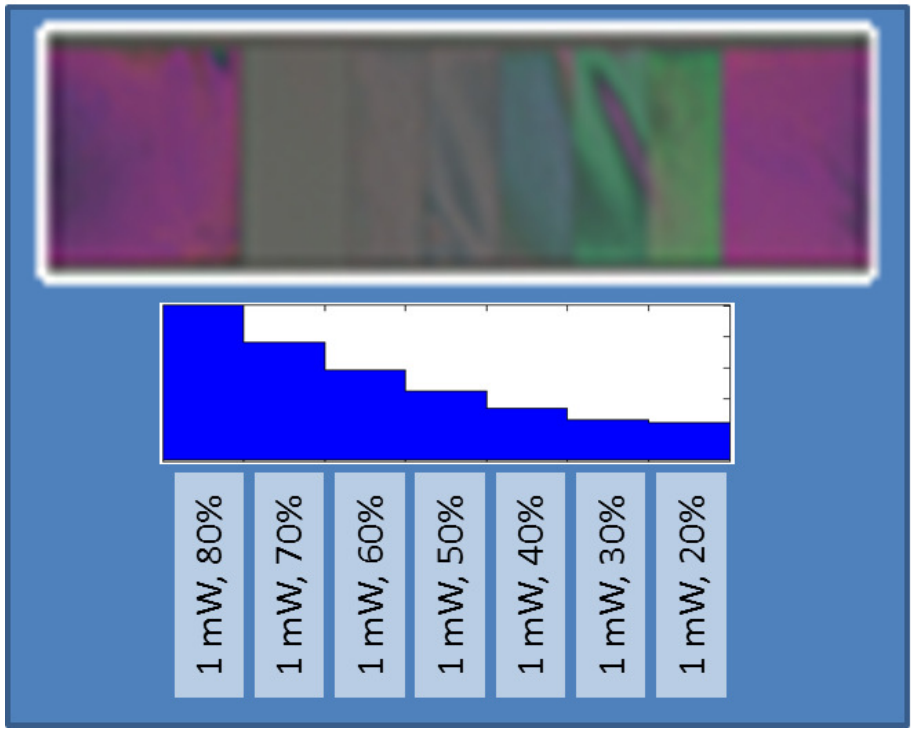

Figure 40. Image showing one resulting pattern from exposure study and corresponding profilometer data below illustrating the resulting cross-section, step change resulting from multiple exposures at the power and duty cycle indicated for each step.

approximately 0.6, we can expect any patterned features are transferred to the silicon nitride with minimal distortion. If in the future we find our photoresist patterns are too shallow, we can revisit this gas ratio to adjust the selectivity and possibly expand these features during the etch process as was illustrated in Figure 22.

Another important point to be made is determination of the true beam width. This is required before design files for the lower contacts could be created as this was a critical factor in feature spacing as pointed out previously. This was easily identified by creating a test pattern which contained a series of channels with decreasing sizes, and observing where the pattern begins to fail. This was conducted and it was determined that the actual beam diameter of the system is approximately 900 nm as shown in Figure 43.

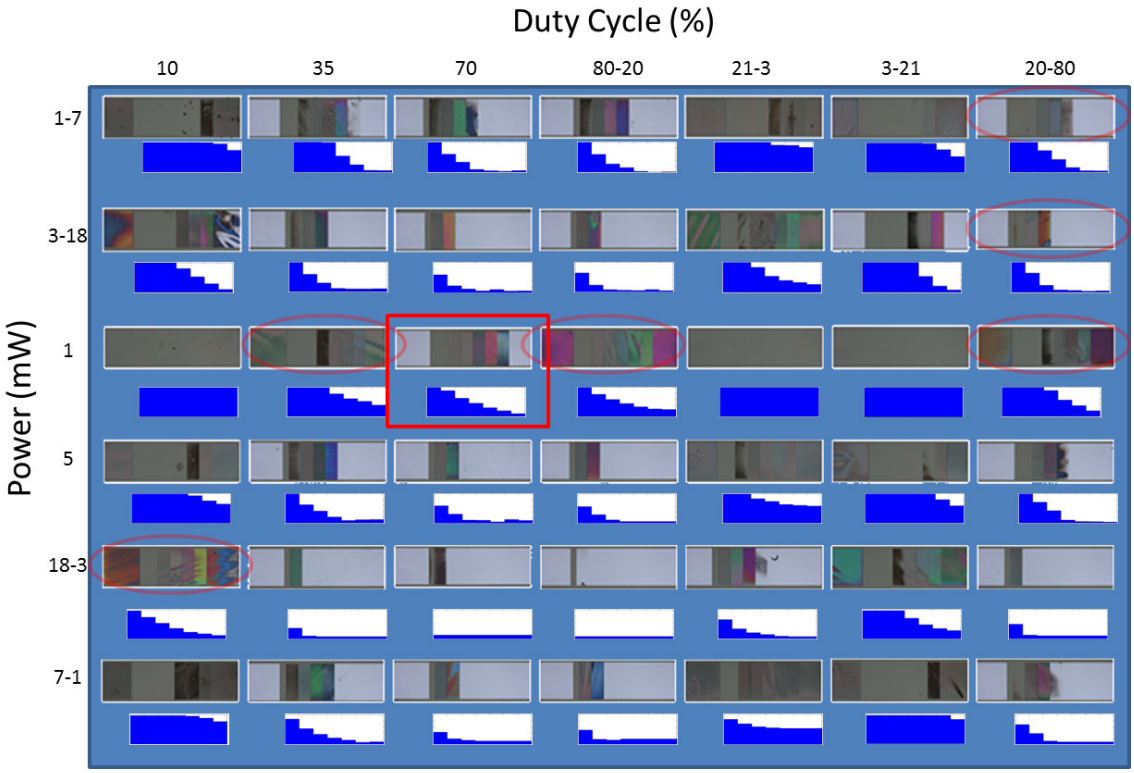

Figure 41. Matrix showing the resulting images from various combinations of power and duty cycle using the seven step process with corresponding profilometer data cross-section profiles below each run showing relative depths of each step. Circled cases represent candidate recipes for use in 2, 4, or 6 step processes with uniform depth change per step.

With this information in hand, the next step was to pattern lower contact surfaces in photoresist, etch them into the nitride substrate, and evaluate the results. Two wafers were run, the first using patterns designed to test the 400nm positioning limit discussed earlier, and the second attempted to push this limitation and used patterns with only 80nm of spacing to see if usable features resulted. An image of the first test is shown in Figure 44. Eight different patterns were run with nine different sets of powers and duty cycles. The eight patterns varied in layout and number of steps, gaining a wide variety of data.

These results were also imaged using an SEM, then exposed to an RIE etch with a theoretical selectivity of 1.0, and re-imaged. Figure 45 shows two sets of results

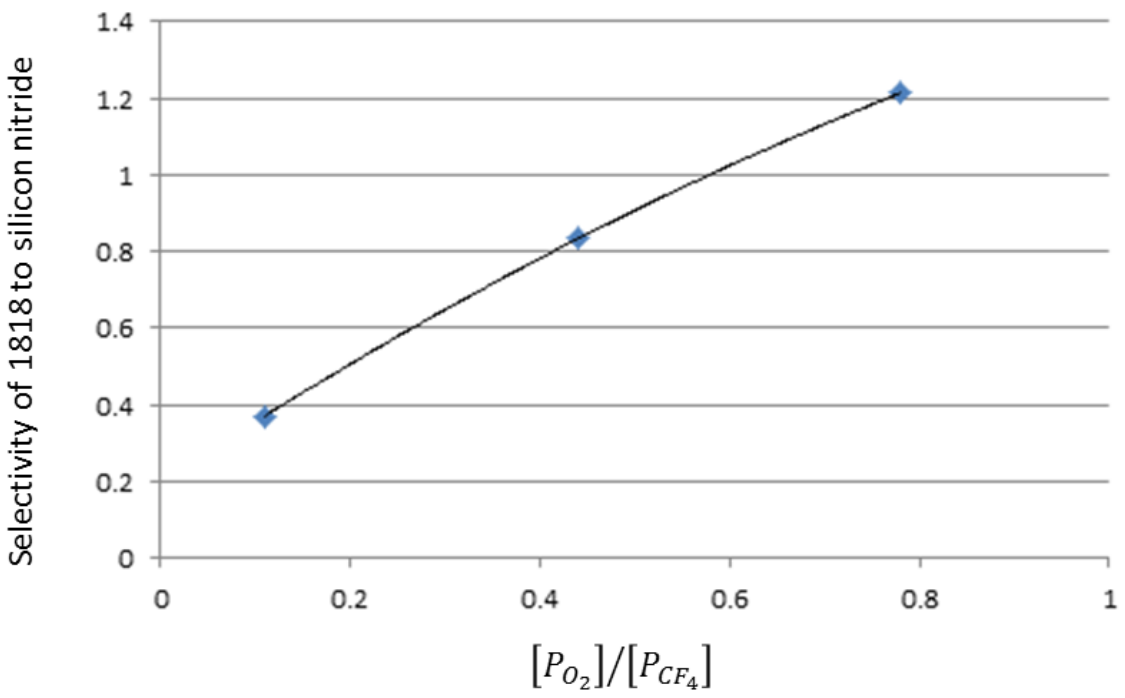

Figure 42. Result of etch study indicating control of selectivity near 1.0 through manipulation of the relative partial pressures of oxygen to trifluoromethane.

from this low resolution test. The upper two images show the photoresist and the lower are the results obtained from imaging the silicon nitride. The left pattern is a simple, close-packed configuration using a 4 step design and the right is a six step repeating pyramid structure. The images of the resulting silicon nitride illustrate that the features did transfer, however they seem to be much shallower than the photoresist versions, indicating a selectivity which favors the photoresist to nitride.

Additional patterns were also attempted, some in preparation for gathering micro-contact resistance data to address some anticipated complications which may arise. While any of these patterns are well suited for estimating true contact area, a scheme which allows for incremental increases of a predictable number of nano-features as the contact force is steadily increased may provide us with a means to determine

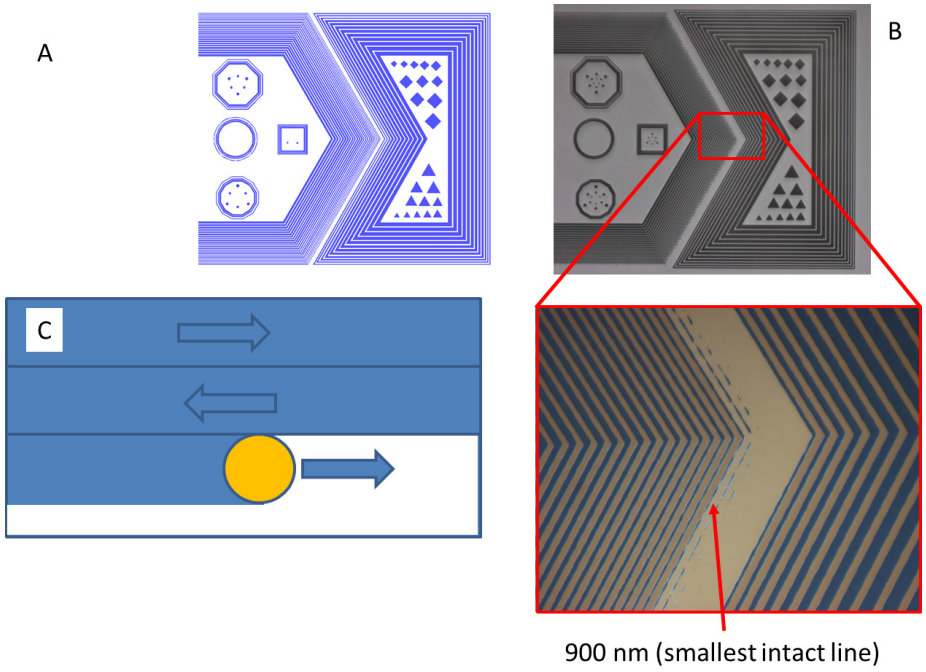

Figure 43. Conceptual illustration of lithographic printing from a CAD-based file (A), resulting in fully exposed or unexposed areas (B). To accomplish this, the beam used to print is swept horizontally along precalculated lines, and beam is activated and deactivated to expose only the geometric shapes provided..

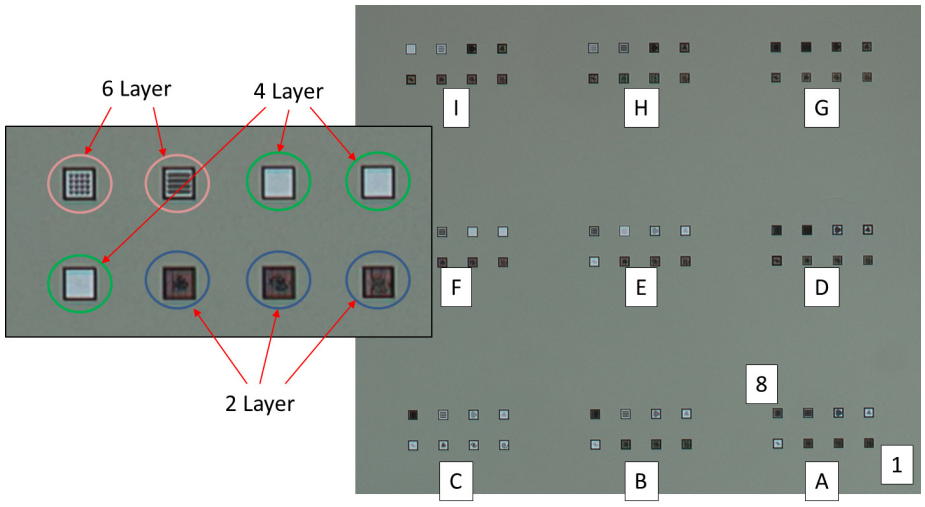

Figure 44. Test matrix of nine variations of power and duty cycle applied to identical eight pattern design for evaluation of optimal settings for two, four, and six layer designs.

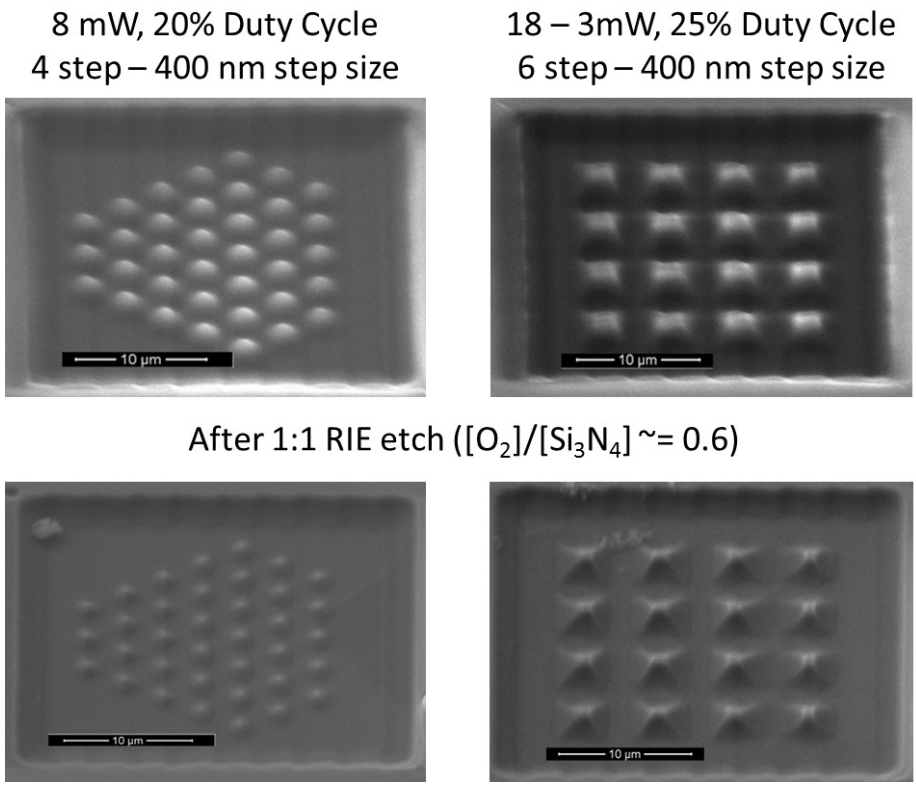

Figure 45. SEM imagery showing grayscale patterned photoresist (top figures) and patterned silicon nitride (bottom figures) after 1.0 selectivity RIE etch for circular close packed formation (left), and rectangular 3-D pyramid formation (right).

variability in this sort of feature scaling. To illustrate this, consider the patterns shown in Figure 46. If the upper contact is a hemispherical bump, 6 μm in radius and positioned directly above these patterned pads, then as the contact closes, the actual contact radius should increase steadily. If we image the concentric rings as representing the outermost extent of the contact as it closes, then these patterns should incrementally increase in contact area by steps which are consistent. On the left, the contact areas will engage in pairs and on the right in triplets. With these engaging in groups, we can then compare the results to two or three areas with an average contact area and compare to determine this variability.

Next, a second wafer was run with designs which assumed an 80nm horizontal tolerance could be held. A comparison of a 400nm 2-D pyramid structure to an

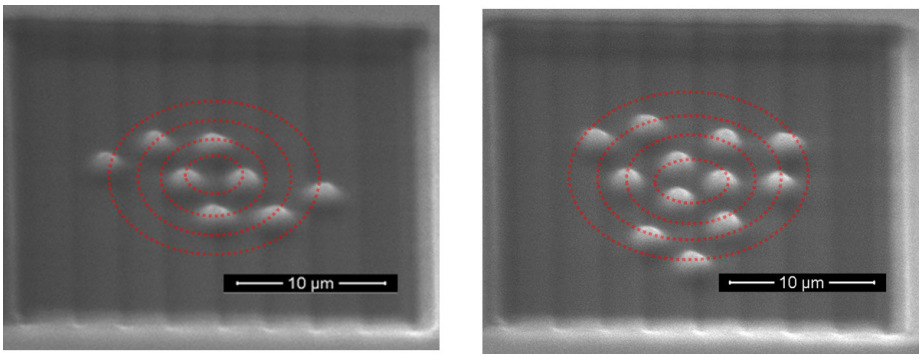

Figure 46. SEM imagery of patterned silicon nitride showing nano dot arrangement for incremental contact engagement as contact force increases on upper hemispherical contact surface. The left figure is arranged to provide for simultaneous contact in pairs of dots, with each pair being encountered in the incremental radii shown, and the right showing simultaneous contact in triplets at similar incremental radii.

80nm 2-D structure are shown in Figure 47. While the height of the features using this much finer resolution is noticeably reduced, it performed well considering it was using designs which were 1/5 the resolution which should have been possible.

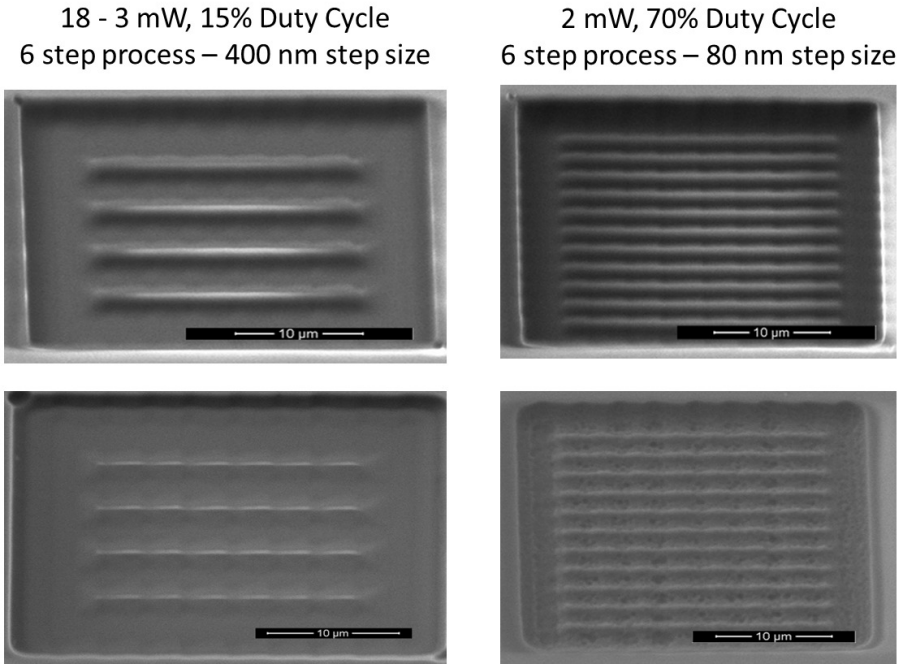

Figure 47. SEM imagery showing comparison of six step designs for horizontal 2-D pyramid structures for both the 400 nm step size (left), and 80 nm step size (right). The top images show the patterned 1800 photoresist and bottom shows the resulting pattern after an RIE etch with selectivity of 1.0.

Finally, another image is provided of another pattern fabricated at this higher resolution and is shown in Figure 48. In this image it is clear that the repeatability was greatly reduced when exposure at this resolution is performed, and for the purposes of creating repeated structures for a micro-contact surface this is likely to create too much variability to be of value. These results were encouraging enough however to indicate that features finer than 400nm can be fabricated with this system, and should be further explored.

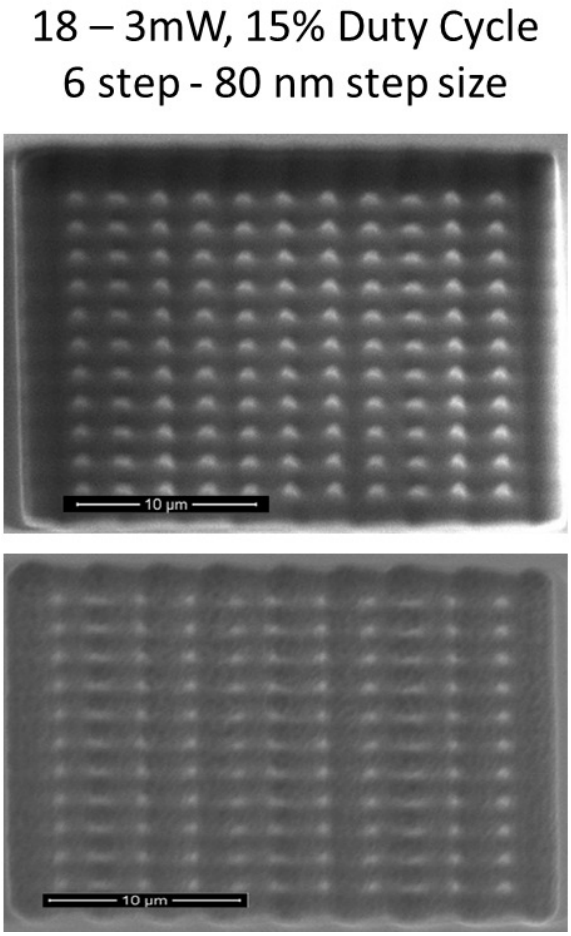

Figure 48. SEM imagery showing patterned photoresist (top) and resulting post etch nitride (bottom) for six step, 80 nm step size design.

4.4 Thin-Film Spreading Resistance

The data which was previously gathered in prior studies was done so with the target contact force of 200 μN. Based on this, it was assumed that only diffuse-based models would apply. Using this force, radial model for spreading resistance, and elastic plastic modeling for contact resistance, a new model was derived by simply applying this correction factor to our previous model. This required resistivity and hardness values for the materials used which were measured / collected and are summarized in Table 2 below:

Table 2. Measured material properties during device fabrication [166].

	Au	Ru	RuOx
$\rho x10^{-8}$	2.8505	241.29	487.59
H	2.45	4.682	9.247

ρ – resistivity in Ωm, H – Meyer hardness in GPa

To properly calculate the correction factor, the thickness of the thin-film lower gold contact layer must also be known. For all devices for this portion of the study, this was 280 nm. Initially it was assumed that this was a fixed value, however in cases where the upper contact was ruthenium or ruthenium oxide, it was possible that some compression occurred, which will be discussed in the next chapter. The radius of the upper contact hemispherical bump was roughly 6 μm wide at its widest point. They were produced by reflow of SF-11, which forms a roughly spherical shape and was assumed to translate into a contact radius of no greater than 6 μm.

Data gathered for Au-Au devices is shown in Figure 49. Data was gathered from three separate devices, at roughly 200 μN of contact force. While data from many more tested devices was available, an additional restriction was put on what data would be considered. In order to avoid the effects of contacts which have not yet broken in as well as the effects due to excessive wear, only devices which had sufficient

data between 1000 and 5000 cycles were considered. While it is possible that this was an overly restrictive range, there were sufficient devices of different compositions with enough data in this range to provide valid results. Note that on this particular plot the scale is on the order of 0.5 Ω. Each resistance measurement was found averaging the final resistance measurements for that cycle.

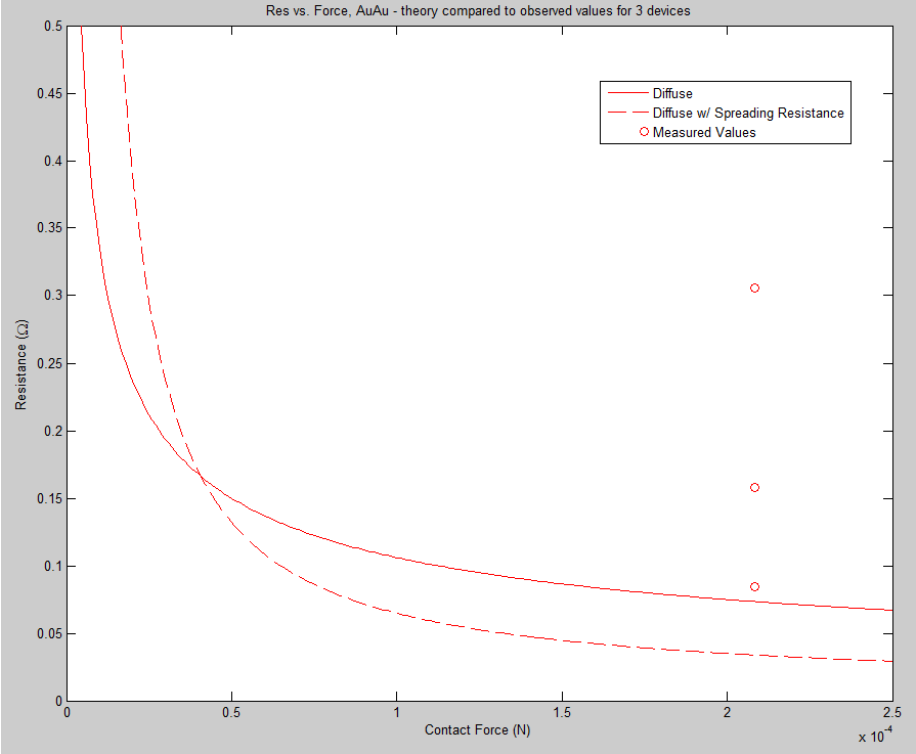

Figure 49. Resistance vs. Force plots for 3 lightly worn (1,000 to 3,000 cycle) Au-Au micro-contacts compared to classical diffusive elastic-plastic contact resistance models with and without spreading resistance compensation [164].

Under these conditions, it was clearly shown that the observed resistance in all three cases was higher than what diffusive elastic-plastic contact resistance modeling predicts. In this particular range of values, spreading resistance predicts a reduction in overall contact resistance. Thus at this point, the benefit of this correction factor does not look justified. However, consider that these are gold gold contacts and that nowhere in the model is any sort of contamination film resistance incorporated.

Previous tests with his gold gold devices commonly showed an additional, otherwise unexplained increasing contact resistance which tended to increase as the devices continued to wear. It is therefore possible that this theory is valid, but contamination resistance is greater than what was previously anticipated. To further explore the applicability of spreading resistance, will need to review the results from other devices.

Next, we considered devices in which the lower contact was still 280 nm of evaporated gold, but the upper contact was composed of a ruthenium oxide film. If we apply the same wear restrictions as in the previous example, and plot the measured contact resistances at 200 μN of contact force against models which do and do not include spreading resistance, the results are shown in Figure 50 below.

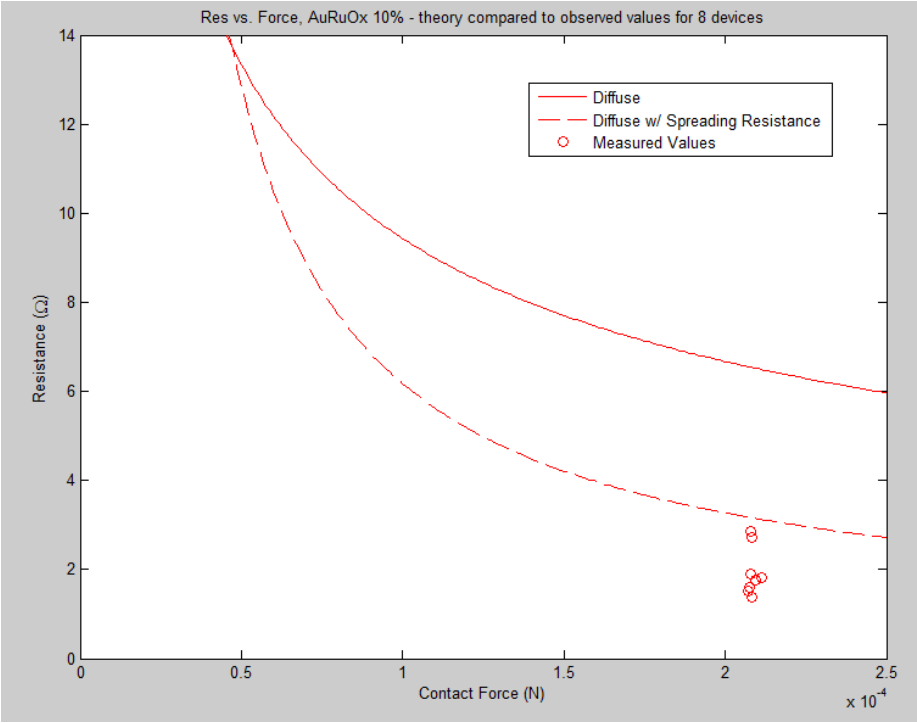

Figure 50. Resistance vs. Force plots for 8 lightly worn (1,000 to 3,000 cycle) Au-RuO_2 micro-contacts compared to classical diffusive elastic-plastic contact resistance models with and without spreading resistance compensation [164].

At first glance, the data appears to contain much less variance in the previous example. Consider however the scale of this plot was considerably higher, and thus the

variation between devices while still somewhat consistent does show some variability. This variability however was negligible compared to the error between the measured values and contact resistance models which do not include spreading resistance. What was significantly different in this case however, was that eight devices were considered, and for all eight the measured resistance was significantly less than predicted. While the application of spreading resistance describes a majority of this variance, even with this adjustment the predicted values were still slightly higher than observed. If the measured values were slightly higher than these corrected values, we again could assume some level of contamination resistance unaccounted for. That however is not the case here, as the model values were still higher than measured. Explanation for this will become apparent when we look at the next case.

The third case to be considered involved two devices of similar design, but with ruthenium upper contacts rather than ruthenium oxide. As in the previous case, model values were slightly higher than observed. When the correction for spreading resistance was applied in this case however it only explained approximately half the variance present as shown in Figure 51.

In addition to the original and corrected models, a third plot was also provided on the graph. Considering that these devices were made with a relatively hard upper contact which was cycled repeatedly onto a thin-film of gold with an extremely small contact area receiving all of the force repeatedly. It was possible that some degree of compression was experienced by the thin-film. If we adjust the thin-film spreading resistance model such that it was 50% of its original value, the result would be the third plot shown. While this does provide correction to further close the gap, it only partially explained the remaining variance but requires a significant amount of compression to do so.

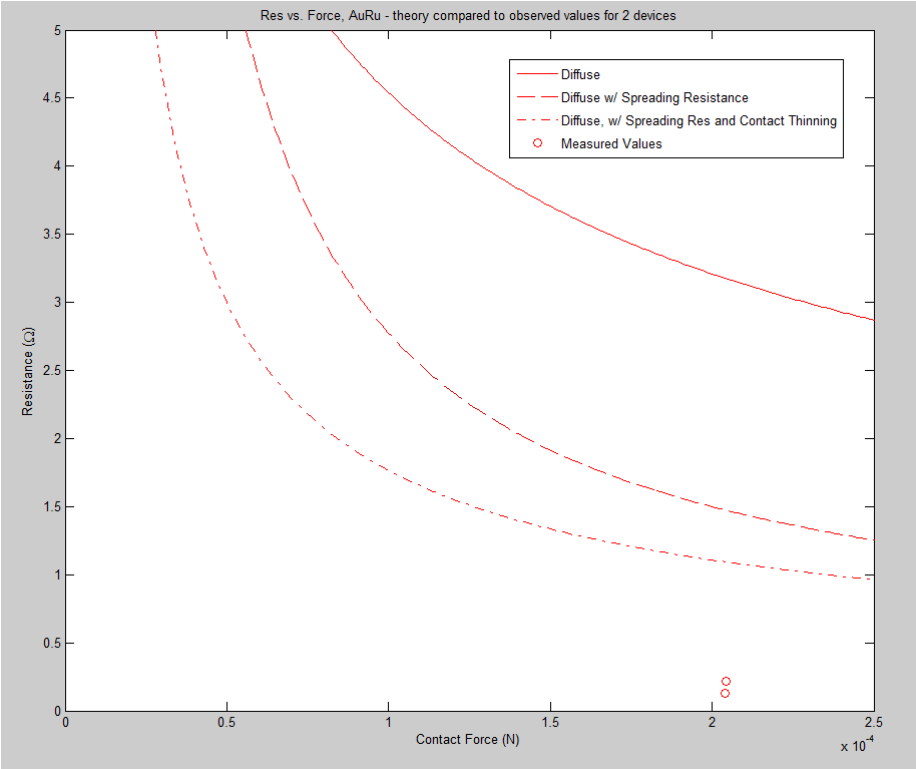

Figure 51. Resistance vs. Force plots for 2 lightly worn (1,000 to 3,000 cycle) Au-Ru micro-contacts compared to classical diffusive elastic-plastic contact resistance models with and without spreading resistance compensation [164].

4.5 External Effects

4.5.1 AC Loading Effects.

In designing the first of these experiments exploring external effect, and taking into consideration the timing which is previously discussed, four frequencies were tested with the goal of reaching 10 million cycles. This value was chosen because even under the low-speed conditions some of these tests would entail, it was still achievable in the time permitted. This number also represents a relatively low number of cycles under standard DC conditions, as most devices fabricated at the same time as those being tested had little issues in reaching this many cycles. Figure 52 below shows the

results of the multiple runs which were done for each of the four frequencies tested: 100 Hz, 1 kHz, 10 kHz, and 100 kHz.

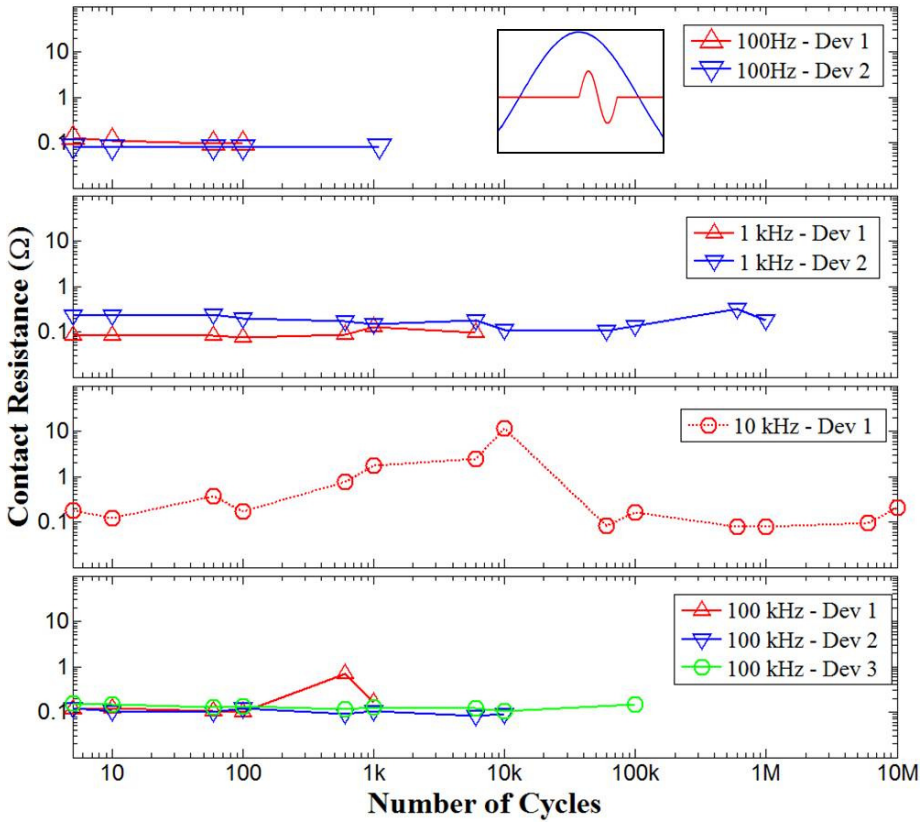

Figure 52. Contact resistance vs. induced cycles with an AC load with signal frequencies of 100 Hz, 1kHz, 10kHz and 100kHz applied to cold-switched Au-Au micro-contacts with 8 μm contact radius [164].

While initially it was expected that this testing would take some time, as can be seen by the data only one of the eight tests lasted to 10 million cycles. These tests were all timed such that a single AC oscillation was applied under cold switch conditions, yet most devices failed well before the goal. The next test investigated the effects of intentionally hot switching and comparing it to these initial results. To do this, we started with the 1 kHz test and simply decreased the frequency of the load while leaving the actuation frequency constant. Both of the tests conducted showed

further reduction in device lifetime, and the results of these tests are shown in Figure 53, part a below.

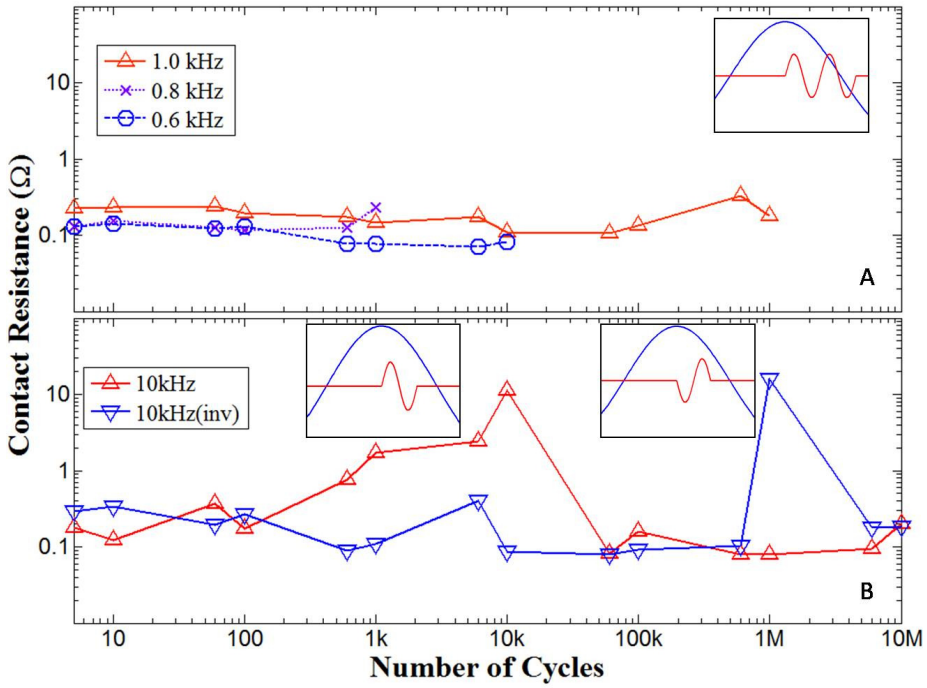

Figure 53. (A) Comparison of hot-switched, AC loads of frequencies 1 kHz, 800 Hz, and 600 Hz where all three devices eventually failed to open. (B) Comparison of cold-switched loading of inverted and non-inverted single cycle, 10 kHz loads applied to 8 μm contact radius Au-Au micro-contact cycled at 2 kHz [164].

Finally, a third test was conducted to see if an obvious change would result from reversing the polarity of the low-frequency AC load applied. Starting with the only test conditions that lasted 10 million cycles (the 10 kHz test), this test was repeated but with a reversed AC load. Interestingly this test also lasted to 10 million cycles, and showed a similar amount of variability in the data, but otherwise there was no obvious difference in this one test case. The data from this test is shown in Figure 53, part b.

A few devices were further investigated through SEM imaging. An identical device which had been tested to 10 million cycles was used as a baseline, and compared to two of the failed devices. These images are shown in Figure 54. In both of the failed

device cases, there is clear indication of pitting on the beam. With little damage directly below the region in which this pitting occurred. The lower contact image does show some of this dislocated material.

4.5.2 External Circuit Effects Under DC Conditions.

The first tests conducted were to validate the effects of external circuit elements on micro-contact performance. These were conducted under DC test conditions with a similar goal of 10 million cycles. Recall the circuit configurations which were to be tested in Figure 27. The first three of these circuits were expected to provide detrimental results as they contained configurations which should induce premature failure. Conditions five, six, and eight also contained reactive elements but in theoretically beneficial configurations. Condition seven was to test both parallel and series resistances, in an effort to evaluate the effectiveness of passive protection. A single baseline (configuration four) was conducted once simply to ensure consistent results with previous DC testing. In approximately 40 devices previously tested, contact resistance typically ranged from 0.1 ohms to 2 ohms, and with greater variation below 1000 cycles as devices were worn in [163, 166, 172, 173]. First consider the results of the three detrimental certain configurations shown in Figure 55.

The results are shown alongside the baseline device (from configuration four), for comparison. Not surprisingly, all of these configurations resulted in premature failure. It should be noted however that these tests were all conducted under cold switch conditions, and thus any effects these devices had on overall performance did so without mimicking hot switching. The worst case where the tests in which a series inductor was present, while parallel capacitance provided slightly better results. The devices tested with both of these elements present tended to fall in between these

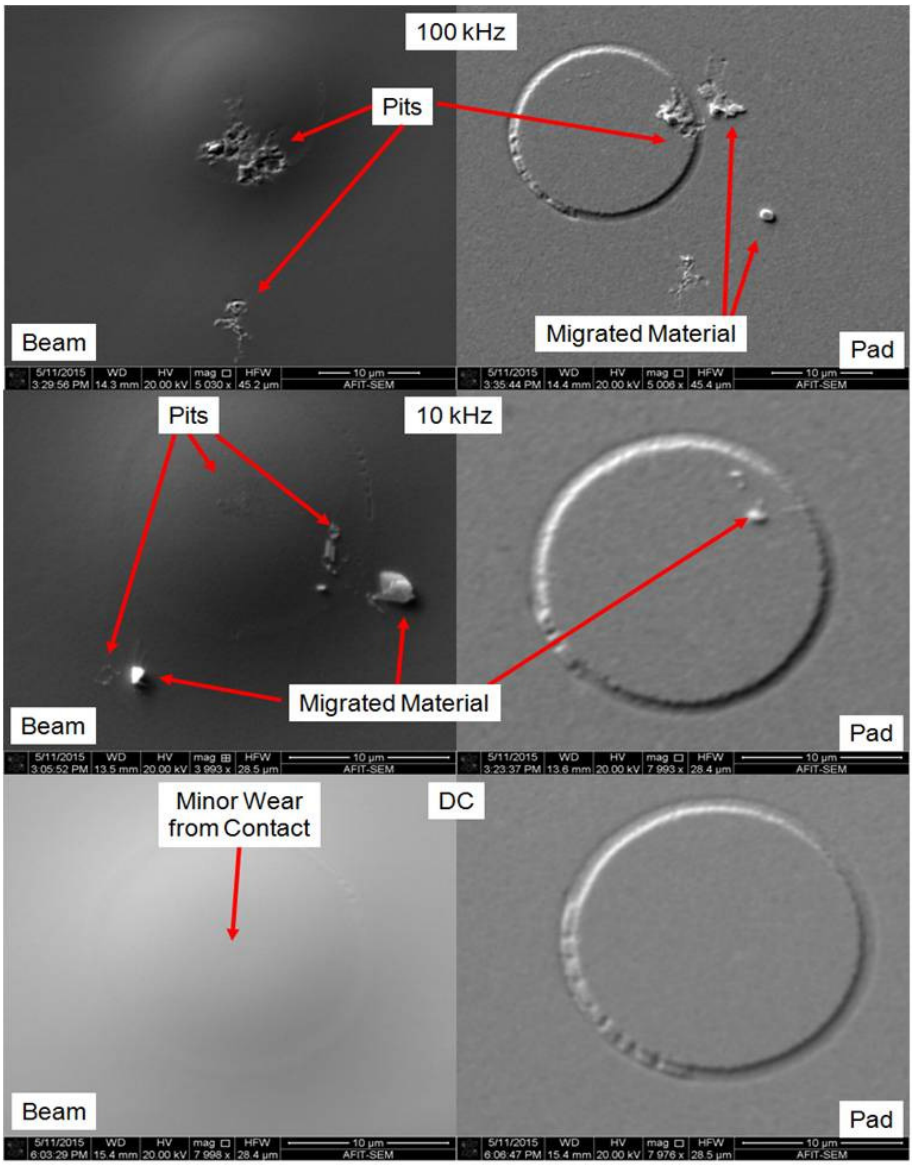

Figure 54. Exposed contacts after folding back the upper beams (left) and their corresponding lower pads (right) from three devices exposed to cold switched loads, at 100 kHz, 10 kHz AC loads (as labeled), compared to identical device tested with cold switched DC to 10M cycles of operation. The circular shape on the pad side is an intentional conformal feature in the bottom evaporated gold layer which marks the corresponding outer radius of the mating bump (in which the same circular shape can be seen, but is diminished during the photoresist reflow process which gives the upper beam contacts a hemispherical shape [164].

extremes. Next we considered the results from the beneficial reactive elements shown in Figure 56.

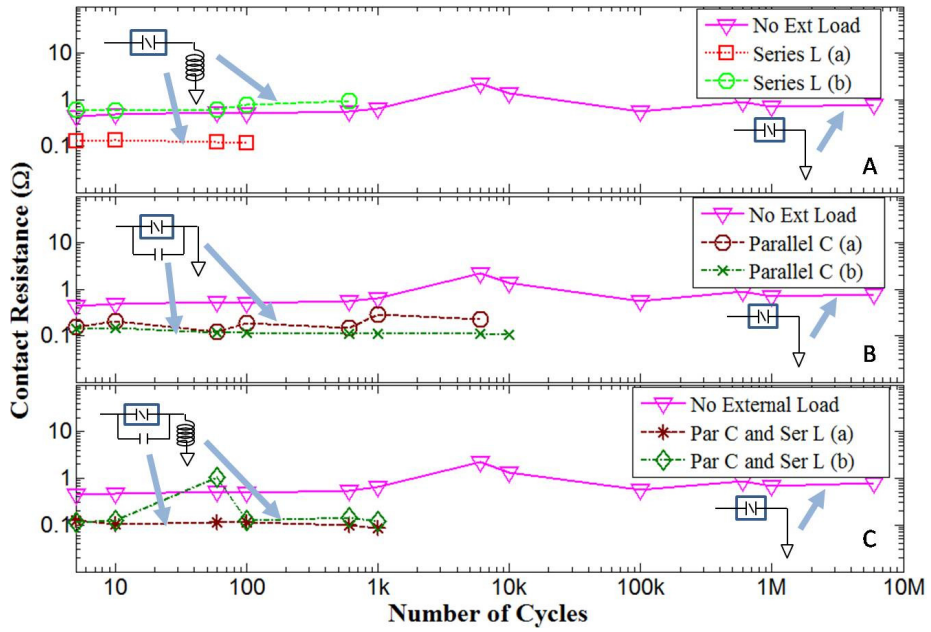

Figure 55. Comparison of the contact resistance of Au-Au 8μm radius micro-contacts to three detrimental circuits. Series inductance of 100 μH was added for (A), parallel capacitance of 0.6 pF was added for (B), and both elements were added to (C). All six devices were tested with a 1 volt, cold-switched DC load, and all failed due to shorting at the number of cycles shown [164].

Overall these tests indicated much better performance, with all but one last in the full 10 million cycles. In one instance, extreme variation in contact resistance was observed, but the device recovered and reached approximately the same contact resistance in all cases as the 10 million cycle case. It is unclear whether this variation was due to the presence of these external circuit elements, or if this was a device which was starting to fail but was able to recover. Finally we considered the results of passive circuit protection as shown in Figure 57.

For both of the devices tested in this configuration, both lasted the full 10 million cycles, showing little variation throughout testing. In one case contact resistance dropped near the end of the test with both devices settling to contact resistance lower than the unprotected device. In addition to these contact resistance measurements taken over the lifetime of these devices, one additional observation was made. Recall

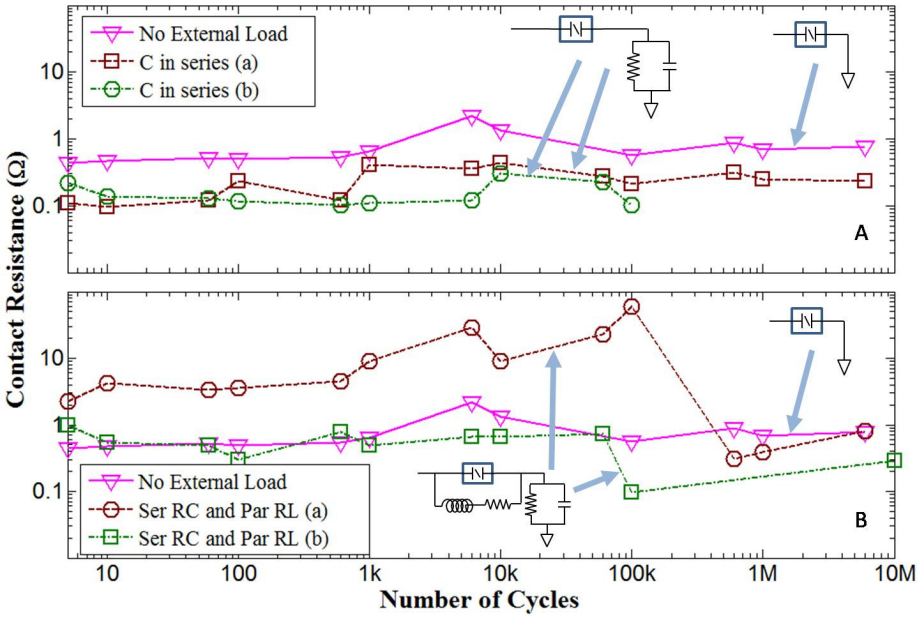

Figure 56. Comparison of the contact resistance of unloaded Au-Au 8μm radius micro-contacts with two protective circuits. The first (A) shows two series RC external loads (a) and (b), the second (B) shows both series RC and parallel RL. The one failed device was due to shorting, the rest all lasted to the target 10M cycles. The external resistor used was 1Ω , the capacitor was 0.6 pF and inductor was 100 μH [164].

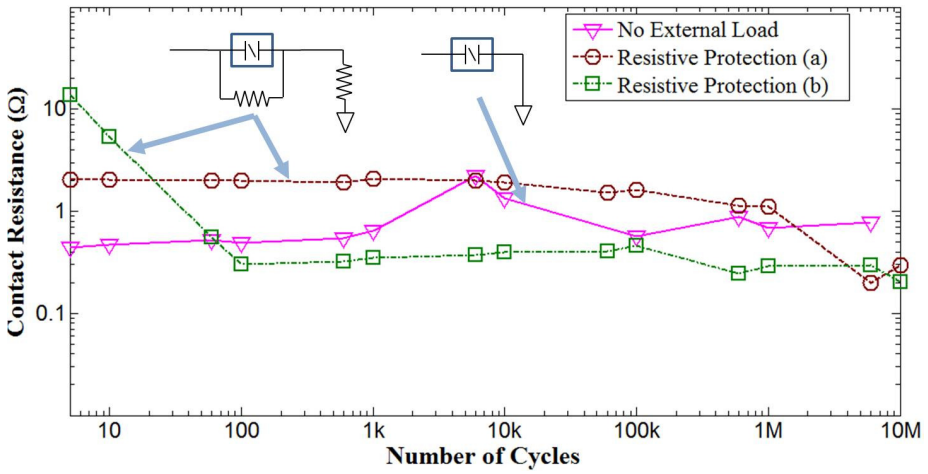

Figure 57. Comparison of the contact resistance of Au-Au 8μm radius micro-contacts showing an unloaded device along with both a 5 MΩ parallel resistance, capable of immediately dissipating any charge during contact opening, and a series resistance of 1Ω, providing the ability to limit current while contact was closed [164].

from previous discussions involving how contact resistance is measured. As the force sensor is advanced current and voltage measurements are constantly monitored and can be tracked allowing us to observe contact resistance as a function of contact force for each resistance measurement taken. While all the previous data shown for these tests shows only the final contact resistance value, each of those points has a resistance versus force curve which was obtained to determine that value. For devices which were failing in this series of tests, one interesting characteristic was observed. This characteristic is best illustrated in Figure 58.

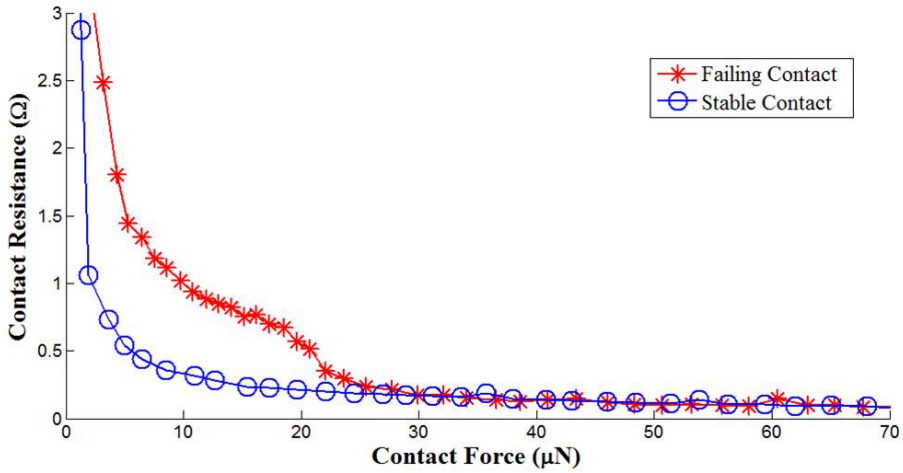

Figure 58. Comparison of two single contact resistance measurements cycles, one at 10 million cycles for a device that remained stable, the second shows a measurement shortly before the device failed, where it no longer conducted current upon closing [164].

This plot shows the contact resistance as a function of contact force of two devices. The device labeled stable contact shows the curve which was produced at 10 million cycles for a contact that was still operational at that point. Compare this data to the failing contact curve which is shown alongside this. Notice that during initial closure, the smooth decaying exponential was not present, but instead curve irregularities are present under extremely low contact force values. This sort of variability was present

in all of the data obtained immediately prior to failure for all of the failed devices from this portion of the test.

4.5.3 External Circuit Effects Under AC Conditions.

Finally, these two conditions were brought together by applying the beneficial circuit configurations to a new set of devices. Those tests were repeated under AC conditions, which previously resulted in premature failure. Overall, 15 tests were ran and 13 of those tests lasted to 10 million cycles indicating clearly that these sort of beneficial circuit configurations were effective in mitigating whatever damaging processes were present under low frequency AC conditions. Evaluating these results, we started with passive circuit protection at three different frequencies as shown in Figure 59.

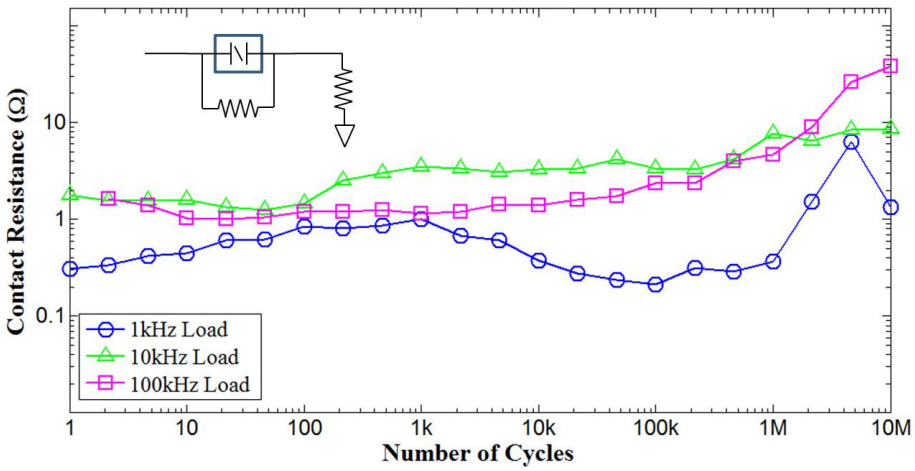

Figure 59. Comparison of contact resistance vs. device life of Au-Au 8μm radius micro-contacts under the three AC loads shown, all cold switched with a parallel 5 MΩ resistor and 1Ω series resistance added external. All three devices remained operational at the 10 million cycles target [164].

As can be seen all three of these devices lasted the full 10 million cycles at 1 kHz, 10 kHz, and 100 kHz of the AC load induced during cycling. While overall contact resistance did seem to drift during testing, and final contact resistance was

significantly higher than expected the devices were still functional in all three cases. The next two tests investigated the effects of having series capacitance and parallel resistance at the same three frequencies with new devices. These tests were repeated twice with two different capacitance values to see if any obvious changes resulted. The results of all six of these tests are shown in Figure 60.

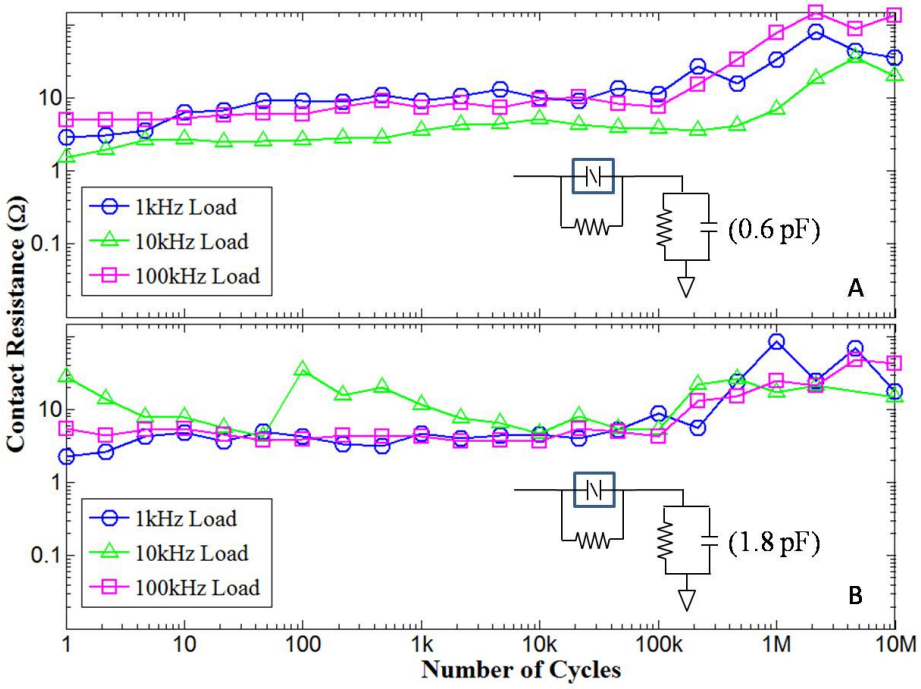

Figure 60. Comparison of contact resistance vs. device life of Au-Au 8μm radius micro-contacts for two test circuits (both with a 5 MΩ parallel resistance, and an RC circuit in series, using a 1Ω series resistance, and along with two different sized capacitances as shown). The tests were conducted at the three frequencies listed, all of which were still operational at the 10 million cycle target [164].

Overall these results were similar to the previous tests in that in all cases 10 million cycles was reached, variability throughout the test was fairly minimal, and contact resistance continued to climb in all cases. While two different capacitance values were used, there was little difference in the overall results. Finally the test was repeated with three more devices at the same three frequencies with both series

capacitance and parallel inductance. The results from these tests are shown in Figure 61.

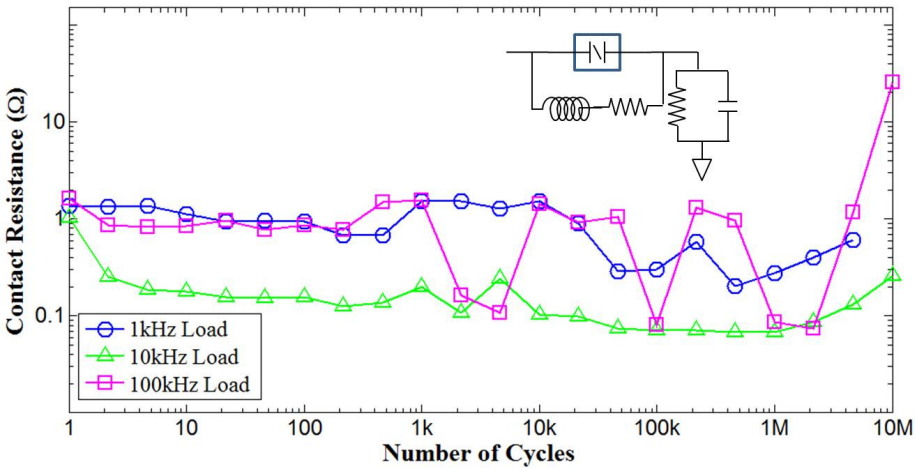

Figure 61. Comparison of contact resistance vs. device life of Au-Au 8μm radius micro-contacts for the test circuit shown. The inductance used was 100 μH along with a 5 MΩ parallel resistance, as well as an RC circuit in series, using a 1Ω series resistance, and 0.6 pF of capacitance). The tests were conducted at the three frequencies listed, two of which were still operational at the 10 million cycle target and one which failed to close just prior to reaching 10 million cycles [164].

In this case, one of the devices which did fail prematurely occurred during the 1 kHz test. Variability with the 100 kHz test was somewhat higher than other tests in the series, but overall contact resistance remained under 10 ohms for most of the testing.

4.6 Chapter summary

Nanosphere lithography was reviewed as one of two potential means of fabricating small features with controllable, predictable contact areas for the purpose of inducing ballistic electron transport. A variation of dip coating was pursued in which the carrier fluid was drained over the surface of the substrate. To accomplish these depositions, a variety of vessels were designed and printed using commercially available 3D printing technology, resulting in vessels which demonstrated success in obtaining

self-patterned layers, but in very limited coverage. Irregularities in concentration also led to variability in the results, as did variations in drain rate.

An alternative method which resulted in much more usable results involved an improved method of conducting grayscale lithography. Through multiple exposures of line-scanned patterns, grayscale like results could be obtained at much higher resolution than with image based gray scale techniques. An exposure study was conducted to develop recipes for a variety of step sizes. Using these recipes, trials were conducted with both 400 nm step size as well as 80 nm. These were patterned and imaged in 1818 photoresist, and transferred to a silicon nitride coated wafer using the results from an etch study between silicon nitride and 1818 photoresist.

In the area of thin-film contact resistance, data from Au-Au, Au-Ru, and Au-RuO_2 contacts were used to test modified theory. Data from a variety of devices was evaluated against models to evaluate the validity of this theory and justify any further activity in this area.

Finally, external effects on micro-contacts were evaluated. Theory involving the effects of circuit loading with both reactive and passive elements was experimentally investigated under DC loads. Next, the effects of low-frequency, low-voltage AC loading was also experimentally investigated under a variety of conditions. Finally, experimentation was performed investigating the combined effects of how micro-contact reliability may be impacted under low-frequency, low-voltage AC conditions with a variety of circuit elements present.

V. Analysis

5.1 Chapter overview

The results presented in the last chapter addressed a variety of micro-contact performance and reliability aspects. How each of these experiments and their results apply to the effort of enhancing performance and reliability need to be discussed individually. In the area of improved contact area of control, two approaches to fabricate improved contact surfaces were presented: Nanosphere Lithography and Improved Grayscale Lithography. In recognizing the next step in device fabrication will include utilization of a thin-film lower contact, and minimizing the thickness of that film will be key in maintaining contact geometry, data which improved contact resistance theory was presented. Finally, various experimental data investigating exterior effects on device performance were presented and the implications of these results need to be reviewed.

5.1.1 Nanosphere Lithography.

Commercially available 3-D printing of ABS plastics proved ideal to design and fabricate a series of deposition vessels uniquely suited to test self-patterning of nanospheres. ABS plastic was used for these vessels as this material proved easier to seal than PLA, however this technology is constantly progressing to meet an ever increasing variety of applications. As new materials become available, a better form of plastic may be better suited for this application in the future. Also, these vessels tended to build up spheres over time and as any aggressive solvent would damage the vessel, the only alternative is to reprint the design. Alternatively, the same designs used in these experiments could be printed using a metal-based 3D printing process which would also allow for solvents to be used on the vessel without affecting its integrity. Conductive

materials are also being introduced which could allow for charging to be integrated into the process. As chemical charging is one method in which adhesion between nanospheres and the substrate can be enhanced, an electrical bias may prove effective as well. Thus, this technology is likely to advance in many ways which could further enhance the results obtained thus far.

These experiments focused exclusively on depositing 500 nm, polystyrene nanospheres onto silicon substrates patterned with 1800 series photoresist. For this size sphere and a de-ionized water carrier fluid, the ideal incident angle between the substrate liquid was approximately 20. Based on prior research, the incident angle and drain rate are both directly influential on the quality of the deposition. This complex interdependence of system parameters suggests that further optimization may be possible, but also could be time consuming without some thought put forth early in the process. Smaller spheres could of course give a smaller pitch between features and also much smaller contact areas, but given the current state of this technology in the literature, spheres smaller than 100 nm begin to become extremely difficult to manage. Another possibility is to utilize metallic nanospheres as the conductive layer, however the interaction of those materials and a pre-assembled monolayer of metallic spheres becomes a very complex issue to address. Polystyrene nanospheres remain near the surface of the carrier fluid when they are no longer floating, metallic spheres may not depending on surface characteristics, density of the material, etc. Since most of the successful results here were obtained from depositing these subsurface particles, metallic spheres would likely have to be transferred from the surface, or from a surface film in which they were confined. Such a process however is currently unknown and little has been published in this area regarding how best to transfer these kinds of monolayers, if they can even be formed using metallic spheres.

Both monolayer and multilayer formations were patterned under a variety of methods indicating suitable structures could be built using either. The two produce different geometries however, and the kind of patterning present would have to be known in order to ensure the modeling used to support the data was developed with the correct features. Based on the results obtained in these experiments, pre-deposition etches proved to be suitable to control the relative size and shape of the features patterned, and the resulting structures could potentially provide the reduced, controllable contact area desired.

Proper positioning of the patterned layers proved to be fairly effective, if only on a small scale. In order to create a hybrid mask, both pre-pattern nanospheres and free-floating subsurface nanospheres were evaluated. Pre-patterning resulted in larger surface area coverage, but with many more discontinuities in irregularities in the pattern. Layers which were formed through capillary forces into smaller open areas were much more controllable in their placement, but the overall coverage was extremely low and would result in very few if any usable devices when compared to what would be necessary to pattern a full wafer. The high sensitivity to variations in surface concentration however, suggests that if a deposition vessel were developed to better control both the drain rate and surface concentration, a better overall result may be attainable.

5.1.2 Improved Grayscale Lithography.

A hybrid method of grayscale lithography was explored which utilized the high resolution capabilities of operating the Heidelberg μPG-101 system with CAD files, but in a repeated pattern to produce 3-D features in the final product which were superior to what could be achieved using an image patterning approach. Due to the repetitive nature of the process, software was implemented to automate the repeated

exposures. This resulted in a reliable, safe method to operate the system in this manner without requiring human supervision. Additionally this prevents the possibility of errors which would likely result from attempting to perform this sort of process manually.

An etch study was performed which determined that rather than etching these features into a silicon substrate, etching into the passivation layer directly was also possible at a selectivity of 1.0. This eliminates one of these steps and the feature blurring which would have occurred. By adjusting the ratio of the partial pressure of oxygen to tetrafloromethane, selectivity near 1.0 can be achieved to slightly alter this etch ratio and the pattern transferring at the same time.

Two feature resolutions were attempted, one which assumed the 400nm horizontal accuracy advertised by the manufacturer was the best which could be achieved, and another which pushed this by a factor of 5 and attempted 80nm accuracy instead. While many of the features at this tighter tolerance were still realized, repeatability for this application is still an issue. The actual beam width for this system was verified at 900 nm when patterning with a step size of 400 nm. The quality of the edge of this beam was not characterized however and part of the issue with reducing the step size may be just as much a factor of the sharpness of the edge of the beam as much as positioning accuracy.

5.2 Thin-film Effects

In reviewing the results from applying thin-film spreading resistance theory to existing contact resistance models, the three combinations of material pairs tended to have somewhat different results. If we consider each individually however, each was explainable in turn. Starting with the Au-Au contact pairs, current models predicted approximately 0.1 Ω of contact resistance, and the three devices considered

were all slightly higher. In this instance, spreading resistance theory reduced the expected values slightly, so at first glance this theory appears to perform worse. There were however factors which may explain this inconsistency. The first was recognizing that the model assumed circular symmetry which we do not have; this point will be discussed shortly as it drives the next steps in this effort. Two other considerations were inaccuracy in predicted vs. actual contact area or a contaminant film. Given the variability between the three measured values and the fact that this variability is greater than the error between both corrected and non-corrected values, the best we can say in this case is that there was no indication that spreading resistance corrections are flawed, but based on only this data they are not justified either.

Far more encouraging results were presented when we consider Au-RuO_2 contact pairs. In this case, 8 devices were tested and all showed approximately 2 Ω of contact resistance, and with very little variance. Prior to spreading resistance theory, the best models predicted nearly 4 times that value, just under 8 Ω. The addition of spreading resistance however brought this predicted value down to approximately half, and while there is still some variance between the mean measured resistance vs. the corrected model, the addition of this theory corrected for a large portion of this error.

For the case of Au-Ru contact pairs however, the difference was much more extreme. The two devices tested showed very similar results and were measured at approximately 0.2 Ω of contact resist. Older models predicted roughly 3 Ω of contact resistance, which was over an order of magnitude in error. Once again, the addition of spreading resistance closed about half of this gap, but a great deal still remained. The first consideration was that since we were dealing with materials with different hardnesses, and the lower thin film was the softer material, perhaps there was compression occurring which may be thinning the film during closure and/or the thickness of the

film used in the calculations was in error. If we recall from Figure 51, a third plot was added which shows the results of a 50 % compression. Even with this extreme adjustment to the thin-film thickness, the change to the predicted contact resistance was minimal, indicating there is some other factor at play if spreading resistance theory is accurate.

As was previously mentioned, this remaining variance between predicted and observed values could possibly be in part due to other material properties changing during operation (e.g. hardness, Poisson's ratio, etc.) Changes in device geometry/contact area may result from these changes as well. One remaining possibility however, and becomes apparent when considering that spreading resistance models for radial contacts assume infinite radial symmetry. In our case however, as current passes into this lower thin-film it rapidly becomes asymmetric in order to accommodate the circuit path it must follow. In Chapter 3, the observation was made that this sort of contact resistance measurement was not strictly the contact, but rather the entire region between where the current was uniform in both the upper and the lower contacts. Thus, the results of this asymmetric radial spreading would be measured as part of this contact resistance measurement, and should result in some level of variance as a result.

While it may be possible to adjust our model to account for this even more complex geometry, another explanation is being explored. Rather than rely on radial contacts and spreading resistance models, an alternate version of the original spreading resistance theory was propose using rectangular Cartesian coordinates. Consider the alternate design for these contacts which was presented earlier in Figure 26. This revision would help to answer the question of how impactful this geometric error is, but as testing has yet to occur on this design that will remain an active research area for now.

5.3 Exterior Considerations

Three variations of testing were performed regarding this topic, and from this portion of testing, several observations were made. First, with respect to testing external circuit elements to devices which were then subjected to a DC load, there is a clear indication that these configurations caused premature failure in nearly all instances. Other configurations seem to provide damage mitigation instead. While the originating theory predicts this behavior overall, one interesting point to note is that these results were all obtained under cold switch test conditions which was not specifically predicted in the original theory presented.

For AC loads applied to similar contacts with no external circuit elements, virtually all frequencies and test variations resulted in some level of performance degradation, and in well over 80% of devices tested, premature failure. While the 100 Hz tests were the quickest to fail, subsequent tests which were conducted with an increased frequency did not follow a clear trend, but they still tended to fail prematurely. The one exception was the one device tested at 10 kHz which did last the 10 million cycles targeted. Interestingly reversing the polarity of this 10 kHz test also led to a device that lasted a full 10 million cycles. While only single devices were tested for these two conditions, the commonality may indicate some characteristic of the device in which less susceptibility is observed at this frequency, but apparently polarity change has little effect on overall results. For the two tests conducted, extending the signal such that hot switching occurred did cause device failure to occur sooner. In those devices which failed prematurely and were imaged, the damage which was inflicted did indicate material transfer from the upper contact with minimal damage to lower contact.

Repeating these AC testing conditions on devices which were configured with protective external circuitry, there was a clear indication that overall performance

was improved. While in almost all cases, overall contact resistance seems to climb steadily, the devices still continue to function to the target lifetime of 10 million cycles before testing was terminated. This may be an indication that the AC loading was still having an effect on the device, but the external circuit elements were able to compensate such that premature failure was avoided. Minor variations in the sizing of reactive components seem to have little effect, and parallel inductance seemed to indicate some level of diminished protection when compared to a passive parallel circuit element (i.e. resistors).

A final important observation was made: in all the devices which failed during AC load testing, investigation of the resistance versus contact force curves indicated a peculiar behavior. One example of this was shown in Figure 58, where an undamaged contact during closure showed a distinctive, exponential decay to the final contact resistance value at full closure, but damage devices showed something quite different. Under very low contact forces (i.e. below 30 micro-newtons), this curve was still smooth, but varied greatly from the expected exponential shape. It is not clear whether this sort of curve is present prior to all failed devices or simply those from this test series, nor is it clear that a smooth decaying exponential is always present in stable devices. However, this commonality among this test series certainly justifies further investigation as this may lead to a method in which device failure can be predicted in advance.

5.4 Chapter Summary

From the analysis of these results, it is apparent that we have techniques which can provide better contact geometry through either nanosphere lithography of improved grayscale lithography. However, for fabricating multiple devices simultaneously with a high probability of success, grayscale lithography is a better option at this time.

Should deposition efficiency be further developed with nanospheres however, they would be more likely to provide the structures needed for these types of devices. Thin-film spreading resistance theory was validated next, as was theory regarding the affects of external factors to micro-contacts. With this analysis, we can now discuss what we can conclude from these efforts as well as the next steps forward.

VI. Conclusions and Recommendations

6.1 Chapter overview

This chapter summarizes this research effort based on the data and results from the various experiments conducted. These results are then applied to our immediate goal of improving micro-contact performance and reliability in order to determine what contributions have been made. Finally, we will take these contributions and compare them to our long term objectives and in each topic determine what the most appropriate next steps are to further this work beyond the scope of this research effort.

6.2 Conclusions

6.2.1 Test Stand.

First we will review what changes have been made to the test stand, what improved capabilities have been realized, and what remains to be done for future testing.

6.2.1.1 Hardware.

The hardware of the test stand has changed little throughout this experiments. A faster, more recent piezo-electric actuator has been identified and purchased, which when integrated will enable testing orders of magnitude faster. Additionally, automated stages were identified and purchased which will serve two purposes. First, they will greatly reduce the likelihood of probe damage during test setup, as the faster piezo-actuator has only 10 μm of travel vs. the 20 μm we currently use. This reduction of travel means the test probe must be positioned much closer to future test devices, and using the current manual stages will certainly result in many probe tips

being destroyed if these stages are not automated. Second, these automated stages will allow for automatic movements other than linear translation of the probe should that be needed. Implementation of this hardware will be required for extremely high cycle counts (in excess of 1 billion cycles).

6.2.1.2 Software.

Unlike the test stand hardware, the software has gone through significant improvements, with many more still to come. The overall modifications to the user interface have made the system much more straightforward for users to follow with reduced chance of operator error. As has been mentioned repeatedly, this stand in its current configuration is suitable for any application which requires either repeated linear cycling and/or precise position control while monitoring application of force along with displacement and other electrical measurements which may be required. These UI modifications will allow for new users to be able to conduct testing with less training required and much less chance for error.

The second major modification addressed how testing automation was handled. While the initial design was more than adequate to conduct the research required, it lacked the ability to perform these tests in an efficient, automated manner. To this end, the basic testing scheme was significantly modified. The original system allowed for the user to select how many cycles should be imposed between test point, and to what final number of cycles testing should cease. This scheme works across the range of a single decade, but once a device has reached a new milestone, the number of cycles between test point needed to be increased by an order of magnitude, which required human intervention. The new software included the following features to correct for this:

- Start counts - the addition of a starting cycle was required to resume testing on a device which had been inadvertently halted premature. The user could specify either that data not be taken until the starting count was reached, or that the system assume that number of cycles had already been imposed on the device.
- Number of Decades - How many decades past the starting count should testing proceed. For example, if the starting count was set to 1,000 and this value was 6, then testing would proceed to 1 billion cycles.
- Test Points per Decade - Any number can be specified, but if this number exceeds the available points in that decade, only testing for each cycle will be conducted. For example, if this value was set to 20, then from 0 to 10 cycles, only 10 points are available, so only 10 points would be measured. From 10 to 100 cycles, and every decade thereafter, 20 points would be taken. The exact number of cycles would be selected so that when plotted on a log scale, the data would be evenly spaced, although the software has the ability to instead test at intermediate values which are spaced evenly on a linear scale instead of a log scale, but wasn't included in the UI when it was implemented.
- Samples per Test Point - To address the issue of variance at high cycle counts, the user was given the ability to specify that each test point be repeated by this factor. For example, if this value was set to 3, and the system was about to take a test point at 1,000 cycles, then 1,000, 1,001 and 1,002 would all be measured and recorded to detect short term variability in the data.
- Starting Actuation Frequency - In anticipation of future hardware upgrades which would increase the actuation frequency, this parameter specifies that at lower counts the actuation frequency can be limited to ensure a higher accuracy on the number of test cycles induced by avoiding extremely large frequencies and extremely small times. For example, if the system was set to cycle at 200

kHz but only 20 cycles were needed, this would require cycling for 0.1 msec. The ability to limit the starting frequency allows for the testing to start at a more reasonable rate and accelerate as testing proceeds.

- Final Frequency - Specifies the maximum frequency to be used throughout the testing process.
- Step Size - Indicates the increase in frequency per decade. For example, if the starting frequency was set to 200 Hz, the final frequency was 2 kHz and this value was set to 400, then each decade the testing frequency would increase by 400 Hz.

This scheme not only addresses the immediate needs for more efficient testing, but also proactively addresses some future concerns.

6.2.2 Micro-contact Surface Engineering.

Next we will discuss the conclusions that can be drawn regarding the ability to fabricate small, repeatable features which posses small, controllable contact areas. This will not only allow for a greater degree of confidence in evaluating existing contact resistance models, but will also be a pre-requisite for future potential projects, such as constructing devices capable of testing ballistic electron transport.

6.2.2.1 Nanosphere Lithography.

While overall the results which were obtained and published were better than existing results from the literature, the applicability of NSL to this research is still limited at this point. Improvements to the overall ability to produce self-assembled layers as well as the ability to precisely position those assemblies are only adequate if large coverage can be produced reliably and repeatably. While this level of repeata-

bility is still lacking, there has been progress toward achieving this goal as well as significant contributions to nanosphere lithography in general, specifically:

- Deposition vessel design - It has been clearly demonstrated and published that basic 3D printing was perfectly suitable for producing the deposition vessels needed for this technique. The quality of these vessels have met the requirements for the process, yet they are easy, fast, and inexpensive to produce. This allowed for quick modifications to adjust for unexpected results or last minute modifications as required.
- Surface assembly - It has been demonstrated and published that this process can be used to assemble monolayers of nanospheres on a carrier fluid and that layer can be transferred to a submerged substrate. It has also been determined that if signifiant quantities of sub-surface nanospheres are present, and the transfer happens too slowly that multi-layer depositions will result.
- Subsurface assembly - It has been demonstrated and published that in the absences of self-assembled layers of nanosphere surface assemblies, self-patterning of nanospheres has still occured from subsurface spheres through the use of capillary forces during the draining process. These types of depositions required much slower drain rates than when transferring pre-assembled layers. They were also sensitive to the concentration of spheres near the deposition and if that concentration is not held constant, it has resulted in both gaps and multilayers on the same surface. If the rate had been kept sufficiently slow and the concentration near the surface of the liquid was held high enough as it passed the substrate, monolayers and multilayer depositions were formed in areas larger than any found in current publications for these types of materials.
- Monolayer vs. Multilayer - The differences between monolayer and bilayer (possibly multilayer) patterning has been demonstrated. It has also been shown that

the characteristic patterning produced was indicative of the type of deposition performed. While multilayer depositions greater than two layers can possibly still serve as a lithographic pattern, each layer has a 50% cumulative chance of preventing the structure from functioning as a lithographic medium. It has not been determined if controlled patterning can influence the placement of multilayers at this time.

- Controlled Placement of Patterned Layers - It has been demonstrated and published that both surface and subsurface patterning can be used with pre-patterned photoresist to aid in the positioning of nanospheres on a substrate. Surface layers of nanospheres which were subjected to disruption in the overall pattern when forced to conform to a feature present in the photoresist can result in tears and dislocations, but the monolayer remains predominantly intact. Subsurface formation has also been demonstrated within properly sized channels of photoresist, presenting another method for direct placement.

6.2.2.2 Improved Grayscale Lithography.

Initial efforts from prior research in this area produced notable results in the data obtained but with limited resolution due to the capabilities of the equipment. The lack of automation within the controls of the laser lithography system itself initially prohibited this from being a viable approach, but once a third party solution to this limitation was added to the system, the results indicated the most promising structures produced yet by any method. Contributions in this area include:

- Integration of 3rd Party Emulation Software - A versatile scheme of integrating keyboard/mouse emulation with the laser lithography system has proven successful. This involved the development of a rudimentary positioning 'language' to specify the placement of CAD designs at predetermined locations,

with specific power and duty cycle settings. This approach included the ability to produce any combination of CAD files at any number for positions as well as the printing of alignment marks for fabrication steps that followed to ensure the process could be merged with micro-contact device fabrication. Matlab code was developed to read this language and produce a script file which could be read by the emulation software. This allowed for completely autonomous printing without any requirements for human intervention, which also removed the possibility of human error during the extremely repetitive processing which is required for this technique.

- Successful Exposure Study - Multiple combinations of power and duty cycles were tested with repeated patterns with partial overlap, allowing for multiple recipes to be identified for a number of different processes depending on the number of steps required.
- Successful Etch Study - To transfer these features directly into a Si_3N_4 substrate, an etch study was conducted and a suitable chemistry which applied a selectivity of 1.0 was found. This recipe was also suitable for selectivities near a value of 1.0, which allowed for subtle feature evaluation. Although this point has not yet been demonstrated, data above and below this selectivity has been recorded.
- Demonstration of Successful Merged Line-scan Approach - Implementation of this approach was demonstrated with a variety of overlapping patterns at both 400nm step size and 80nm step size, both at combinations of 2, 4, and 6 layer processes. While the 400nm step size produced extremely well patterned results, the spacing between these features was relatively large. Using the 80nm step size produced many smaller features with a much smaller pitch spacing, but the variability in both placement and shape was much more dramatic. One of two possible conclusions can be made from this - either the best resolution is

somewhere between these 80 to 400 nm step sizes, or further optimization of the exposure recipe may clear up the higher resolution patterning.

- Successful Structure Patterned in Si_3N_4 - Several of these patterned features have been successfully transferred to a thick passivated substrate, and the results presented here. While much of the original detail was preserved, overall there was some level of degradation which may be due to slight inaccuracies in the selectivity, an overaggressive nitride etch, or some other yet to be determined factor. The results are suitable for use in fabricating the desired structures for application in micro-contact surface area control.

6.2.3 Thin-film Spreading Resistance.

Applying thin-film spreading resistance theory to existing contact resistance models provided encouraging results overall. Specifically:

- Au/Au Contact Pairs - Existing models predicted a slightly lower resistance than what was experimentally measured. Application of thin-film spreading resistance lowered the expected value even further. However, the variability in the three devices tested is roughly three times as much as the change to the model. We can theorize plausible causes for the remaining variance, but can not draw any conclusions based on these devices.
- Au / Ru Contact Pairs - All eight devices tested of this type resulted in contact resistances near 2-3 Ω with very little variance overall. Existing models predicted the contact resistance for these materials should be roughly 8 Ω. The addition of spreading resistance reduced the predicted value to less than 4 Ω, eliminating nearly all the variance observed, indicating validity to this approach.
- Au / RuO_2 Contact Pairs - Both devices tested experimentally showed extremely low contact resistance (0.2 Ω), but existing models predicted nearly

3.5 Ω. Spreading resistance theory reduced this expectation to 1.6 Ω, but a great deal of variance remains. Compression of the film doesn't provide enough of a correction to explain the remaining variance, thus some other factor remains unexplained.

6.2.4 External Factors.

Based on the experimental results from the three topics in this area, a number of conclusions can be drawn.

- Low-Frequency, Low-Amplitude Loading - It has been experimentally verified and published that applying low-frequency, low-amplitude AC loads to micro-contacts results overwhelmingly in premature failure. The occurrences did not seem to have a correlation to frequency, and occurred under both hot and cold-switched conditions. Inverting the phase of the load also seemed to have little effect. As this failure was present even under cold-switched conditions, this strongly suggests that the devices tested have a particular sensitivity to polarity. While it had been previously noted in prior works that in contacts with dissimilar materials, there was a definite favorable polarity, and even with Au/Au contact pairs used here this effect was overwhelming with nine out of ten devices failing prematurely.
- Detrimental Circuit Configurations - It has been experimentally verified and published that theoretically detrimental circuit configurations had a profound effect on accelerating device failure. Both parallel capacitance and series inductance or both resulted in six premature failures for the six devices tested under cold-switched, DC loading conditions.
- Beneficial Circuit Configurations - It has been experimentally verified and published that theoretically beneficial circuit configurations resulted in five of the

six devices tested under cold-switched, DC conditions to last to the full 10 million cycles. While this may not be an indication of beneficial behavior, if we then consider the effects of using these configurations in conjunction with AC loading, the benefit is clear. Using identical conditions as above, the addition of this protective circuitry resulted in all eight of the eight devices tested to last the full 10 million cycles.

- Pre-failure Detection - In addition to the objectives from these tests, another interesting characteristic was observed. For the low frequency AC tests, when data from the failed devices was more closely examined, it was observed that immediately prior to failure the shape of the resistance vs. force curve displayed some distinctive irregularities. While initial attempts at mathematically fingerprinting this phenomena have as of yet been unsuccessful, it is likely that a description for this can be mathematically found and may warrant further investigation.

6.3 Recommendations for future research

While several conclusions presented themselves during the course of this research, it was equally apparent that there are many topics which arose that were not possible to pursue as part of this work, but are worth further investigation.

6.3.1 Test Stand.

Overall, the current configuration of the test stand is well suited for operation at 2.5 kHz maximum test frequency, but test setup with this hardware is an extremely delicate operation. This and other minor issues could be addressed with a few improvements. These include:

- Piezo Actuator Upgrades - The single biggest area of improvement lies in the piezo-actuator which drives the force sensor. The current device is an older model, with a theoretical maximum operating frequency of just under 2.5 kHz. A faster version has been obtained which can greatly improve the actuation frequency of the test stand, with a theoretical operating frequency approximately 50x greater. While the physical packaging is a direct replacement, one difference is important to note: a reduction in travel. The current devices have a full 20 μm of travel, and thus setup must be done such that the probe tip at it's full range of travel is less than 20 μm. Faster devices reduce this range by a factor of 2-4, making setup much more precarious. To address this, two other systems would require an improvement, the device alignment camera and the alignment stages.
- Device Alignment Camera - One of the biggest issues with the current stand is the difficulty in determining the relative position of the sensor to the devices during setup. Including smaller, more sensitive cameras would address this issue. These units could be provided with moveable mounts which could attach in a variety of locations, and could easily be integrated into the control system with multiple views. They would require some magnification for optimal effect but minimal magnification would be required and are also currently available for relatively low cost.
- Alignment Stages - Alignment of the sensor to the devices under test is currently accomplished by adjustment of multiple stages which are actuated by hand through positioning rods. This setup makes it extremely easy to destroy test probes as the rods which control stage movement must penetrate the enclosure to allow for adjustment while the system is purged, and tend to stick and cause the stages to jump as the controls break free. Motorized stages designed for

aligning high precision optics are available and have been obtained which would allow for electronic positioning with far greater accuracy, at a much slower and safer rate. These devices are designed to operate in an extremely clean environment and can be controlled using the same electronics which are used to control the rest of the stand (i.e. via a National Instrument electronics rack).

- Device Interconnections - The current device carrier is a socket which receives 72 pin devices carrier to which device reticules have been wire bonded. This socket is wired to a breadboard on the outside of the enclosure to allow for virtually any wiring required. While this is a versatile solution, it is not particularly robust, and should RF devices or devices with other special wiring considerations be required it would have to be addressed. One relatively simple yet effective solution would be to first break the wiring into two sections: the section within the enclosure and the exterior wiring. The interior wiring could use the current sample holders or any similar devices, but would wire to an interchangeable plate which replaces a portion of the back wall of the enclosure. On this plate would be panel mounted electrical connections sockets, which could be individual RF connectors, ribbon cable sockets, etc. The exterior wiring would then be suitable mating cables and hardware which would connect these sockets and exterior test equipment, providing a much more stable and consistent electrical connection critical during long test runs and with more sensitive signals.

6.3.2 Nanosphere Lithography.

While NSL is not the method of choice for this application at this time, with some improvements and further effort it may become as good as if not better than grayscale lithography. To do so however, the next deposition vessel would need to address a few issues. First, it must be able to accommodate a full wafer during deposition.

Additionally, more research would be required to address the concentration variability and unpredictable results it can cause. To address this, a prototype of the next vessel was printed but has not yet been evaluated, and is shown in Figure 62.

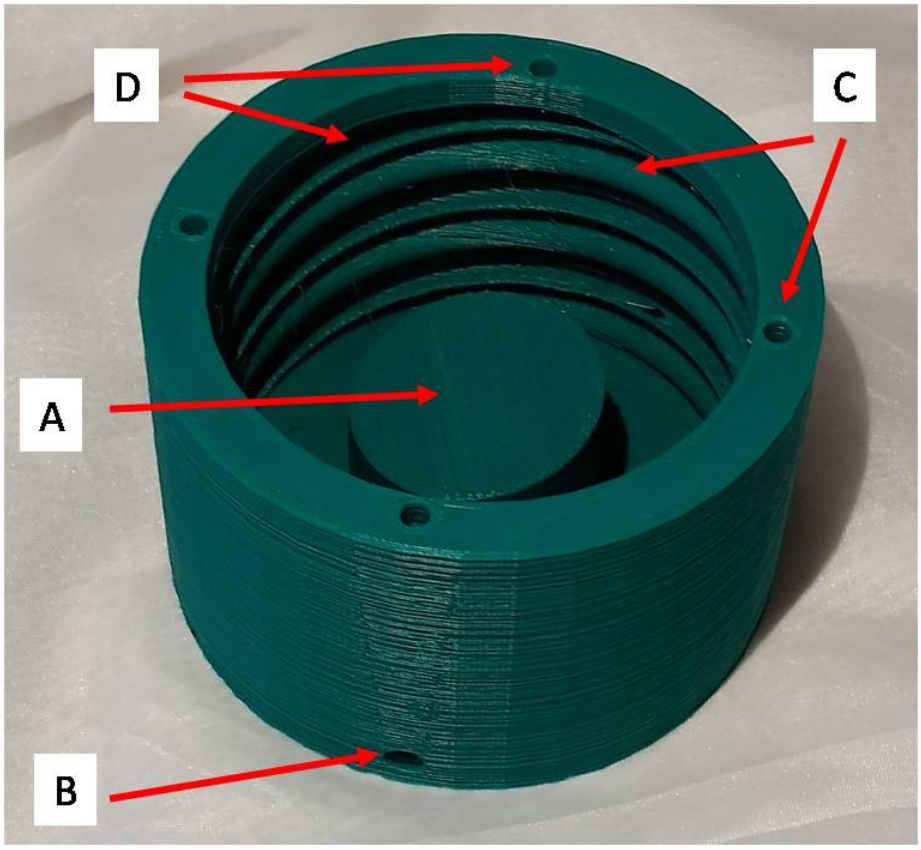

Figure 62. Image of a prototype full wafer vessel for depositon of nanospheres. This includes a replaceable inner pillar (A) for adjustment of angle between the substrate and carrier fluid, a drain port (B) for controlling the removal of carrier fluid, and two pairs of supply ports. The first set (C) are enclosed and supply return fluid to the bottom of the vessel without disrupting the surface, and the second pair (D) are open channels which would allow for nanospheres to be resupplied to the surface during deposion.

By using a vessel such as this with a pair of diastolic pumps, the overall drain rate, the rate of removal of nanospheres, and surface agitation could all be actively controlled. While peristaltic pumps typically operated at a much faster rate than we would desire, we could instead have one pump removing fluid from the bottom of the vessel (item (B) in Figure 62) at one rate, and at a slightly lower rate a second

pump return that fluid to the bottom of the vessel through the covered channels, shown as (C) in Figure 62. The difference between these pumping rates would be the removal rate, and the by increasing or decrease both pumps together we should expect some ability to facilitate mixing of the spheres which may avoid the concentration variations which have been observed. To address the ever decreasing concentration of nanospheres, the second pair of channels (item (D) in Figure 62) could be used with a third pump which resupplies fresh nanospheres directly to the surface. In this case, the drain rate would be the difference between the rate of the drain pump, and the sum of the two pumps returning material to the vessel.

6.3.3 Improved Grayscale Lithography.

As was previously mentioned, the hybrid approach has been able to produce results which are worth further investigation. To attempt the fabrication of micro-contacts however, further improvements could be made. With the current system and results observed, there are two areas which are both worth further experimentation. The first is to repeat the 80nm step size patterning with a wider variety of exposure recipes. Since the edge characteristics of the beam are still not entirely clear, it is possibly that trading power for duty cycle may in fact make better resolved final patterns. In the event that this does not, the second item worth investigating would be to develop and test other patterns with step sizes between 80 to 400 nm to determine what the optimal step size is which balances the quality in the final structures with minimal pitch spacing and final contact area. By further refining the recipe, the impact on the features produced are substantial as shown in Figure 63.

The top two SEM images show two of the recipes which were attempted using the same CAD files. Note that the profile produced by these recipes can change the overall structure. The three sample recipes shown in the bottom of Figure 63

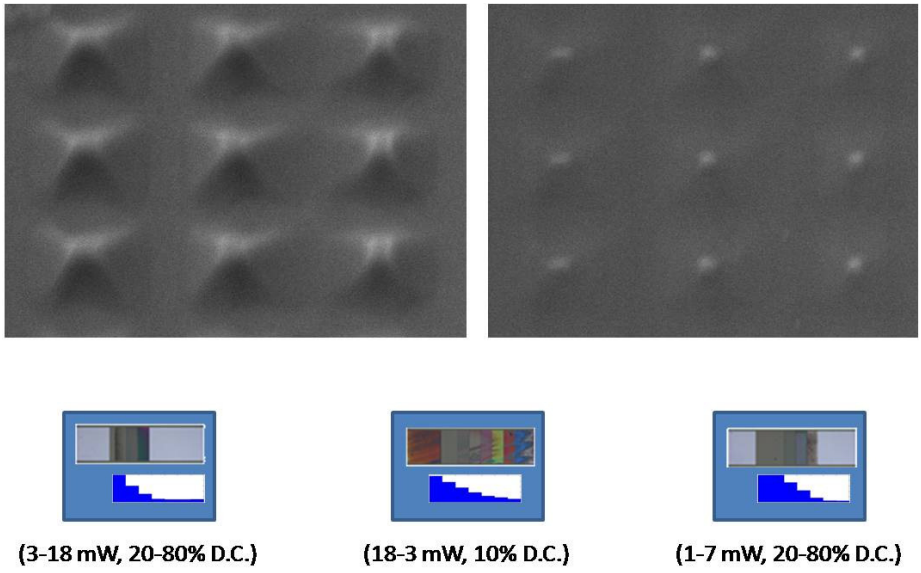

Figure 63. SEM image comparing identicle design files exposed to different recipes (top). By using the exposure study data, and conducting refined recipes and retesting, the side profiles of these 3D structures can be better shaped to any slope desired.

demonstrate that a curved edge, broad and more linear edge, or a sharper edge are all possible just through modification of this recipe.

It is also worth noting that the next generation of these laser lithography systems are currently available. According to the most recent product information, these newer systems are capable of a 1 μm beam width but with patterns which are the full size of the wafer. This eliminates the need for part of the additional automation, but it is not clear that the software that comes with this new system is any more advanced, and therefore the multiple exposure process may still be required for higher resolution grayscale profiles.

6.3.4 Thin-film Spreading Resistance.

The next step in optimizing thin-film spreading resistance models will involve fabrication and testing of the alternate geometry discussed which more closely matches Cartesian geometries rather than circular. These designs and masks have been com-

pleted and fabrication of the first prototypes have been completed as shown in Figure 64.

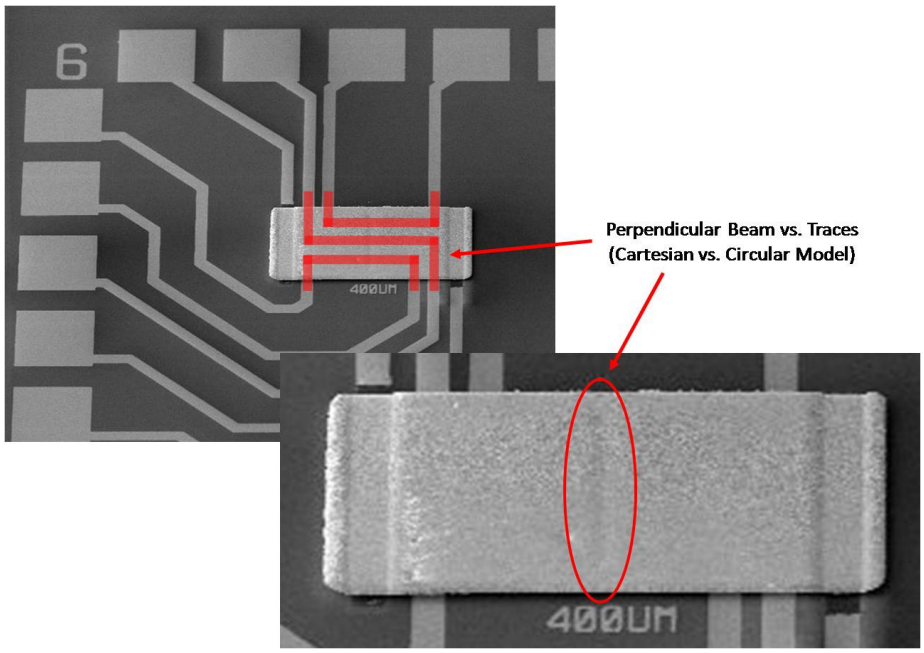

Figure 64. SEM image showing test run of micro-contact with cartesian rather than circular current flow pattern. The elongated bump on the underside of the beam runs perpendicular to the three traces on the lower thin-film contact, providing a much more predictable current geometry.

Once the first working devices are made ready for testing, the models will have to be adjusted not only with the alternate spreading resistance theory, but also to account for the change from a circular contact to a rectangular shape as the existing models are based on an ideal contact radius which will no longer be as easy to approximate with rectangular contacts. This should be able to use a similar approach as in prior publications by applying a scaling factor to relate the two overall test areas, regardless of contact geometry. These can be applied to the models along with the spreading resistance corrections and compared to data collected. Should these match well, then we can safely assume that the variability observed with the radial models was in fact due to non-symmetries with the circular model. If there is a discrepancy

however, we can begin to look more closely at the thin-film thickness as multiple thicknesses should be evaluated during the next round of testing.

6.3.5 External Effects.

Further work in this loading and surrounding circuitry is minimal, however the results do provide some essential guidelines for future designs and applications. Clearly, regardless of how these devices are operated, parallel capacitance should be avoided at any cost. The effectiveness of passive contact protection does also provide a strong argument for the inclusion of these kinds of resistors in future applications. Ideally, if an application can be designed such that these protective circuit configurations can be included permanently, it greatly reduces the odds of damage.

6.3.6 Micro-Contact Failure Prediction.

The peculiar behavior of the contact resistance vs. force during the AC loading tests provided a hint regarding a possible figure of merit which might be developed to aid in predicting failures in the future. This data is shown in Figure 65.

To explore if this phenomena could be used in such a manner, the following steps are recommended:

1. Characterize Cause of Variation

   The variation observed was noticed during low-frequency, low-amplitude AC tests without any external circuits, but was observed in all failures during that test series. The first step would be to go back to the data of other devices which failed prematurely and look for a similar result to determine if it was unique to these tests.

2. Verify stable contact performance

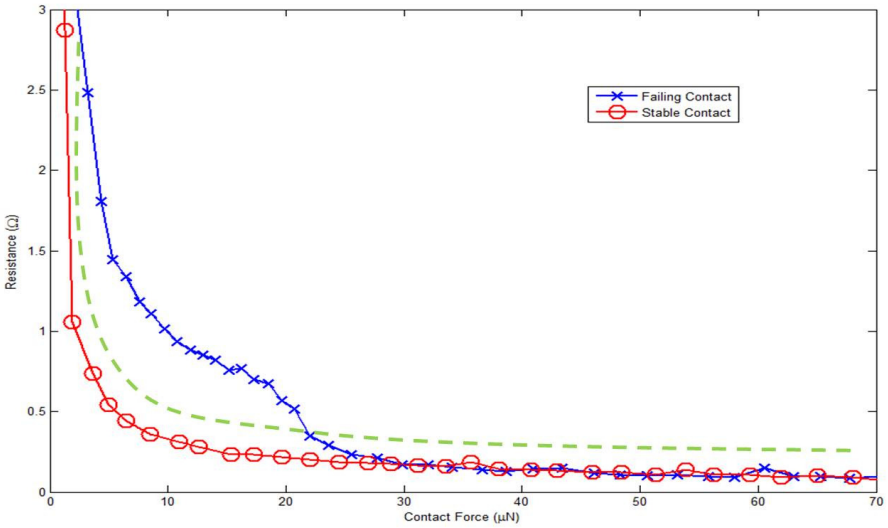

Figure 65. Comparison of the last contact resistance measurements of a stable device at 10 million cycles vs. a failing device. Variations in resistance from cycle to cycle can occur (such as shown by the green line), so a mathematical method of detection must be able to differentiate between the two conditions.

While several stable devices have been observed, gathering similar data on several devices which did not fail would be the next step, to further validate the tie between this behavior and contact failure. Once it is clear that there is a correlation, then the next step would be prudent.

3. Model Identification Scheme

Attempts have been made to differentiate between a few of the failed curves and stable results using a basic χ^2 method, but proved unsuccessful. The first issue with this method is that low contact resistance is often prone to large spikes in which extremely low resistance is observed during semi-ballistic transport, and these spikes can appear to be alarge variation in a χ^2 analysis. The second issue involves shifting in the final contact resistance during a micro-contact's lifetime as shown as the green plot in Figure 65. Stable devices have been observed in which the curve retains a smooth shape, but approaches an entirely

different final value. This also provides an issue in a χ^2 type comparison. It is possible that instead the derivatives of the two be obtained and compared to address the offset, but this approach would likely exaggerate any quasi-ballistic measurements. Confining the observations to higher contact force values along with this mathematical adjustment may be the key to devising a mathematical means of predicting failure, or the application of multiple levels of derivatives. If successful, this could then be used with real time measurement techniques to provide a new level of reliability in future applications provided false-positive predictions could be avoided.

6.3.7 RF Device Testing.

While not mentioned previously, along with other prototype devices, a basic prototype of an RF device was included in these fabrication efforts. This design is based roughly on others found in the literature [2], and included only to demonstrate one possible method in which micro-contacts more suitable for RF applications could be tested with the current hardware.

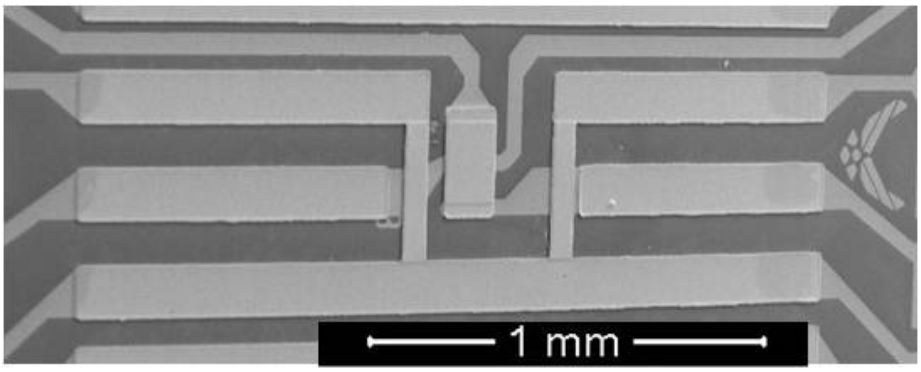

Figure 66. Prototype RF MEMS test structure capable of interfacing with test station, based loosely on design proposed in literature [2].

6.4 Chapter summary

Several conclusions have been drawn from this effort which can contribute to the improved performance and reliability of micro-contacts. The testing of these devices which used the custom build stand discussed has proven extremely successful. A few minor modifications have increased testing efficiency, and a few additional modifications would greatly increase capabilities as well as make test setup more efficient, versatile, and less prone to hardware damage. Methods for fabricating micro-contact surfaces with smaller, more tightly controlled surface areas have been outlined using both NSL and an improved grayscale lithographic method. While NSL provided some encouraging intermediate results, there is still a great deal of work needed before that approach could be used for fabricating wafers of devices. On the other hand, improvements to grayscale lithography have demonstrated results comparable to what NSL could produce, but in a much more reliable process. These results have been fabricated in 1818 photoresist, transferred to nitride, and have retained much of their features. The next step in applying these structures to usable devices is to apply a thin-film of conductive metal to complete the micro-contact surface. Along these lines, improvements in modeling thin-films contact resistance has been experimentally validated. There still remains some variance in some instances, however there are plausible explanations for these variances and further validation efforts continue to eliminate more of the variance that remains. The effect of low-frequency, low-amplitude electrical loading was demonstrated to be highly detrimental to reliability. While these results are interesting, a larger take-away is that these results are indicative of an inherent polarity vulnerability of these devices and an opportunity for further work characterizing this vulnerability. Regardless of the cause of these failures, the application of external circuit components in the proper configuration was proven as extremely effective in mitigating this damage. Additionally, detrimental

circuit configurations proved to also contribute significantly to the premature failure of micro-contacting surfaces, even under DC loads,

Appendix A. Masks layout

The masks generated for this research were based on previous research efforts, but included improvements to address both prior issues from other designs as well as address the requirements for the next stage of testing. The overall mask design for all five layers of the new design are shown in Figure 67.

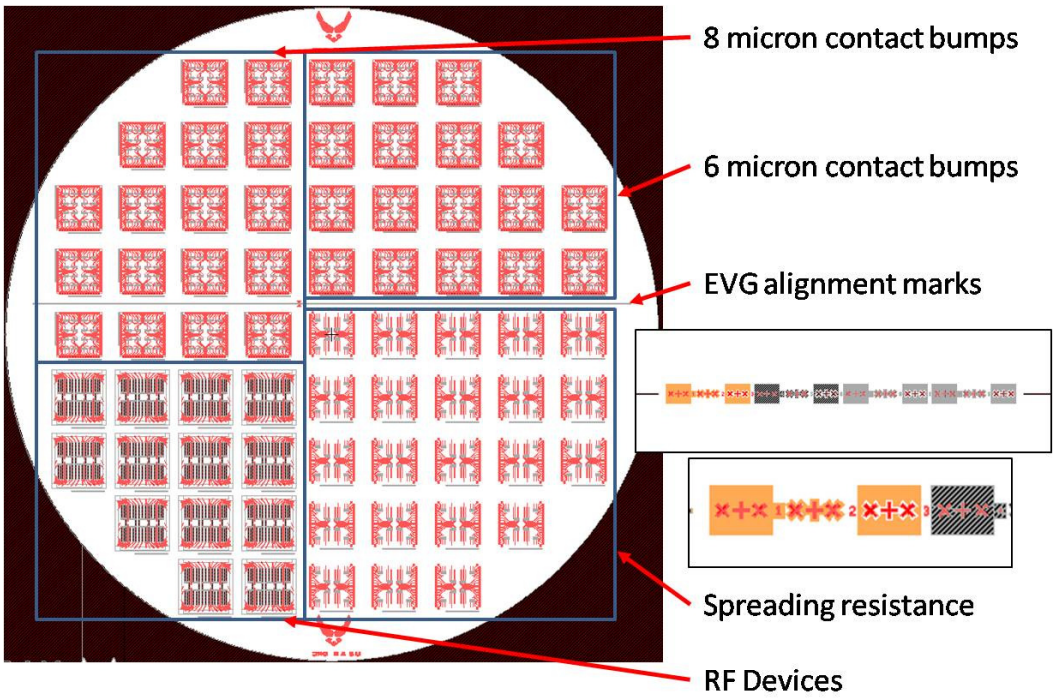

Figure 67. Revised overlay of five layered mask. Designed for use with a dual camera alignment system, this mask includes a single horizontal strip and alignment marks positioned for full wafer processing. Devices are divided in 4 regions. The tops two contain 16 devices per reticle of the standard fixed-fixed beam with 8 or 6 micron contact bumps, the spreading resistance region containing 8 devices per reticle of rectangular contacts and an RF region containing 5 devices per reticle of prototype RF devices.

The layout for these masks was to address all devices of interest for this research. The top two regions are for reticles with 16 devices each, with the upper contact bump radius of either 6 or 8 microns. The lower right corner contains reticles which utilize rectangular contact regions for further testing of spreading resistance. The lower left region contains reticles with 5 RF devices per reticle. Additionally, a single horizontal

bar and alignment marks are present to allow for easy alignment using a dual camera mask aligner (rather than relying on alignment marks within the reticles). Each of these regions will be discussed in more detail.

1.1 Grayscale and NSL Devices

The first set of devices are those in the upper regions. These devices are suited for testing the controlled lower contact regions discussed at length, but depending on which method is used, these masks are utilized differently. First consider if we wish to pattern the lower contacts using NSL. An enlarge image of these reticles and their devices is shown in Figure 68.

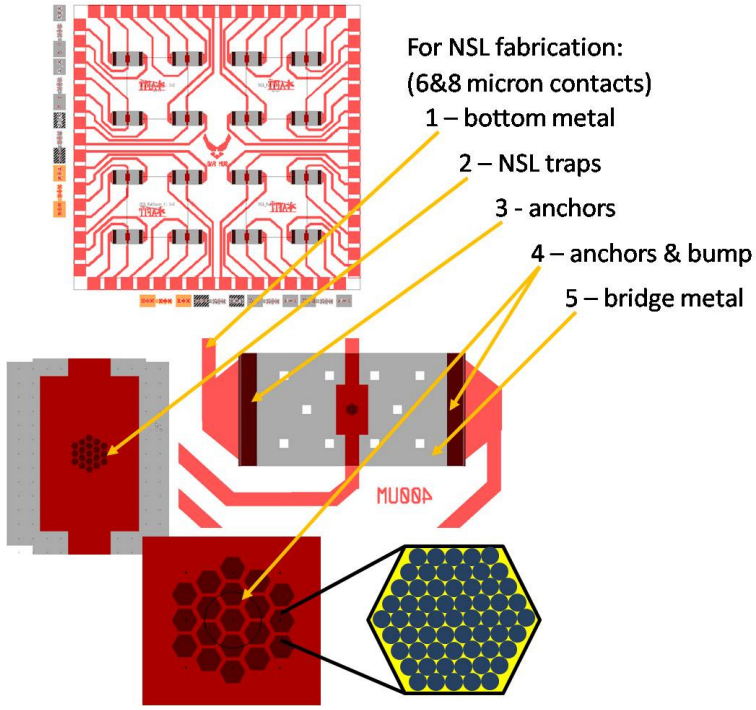

Figure 68. Device mask layouts for standard fixed-fixed beams with hybrid NSL lower contact mask. The five step fabrication processes occur in the numbered sequence indicated. The NSL well patterns produced in step 2 are designed for use with 500nm polystyrene nanospheres.

This is the only design which requires the use of all five masks for fabrication. As explained in the process follower appendix, the starting mask is the bottom metal mask. This is followed by a mask designed to capture nanospheres in selected locations in an attempt to control patterning. The following three masks are based on prior research and contain the anchors only on mask 3, the anchors and contact bumps on mask 4, and upper bridge metal on mask 5.

The same sets of reticles are also used if grayscale patterning is conducted. To accomplish this method of fabrication however, the second mask is not used. Instead, the grayscale patterning occurs prior to the first mask, and include the horizontal alignment marks mentioned so the bottom metal mask can be properly aligned as shown in Figure 69.

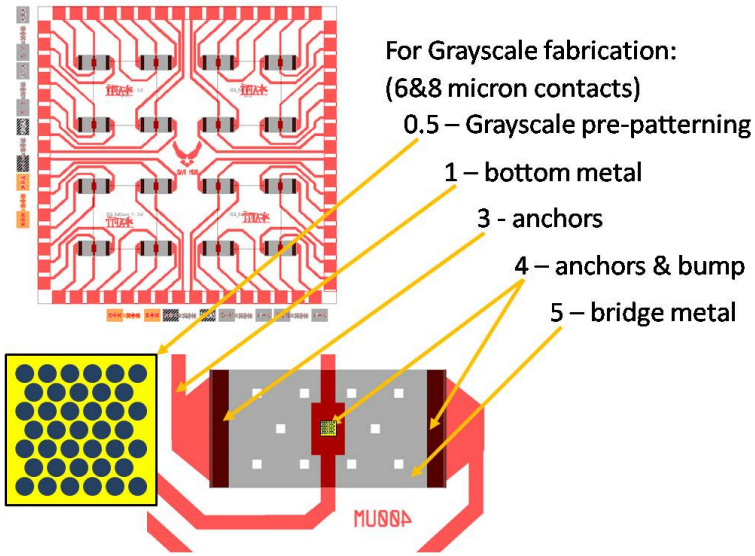

Figure 69. Device mask layouts for standard fixed-fixed beams with grayscale lower contacts. Prior to the four masks used, the lower contact geometry is fabricated using grayscale lithography with a samply pattern shown.

Aside from the absence of the second mask, the fabrication process after the initial grayscale lithography is identical to the previous devices. While Figure 69 shows one possible pattern, several were designed and integrated into files for use with the

grayscale fabrication process. These can be grouped into two general categories based on the step size used between layers (as previously discussed). The first of the pattern sets designed is shown in Figure 70 which utilize 80 nm steps.

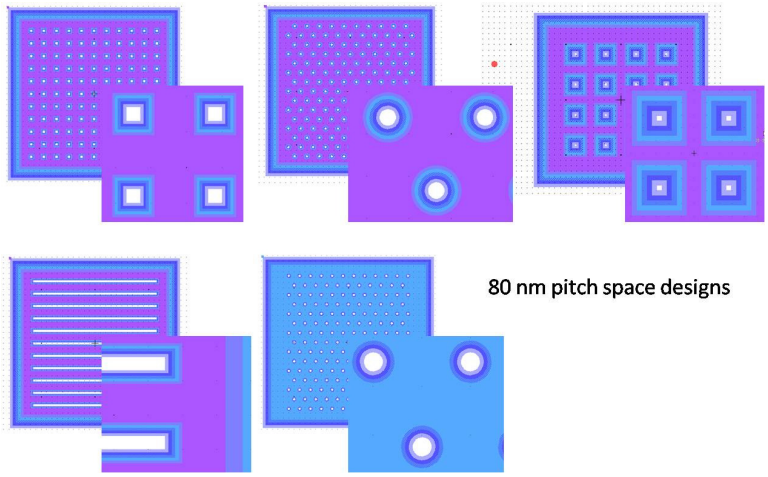

Figure 70. Five lower contact pattern designs which utilize an 80nm step size, one of which using a six step process (upper right), three using a four step process and the last device (bottom right) using a three step process.

The second set of patterns is based on a much lower resolution, using only 400nm step sizes and is shown in Figure 71.

1.2 Spreading Resistance

Devices were also included to accomplish the next phase of testing in spreading resistance validation. Recall previous discussions that circular contacts lack the ability to produce symmetric current patterns, and that rectangular geometries may be better suited. Such devices are included in these masks and are shown in Figure 72. As part of this design concept included the ability to test varying widths of thin-film, each contact has three separate lower traces, which can either be measured individually or in parallel. This design requires that each of these smaller traces has unique contact

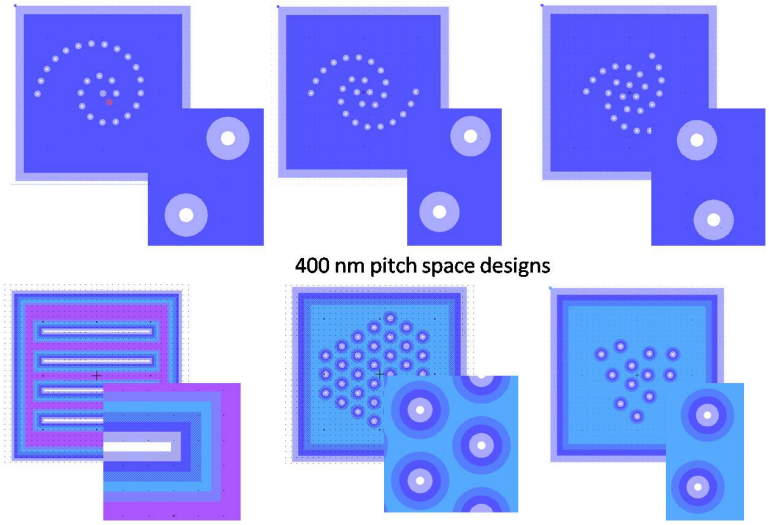

Figure 71. Six lower contact designs utilizing grayscale lithography with a 400nm step size between layers. The upper three use a two step process with incrementally increasing contact points, the lower left uses a six step process with 2D pyramidal structures, and the two lower right utilize four steps with packed circular patterns.

pins, and thus only half the devices are available given the 72 available pins on the sample carrier installed in the test station.

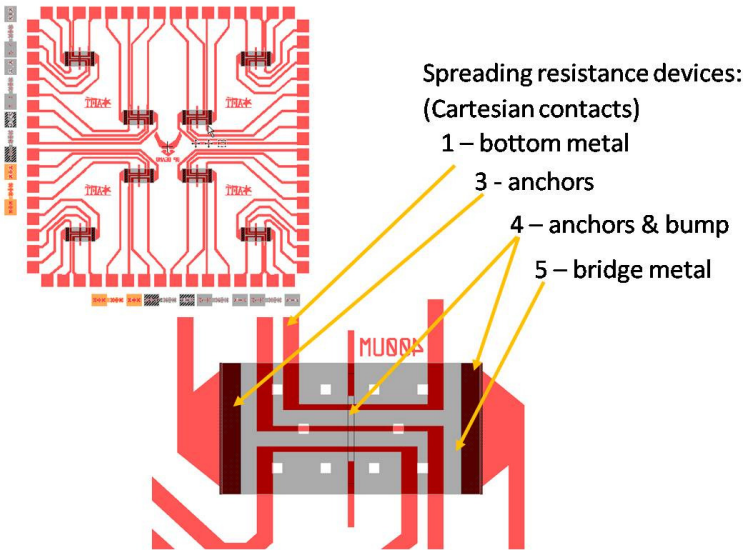

Figure 72. Device mask layouts for modified fixed-fixed beams with rectangular contact geometry. Three multiple lower contacts can be tested individually or in parallel to test the effect of altering the width of the thin film contact as per the model being evaluated.

The center bump normally present has been elongated to product the rectangular cross section, but otherwise these devices are identical to those previously discussed.

1.3 RF Devices

The final section of the revised masks includes several RF device prototypes as shown in Figure 73. The basic design is taken from the literature, but modified to incorporate a compatible contact which will function with the existing test stand.

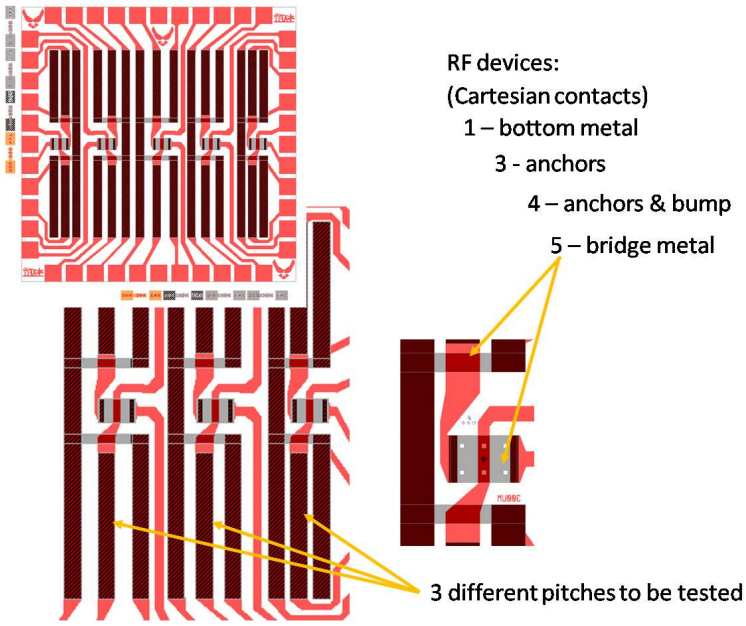

Figure 73. Device mask layouts for prototype RF devices with integrated fixed-fixed contact suitable for test station evaluation.

To accommodate proper scaling and provide adequate grounding, significantly less devices per reticle are available., however three differently spaced devices are present and should initial testing prove promising, the effects of miniaturization can be better characterized.

Note that testing of these devices would also require further test stand modifications to provide proper shielding of incoming and outgoing signals. The device

carrier itself could remain unchanged initially, however this would limit the number of devices to that shown.

Appendix B. Process Followers

The following is a copy of process followers used in this research.

Wafer	Purpose	Masks	Process	Print Date
Wafer ID	**µ-contacts**	***Bottom Metal***	**Bottom Metal**	**8/16/2016**

Init.	Process Step	Notes	Date Time
	INSPECT WAFER: ☐ Note any defects ☐ For grayscale lithography, use wafer with sufficient Si_2N_3 passivation for pattern transferring (>1 µm minimum)	**Start Date** **Start Time**	
	SOLVENT CLEAN WAFER: ☐ 30 sec acetone rinse at 500 rpm ☐ 30 sec methanol rinse at 500 rpm ☐ 30 sec isopropyl alcohol rinse at 500 rpm ☐ 30 sec DI water rinse at 500 rpm ☐ Dry with nitrogen at 500 rpm ☐ Dry wafer with nitrogen on clean texwipes		
	DEHYDRATION BAKE: ☐ 1 min 110°C hot plate bake		
	OPTIONAL - For Grayscale Lithography:		
	1818 COAT: ☐ Flood wafer with 1818 ☐ 4 sec spread at 500 rpm ☐ 30 sec spin at 4,000 rpm, ramp=200 ☐ 75 sec 110°C hot plate bake		
	GRAYSCALE PATTERNING: ☐ Follow grayscale patterning process for patterns required		
	1818 DEVELOP: ☐ 40 sec develop with 351:DI (1:5), use a spin/stop/spin/stop method at 500 rpm ☐ 30 sec DI water rinse at 500 rpm ☐ Dry with nitrogen at 500 rpm ☐ Dry wafer with nitrogen on clean texwipes		
	PATTERN INSPECTION: ☐ Verify patterning and alignment marks are present, fully exposed and clean		
	RIE PATTERN TRANSFER TO NITRIDE LAYER: ☐ Conduct RIE using the following settings: o 60 W plasma power o 350 W ICP power o 150 mT pressure o use O2 / CF4 flow rate ratio of ~.6 for 1.0 selectivity (20:33 SCCM) o Etch rate ~0.3 µm/min		
	CLEAN AND INSPECT: ☐ Inspect for complete etch, expose longer if needed ☐ When satisfactory, clean and dry with acetone/DI water		
	SF-11 RESIST COAT: ☐ Flood wafer with SF-11 ☐ 30 sec spin at 4,000 rpm - Hold swab between wafer and Al foil during spin to capture excess photoresist which spins like 'cotton candy' ☐ 2 min 200°C hot plate bake		
	1818 COAT: ☐ Flood wafer with 1818 ☐ 4 sec spread at 500 rpm ☐ 30 sec spin at 4,000 rpm, ramp=200 ☐ 75 sec 110°C hot plate bake		
	EXPOSE 1805 WITH Bottom Metal MASK #1: ☐ No alignment for first level mask needed, however mask should be straight ☐ 7.0 sec exposure using EVG 620; 7 sec exposure using MJB3		

Init.	Process Step	Notes	Date Time
	1818 DEVELOP: ☐ 40 sec develop with 351:DI (1:5), use a spin/stop/spin/stop method at 500 rpm ☐ 30 sec DI water rinse at 500 rpm ☐ Dry with nitrogen at 500 rpm ☐ Dry wafer with nitrogen on clean texwipes		
	INSPECT RESIST: ☐ Inspect photoresist under microscope, look for fringe patterns indicating residual SF-11		
	SF-11 EXPOSURE (~1.5 um / cycle): ☐ Place wafer in center of circle ☐ 300 sec DUV exposure with OAI DUV		
	SF-11 DEVELOP: ☐ 60 sec develop with SAL 101, use a spin/stop/spin/stop method at 500 rpm ☐ 30 sec DI rinse at 500 RPM or hold under DI faucet for 30 sec ☐ Dry with nitrogen at 500 RPM ☐ Dry wafer with nitrogen on clean texwipes		
	INSPECT RESIST: ☐ Inspect photoresist under microscope		
	TENCOR MEASUREMENT: ☐ Measure metal step height T _____ C _____ B _____		
	ASHER DESCUM ☐ 4 min, 75W, LFE Barrel Asher - Immediately before Evaporation		
	BOTTOM METAL DEPOSITION ☐ *Evaporate* 200 Å Ti / 2800 Å Au		
	LIFT-OFF METAL: ☐ Heat 1165 remover to 90°C (set hot plate to 170°C) ☐ Use packing tape to lift off *evaporated* Au/Ti ☐ 5 min ultrasonic bath in acetone ☐ 30 sec acetone rinse at 500 rpm ☐ 30 sec isopropyl alcohol rinse at 500 rpm ☐ 30 sec DI water rinse at 500 rpm ☐ Dry with nitrogen at 500 rpm ☐ 5 min soak in 1165 at 90º C ☐ 30 sec DI rinse at 500 rpm ☐ Dry wafer with nitrogen on clean texwipes		
	INSPECT METAL: ☐ Inspect metal under microscope		
	ASHER DESCUM ☐ 4 min, 150W, LFE Barrel Asher		
	TENCOR MEASUREMENT: ☐ Measure metal step height T _____ C _____ B _____		
	Electrical Isolation Test: ☐ Verify electrical isolation between contact pads		
	OPTIONAL - For NSL		
	☐ Conduct patterning and deposition process for NSL lower contact patterning as required.		

Wafer	Purpose	Masks	Process	Print Date
Wafer ID	**µ-contacts**	***Bottom Metal***	**Bottom Metal**	**8/16/2016**

Init.	Process Step	Notes	Date Time

Wafer	Purpose	Masks	Process	Print Date
Wafer ID	**µ-contacts**	***Anchor/Bump***	**Anchor & Bump**	**8/16/2016**

Init.	Process Step	Notes	Date Time
	DEHYDRATION BAKE: ☐ 5 min 110°C hot plate bake	**Start Date** **Start Time**	
	FIRST SF-11 (PMGI) COAT: ☐ Flood wafer with SF-11 ☐ 30 sec spin at 4,000 rpm, ramp= 999, 5 sec spread=500 ☐ 2 min 200º C hot plate bake		
	SECOND SF-11 (PMGI) COAT: ☐ Flood wafer with SF-11 ☐ 30 sec spin at 4,000 rpm ☐ 2 min 200º C hot plate bake		
	1818 COAT: ☐ Flood wafer with 1818 ☐ 4 sec spread at 500 rpm ☐ 30 sec spin at 4,000 rpm, ramp=200 ☐ 75 sec 110°C hot plate bake		
	EXPOSE 1818 WITH Anchor MASK #3: ☐ Align to bottom metal alignment marks ☐ 7.0 sec exposure using EVG 620; 7 sec exposure using MJB3		
	1818 DEVELOP: ☐ 40 sec develop with 351:DI (1:5), use a spin/stop/spin/stop method at 500 rpm ☐ 30 sec DI water rinse at 500 rpm ☐ Dry with nitrogen at 500 rpm ☐ Dry wafer with nitrogen on clean texwipes		
	INSPECT RESIST: ☐ Inspect photoresist under microscope		
	FIRST DUV EXPOSURE (~1.5 um / cycle): ☐ Place wafer in center of circle ☐ 200 sec DUV exposure with OAI DUV		
	SF-11 DEVELOP: ☐ 60 sec develop with SAL 101, use a spin/stop/spin/stop method at 500 rpm ☐ 30 sec DI rinse at 500 RPM ☐ Dry with nitrogen at 500 RPM ☐ Dry wafer with nitrogen on clean texwipes		
	INSPECT RESIST: ☐ Inspect photoresist under microscope, look for fringe patters indicating residual SF-11		
	SECOND DUV EXPOSURE (~1.5 um / cycle): ☐ Place wafer in center of circle ☐ 200 sec DUV exposure with OAI DUV		
	SF-11 DEVELOP: ☐ 60 sec develop with SAL 101, use a spin/stop/spin/stop method at 500 rpm ☐ 30 sec DI rinse at 500 RPM ☐ Dry with nitrogen at 500 RPM ☐ Dry wafer with nitrogen on clean texwipes		
	INSPECT RESIST: ☐ Inspect photoresist under microscope, look for fringe patters indicating residual SF-11		
	TENCOR MEASUREMENT: ☐ Measure metal step height T _____ C _____ B _____		

Init.	Process Step	Notes	Date Time
	REMOVE 1818: ☐ ~12 sec acetone rinse at 500 rpm *As Needed* ☐ 30 sec isopropyl alcohol rinse at 500 rpm ☐ 30 sec DI rinse at 500 rpm ☐ Dry with nitrogen at 500 rpm ☐ Dry wafer with nitrogen on clean texwipes	When using Acetone, the 1818 in the center of wafer will open up, immediately apply IPA to center and concurrently use acetone to remove remaining 1818 (do not dry until removal is complete)	
	INSPECT RESIST: ☐ Inspect photoresist under microscope		
	TENCOR MEASUREMENT: ☐ Measure metal step height T _____ C _____ B _____		
	1818 COAT: ☐ Flood wafer with 1818 ☐ 4 sec spread at 500 rpm ☐ 30 sec spin at 4,000 rpm, ramp=200 ☐ 75 sec 110°C hot plate bake		
	EXPOSE 1818 WITH Contact Bump MASK #4: ☐ Align to bottom metal alignment marks ☐ 7 sec exposure using EVG 620; 7 sec exposure using MJB3		
	1818 DEVELOP: ☐ 40 sec develop with 351:DI (1:5), use a spin/stop/spin/stop method at 500 rpm ☐ 30 sec DI water rinse at 500 rpm ☐ Dry with nitrogen at 500 rpm ☐ Dry wafer with nitrogen on clean texwipes		
	INSPECT RESIST: ☐ Inspect photoresist under microscope		
	TENCOR MEASUREMENT: ☐ Measure metal step height T _____ C _____ B _____		
	PARTIAL DUV EXPOSURE (~0.7um BUMP DEPTH): ☐ 60 sec DUV exposure @ 35 mW/cm² , 254 nm		
	SF-11 DEVELOP: ☐ 60 sec develop with SAL 101, use a spin/stop/spin/stop method at 500 rpm ☐ 30 sec DI rinse at 500 RPM ☐ Dry with nitrogen at 500 RPM ☐ Dry wafer with nitrogen on clean texwipes		
	INSPECT RESIST: ☐ Inspect photoresist under microscope		
	TENCOR MEASUREMENT: ☐ Measure metal step height T _____ C _____ B _____		

Init.	Process Step	Notes	Date Time
	REMOVE 1818: ☐ ~12 sec acetone rinse at 500 rpm *As Needed* ☐ 30 sec isopropyl alcohol rinse at 500 rpm ☐ 30 sec DI rinse at 500 rpm ☐ Dry with nitrogen at 500 rpm ☐ Dry wafer with nitrogen on clean texwipes	When using Acetone, the 1818 in the center of wafer will open up, immediately apply IPA to center and concurrently use acetone to remove remaining 1818 (do not dry until removal is complete)	
	INSPECT RESIST: ☐ Inspect photoresist under microscope		
	TENCOR MEASUREMENT: ☐ Measure metal step height T _____ C _____ B _____		
	ASHER DESCUM ☐ 8 min, 75W, LFE Barrel Asher		
	TENCOR MEASUREMENT: ☐ Measure metal step height T _____ C _____ B _____		
	ANCHOR AND BUMP REFLOW & INSPECT WAFER: ☐ 7 sec 270ºC hot plate bake		
	TENCOR MEASUREMENT: ☐ Measure metal step height T _____ C _____ B _____		

Wafer	Purpose	Masks	Process	Print Date
Wafer ID	**µ-contacts**	***Bridge Metal***	**Bridge Metal & Release**	**8/16/2016**

Init.	Process Step	Notes	Date Time
	ASHER DESCUM: ☐ 4 min, 75W, LFE Barrel Asher	**Start Date** **Start Time**	
	SPUTTER CONTACT METAL LAYER: ☐ Sputter bottom contact metal (optional) ☐ Sputter 2000 Å Au using Discovery-18		
	AZ3350 COAT: ☐ Flood wafer with AZ3350 ☐ 4 sec spread at 300 rpm ☐ 30 sec spin at 3,000 rpm, ramp=500 ☐ 5 min 110°C hot plate bake		
	EXPOSE AZ3350 WITH Bridge Metal MASK: ☐ Align to bottom metal alignment marks ☐ 7 sec exposure using EVG 620;		
	AZ3350 DEVELOP: ☐ 60 sec develop with 300MIF, use a spin/stop/spin/stop method at 500 rpm ☐ 30 sec DI water rinse at 500 rpm ☐ Dry with nitrogen at 500 rpm ☐ Dry wafer with nitrogen on clean texwipes		
	INSPECT RESIST: ☐ Inspect photoresist under microscope		
	TENCOR MEASUREMENT: ☐ Measure metal step height T _____ C _____ B _____		
	SOLVENT BAKE: ☐ Bake in 110ºC oven for 20 min		
	ASHER DESCUM ☐ 4 min, 75W, LFE Barrel Asher		
	PREPARE AU ELECTROPLATING BATH (EPB) (AFRL PROCESS): □ Open blue N2 valve on top-left side of the EPB. □ Open DI water valve on bottom-left side of the EPB. □ Main Power "ON", Turn "ON" pump, Turn "ON" hold □ Turn "ON" power switch below EPB computer Wait until temperature is ~58.5C	If "LL" alarm sounds, check EPB water level. Use DI water gun and fill EPB tank until the bottom of the sensor is visibly in the water.	
	Au BRIDGE PLATING: □ Target deposition depth of 2.3 microns Settings for one 2W 4" wafer: • Duty Cycle 40/60 • Bath Temp 58.5C • Constant current density: 2.0 mA/cm^2 • Rule of thumb: plate ~1.2um every 10min need ~6um; so approx ~50min total plating Calculate mA, amp-min For **One WAFERS** □ mA = 2.0 mA/cm^2 x area: **24.08 mA for GAN 2W** amp-min=A x 60 min: **1.444 amp-min for GAN 2W** Calculate mA, amp-min For **TWO WAFERS** □ mA = 2.0 mA/cm^2 x area: **48.16 mA for GAN 2W** amp-min=A x 60 min: **2.888 amp-min for GAN 2W**	**Area for 4" wafer is 12.04cm^2**	

Wafer	Purpose	Masks	Process	Print Date
Wafer ID	**µ-contacts**	***Bridge Metal***	**Bridge Metal & Release**	**8/16/2016**

Init.	Process Step	Notes	Date Time
	TENCOR MEASUREMENT: ☐ Measure metal step height T _____ C _____ B _____		
	REMOVE AZ3350: ☐ 30 sec acetone rinse at 500 rpm ☐ 30 sec isopropyl alcohol rinse at 500 rpm ☐ 30 sec DI water rinse at 500 rpm ☐ Dry with nitrogen at 500 rpm ☐ Dry wafer with nitrogen on clean texwipes		
	ASHER DESCUM ☐ 2 min, 75W, LFE Barrel Asher		
	CONTACT METAL ETCH: ☐ 40 sec Au Etchant, agitated ☐ 30 sec DI water rinse (stops the etching) ☐ Dry with nitrogen on clean texwipes		
	INSPECT CONTACT METAL: ☐ Make sure contact metal layer is completely removed		
	ASHER DESCUM: ☐ 5 min, 150W, LFE Barrel Asher		
	STRIP SF-11 SACRIFICIAL LAYER (RELEASE PROCESS): ☐ Do NOT place devices in ultrasonic bath ☐ Place devices in 1165 at room temperature ☐ Heat 1165 remover to 90ºC (set hot plate to 120ºC) ☐ 35 min soak in 1165 at 90ºC ☐ Wet transfer from 1165 beaker to 1st IPA in petri dish, 30 sec soak ☐ Wet transfer to 2nd IPA in petri dish, 30 sec soak ☐ Wet transfer to 3rd IPA in petri dish, 30 sec soak ☐ Wet transfer to 4th IPA in petri dish, 30 sec soak ☐ Wet transfer to 1st methanol in petri dish, 30 sec soak ☐ Wet transfer to 2nd methanol in petri dish, 30 sec soak ☐ Wet transfer to 3rd methanol in petri dish, 30 sec soak ☐ Wet transfer to 4th methanol in petri dish, 30 sec soak ☐ Fill CO2 dryer chamber with enough methanol to cover the wafer ☐ Remove wafer from 4th methanol dish and place in CO2 dryer chamber ☐ Immediately cover CO2 dryer and start process		
	ASHER DESCUM ☐ 15-30 min, 75W, LFE Barrel Asher		

Appendix C. Visual Bibliography

The next section shows several visual bibliographies, or pictorial representation of related works citing previous research. These are presented chronologically from top to bottom. First, we show a breakdown of some of the work that's been done specifically in the area of quantized conduction research which applies to micro-contacts.

The second we show a visual representation of the current state of research conducted in the use of induced ballistic electron transport through the use of metamaterials:

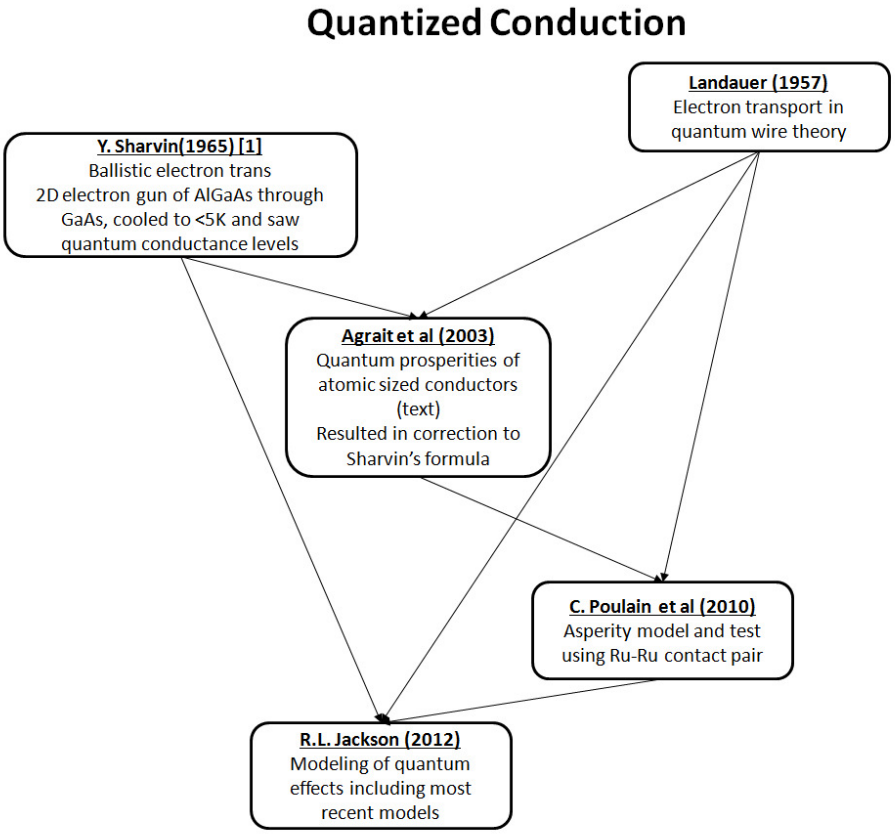

Figure 74. Chronology of the study of quantum conduction research highlights as applicable to micro-contact theory.

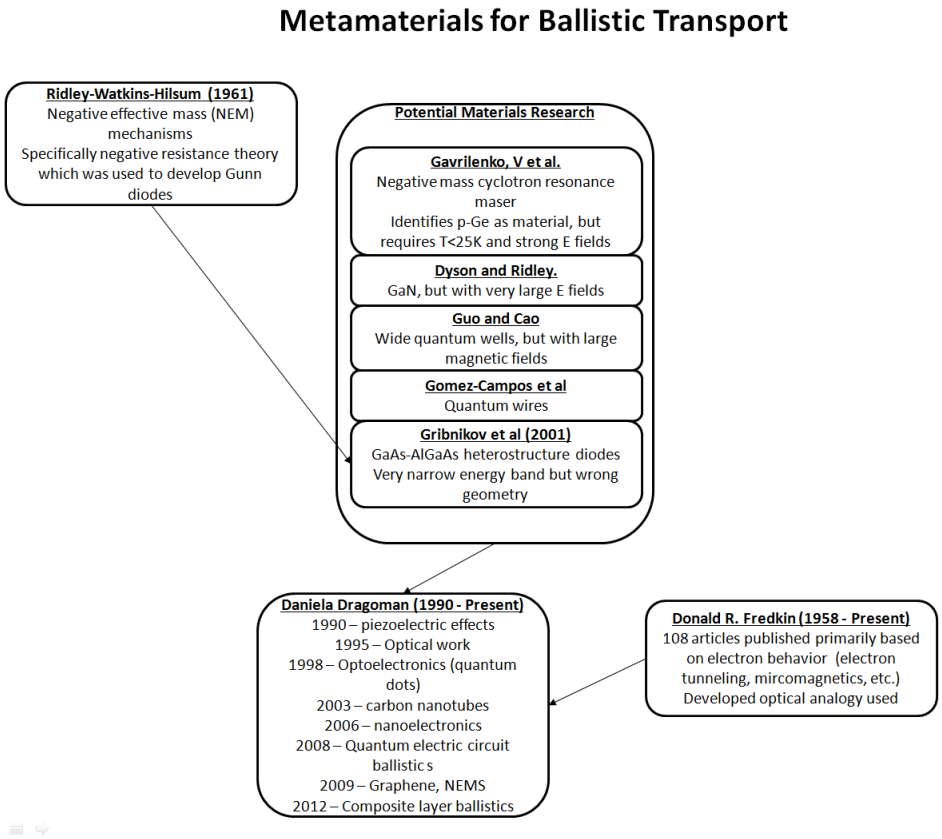

Figure 75. Chronology of the study of composite metamaterials research and related materials highlights as applicable to micro-contact theory.

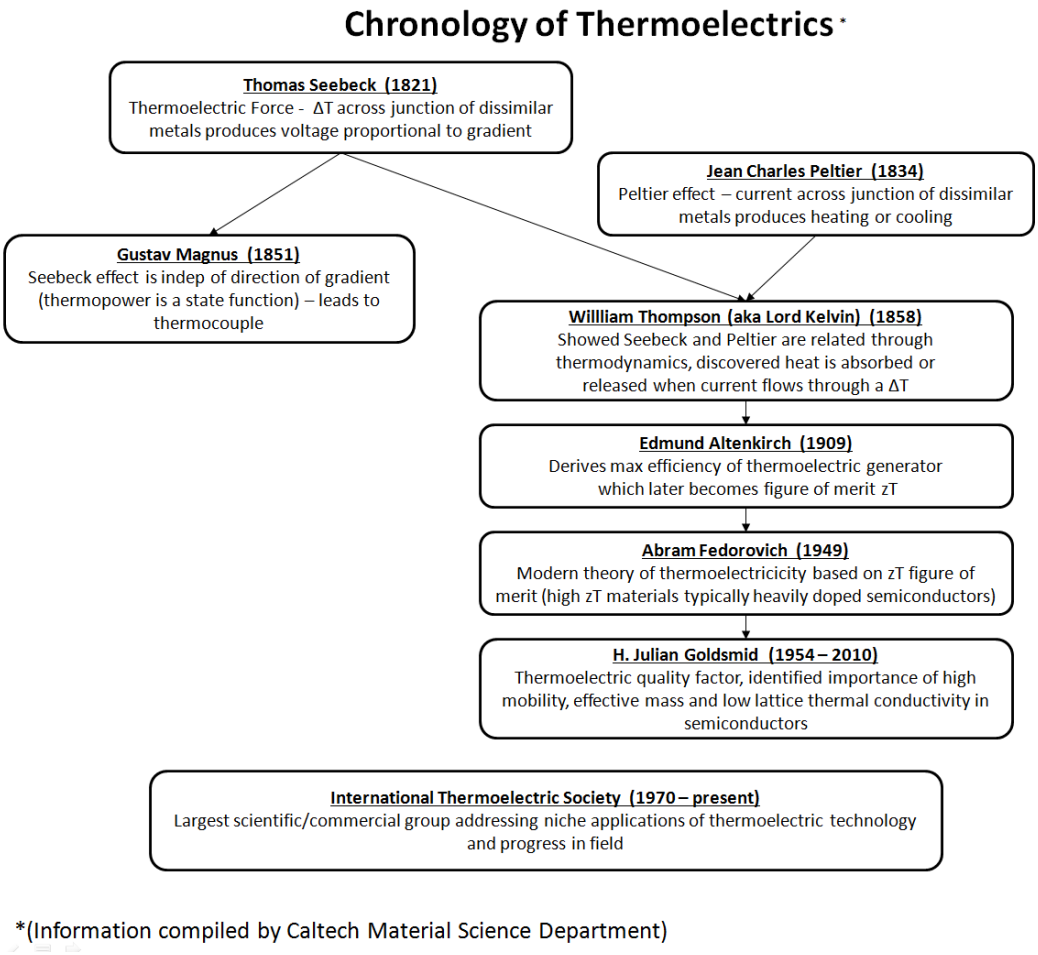

Figure 76. Chronology of thermoelectric research.

Next is some of the work relating to micro-contact research in the area of thermoelectrics.

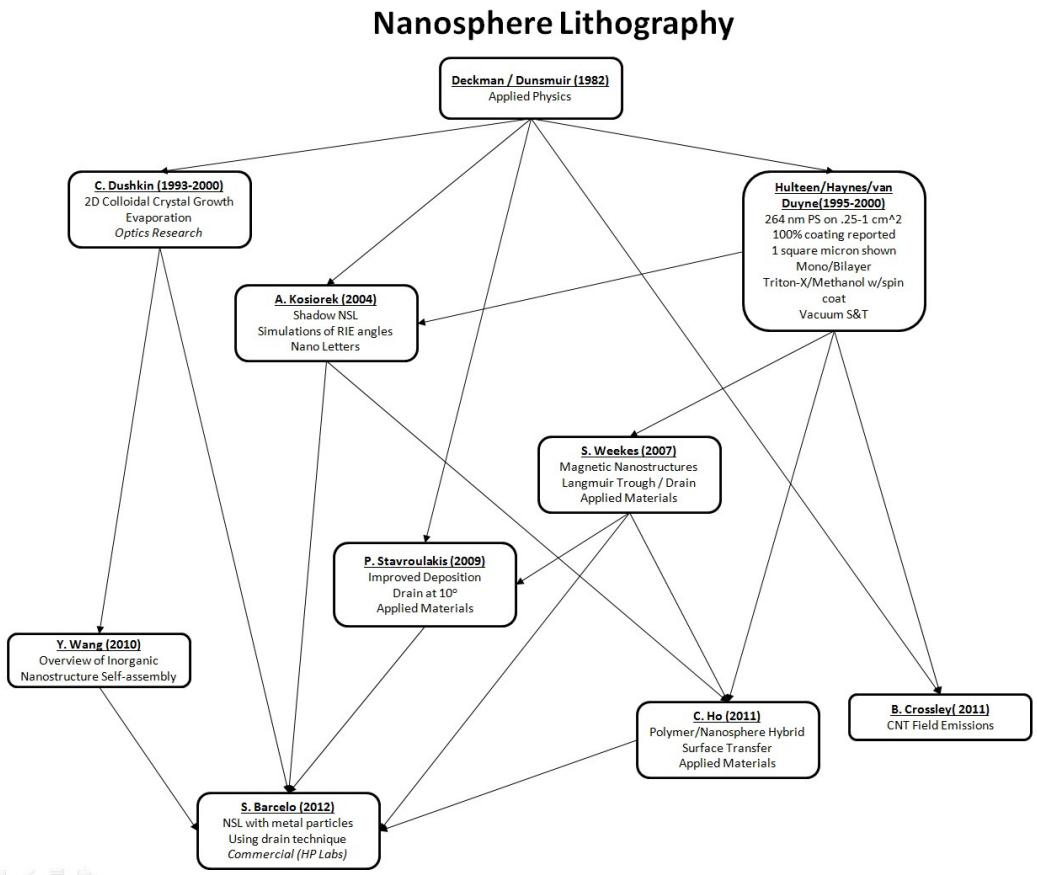

Figure 77. Chronology of nanosphere lithography research.

The fourth section of our visual bibliography illustrates some highlights in NSL research over the past several decades.

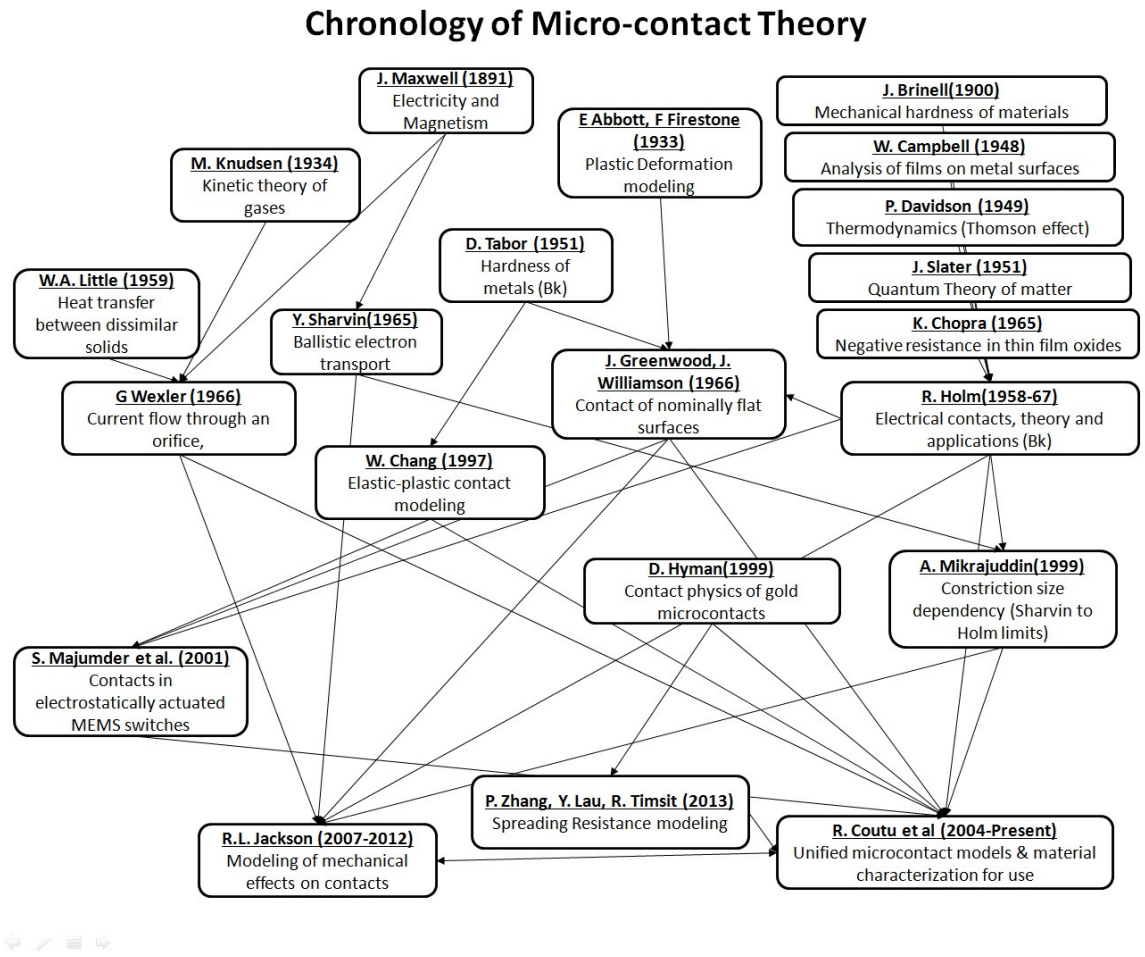

Figure 78. Chronology of mechanical effects contributing to micro contact resistance modeling.

Finally, we present a similar visual bibliography showing research in both macro and micro switches.

Appendix D. Labview Modifications

The following is a copy of the labview modifications described in this document. The first section outlines a number of changes that were made to the organization of the existing controls. The UI was divided into four functional groups and like controls grouped together for better organization and ease of operation.

4.1 Organizational Changes

The setup screen is the first of these groups, and is shown in Figure 79. This section is accessed through the tab controls at the top (A). Data is saved to the folder specified at top of this screen (B). The most significant change to the software overall is in section (C), where the controls have been modified regarding how to determine the number of cycles between test point. The original controls are still present (D), which simply allows for regular interval based testing based on the three parameters shown: number of cycles to test, cycles between test point, and frequency of actuation.

Alternate control of these settings was added which improved controllability in a number of ways, principally in allowing for the number of cycles between test point to increase by a factor of 10 for each subsequent decade. The inner working of this function block will be discussed later, however this addition allows for a single device to be tested until failure with a single run, where the original controls required the test stand controls to be modified every decade by the user until completion.

The remaining controls are again simply reorganized, grouping the initial approach parameters (E), the initial contact test settings (F), and the key parameter readouts critical during testing (G). All of these are still present and available but grouped in a more orderly fashion.

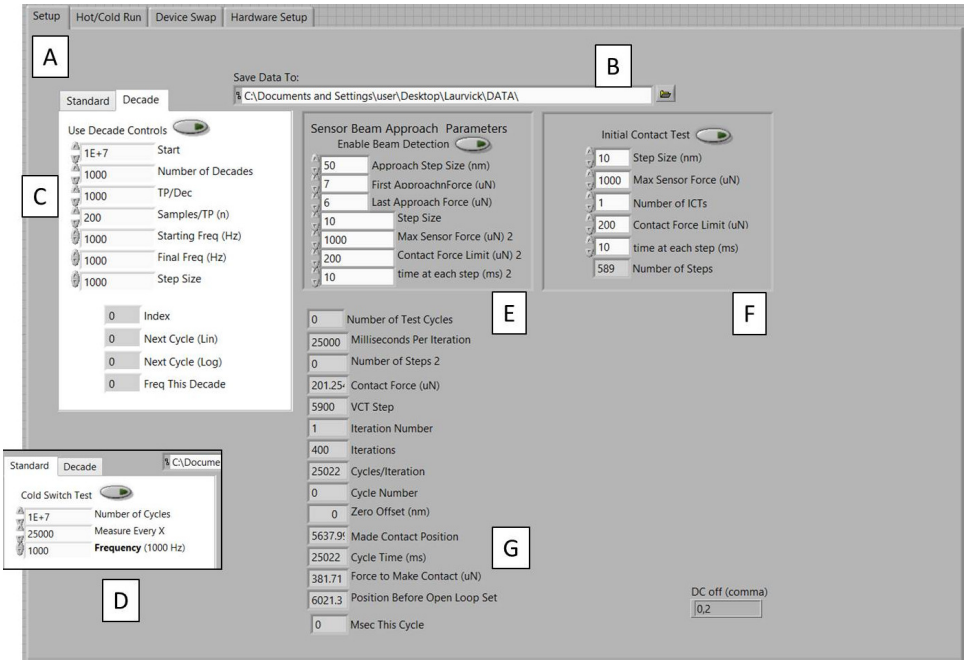

Figure 79. The setup tab of the revised test stand controls. This is accessed through the setup tab (A), and contains the input for the location of the folder in which to store data (B), the newly implimented decade controls (C), the original linearly spaced controls (D), approach parameters (E), the initial contact test settings (F), and the key parameter readouts critical during testing (G).

The next tab contains the controls critical during the actual execution of the test, shown in Figure 80. This screen now contains the start and stop buttons (A), the indicator lights which update during each cycle of test and show exactly what stage testing is in during execution (B), realtime chart strips for the force, resistance, voltage, and current measured (C), the piezo actuator controls (D), and readings from the last test run (E).

The third tab currently contains only a single element as shown in Figure 81. This space is reserved for all the critical controls to be displayed when switching from device to device on the same reticle or switching to a new reticle. The current system of operation requires this interface to be closed so that a number of stand alone pieces of software can run the system in the correct configuration. Currently the force sensor has been integrated to support this feature but future revisions will include controls

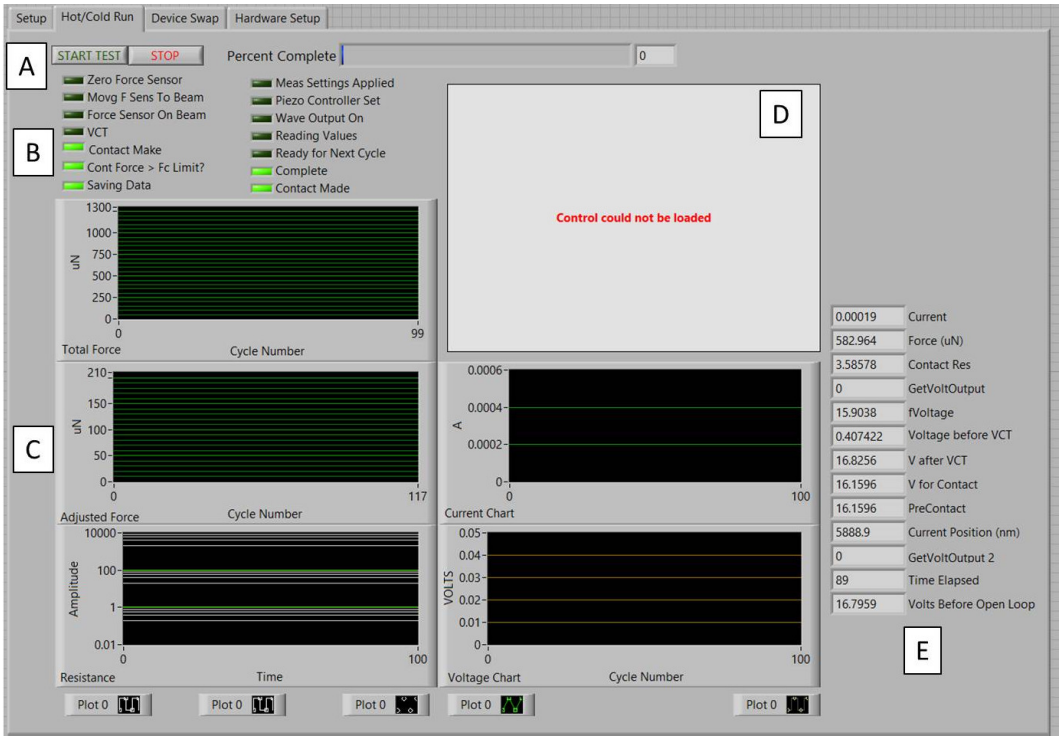

Figure 80. The run screen is accessed through the "Hot/Cold Run" tab located at the top. The start/stop controls are on this screen (A), along with the status indicator lights (B), the chart strips for key test parameters (C), the piezo actuator control software (D), and key process parameters of interest during test (E).

which show the multimeter-mode display for the voltage and current, piezo controls, and camera displays for future test station revisions. When motorized stage controls are implemented, this is the point of the testing process in which they will need to be accessed, and this is the screen on which they will be added.

The fourth screen is accessed through the hardware tab, and is intended to contain all the controls pertaining to the hardware itself as shown in Figure 82. The top section (A) contains the controls which are required to switch to different channels on the current devices to maintain functionality in the event of a partial hardware failure, and the bottom section (B) contains the controls need to change functionality (such as the signal generator output form, phase, biases, etc.)

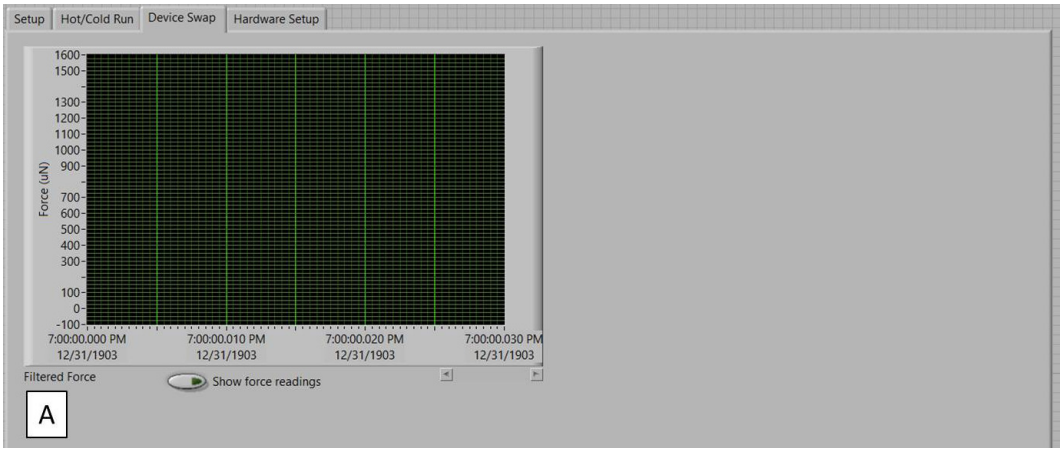

Figure 81. The device swap screen is accessed through the third tab in the user interface. This screen currently contains the force sensor controls (A), but has reserved space for other controls and instrumentation critical during swapping devices between tests.

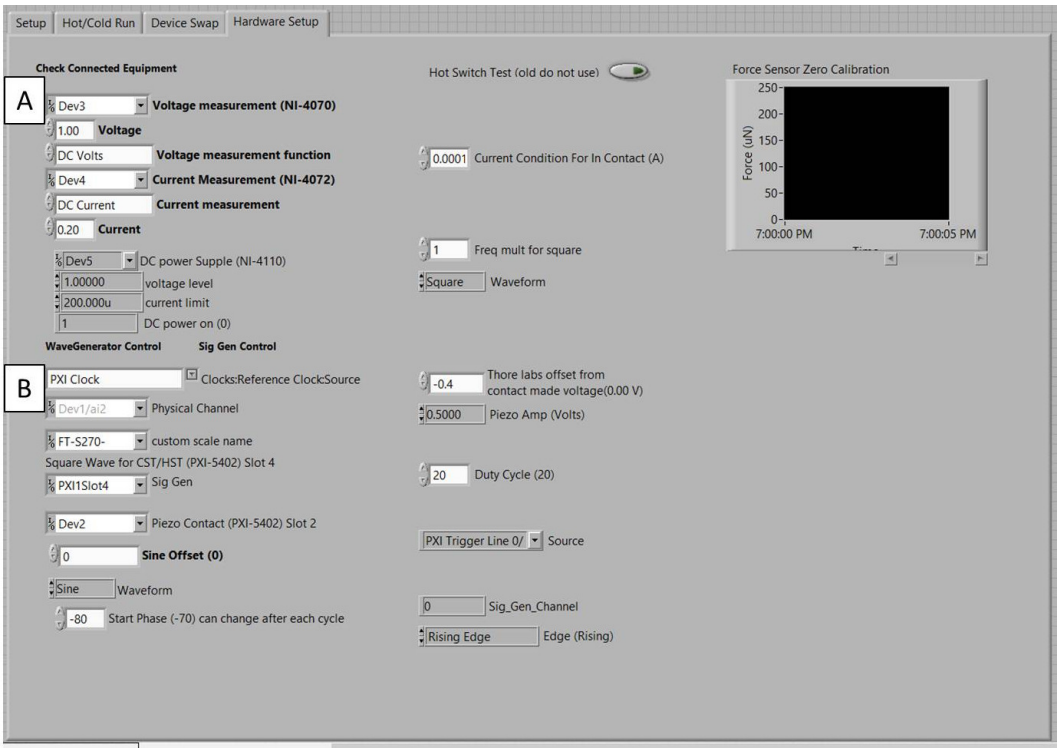

Figure 82. The hardware screen containing all hardware related control interfaces. These include both the configuration parameters of all the hardware blocks (A), as well as the functional paremeter blocks (B) .

4.2 Decade Controls

While the code for controlling the test station remained relatively unchanged from previous efforts, the previously mentioned change to testing frequency was implemented. To accomplish this, a subUI was developed (which will be discussed in detail) which takes key parameters as inputs from the operator and from those parameters, builds a test matrix. Key points in the code then check to see which mode is being executed, and either the values from the original mode of operation (i.e. constant step change) or the appropriate values from this new test matrix are used.

To execute this successfully, three areas of the code need to be modified. The first is shown in Figure 83. Here the software needs to determine the total number of test/cycle iterations, and that value is fed into the variable called 'Number of Test Cycles.' The calculated value for this parameter will match the number of lines in the test matrix, and both this number and the matrix itself are fed forward in the code. However, depending on the mode of operation a check later in the code will decide with count to use.

The second point at which the code is modified is immediately upon entering the test/cycle for...loop as shown in Figure 84. At this point, the index of the loop extracts the appropriate line from the test matrix and stores both the number of cycles between the last test and the next test, as well as the frequency for this cycle stage. Note that the matrix actually contains this test point per decade value calculated in two different ways (with the distribution evenly spaced linearly or logarithmically), which will be described in more detail when the subroutine is discussed. As shown, the only value used is the one which evenly spaces the test points on a log plot, and the linearly spaced values are not currently used, but available.

The third location in which the code requires modification is the immediately prior to conducting device cycling. Under the old method of operation, the duration

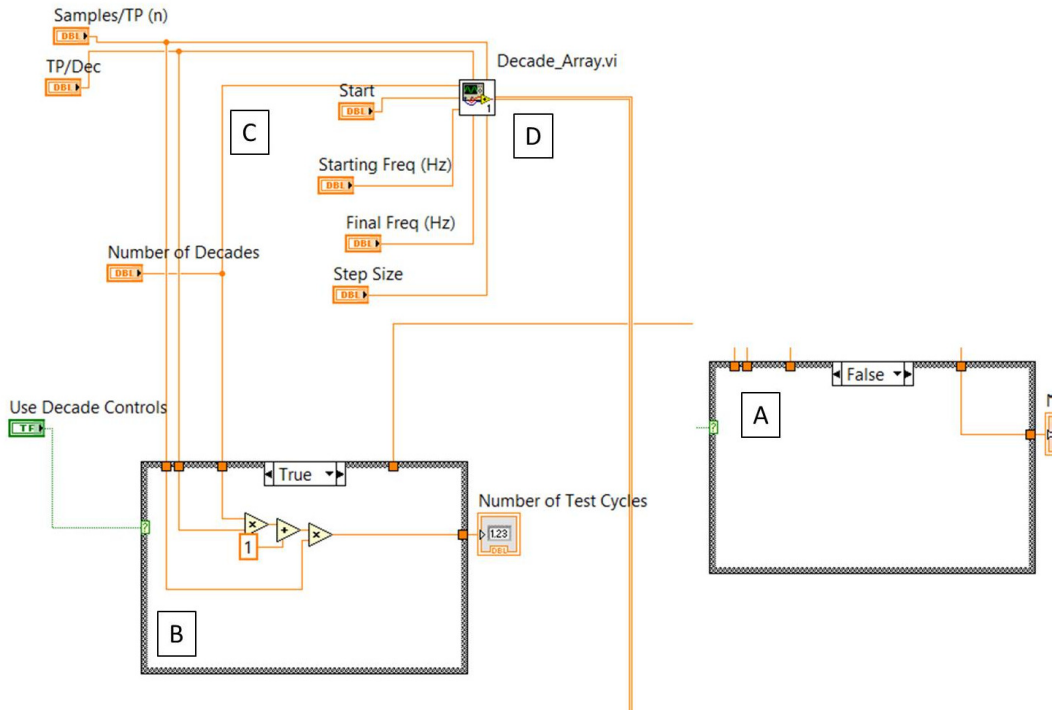

Figure 83. Labview code showing both the connectivity between the new user interfaces, the decade array generation block, and the selection software to switch between the two options during run time.

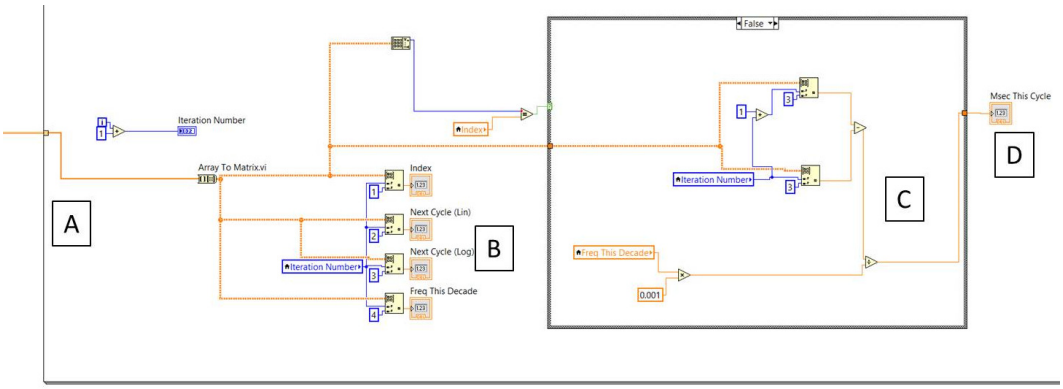

Figure 84. The code which illustrates the extraction of the appropriate line of the test matrix based on which step of testing is currently occuring.

and frequency of the cycling process were from fixed values. Now the same check is conducted to see if the new method of operation is being performed and if so those values are updated dynamically as shown in Figure 85.

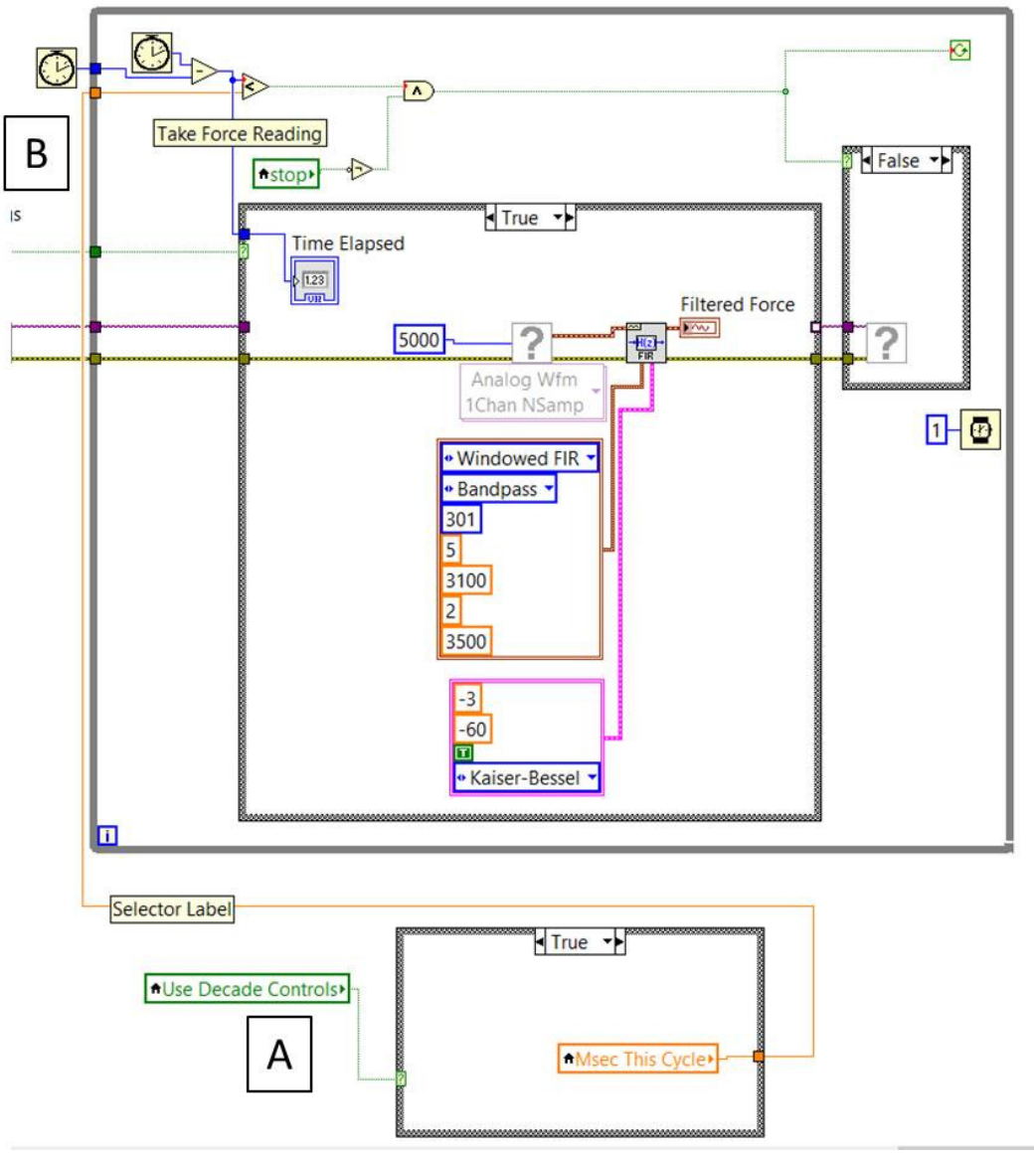

Figure 85. The code which illustrates the decision block based on mode of operation, and the passing of the appropriate duration of cycling to be conducted for that stage of testing.

4.3 Decade UI Development

The functional block which was written to generate the test matrix described is shown in Figure 86, along with some results from a sample calculation to better illustrate how this block functions.

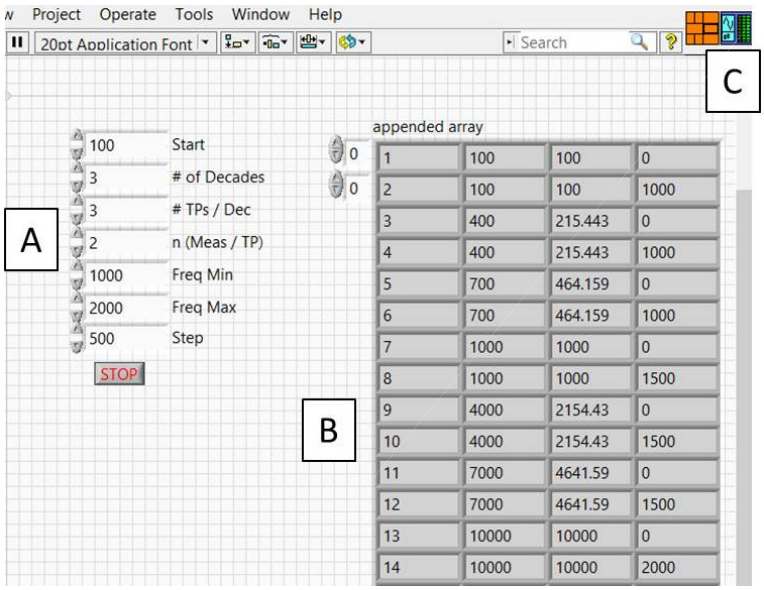

Figure 86. Input controls (A), sample calculations (B) and the UI icon (C) for implementing the custom written decade testing block of logic.

As shown, the routine has the seven inputs shown and generates a matrix described by those values. In the case shown in Figure 86, the test is to start with 100 cycles already imposed on the device, and is to proceed over three decades (i.e. until 100,000 cycles are reached). Three test points per decade are to be taken, and each is to be repeated twice (n=2).

As previously mentioned, the term "test points per division' can be calculated in two different ways. Either the divisions are linearly spaced, resulting in the values in the second column, or logarithmically spaced which would result in the values in the third column. The first method is more evenly distributed from a test standpoint, however the second are much easier to read when plotted on a log scale, particularly when a large number of test points are collected.

The final three parameters specify that the cycling frequency should start at 1 kHz, increase each decade by 500 Hz until a test frequency of 2 kHz is reached. Thus, the third column shows the frequency which should be used after that test cycle. Note that since we are taking data in pairs, every other value for the frequency is

zero. When the main program uses this value, the actual duration of cycling becomes zero, which ensures the next test is actually just the next cycle, and induces no wear (which accomplishes the 2 measurements for test point criteria). Using this test matrix approach also corrects another bug in the original software and ensures that test points are taken at the beginning and the end of the test. Prior controls didn't take the final test point unless the operator remembered to do so manually.

The code which generates this matrix is simply a series of nested loops, which mathematically steps through the input parameters, building the matrix as it executes as shown in Figure 87.

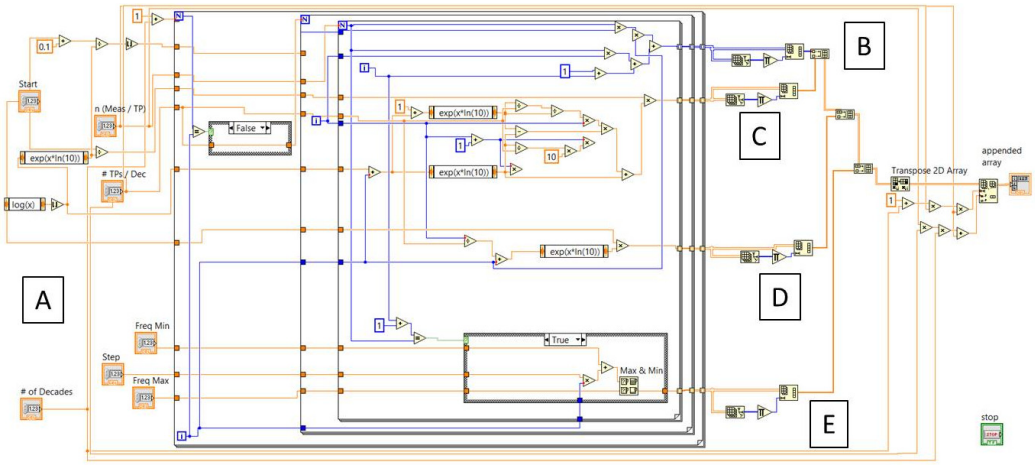

Figure 87. Code required to generate decade based test matrix. The seven input values (A) are fed into nested loops which mimic the testing process. The output is used to build 4 arrays which are then joined including the index array (B), the linear cycle count array (C), the logrithmic cycle count array (D), and the test frequency array (E)

LabVIEW data which exits any loop can be set to provide either single values for that loop, or generate an array of values. The matrix then is built simply by stacking those arrays and sending the values to the table on the user interface. To change this to a usable UI which can be called by other LabVIEW programs, the only remaining step is to tie the inputs and outputs to the icon shown in the upper right corner of Figure 86 and it can be called as any other LabVIEW function block is.

Appendix E. Grayscale Automation

The following is a detailed description of the process for automating the Heidelberg μ-100 to produce a modified form of grayscale lithography which uses the resolution of CAD based designs. The process involves the following steps, but if performed properly will automate the repeated patterning process for a virtually unlimited number of runs. The steps in this process are:

1. Create CAD files require for grayscale structure

   The dimension of these design files must not exceed the capability of the Heidelberg, but this is the only limitation on size. Each file is a single, .cif layered design, but any number of layers can be stacked in this manner through several files designed to work together. However, a suitable recipe for that number of layers in conjunction with the photoresist used must be determined. All files which are to be used are then stored in .cif format on a single folder on the Heidelberg system, and the location of those files noted for future use.

2. Create script file

   The next step is the creation of a script file which details the location, power and duty cycle of each step in the process. This can be done in any software, but the end result must be a comma delimited file which follows the format discussed here. Excel was used for this research and proved effective. To explain the details of how to build this file, first refer to Figure 88.

   A sample of one of these files is shown in the upper left portion of this figure. While this file may become long depending on the number of patterns to be exposed, the format is relatively simple. This scheme was developed with a particular fabrication approach, specifically to expose several common reticles across a wafer, but with several groups of reticles being produced as identical

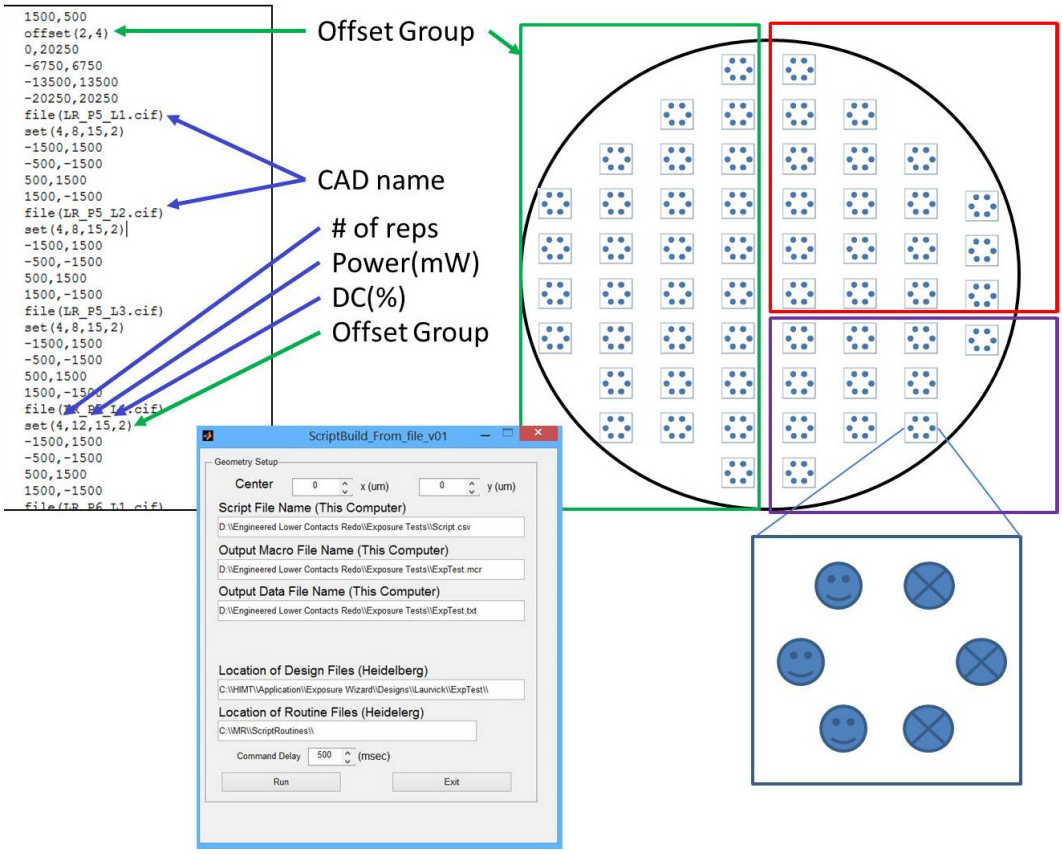

Figure 88. Grayscale process showing an example script file (upper left) which shows the four basic commands required. Offset groups define common reticles (upper right) which can be used for repeated patternings. Each set common specifies each step required for each reticle (lower right) is contained in the set command and coordinates following it. The resulting script is ran through the MATLAB software to generate the emulator macro.

units. This requires a somewhat sophisticated scheme of operation, but was developed to be adaptable enough to suit many applications. As shown, there are only 4 possible formats each line of this script file can take, and each will be discussed individually:

- offset(ID, number) - For the devices to be patterned here, individual reticles were created with several devices per reticle. Thus, the first step in the process is to identify where each reticle is located and group them accordingly. Suppose a patterning is desired as shown in Figure 88, in

the upper right corner. In this example, three types of devices are to be exposed, 29 in the first group on the left (which would be defined as group 1), 18 in the upper right corner (group 2), and 11 in the lower right (group 3). These groups only define where each reticle is located; not the details of what is in each reticule. The first number in the parenthesis following the 'offset' statement is simply an ID number which will be used during the next steps. These ID numbers are sequential and unique, but up to 999 of them are allowed. The second value in the calling statement is the number of reticles in that group. Note that using offset groups is optional, however if an offset group is called later and hasn't been defined an error will result - it is possible to conduct the process and simply not call out an offset if it isn't required.

- X coordinate , Y coordinate - The second form the script file entries may take is a pair of coordinates. Following each offset group statement, enough coordinates must be supplied to define that group. In the examples mentioned above, if the first offset group is to have 29 reticules, then the next 29 lines following the 'offset' statement must be 29 sets of coordinates detailing the reticle location relative to the center of the wafer.

- file(filename) - The third of the four possible options is the definition of the file which is to be exposed next. Note that only the name is needed (the folder in which the file is located will be used later) and should be provided without quotes and in a 'cif' file format. This is the file which is to be loaded by the Heidelberg software, so it is beneficial to ensure each file loads correctly prior to running this process.

- set(Reps,Power,DC,Optional Offset) - The fourth and final type of command is the set command, which actually performs the exposure, and can

include either 3 or 4 parameters (if the offset is omitted, no offset will be used). The set command MUST immediately follow a file command, and will operate on that file only (subsequent files are processed through new file/set commands). The first parameter used defines the number of times that file is to be exposed in each reticule, the power is at what power (in mW), the DC is the duty cycle (between 0 to 100), and the fourth optional parameter is the offset group.

Lets assume each reticle shown in Figure 88, lower right corner is to be exposed, and lets assume the smiley faces require only a single file, while the pies require four steps to accomplish. The first file/set pair will load the smiley face, and define three repetitions per reticle at the desired power and duty cycle, using offset group 3. Since each reticle requires three and there are 11 reticles in that group, this pattern will be exposed 33 times. The last piece of information needed are the location of the smiley faces in each set. That information is passed in the lines immediately following the 'set' command, just as they were with the offset groups. In this case, three repetitions are required so the next three lines in the script file must contain the x and y coordinates of each repetition relative to the center of the RETICLE. Note that if multiple files are to be overlaid, the user must ensure that the center of each .cif file coincide through whatever means necessary (e.g. constructing a common frame around all files, etc.) Once all the smiley faces are completed, then the first of the four pie files can be opened, and another set command for that exposure is defined, followed with the coordinates of those devices on each reticle. This process is repeated until the entire wafer patterning is defined.

Note that other objects can be exposed in this manner and positioned relative to the center of the wafer as well. If for example the wafer is to be used in subsequent fabrication steps, then alignment marks may be required. In that case, a CAD file with a single set of alignment patterns needs to be saved as well, and the position of these included in the same manner.

Once this file is completed and verified, it needs will be used with a piece of software which was developed to build the emulator file, as outlined in the next step.

3. Generation of emulator macro

The next step utilizes a script which was written in MATLAB, and requires a few pieces of information as well as the script file from the previous step before it can be performed. The information needed specifically is:

- X and Y offset for entire wafer (if required)
- name and location of script file
- name and location of where the macro file which will be generated is to be saved
- name and location of where the report file which describes this macro is to be saved
- the name of the folder (on the Heidelberg system) where the design files can be found)
- the name of the folder (on the Heidelberg system where the routine files can be found (which will be discussed next)
- the desired delay between each step

Once that information is entered, the MATLAB macro is run and generates the script file along with a text file which outlines the order of operations in an easy to read format (useful for determining the order in which a wafer will be patterned or debugging an issue with the script file later). If the alignment of the wafer is critical, the wafer must first be loaded and the overall offset determined by the Heidelberg, and that offset used before the macro is generated, and that offset will be applied to EVERY exposure performed. If it is not critical, this offset can be set to 0,0 and the macro made before the wafer is loaded. This macro file is then moved to the Heidelberg, the design files put in the specified folder.

At this point, the wafer can be run. After being loaded into the Heidelberg, load any design file and advance to the load screen. While the script should start from any screen, in some instances it can lock up, but has always worked when starting with the load screen as that is where the process begins. With that screen visible and no other programs running or windows open, start the emulation software and load the macro which was generated. Once that macro is run, ensure the status bar is not in front of the Heidelberg screen and the process will proceed.

To understand the process, and specifically the routine files which are required, consider Figure 89.

The emulation software functions by continually monitoring the screen and looks for specific bitmap patterns to appear, indicating the next step in the process was reached. If an error occurs, then the image which indicates success will simply not appear and the system will wait for user intervention, ensuring safe overall operation. This does require that no other windows be present which may obstruct the view of the emulator, or the process will stop prematurely as a result.

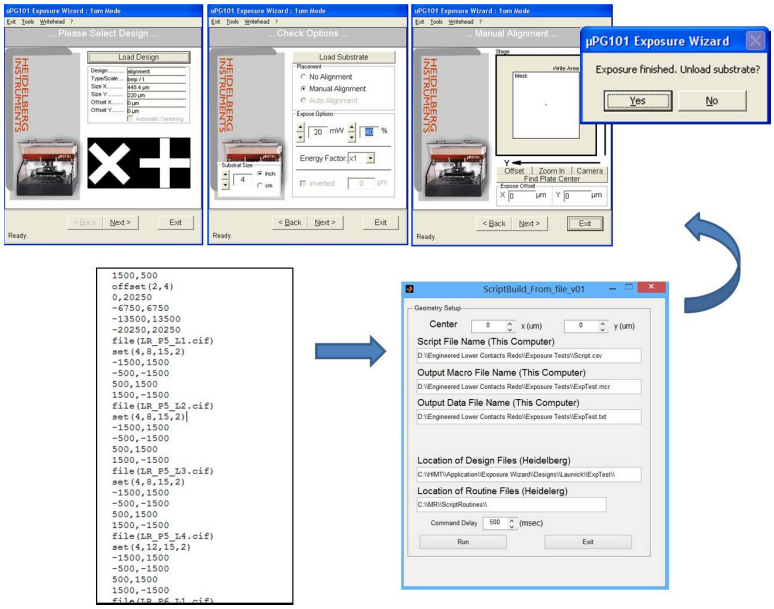

Figure 89. Emulation macro creation from script file and basic additional information, the output is used to autmatically step through the screens during the exposure process, load new patterns and repeat as needed.

As the bitmaps which the software is looking for are stored within the emulator macros, and the several step may be repeated thousands of times, any macro which looks for an image was saved as a routine file and saved locally. The file which is created in the above process then just calls these locally stored 'routine' files. A list of the 22 required routine files are listed in Table 3, which shows the name of the file (in the second column, without the required '.mcr' extension) and a description of what each file accomplishes.

R01	RStartup	from any screen, get to the load design screen
R02	RLoadDes	click "load design" button, x2 click filename box (or types alt-n?)
R03	ROKLoad	clicks ok, checks for cif.units screen, enters a 1, clicks ok
R04	RAutoCent	checks for auto-centering checkbox on design screen, then clicks next on design screen
R05	RManRadio	verifies manual alignment radio button is checked
R06	RPowerSet	x2 click expose power box
R07	RDCSet	x2 click duty cycle box
R08	REnerX1	set energy factor to x1
R09	REnerX2	set energy factor to x2
R10	REnerX4	set energy factor to x4
R11	RInverDes	inverted design box checked, then x2 click the buffer box
R12	RNonInvDes	inverted design box unchecked
R13	RXOffset	x2 clicks x offset box
R14	RYOffset	x2 clicks y offset box
R15	RExposeStart	clickes 'expose' button
R16	RNoUnload	waits for exp finished, 'no' to unload substrate
R17	RYesUnload	waits for exp finished, 'yes' to unload substrate
R18	RSameDes	clicks 'expose same design' button
R19	RNewDes	clicks 'expose new design' button
R20	RExitWiz	clicks 'exit wizard' button
R21	RNextPower	Next button on substrate load screen (where power setttings are)
R22	RNextPos	Next button on x and y offset screen

Table 3. Routines required to conduct grayscale lithography including brief description of each.

Appendix F. Nanosphere Vessel Drawings

The following are drawings of those nanosphere deposition vessels discussed in this document which produced successful, reportable results. The first is the vessel used to optimize liquid surface to substrate angle and is shown in Figure 90.

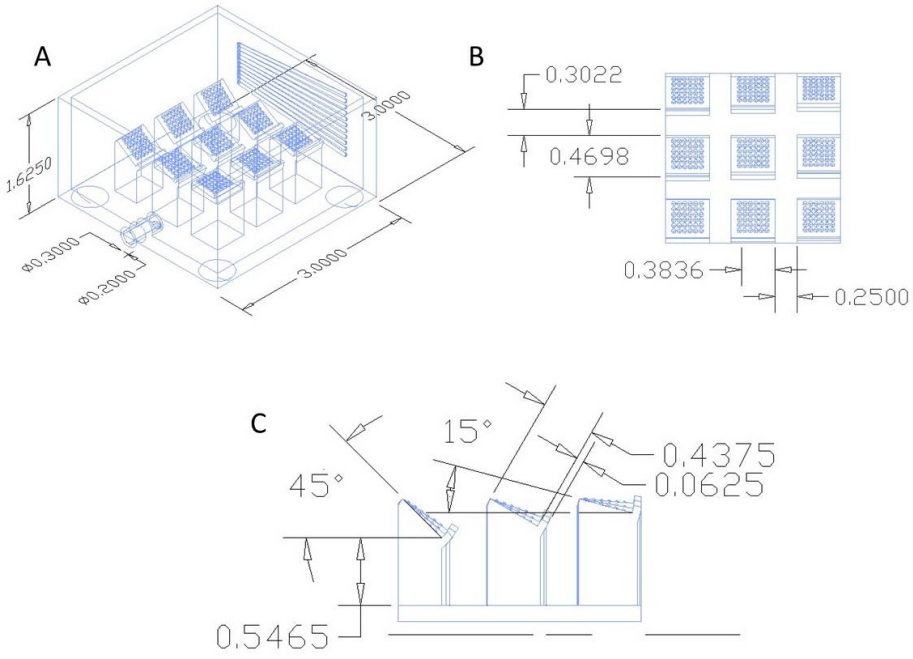

Figure 90. Nanosphere deposition vessel with nine sample holders with incremental surface to substrate angles ranging from 5 degrees to 45 degrees. Critical dimensions are indicated, with all units in inches.

The second vessel specifications provided are for a similar design but with two modifications. The pillars for this model are set to 20 degrees inclination angle, and a slide carrier surface was added as shown in Figure 91.

The third vessel was constructed in two parts. The first part is the shell which is shown in Figure 92. This vessel still uses the 20 degree inclination angle, but is designed for surface area constriction and as such has the characteristic funnel shape. To prevent nanospheres from adhering to the funnel during the drain process, it

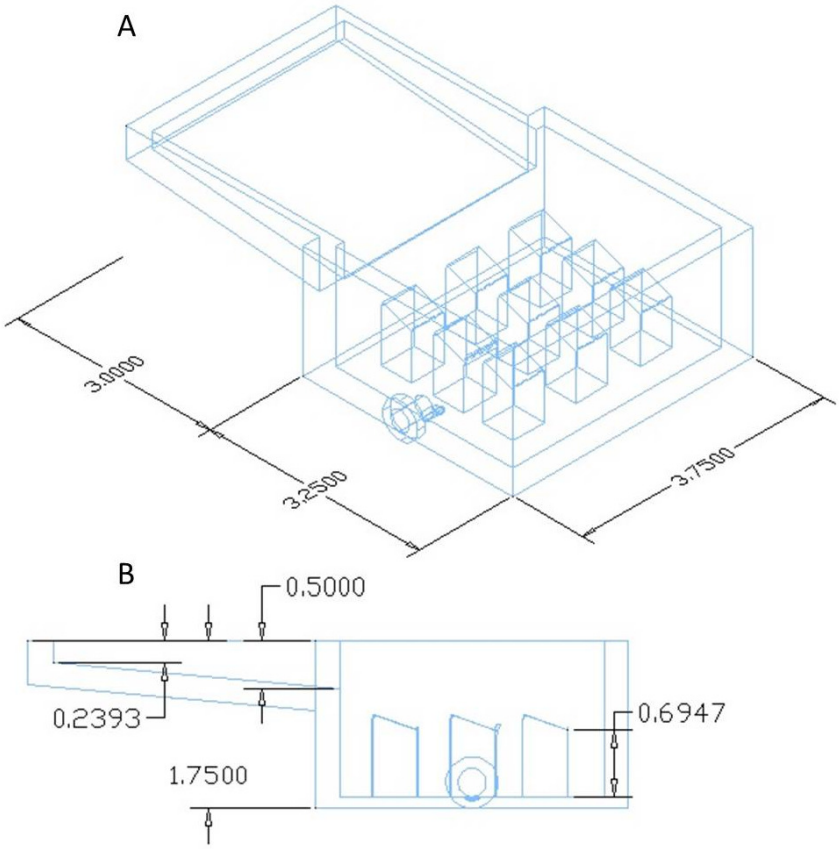

Figure 91. Nanosphere deposition vessel with nine sample holders set to 20 degrees, and a glass side carrier stage for nanosphere loading to the surface. Critical dimensions are indicated, with all units in inches.

needed to be lined with a hydrophobic material, and to do that an insert was printed as a separate piece to allow for this feature.

To accomplish this, the second part of this vessel is shown in Figure 93. This piece is sized to fit snugly within the shell, and allow for separate treatment through whatever means are desired to coat with part of the vessel.

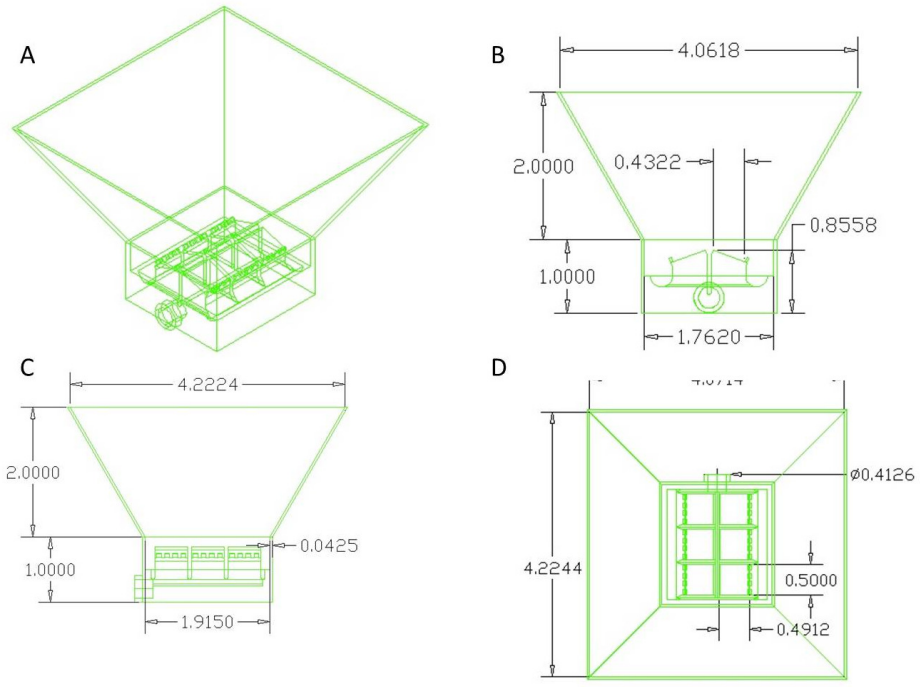

Figure 92. Nanosphere deposition vessel with six sample holders and a surface compression funnel integrated into the design. Critical dimensions are indicated, with all units in inches.

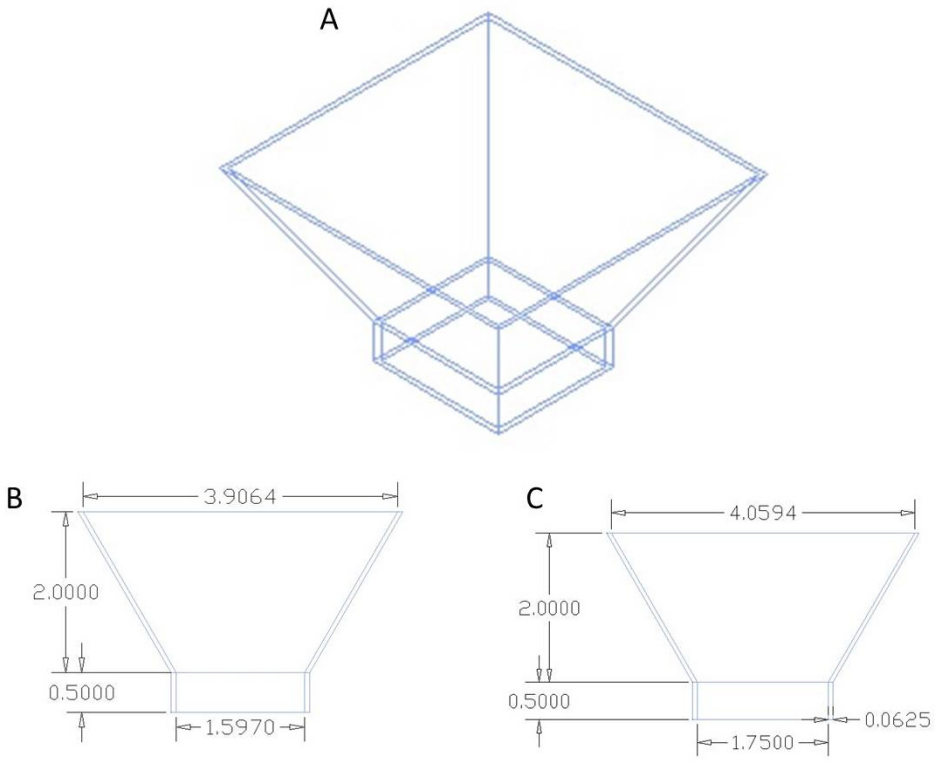

Figure 93. Nanosphere deposition vessel insert. Critical dimensions are indicated, with all units in inches.

Bibliography

1. G. M. Rebeiz, "Rf mems switches: Status of the technology." Boston, MA: 12th International Conference on Solid State Sensors, Actuators and Microsystems, 2003, pp. 1726–1729.

2. G. M. Rebeiz, *RF MEMS: Theory, Design, and Technology*. Wiley, 2004. [Online]. Available: http://books.google.com/books?id=A7728XHtmzAC

3. K. V. Caekenberghe, "Rf mems on the radar," *Microwave Magazine, IEEE*, vol. 10, no. 6, pp. 99–116, 2009.

4. M. Kaynak, K. E. Ehwald, R. Scholz, F. Korndörfer, C. Wipf, Y. M. Sun, B. Tillack, S. Zihir, and Y. Gurbuz, "Characterization of an embedded rf-mems switch," *2010 10th Topical Meeting on Silicon Monolithic Integrated Circuits in RF Systems, SiRF 2010 - Digest of Papers*, pp. 144–147, 2010.

5. R. H. Dennard, J. Cai, and A. Kumar, "A perspective on today's scaling challenges and possible future directions," *Solid-State Electronics*, vol. 51, no. 4, pp. 518–525, 2007. [Online]. Available: http://www.sciencedirect.com/science/article/B6TY5-4NC5V76-2/2/68f350b39012420782654df814b85bd3

6. Z. Yang, D. J. Lichtenwalner, A. S. Morris, J. Krim, and A. Kingon, "Comparison of au and au–ni alloys as contact materials for mems switches," *Microelectromechanical Systems, Journal of*, vol. 18, no. 2, pp. 287–295, 2009.

7. C. Borgnakke and R. Sconntag, *Fundamentals of Thermodynamics*, 8th ed., Wiley, Ed. Wiley, 2012.

8. H. Lee, R. a. Coutu, S. Mall, and K. D. Leedy, "Characterization of metal and metal alloy films as contact materials in mems switches," *Journal of Micromechanics and Microengineering*, vol. 16, no. 3, pp. 557–563, 2006.

9. K. E. Pitney, "Ney contact manual," *Electrical Contacts for Low Energy Uses*, 1973.

10. B. Toler and R. A. Coutu, "Characterizing external resistive, inductive and capacitive loads for micro-switches â," *MEMS and Nanotechnol.*, vol. 42, pp. 11–11–18, 2013.

11. J. W. McBride, "Electrical contact bounce in medium-duty contacts," *IEEE Trans. Compon. Hybrids Manuf. Technol.*, vol. 12, pp. 82–82–90, 1989.

12. B. McCarthy, G. G. Adams, N. E. McGruer, and D. Potter, "A dynamic model, including contact bounce, of an electrostatically actuated microswitch," *Microelectromechanical Systems, Journal of*, vol. 11, no. 3, pp. 276–283, Jun 2002.

13. D. A. Czaplewski, C. W. Dyck, H. Sumali, J. E. Massad, J. D. Kuppers, I. Reines, W. D. Cowan, and C. P. Tigges, "A soft-landing waveform for actuation of a single-pole single-throw ohmic rf mems switch," *Microelectromechanical Systems, Journal of*, vol. 15, no. 6, pp. 1586–1594, Dec 2006.

14. H. Sumali, J. E. Massad, D. A. Czaplewski, and C. W. Dyck, "Waveform design for pulse-and-hold electrostatic actuation in mems," *Sensors Actuators A*, vol. 134, pp. 213–213–20, 2007.

15. Z. J. Guo, N. E. McGruer, and G. G. Adams, "Modeling, simulation and measurement of the dynamic performance of an ohmic contact, electrostatically actuated rf mems switch," *J. Micromech. Microeng.*, vol. 17, no. 1899, pp. 1899–909, 2007.

16. J. C. Blecke, D. S. Epp, H. Sumali, and G. G. Parker, "A simple learning control to eliminate rf mems switch bounce," *J. Microelectromech. Syst.*, vol. 18, pp. 458–458–65, 2009.

17. A. Tazzoli, M. Barbato, F. Mattiuzzo, V. Ritrovato, and G. Meneghesso, "Study of the actuation speed, bounces occurrences, and contact reliability of ohmic rf-mems switches," *Microelectronics Reliability*, vol. 50, pp. 1604 – 1608, 2010, 21st European Symposium on the Reliability of Electron Devices, Failure Physics and Analysis. [Online]. Available: http://www.sciencedirect.com/science/article/pii/S0026271410003070

18. M. Spasos and R. Nilavalan, "On the investigation of a reliable actuation control method for ohmic rf mems switches," *Microelectron. J.*, vol. 42, pp. 1239–1239–51, 2011.

19. A. Peschot, C. Poulain, N. Bonifaci, and O. Lesaint, "Contact bounce phenomena in a mem switch," in *Electrical Contacts (Holm), 2012 IEEE 58th Holm Conference on*, Sept 2012, pp. 1–7.

20. Z. Yang, D. Lichtenwalner, A. Morris, J. Krim, and A. Kingon, "Contact degradation in hot/cold operation of direct contact micro-switches," *Journal of Micromechanics and Microengineering*, vol. 20, no. 10, p. 105028, 2010.

21. P. M. Zavracky, S. Majumder, and N. E. McGruer, "Micromechanical switches fabricated using nickel surface micromachining," *Microelectromechanical Systems, Journal of*, vol. 6, no. 1, pp. 3–9, 1997.

22. S. Majumdar, J. Lampen, R. Morrison, and J. Maciel, "Mems switches," *IEEE Instrum. Meas. Mag.*, vol. 6, pp. 12–12–15, 2003.

23. H. Newman, J. Ebel, D. Judy, and J. Maciel, "Lifetime measurements on a high-reliability rf-mems contact switch," *IEEE Microw. Wirel. Compon. Lett.*, vol. 2, pp. 100–100–2, 2008.

24. J. Maciel, S. Majumder, R. Morrison, and J. Lampen, "A lifetime measurement on a high-reliability rf mems contact switch," *Proc. SPIE*, vol. 5343, pp. 1–1–6, 2004.

25. J. McBride, "The wear processes of gold coated multi-walled carbon nanotube surfaces used as electrical contact for micro-mechanial switching," *Nanosci. Nanotechnol. Lett.*, vol. 4, pp. 357–357–61, 2010.

26. N. Jemaa, "Short arc duration laws and distributions at low current(¡1a) and voltage (14–42vdc)," *IEEE Trans. Compon. Packag. Technol.*, vol. 24, pp. 358–358–63, 2001.

27. N. Jemaa, "Contacts conduction and switching in dc levels," in *Proc. 48th IEEE Holm Conf. on Electrical Contacts*, 2002, pp. 1–1–15.

28. M. Hasegawa and Y. Kamada, "An experimental study on re-interpretation of minimum arc current of electrical contacts," *IEICE Trans. Electron.*, vol. 8, pp. 1616–1616–9, 2005.

29. W. Johler, "Basic investigations for switching of rf signals," in *Proc. 53rd IEEE Holm Conf. on Electrical Contacts*, 2007, pp. 229–229–38.

30. N. Miki and K. Sawa, "Arc extinction characteristics in power supply frequencies from 50 hz to 1 mhz," *Eur. Phys. J—Appl. Phys.*, vol. 50, p. 12903, 2010.

31. E. Kruglick and K. Pister, "Lateral mems microcontact considerations," *J. Micromech. Syst.*, vol. 8, pp. 264–264–71, 1999.

32. J.-M. Kim, S. Lee, C.-W. Baek, Y. Kwon, and Y.-K. Kim, "Cold- and hot-switching lifetime characterizations of ohmic-contact rf mems switches," *IEICE Electronics Express*, vol. 5, no. 11, pp. 418–423, 2008. [Online]. Available: http://joi.jlc.jst.go.jp/JST.JSTAGE/elex/5.418?from=CrossRef

33. M. Braunovic, N. K. Myshkin, and V. V. Konchits, *Electrical contacts: fundamentals, applications and technology.* CRC press, 2010, vol. 132.

34. B. Nikoli and P. B. Allen, "Electron transport through a circular constriction," *Phys. Rev. B*, vol. 60, pp. 3963–3969, Aug 1999. [Online]. Available: http://link.aps.org/doi/10.1103/PhysRevB.60.3963

35. M. Sun, M. G. Pecht, M. a. E. Natishan, and R. I. Martens, "Lifetime resistance model of bare metal electrical contacts," *IEEE Transactions on Advanced Packaging*, vol. 22, no. 1, pp. 60–67, 1999. [Online]. Available: http://ieeexplore.ieee.org/lpdocs/epic03/wrapper.htm?arnumber=746544

36. E. Takano and K. Mano, "Theoretical lifetime of static contacts," *IEEE Trans. Parts Mater. Packag.*, vol. 22, pp. 60–60–7, 1967.

37. R. Holm, *Electric Contacts: Theory and Applications, Fourth Edition ed*, 4th ed., 1967.

38. S. Majumder, N. E. McGruer, G. G. Adams, P. M. Zavracky, R. H. Morrison, and J. Krim, "Study of contacts in an electrostatically actuated microswitch," *Sensors and Actuators, A: Physical*, vol. 93, no. 1, pp. 19–26, 2001.

39. G. Wexler, "The size effect and the non-local boltzmann transport equation in orifice and disk geometry," *Proceedings of the Physical Society*, vol. 89, no. 4, p. 927, 1966.

40. W. R. Chang, "An elastic-plastic contact model for a rough surface with an ion-plated soft metallic coating," *Wear*, vol. 212, no. 2, pp. 229–237, 1997.

41. R. A. Coutu Jr., J. W. McBride, and L. A. Starman, "Improved micro-contact resistance model that considers material deformation, electron transport and thin film characteristics," *2009 Proceedings of the 55th IEEE Holm Conference on Electrical Contacts*, pp. 298–302, 2009. [Online]. Available: http://ieeexplore.ieee.org/lpdocs/epic03/wrapper.htm?arnumber=5284384

42. J. A. Greenwood and J. H. Tripp, "The contact of two nominally flat rough surfaces," *Proceedings of the Institution of Mechanical Engineers*, vol. 185, no. 1, pp. 625–633, 1970. [Online]. Available: http://pme.sagepub.com/content/185/1/625.abstract

43. T. Thomas, "Characterization of surface roughness," *Precision Engineering*, vol. 3, no. 2, pp. 97–104, 1981.

44. A. Majumdar and C. Tien, "Fractal characterization and simulation of rough surfaces," *Wear*, vol. 136, no. 2, pp. 313–327, 1990.

45. F. Borodich and D. Onishchenko, "Similarity and fractality in the modeling of roughness by a multilevel profile with hierarchial struture," *Int. J. Solids Struct.*, vol. 36, pp. 2585–12, 1999.

46. O. Rezvanian, M. Zikry, C. Brown, and J. Krim, "Surface roughness, asperity contact and gold rf mems switch behavior," *Journal of micromechanics and microengineering*, vol. 17, no. 10, p. 2006, 2007.

47. F. Firestone and E. Abbot, "Specifying surface quantity - a method based on the accurate measurement and comparison," *ASME Mech. Eng*, vol. 55, p. 569, 1933.

48. J. Greenwood and J. Williamson, "Contact of nominally flat surfaces," *Proceedings of the Royal Society of London. Series A. Mathematical and Physical Sciences*, vol. 295, no. 1442, pp. 300–319, 1966.

49. C. Stilson, "Contact resistance evolution and degradation of highly cycled micro-contacts," Master's thesis, Air Force Institute of Technology, 2014.

50. N. Agraït, A. L. Yeyati, and J. M. van Ruitenbeek, "Quantum properties of atomic-sized conductors," *Physics Reports*, vol. 377, no. 2-3, pp. 81–279, 2003.

51. A. Mikrajuddin, F. G. Shi, H. Kim, and K. Okuyama, "Size-dependent electrical constriction resistance for contacts of arbitrary size: from sharvin to holm limits," *Materials Science in Semiconductor Processing*, vol. 2, no. 4, pp. 321–327, 1999.

52. Y. Sharvin, "Sharvin resistance formula," *Sov. Phys JETP*, vol. 21, p. 655, 1965.

53. R. A. Coutu, J. R. Reid, R. Cortez, R. E. Strawser, and P. E. Kladitis, "Microswitches with sputtered au, aupd, au-on-aupt, and auptcu alloy electric contacts," *IEEE Transactions on Components and Packaging Technologies*, vol. 29, no. 2, pp. 341–349, 2006.

54. R. L. Jackson and J. L. Streator, "A multi-scale model for contact between rough surfaces," *Wear*, vol. 261, no. 11-12, pp. 1337–1347, 2006.

55. J. I. McCool, "Comparison of models for the contact of rough surfaces," *Wear*, vol. 107, no. 1, pp. 37–60, 1986.

56. F. Pennec, D. Peyrou, D. Leray, P. Pons, R. Plana, and F. Courtade, "Impact of the surface roughness description on the electrical contact resistance of ohmic switches under low actuation forces," *Components, Packaging and Manufacturing Technology, IEEE Transactions on*, vol. 2, no. 1, pp. 85–94, 2012.

57. J. A. Greenwood, "A unified theory of surface roughness," *Proceedings of the Royal Society A: Mathematical, Physical and Engineering Sciences*, vol. 393, no. 1804, pp. 133–157, 1984. [Online]. Available: http://rspa.royalsocietypublishing.org.ezlibproxy1.ntu.edu.sg/content/393/1804/133.short

58. A. Majumdar and B. Bhushan, "Role of fractal geometry in roughness characterization and contact mechanics of surfaces," *ASME J. Tribol.*, vol. 112, pp. 205–205–216, 1990.

59. L. Kogut and R. L. Jackson, "A comparison of contact modeling utilizing statistical and fractal approaches," *Journal of Tribology*, vol. 128, no. 1, pp. 213–217, 2006. [Online]. Available: http://link.aip.org/link/?JTQ/128/213/1

60. L. Kogut and I. Etsion, "A finite element based elastic-plastic model for the contact of rough surfaces," *Tribology Transactions*, vol. 46, no. 3, pp. 383–390, 2003.

61. M. Borri-Brunetto, B. Chiaia, and M. Ciavarella, "Incipient sliding of rough surfaces in contact: a multiscale numerical analysis," *Computer Methods in Applied Mechanics and Engineering*, vol. 190, pp. 6053 – 6073, 2001. [Online]. Available: http://www.sciencedirect.com/science/article/pii/S0045782501002183

62. K. Komvopoulos and N. Ye, "Three-dimensional contact analysis of elastic-plastic layered media with fractal surface topographies," *Journal of tribology*, vol. 123, no. 3, pp. 632–640, 2001.

63. B. Persson, F. Bucher, and B. Chiaia, "Elastic contact between randomly rough surfaces: comparison of theory with numerical results," *PHYSICAL REVIEW-SERIES B-*, vol. 65, no. 18, pp. 184 106–184 106, 2002.

64. B. Persson, "Elastoplastic contact between randomly rough surfaces," *Physical Review Letters*, vol. 87, no. 11, p. 116101, 2001.

65. W. E. Wilson, S. V. Angadi, and R. L. Jackson, "Electrical contact resistance considering multi-scale roughness," in *Electrical Contacts, 2008. Proceedings of the 54th IEEE Holm Conference on.* IEEE, 2008, pp. 190–197.

66. R. A. Coutu Jr, P. E. Kladitis, K. D. Leedy, and R. L. Crane, "Selecting metal alloy electric contact materials for mems switches," *Journal of Micromechanics and Microengineering*, vol. 14, no. 8, p. 1157, 2004.

67. a. Broue, J. Dhennin, P. L. Charvet, P. Pons, N. B. Jemaa, P. Heeb, F. Coccetti, and R. Plana, "Multi-physical characterization of micro-contact materials for mems switches," *Electrical Contacts, Proceedings of the Annual Holm Conference on Electrical Contacts*, pp. 363–372, 2010.

68. D. a. Czaplewski, C. D. Nordquist, G. a. Patrizi, G. M. Kraus, and W. D. Cowan, "Rf mems switches with ruo 2 –au contacts cycled to 10 billion cycles," *Journal of Microelectromechanical Systems*, vol. 22, no. 3, pp. 655–661, 2013. [Online]. Available: http://ieeexplore.ieee.org/lpdocs/epic03/wrapper.htm?arnumber=6425388

69. L. Kogut and K. Komvopoulos, "Electrical contact resistance theory for conductive rough surfaces separated by a thin insulating film," *Journal of Applied Physics*, vol. 95, no. 2, pp. 576–585, 2004. [Online]. Available: http://scitation.aip.org/content/aip/journal/jap/95/2/10.1063/1.1629392

70. J. W. McBride, R. A. Coutu, and L. A. Starman, "Improved micro-contact resistance model that considers material deformation, electron transport and thin film characteristics," *IEEE 55th Holm Conference on Electrical Contacts (Holm)*, pp. 296–9, 2009.

71. R. L. Jackson, "A model for the adhesion of multiscale rough surfaces in mems," in *System Theory (SSST), 2011 IEEE 43rd Southeastern Symposium on*. IEEE, 2011, pp. 257–262.

72. B. F. Toler, R. A. Coutu, and J. W. McBride, "A review of micro-contact physics for microelectromechanical systems (mems) metal contact switches," *Journal of Micromechanics and Microengineering*, vol. 23, no. 10, p. 103001, 2013.

73. R. Budakian and S. Putterman, "Time scales for cold welding and the origins of stick-slip friction," *Phys. Rev. B*, vol. 65, pp. 2354–2354–9, 2002.

74. N. Dowling, *Mechanical Behavior of Materials: Engineering Methods for Deformation, Fracture and Fatigue*, 3rd ed. Pearson Prentice Hall, 2007.

75. D. J. Dickrell and M. T. Dugger, "Electrical contact resistance degradation of a hot-switched simulated metal mems contact," *IEEE Transactions on Components and Packaging Technologies*, vol. 30, no. 1, pp. 75–80, 2007. [Online]. Available: http://ieeexplore.ieee.org/articleDetails.jsp?arnumber=4135390

76. S. Patton, K. Eapen, and J. Zabinski, "Effects of adsorbed water and sample aging in are on un level adhesion force between si(1 0 0) and silicon nitride," *Tribol. Int.*, vol. 34, pp. 481–481–91, 2001.

77. A. Lumbantobing, L. Kogut, and K. Komvopoulos, "Electrical contact resistance as a diagnostic tool for mems contact interfaces," *J. Microelectromech. Syst.*, vol. 13, pp. 977–977–987, 2004.

78. A.S.M., *ASM 1990 Metals Handbook*. Materials Park, OH: American Society for Metals Int., 1990, vol. 2.

79. B. Arrazat, P.-Y. Duvivier, V. Mandrillon, and K. Inal, "Discrete analysis of gold surface asperities deformation under spherical nano-indentation towards electrical contact resistance calculation," in *Electrical Contacts (Holm), 2011 IEEE 57th Holm Conference on*, 2011, pp. 1–8.

80. A. Broue, J. Dhennin, F. Courtade, C. Dieppedale, P. Pons, X. Lafontan, and R. Plana, "Characterization of au/au, au/ru and ru/ru ohmic contacts in mems switches improved by a novel methodology," in *Proceedings of SPIE*, vol. 7592, 2010, p. 75920A.

81. Y. Chai, A. Hazeghi, K. Takei, H.-Y. Chen, P. C. H. Chan, A. Javey, and H. S. P. Wong, "Low-resistance electrical contact to carbon nanotubes with graphitic interfacial layer," *Electron Devices, IEEE Transactions on*, vol. 59, no. 1, pp. 12–19, 2012, iD: 1.

82. Y. Chai, I. A. Hazegh, K. Takei, Y. Chen, P. Chan, A. Javey, and H. Wong, "Graphitic interfacial layer to carbon nanotube for low electrical contact resistance," *IEDM Technol. Digest*, vol. 9, pp. 210–210–3, 2010.

83. H. Kwon, D.-J. Choi, J.-H. Park, H.-C. Lee, Y.-H. Park, Y.-D. Kim, H.-J. Nam, Y.-C. Joo, and J.-U. Bu, "Contact materials and reliability for high power rf-mems switches," *2007 IEEE 20th International Conference on Micro Electro Mechanical Systems (MEMS)*, no. January, pp. 231–234, 2007. [Online]. Available: http://ieeexplore.ieee.org/lpdocs/epic03/wrapper.htm?arnumber=4433055

84. O. Yaglioglu, A. J. Hart, R. Martens, and A. H. Slocum, "Method of characterizing electrical contact properties of carbon nanotube coated surfaces," *Review of Scientific Instruments*, vol. 77, no. 9, p. 095105, September 2006 2006. [Online]. Available: http://dx.doi.org/10.1063/1.2349300

85. E. Thostenson, Z. Ren, and T. Chou, "Advances in the science and technology of carbon nanotubes and their composites: a review," *Compos. Sci. Technol.*, vol. 61, pp. 1899–1899–912, 2001.

86. E. M. Yunus, S. M. Spearing, and J. W. McBride, "The relationship between contact resistance and contact force on au-coated carbon nanotube surfaces under low force conditions," *Components and Packaging Technologies, IEEE Transactions on*, vol. 32, no. 3, pp. 650–657, 2009, iD: 1.

87. J. Choi, J.-I. Lee, Y. Eun, M.-O. Kim, and J. Kim, "Microswitch with self-assembled carbon nanotube arrays for high current density and reliable contact," in *Micro Electro Mechanical Systems (MEMS), 2011 IEEE 24th International Conference on*, 2011, pp. 87–90, iD: 1.

88. J. P. Gambino and E. G. Colgan, "Silicides and ohmic contacts," *Materials Chemistry and Physics*, vol. 52, no. 2, pp. 99–146, 1998.

89. W. Kim, A. Javey, R. Tu, J. Cao, Q. Wang, and H. Dai, "Electrical contacts to carbon nanotubes down to 1nm in diameter," *Appl. Phys. Lett.*, vol. 87, pp. 101–73, 2005.

90. W. S. Chen Q and P. L, "Establishing ohmic contacts for in situ current–voltage characteristic measurements on a carbon nanotube inside the scanning electron microscope," *Nanotechnology*, vol. 17, pp. 1087–1087–98, 2006.

91. K. Rykaczewski, M. Henry, S. Kim, A. Fedorov, D. Kulkarni, S. Singamaneni, and V. Tsukruk, "The effect of geometry and material properties of a carbon joint produced by electron beam induced deposition on the electrical resistance of a multiwalled carbon nanotube-to-metal contact interface," *Nanotechnology*, vol. 21, pp. 1–1–12, 2010.

92. D. A. Czaplewski, C. D. Nordquist, C. W. Dyck, G. A. Patrizi, G. M. Kraus, and W. D. Cowan, "Lifetime limitations of ohmic, contacting rf mems switches with au, pt and ir contact materials due to accumulation of 'friction polymer'on the contacts," *Journal of Micromechanics and Microengineering*, vol. 22, no. 10, pp. 105 005–105 005, 2012. [Online]. Available: http://stacks.iop.org/0960-1317/22/i=10/a=105005?key=crossref.90c824b0d4b2052f7d7cc54c098a7020

93. T. Fischer, "Tribochemistry," *Annual Review of Materials Science*, vol. 18, pp. 303–323, 1988.

94. N. McGruer, G. Adams, L. Chen, Z. Guo, and Y. Du, "Mechanical, thermal, and material influences on ohmic-contact-type mems switch operation," in *Micro Electro Mechanical Systems, 2006. MEMS 2006 Istanbul. 19th IEEE International Conference on.* IEEE, 2006, pp. 230–233.

95. Y. Tong, H. Kim, P. Babu, P. Waszczuk, A. Wieckowski, and E. Oldfield, "An nmr investigation of co tolerance in a pt/ru fuel cell catalyst," *J. Am. Chem. Soc.*, vol. 124, no. 3, pp. 468–473, 2002.

96. S. Oh and J. Carpenter, "Platinum-rhodium synergisn in hree-way automotive catalysts," *Journal of Catalysis*, vol. 98, no. 1, pp. 178–190, 1986.

97. W. Crossland and P. Murphy, "The formation of insulating organic films on palladium-silver contact alloys," *Parts, Hybrids, and Packaging, IEEE Transactions on*, vol. 10, no. 1, pp. 64–73, 1974.

98. H. Klauk, G. Schmid, W. Radik, W. Weber, L. Zhou, C. Sheraw, J. Nichols, and T. Jackson, "Contact resistance in organic thin film transistors," *Solid-State Electronics*, vol. 47, no. 2, pp. 297 – 301, 2003. [Online]. Available: http://www.sciencedirect.com/science/article/pii/S0038110102002101

99. P. Cha, D. Srolovitz, and T. Vanderlick, "Molecular dynamics simulation of single asperity contact," *Acta Mater.*, vol. 52, pp. 3983–3983–96, 2004.

100. J. Song and D. J. Srolovitz, "Atomistic simulation of multicycle asperity contact," *Acta Materialia*, vol. 55, no. 14, pp. 4759 – 4768, 2007. [Online]. Available: http://www.sciencedirect.com/science/article/pii/S135964540700300X

101. L. Kuipers and J. Frenken, "Jump to contact, neck formation, and surface melting in the scanning tunneling microscope," *Phys. Rev. Lett.*, vol. 70, pp. 3907–3907–10, 1993.

102. R. P. Hennessy, A. Basu, G. G. Adams, and N. E. McGruer, "Hot-switched lifetime and damage characteristics of mems switch contacts," *J. Micromech. Microeng.*, vol. 23, pp. 1–1–11, 2013.

103. S. T. Patton and J. S. Zabinski, "Fundamental studies of au contacts in mems rf switches," *Tribology Letters*, vol. 18, no. 2, pp. 215–230, 2005.

104. A. Fortini, M. I. Mendelev, S. Buldyrev, and D. Srolovitz, "Asperity contacts at the nanoscale: Comparison of ru and au," *Journal of Applied Physics*, vol. 104, no. 7, pp. 074 320–074 320, 2008.

105. M. Sorensen, M. Brandbyge, and K. Jacobsen, "Mechanical deformation of atomic-scale metallic contacts: Structure and mechanisms," *Phys. Rev. B*, vol. 57, pp. 3283–3283–94, 1998.

106. Y. Du, L. Chen, N. McGruer, G. Adams, and I. Etsion, "A finite element model of loading and unloading of an asperity contact with adhesion and plasticity," *J. Colloid Interface Sci.*, vol. 312, pp. 522–8, 2007.

107. S. Klein, S. Thilmont, V. Ziegler, U. Prechtel, U. Schmid, and H. Seidel, "High temperature stable rf mems switch based on tungsten-titanium," *TRANSDUCERS 2009 - 2009 International Solid-State Sensors, Actuators and Microsystems Conference*, pp. 1409–1412, 2009.

108. Y. Chen, R. Nathanael, J. Jeon, J. Yaung, L. Hutin, and T.-J. K. Liu, "Characterization of contact resistance stability in mem relays with tungsten electrodes," *Microelectromechanical Systems, Journal of*, vol. 21, no. 3, pp. 511–513, 2012.

109. H. Kam, V. Pott, R. Nathanael, J. Jeon, E. Alon, and T.-J. K. Liu, "Design and reliability of a micro-relay technology for zero-standby-power digital logic applications," in *Electron Devices Meeting (IEDM), 2009 IEEE International*. IEEE, 2009, pp. 1–4.

110. K. Murphy and R. Goon, "Thermionic emission, field emission and the transition region," *Physical Review*, vol. 102, no. 6, pp. 1464–1473, 1956.

111. M. C. Pochet, "Characterization of the field emission properties of carbon nanotube films formed on silicon carbide substrates by surface decomposition," Ph.D. dissertation, Air Force Institute of Technology, 2006.

112. C. Poulain, G. Jourdan, A. Peschot, and V. Mandrillon, "Contact conductance quantization in a mems switch," *Electrical Contacts, Proceedings of the Annual Holm Conference on Electrical Contacts*, pp. 356–362, 2010.

113. R. Timsit, "Electrical conduction through small contact spots," *IEEE Trans. Compon. Packag. Technol.*, vol. 29, pp. 727–727–734, 2006.

114. C. Poulain, A. Peschot, M. Vincent, and N. Bonifaci, "A nano-scale investigation of material transfer phenomena at make in a mems switch," in *Electrical Contacts (Holm), 2011 IEEE 57th Holm Conference on*, 2011, pp. 1–7, iD: 1.

115. R. Baughman, A. Zakhidov, and W. deHeer, "Carbon nanotubes - the route toward applications," *Science*, vol. 297, p. 787, 2002.

116. A. Dumitriu and D. Dragoman, "Composite metamaterial for ballistic electrons," *Journal of Physics D: Applied Physics*, vol. 45, no. 48, p. 485104, 2012. [Online]. Available: http://stacks.iop.org/0022-3727/45/i=48/a=485104

117. A. Dyson and B. K. Ridley, "High-field transport and terahertz generation in gan," *Journal of Applied Physics*, vol. 104, no. 11, pp. –, 2008. [Online]. Available: http://scitation.aip.org/content/aip/journal/jap/104/11/10.1063/1.3032272

118. V. Favrilenko and Z. Krasil'nik, "Negative mass cyclotron resonance maser," *Opt. Quantum Electron.*, vol. 23, pp. S323–39, 1991.

119. Z. Gribnikov, R. Bashirov, and V. Mitin, "Negative effective mass mechanism of negative differential drift velocity and terahertz generation," *Selected Topics in Quantum Electronics, IEEE Journal of*, vol. 7, no. 4, pp. 630–640, Jul 2001.

120. F. Gomez-Campos, S. Rodriguez-Bolivar, and J. Carceller, "A new approach to analyzing anisotropic and non-parabolic effects on quantum wires," *J. Comput. Electron.*, vol. 7, pp. 342–5, 2008.

121. X. Guo and J. Cao, "Negative effective mass induced by in-plane magnetic fields in n-doped wide quantum wells," *Physics Letters A*, vol. 354, no. 3, pp. 226 – 231, 2006. [Online]. Available: http://www.sciencedirect.com/science/article/pii/S0375960106001447

122. C. Volkert and A. Minor, "Focused ion beam: Microscopy and micromachining," *MRS Bulletin*, vol. 32, no. 389, p. 1557, 2007.

123. B. L. Crossley, "Carbon nanotube field emission arrays," Ph.D. dissertation, Air Force Institute of Technology, 2011.

124. H. W. Deckman and J. H. Dunsmuir, "Natural lithography," *Applied Physics Letters*, vol. 41, no. 4, pp. 377–379, 1982. [Online]. Available: http://scitation.aip.org/content/aip/journal/apl/41/4/10.1063/1.93501

125. C. L. Haynes and R. P. Van Duyne, "Nanosphere lithography:? a versatile nanofabrication tool for studies of size-dependent nanoparticle optics," *The Journal of Physical Chemistry B*, vol. 105, no. 24, pp. 5599–5611, 2001. [Online]. Available: http://pubs.acs.org/doi/abs/10.1021/jp010657m

126. B. Lee, S. Kim, J. Lee, N. Kim, and Y. Roh, "Nanometer-scaled triangular platinum islands fabricated using the bridge phenomenon of polystyrene beads," *J. Vac. Sci. Technol. A*, vol. 26, pp. 819–823, 2008.

127. C. Haginoya, M. Ishibashi, and K. Koike, "Nanostructure array fabrication with a size-controllable natural lithography," *Applied Physics Letters*, vol. 71, no. 20, pp. 2934–2936, 1997. [Online]. Available: http://scitation.aip.org/content/aip/journal/apl/71/20/10.1063/1.120220

128. S. Baek and R. Fearing, "Reducing contact resistance using compliant nickel nanowire arrays," *IEEE Trans.Compon. Packag. Technol.*, vol. 31, pp. 859–859–68, 2008.

129. Y. Wang, W. Zhou, and Z. Weidong, "A review on inorganic nanostructure self-assembly." *Journal of Nanoscience and Nanotechnology*, vol. 10, no. 3, pp. 1563–1583, 2010. [Online]. Available: http://openurl.ingenta.com/content/xref?genre=article&issn=1533-4880&volume=10&issue=3&spage=1563

130. S. J. Barcelo, S.-t. Lam, G. a. Gibson, X. Sheng, and D. Henze, "Nanosphere lithography based technique for fabrication of large area , well ordered metal particle arrays abstract : Nanosphere lithography based technique for fabrication of large area , well ordered metal particle arrays," *Advances*, 2012.

131. T. Laurvick, R. A. Coutu Jr., J. M. Sattler, and R. A. Lake, "Surface feature engineering through nanosphere lithography," *Journal of Micro/Nanolithography, MEMS, and MOEMS*, 2016.

132. A. Kosiorek, W. Kandulski, P. Chutzinski, K. Kempa, and M. Giersig, "Shadow nanosphere lithography: Simulation and experiment," *Nano Letters*, vol. 4, no. 7, pp. 1359–1363, 2004.

133. P. Stravroulakis, N. Christou, and D. Bagnall, "Improved deposition of large scale ordered nanosphere monolayers via liquid surface self-assembly," *Materials Science and Engineering B*, vol. 165, pp. 186–189, 2009.

134. C. C. Ho, P. Y. Chen, K. H. Lin, W. T. Juan, and W. L. Lee, "Fabrication of monolayer of polymer/nanospheres hybrid at a water-air interface," *ACS Applied Materials and Interfaces*, vol. 3, no. 2, pp. 204–208, 2011.

135. C. D. Dushkin, H. Yoshimura, and K. Nagayama, "Nucleation and growth of two-dimensional colloidal crystals," *Chemical Physics Letters*, vol. 204, no. 5-6, pp. 455–460, 1993.

136. J. Hulteen and R. V. Duyne, "Nanosphere lithography: A materials general fabrication process for periodic particle array surfaces," *J. Vac. Sci. Technolo. A*, vol. 13, no. 3, pp. 153–1558, 1994.

137. Y. H. Song, D. H. Choi, H. H. Yang, and J. B. Yoon, "An extremely low contact-resistance mems relay using meshed drain structure and soft insulating layer," *Microelectromechanical Systems, Journal of*, vol. 20, no. 1, pp. 204–212, Feb 2011.

138. M. Myers, M. Leidner, S. Sachs, and A. Baeumer, "Contact resistance reduction by matching current and mechanical load carrying asperity junctions," 2012.

139. B. Toler, C. Stilson, and R. Coutu, "Contact resistance evolution of au-au microcontacts with encapsulated ag colloids," in *Holm Conference on Electrical Contacts (HOLM), 2013 IEEE 59th.* IEEE, 2013, pp. 1–8.

140. B. Wagner, H. Quenzer, W. Henke, W. Hoppe, and W. Pilz, "Microfabrication of complex surface topographies using grey-tone lithography," *Sensors and Actuators A: Physical*, vol. 46, no. 1, pp. 89–94, 1995.

141. T.-K. Chou and K. Najafi, "Fabrication of out-of-plane curved surfaces in si by utilizing rie lag," in *Micro Electro Mechanical Systems, 2002. The Fifteenth IEEE International Conference on.* IEEE, 2002, pp. 145–148.

142. C. Waits, B. Morgan, M. Kastantin, and R. Ghodssi, "Microfabrication of 3d silicon mems structures using gray-scale lithography and deep reactive ion etching," *Sensors and Actuators A: Physical*, vol. 119, no. 1, pp. 245–253, 2005.

143. C. Beuret, G.-A. Racine, J. Gobet, R. Luthier, and N. de Rooij, "Microfabrication of 3d multidirectional inclined structures by uv lithography and electroplating," in *Micro Electro Mechanical Systems, 1994, MEMS'94, Proceedings, IEEE Workshop on.* IEEE, 1994, pp. 81–85.

144. Y. Oppliger, P. Sixt, J. Stauffer, J. Mayor, P. Regnault, and G. Voirin, "One-step 3d shaping using a gray-tone mask for optical and microelectronic applications," *Microelectronic Engineering*, vol. 23, no. 1, pp. 449–454, 1994.

145. T. J. Suleski, D. C. O?Shea *et al.*, "Gray-scale masks for diffractive-optics fabrication: I. commercial slide imagers," *Applied Optics*, vol. 34, no. 32, pp. 7507–7517, 1995.

146. H. Wu, T. W. Odom, and G. M. Whitesides, "Reduction photolithography using microlens arrays:? applications in gray scale photolithography," *Analytical Chemistry*, vol. 74, no. 14, pp. 3267–3273, 2002, pMID: 12139028. [Online]. Available: http://pubs.acs.org/doi/abs/10.1021/ac020151f

147. A. Ahnood, K. Ghaffarzadeh, A. Nathan, P. Servati, F. Li, M. R. Esmaeili-Rad, and A. Sazonov, "Non-ohmic contact resistance and field-effect mobility in nanocrystalline silicon thin film transistors," *Applied Physics Letters*, vol. 93, no. 16, pp. –, 2008. [Online]. Available: http://scitation.aip.org/content/aip/journal/apl/93/16/10.1063/1.2999590

148. S. Karmalkar, P. V. Mohan, and B. P. Kumar, "A unified compact model of electrical and thermal 3-d spreading resistance between eccentric rectangular and circular contacts," *IEEE Electron Device Letters*, vol. 26, no. 12, pp. 909–912, 2005.

149. G. Norberg, S. Dejanovic, and H. HesselBom, "Contact resistance of thin metal film contacts," *IEEE Trans. Compon. Packag. Technol.*, vol. 29, pp. 371–371–378, 2006.

150. M. W. Denhoff, "An accurate calculation of spreading resistance," *Journal of Physics D: Applied Physics*, vol. 39, no. 9, p. 1761, 2006. [Online]. Available: http://stacks.iop.org/0022-3727/39/i=9/a=009

151. R. Timsit, "Constriction resistance of thin film contacts," *Components and Packaging Technologies, IEEE Transactions on*, vol. 33, no. 3, pp. 636–642, 2010.

152. S. Sawada, S. Tsukiji, S. Shimada, T. Tamai, and Y. Hattori, "Current density analysis of thin film effect in contact area on led wafer," *2012 IEEE 58th Holm Conference on Electrical Contacts (Holm)*, pp. 1–6, 2012. [Online]. Available: http://ieeexplore.ieee.org/lpdocs/epic03/wrapper.htm?arnumber=6336576

153. P. Zhang, Y. Y. Lau, and R. S. Timsit, "Spreading resistance of a contact spot on a thin film," *2013 IEEE 59th Holm Conference on Electrical Contacts (Holm 2013)*, pp. 1–7, 2013. [Online]. Available: http://ieeexplore.ieee.org/lpdocs/epic03/wrapper.htm?arnumber=6651426

154. M. Read, J. Lang, A. Slocum, and R. Martens, "Contact resistance in flat thin films." Institute of Electrical and Electronics Engineers, 2009.

155. L. Meng and M. P. dos Santos, "A study of residual stress on rf reactively sputtered ruo¡ sub¿ 2¡/sub¿ thin films," *Thin Solid Films*, vol. 375, no. 1, pp. 29–32, 2000.

156. H. Y. Lee, Y. W. Hsieh, C. H. Hsu, and K. S. Liang, "Characteristics of sputter-deposited ru thin films on si substrates," *Materials chemistry and physics*, vol. 82, no. 3, pp. 984–990, 2003.

157. G. Gregori and D. R. Clarke, "The interrelation between adhesion, contact creep, and roughness on the life of gold contacts in radio-frequency microswitches," *Journal of Applied Physics*, vol. 100, pp. 1–10, 2006.

158. V. S. Cortes and G. Fischer, "Shunt mems switch requirements for tunable matching network at 1 . 9 ghz in composite substrates," *GeMiC*, vol. March 16-1, pp. 422–425, 2015.

159. A. K. Chaurasia and R. Mehra, "Robust design of rf mems switch design with reduced buckeling effect," *International Journal of Computer Applications*, vol. 119, no. 24, 2015.

160. V. Mulloni, B. Margesin, F. B. Kessler, R. Marcelli, G. D. Angelis, C.-i. Roma, and P. Farinelli, "Cycling reliability of rf-mems switches with gold-platinum multilayers as contact material," 2015.

161. A. Basu, R. P. Hennessy, G. G. Adams, and N. E. McGruer, "Hot switching damage mechanisms in mems contacts—evidence and understanding," *Journal*

of Micromechanics and Microengineering, vol. 24, no. 10, pp. 1–16, 2014. [Online]. Available: http://stacks.iop.org/0960-1317/24/i=10/a=105004?key=crossref.584c89374b9d105728badfdb62795a31

162. B. Toler, "Novel test fixture for characterizing microcontacts: Performacne and reliability," Master's thesis, Air Force Institute of Technology, 2013.

163. C. Stilson, B. Toler, and R. Coutu, "Micro-contact performance characterization of carbon nanotube (cnt)-au composite micro-contacts," in *Holm Conference on Electrical Contacts (HOLM), 2013 IEEE 59th*. IEEE, 2013, pp. 1–9.

164. T. Laurvick, C. Stilson, and R. A. Coutu Jr., "Experimental investigation of thin film spreading resistance in micro-contacts," *Electrical Contacts (Holm), 2014 IEEE 60th Holm Conference on*, pp. 1–6, 2014.

165. C. Stilson, R. Pal, and R. A. Coutu Jr., "Fabrication of 3d surface structures using grayscale lithography," *Micromachining and Microfabrication Process Technology XIX, February 4, 2014 - February 6*, vol. 8973, no. 937, 2014.

166. C. Stilson and R. Coutu, "Reliability evolution of au-au, au-ru and au-ruo2 micro-contacts," *Proceedings of the 27th International Conference on Electrical Contacts; ICEC 2014*, pp. 1–6, 2014.

167. S. Weekes, F. Ogrin, W. Murray, and P. Keatley, "Macroscopic arrays of magnetic nanostructures from self-assembled nanosphere templates," *Langmuir*, vol. 23, pp. 1057–1060, 2007.

168. T. Laurvick, R. A. Coutu, and R. A. Lake, "Integrating nanosphere lithography in device fabrication," *SPIE Advanced Lithography*, vol. 9779, pp. 97 791S–13, 2016.

169. P. Zhang, Y. Y. Lau, D. Hung, and R. M. Gilgenbach, "Spreading resistance on thin film contacts," in *APS Meeting Abstracts*, oct 2012, p. 7011, provided by the SAO/NASA Astrophysics Data System. [Online]. Available: http://adsabs.harvard.edu/abs/2012APS..DPPJO7011Z

170. T. V. Laurvick and R. A. Coutu, "Experimental validation of external load effects on micro-contact performance and reliability," *2015 IEEE 61st Holm Conference on Electrical Contacts (Holm)*, pp. 353–357, 2015. [Online]. Available: http://ieeexplore.ieee.org/lpdocs/epic03/wrapper.htm?arnumber=7355120

171. Y. H. Ting, C. C. Liu, S. M. Park, H. Jiang, P. F. Nealey, and A. E. Wendt, "Surface roughening of polystyrene and poly(methyl methacrylate) in ar/o2 plasma etching," *Polymers*, vol. 2, no. 4, pp. 649–663, 2010.

172. C. Stilson, T. Laurvick, and R. A. Coutu Jr., "Contact resistance evaluation of micro-contacts with upper hemisphere and lower planar or engineered surfaces," *Electrical Contacts (Holm), 2014 IEEE 60th Holm Conference on*, pp. 1–8, 2014.

173. C. Stilson and R. Coutu, "Micro-contact resistance of au-au on engineered contact surfaces using gray-scale lithography," pp. 381–386, 2014.

Vita

Maj. Tod Laurvick grew up in Superior, WI, where he graduated from Superior Senior High School in 1989 before attending college first at the Univeristy of Minnesota, Duluth followed by Michigan Technological University. After obtaining his B.S. in Electrical Engineering, he went on to spend the next 9 years working in California, using his degree in industry where he designed factory automation systems and applied robotics applications. In 2004 he commissioned as a Second Lieutenant, and started his Air Force career at Edwards AFB as a flight test engineer for the Airborn Laser program, first with the 452nd flight test squadron and later helped to stand up the 417th flight test squadron. In 2008 he was selected to attend the Air Force Institute of Technology (AFIT) where he received his M.S. in Electrical Engineering. He went on to serve at Kirtland AFB at the Starfire Optical Range, where he was both a program manager for the Sodium Guidestar program as well as a section chief for the Space Programs section. In 2012 he was again selected to attend AFIT to continue his education, and after completing his PhD, to continue at AFIT as an Assistant Professor of Microelectronics and Microelectromechanical Systems.

REPORT DOCUMENTATION PAGE

Form Approved
OMB No. 0704–0188

1. REPORT DATE *(DD–MM–YYYY)*	2. REPORT TYPE	3. DATES COVERED *(From — To)*
22-12–2016	Doctoral Dissertation	Oct 2013–Dec 2016

4. TITLE AND SUBTITLE

Improvements to Micro-Contact Performance and Reliability

5a. CONTRACT NUMBER

5b. GRANT NUMBER

5c. PROGRAM ELEMENT NUMBER

6. AUTHOR(S)

Laurvick, Tod V., Maj, USAF

5d. PROJECT NUMBER

5e. TASK NUMBER

5f. WORK UNIT NUMBER

7. PERFORMING ORGANIZATION NAME(S) AND ADDRESS(ES)

Air Force Institute of Technology
Graduate School of Engineering and Management (AFIT/EN)
2950 Hobson Way
WPAFB OH 45433-7765

8. PERFORMING ORGANIZATION REPORT NUMBER

AFIT-ENG-DS-16-D-003

9. SPONSORING / MONITORING AGENCY NAME(S) AND ADDRESS(ES)

Intentionally Left Blank

10. SPONSOR/MONITOR'S ACRONYM(S)

11. SPONSOR/MONITOR'S REPORT NUMBER(S)

12. DISTRIBUTION / AVAILABILITY STATEMENT

DISTRIBUTION STATEMENT A: APPROVED FOR PUBLIC RELEASE; DISTRIBUTION UNLIMITED.

13. SUPPLEMENTARY NOTES

This material is declaired a work of the U.S. Government and is not subject to copyright protection in the United States.

14. ABSTRACT

Microelectromechanical Systems (MEMS) based devices, and specifically micro switches, continue to offer many advantages over competing technologies. To realize the benefits of micro-switches, improvements must be made to address performance and reliability shortfalls which have long been an issue with this application. To improve the performance of these devices, the micro-contacts used in this technology must be understood to allow for design improvements, and offer a means for testing to validate this technology and determine when such improvements are ready for operational environments. To build devices which are more robust and capable of continued operation after billions of cycles requires that improved fabrication techniques be identified and perfected to allow for more sophisticated designs to be tested. This work explores and advances two potential fabrication techniques to suit this task: nanosphere lithography and grayscale lithography. By utilizing 3-D printed deposition vessels, a method of nanosphere assembly is demonstrated which repeatably produces over 50% surface coverage. A hybrid photoresist / nanosphere patterning technique is then demonstrated, to allow for precise alignment of nanospheres required for integration into device fabrication. An alternate method of fabrication which utilizes improved grayscale lithography is also demonstrated. This technique allows for rapid fabrication of complex three dimensional structures as part of a full wafer fabrication process, resulting in twice the resolution from previous efforts using the same hardware. This provides a customizable patterning technique for the thousands of devices with near-perfect repeatability of duplicate devices, or complete customization of each device if desired. Another crucial fabrication characteristic of micro-contacts involves the thin-films used as a contact surface. This work demonstrates that integration of thin-film spreading resistance theory into the most advanced contact resistance models to date results in a reduction in the variance between predicted vs. observed results by approximately 70%. External factors to micro-contact performance are also explored, providing information critical to designers to create devices better suited for extremely long performance. Low frequency AC testing was conducted to bridge the gap between RF applications and DC conditions typically used to characterized these devices. The results show that low frequency, low amplitude AC signals have potential to greatly accelerate device failure. For example, in devices proven to work well under DC conditions (e.g. still operating after 10 million cycles), with AC signals applied, 10 out of 11 devices failed before reaching 10 million cycles. However, the addition of protective external circuit configurations conclusively shows this damage can be mitigated, with only 2 out of 15 devices failing in subsequent tests. Finally, data gathered from devices during failure reveal an indicator which may provide a novel method of predictive failure detection. This method could one day be applied in-situ, to diagnose and identify devices in which failure is imminent and allow for corrective action to minimize impacts to overall functionality.

15. SUBJECT TERMS

Micro-contact, Gray-scale, Nanosphere Lithography, Thin-film resistance

16. SECURITY CLASSIFICATION OF:			17. LIMITATION OF ABSTRACT	18. NUMBER OF PAGES	19a. NAME OF RESPONSIBLE PERSON
a. REPORT	b. ABSTRACT	c. THIS PAGE			Capt. Robert A. Lake, Ph.D.(ENG)
U	U	U	U	240	19b. TELEPHONE NUMBER *(include area code)* (937) 255-3636 x4550 Robert.Lake@afit.edu